Matrix Development for Water Vapor Resistant SiC-Based Ceramic Matrix Composites

A Dissertation

Presented to

the faculty of the School of Engineering and Applied Science

University of Virginia

in partial fulfillment

of the requirements for the degree

Doctor of Philosophy

by

Robert Alexander Sean Golden

May

2017

APPROVAL SHEET

The dissertation

is submitted in partial fulfillment of the requirements

for the degree of

Doctor of Philosophy

_____
AUTHOR

The dissertation has been read and approved by the examining committee:

Elizabeth Opila, Advisor
_____
Advisor

Hadyn Wadley
_____

Harsha Chelliah
_____

William Soffa
_____

Olivier Sudre, PhD
_____

_____

Accepted for the School of Engineering and Applied Science:

Craig H. Benson, Dean, School of Engineering and Applied Science

May

2017

Acknowledgements

Abstract

SiC fiber-reinforced SiC matrix Ceramic Matrix Composites (SiC/SiC CMCs) have entered service in gas turbine engines to increase engine efficiency by operating at higher temperatures and reducing the weight of engine components. In this environment the SiC fibers and matrix oxidize to form a SiO_2 scale that reacts with water vapor to produce volatile $Si(OH)_4$ (g). Formation of volatile $Si(OH)_4$ (g) leads to recession of SiC fibers and matrix which will shorten the life of SiC/SiC CMC engine components. This work explores three alternative matrix material concepts for improving the water vapor resistance of SiC-based CMCs. These candidate matrix materials include 1) yttrium disilicate ($Y_2Si_2O_7$), 2) SiC particulate – $Y_2Si_2O_7$ and 3) yttrium silicides. The thermochemical stability of these matrix candidates was investigated in oxidizing and high-velocity water vapor environments.

The thermochemical stability of Spark Plasma Sintered (SPS) $Y_2Si_2O_7$ was assessed at temperatures of 1000 – 1200°C for times up to 250 hours at steam velocities of 130 – 180 m/s. These exposures resulted in the selective volatilization of SiO_2 to form volatile $Si(OH)_4$ (g) and porous Y_2SiO_5. SiO_2 depletion from $Y_2Si_2O_7$ followed parabolic kinetics at 1200°C. Mechanisms contributing to the overall depletion reaction were evaluated and include gas diffusion through pores, Y_2SiO_5 coarsening and development of tortuosity in the pore network.

The diffusivity of oxygen in a candidate matrix material must be sufficiently low to limit the oxidation of SiC fibers and matrix within the composite. Oxygen diffusion coefficients in SPS $Y_2Si_2O_7$ and SPS Y_2SiO_5 were determined using the oxygen tracer diffusion technique. The [18]O diffusion concentration profiles were measured after exposure at diffusion temperatures of 1000 – 1300°C using Time-of-Flight Secondary Ion Mass Spectrometry (ToF-SIMS). Oxygen tracer diffusion coefficients were obtained by fitting the semi-infinite solution of the diffusion

equation to the concentration profiles. Oxygen diffusion coefficients in yttrium silicates ranged from $10^{-12} – 10^{-14}$ cm^2/s. Preferred transport of ^{18}O along grain boundaries, pores and in some grain orientations (anisotropic diffusion) was observed.

The thermochemical stability of SPS 60 vol% SiC particulate – 40 vol% $Y_2Si_2O_7$ in oxidizing and high-velocity water vapor environments was investigated at temperatures from 1000 – 1200°C for times of 60 – 250 hours. Oxidation in air resulted in the formation of a multiphase oxide scale consisting of SiO_2 and $Y_2Si_2O_7$. Parabolic oxidation kinetics were observed at 1200°C indicating the oxidation rate was controlled by the diffusion of oxygen through the SiO_2 scale. Slower oxide growth at 1000°C prevented the rapid sealing of pores and cracks resulting in higher overall weight changes. In high-temperature high-velocity water vapor, SiC particulate – $Y_2Si_2O_7$ specimens suffered from rapid material loss due to the preferential oxidation/volatilization of SiC and erosion of remaining $Y_2Si_2O_7$ particles.

The ability of yttrium silicides to form yttrium silicates (phases with greater stability in high-temperature water vapor than SiO_2) in high-temperature oxidizing environments was investigated. Yttrium silicides with compositions of 41, 67 and 95 at% Si-Y were fabricated using arc melting and oxidized at 1000°C and 1200°C for times up to 24 hours in air. Oxidation resulted in the rapid formation of a non-protective Y_2O_3 scale and rejected Si with additional minor oxide phases. Thermodynamic and kinetic considerations indicate that rare-earth silicides are unsuitable as matrix materials for CMCs.

The findings in this study demonstrate that the $Y_2Si_2O_7$ matrix is the most promising matrix concept as it possesses sufficient thermochemical stability in high temperature water vapor and sufficiently low oxygen diffusivities.

Table of Contents

List of Figures

List of Tables

1. Introduction

Demands for next generation gas turbine engines that are more powerful and fuel efficient will require a significant increase in the turbine inlet temperature [1–3]. Over the past 50 years the gas turbine inlet temperature has increased due to advances in nickel-base superalloys, Thermal Barrier Coatings (TBCs) and air-cooling technologies (Figure 1.1) [1, 2, 4–7]. The operating temperatures of today's engines are now approaching the melting temperature (T_m) of nickel-base superalloys, therefore, further increases to the gas turbine inlet temperature are not possible without the implementation of advanced TBCs with lower thermal conductivity or new material systems that can operate at higher temperatures. Silicon Carbide fiber reinforced Silicon Carbide matrix Ceramic Matrix Composites (SiC/SiC CMCs) are attractive materials to replace nickel-base superalloy hot section components because they possess requisite toughness and damage tolerance with the added advantages of lower density (~1/3 of nickel-base superalloys) and the ability to operate at higher temperatures (~1400°C) without the need for cooling air [2, 3, 8, 9]. The first SiC/SiC CMCs entered service in 2016 as high-pressure turbine shrouds in CFM LEAP engines [10].
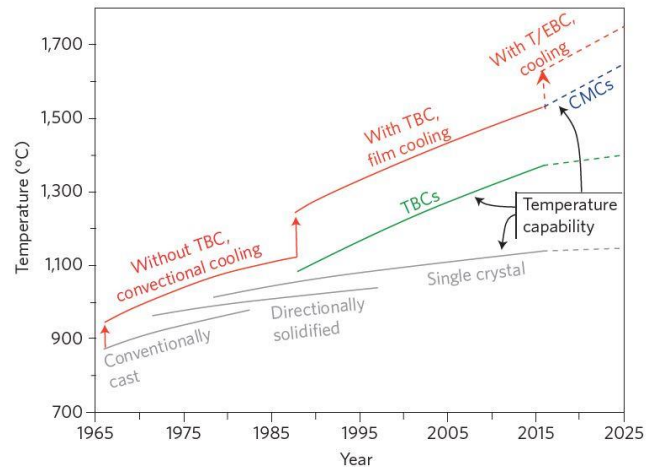
Figure 1.1. Evolution of turbine inlet gas temperature with the implementation of turbine blade materials, cooling concepts, coatings and SiC/SiC CMCs [2].

1.1. Silicon Carbide Ceramic Matrix Composites

1.1.1. SiC/SiC CMC Architecture and Fabrication

A SiC/SiC CMC is composed of a layup of or woven SiC fibers (such as Hi-Nicalon, HiNicalon S and Sylramic [8, 11–14]) that are coated with a thin boron nitride (BN) interphase (< 1 µm) which is embedded in a Si/SiC matrix (Figure 1.2). The BN interphase is typically applied by Chemical Vapor Deposition (CVD) or Chemical Vapor Infiltration (CVI) from a gaseous precursor. Its main function is to arrest and/or deflect microcracks in the matrix that form under load thereby protecting the SiC fibers from early failure and allowing for fiber pullout during crack propagation, imparting damage tolerance [2, 11, 15–17]. The Si/SiC matrix is incorporated into the CMC by one or more of the following processing routes [3, 11, 14, 16, 17]. The first route involves CVI where SiC is infiltrated into the fiber preform from a gaseous precursor. This process yields fully dense SiC and a composite with 10 – 15% residual porosity. The second route involves infiltrating particle slurries into fiber preforms via immersion or pressure assisted routes followed by sintering. Sintering alone does not densify the matrix so this route is combined with

2

one involving precursor derived ceramics or melt-infiltration, as described below. The third route

uses a polymer impregnation and pyrolysis (PIP) process to infiltrate a polymer precursor of the

matrix into the fiber preform that will form SiC upon pyrolysis. This process results in composite

with $\geq$ 10% porosity. The fourth route uses melt-infiltration where the fiber preform is

consolidated with carbon and infiltrated with liquid Si where the liquid Si reacts with carbon to

form SiC + residual Si. This processing route yields a SiC/SiC CMC with low residual porosity,

high thermal conductivity and hermeticity allowing for good thermal shock resistance, damage

tolerance and resistance to internal oxidation of the fibers, interphase and matrix via fast

diffusion pathways.
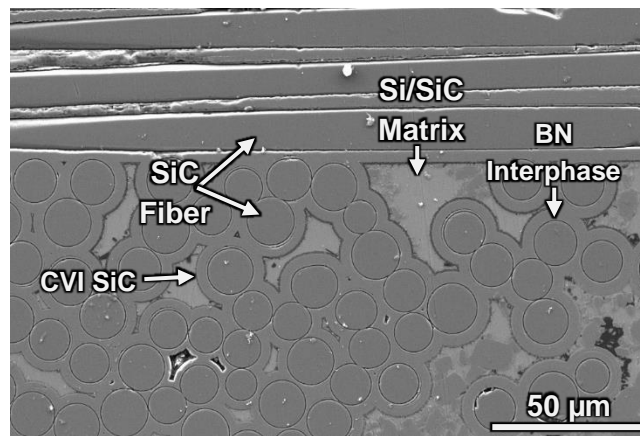
Figure 1.2. SEM image of a cross-sectioned SiC/SiC CMC.

1.1.2. *Oxidation and Volatilization Behavior of SiC*

SiC possess excellent oxidation resistance at high temperatures in a dry oxygen

environment due to the formation of a solid, slow growing, protective silica scale (Equation

(1.1)) [18–21].

$$SiC + \frac{3}{2}O_2 \ (g) = \ SiO_2 + CO \ (g) \qquad\qquad (1.1)$$
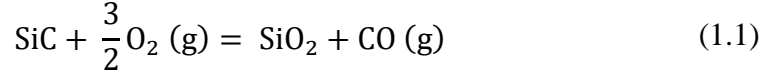
The slow growth of the protective SiO_2 scale exhibits parabolic oxidation kinetics [18, 19, 21–23]. In a combustion environment however, SiC undergoes an oxidation and volatilization reaction where the silica scale reacts with water vapor (Equation (1.2)), a product of combustion reactions (~10% independent of the fuel-to-air ratio [24]), and forms a gaseous silicon hydroxide species (Equation (1.3)) [20–23, 25, 26].

$$SiC + \ 3H_2O \ (g) = \ SiO_2 + 3H_2 \ (g) + \ CO \ (g) \qquad\qquad (1.2)$$

$$SiO_2 + \ 2H_2O \ (g) = \ Si(OH)_4 \ (g) \qquad\qquad (1.3)$$
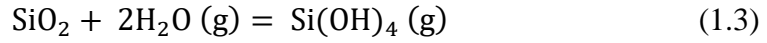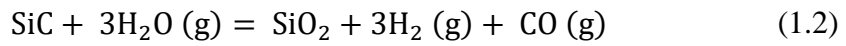
The SiC oxidation kinetics remain parabolic whereas the volatilization of SiO_2 exhibits linear kinetics [20–23, 25, 26]. Since these reactions occur simultaneously the oxidation and volatilization behavior of SiC is described by paralinear kinetics. In high-temperature high-velocity water vapor environments that are representative of a turbine engine (T= 1200 – 1500°C, $v_{(g)}$= 20 – 250 m/s, $P(H_2O)$= 0.27 – 1 atm) SiC recession rates greater than 0.2 µm/h have been reported [20, 27–30]. These unacceptably high recession rates would lead to significant degradation of SiC/SiC CMCs over the thousands of hours required for the service lives of gas turbine engine components. Therefore an oxide that is more thermochemically stable than SiO_2 must be applied in the form of an Environmental Barrier Coating (EBC) to protect SiC/SiC CMCs from high temperature water vapor.

Currently it is assumed that the EBC will remain adhered to the SiC/SiC CMC substrate during the full life of the component (e.g. CMCs are used with prime reliant EBCs). However, this is difficult to guarantee for civil turbine engine applications that can require a service life greater than 10,000 hours. This prime reliance on EBCs could limit the number of applications available for SiC/SiC CMCs in a gas turbine engine. An alternative method of limiting the

volatilization of SiC/SiC CMCs is to develop a matrix that is more resistant to high temperature water vapor attack than the current Si/SiC matrix. Improving the water vapor resistance of a CMC could move the function of the EBC to life extension rather than being the prime reliant method of protection against high temperature water vapor. The objective of this work is to explore concepts for the development of a water vapor resistant CMC matrix material for SiC-based CMCs.

1.2. Matrix Material Requirements

A water vapor resistant matrix material must meet several criteria to adequately protect the load bearing SiC fibers in SiC-based CMCs. These criteria are similar to those for EBCs [31]. Firstly, the matrix must be thermochemically stable in high temperature water vapor. Secondly, the matrix must possess a CTE close to that of the substrate material to prevent cracking of the CMC during thermal cycling due to CTE mismatch stress. Thirdly, the matrix must maintain a stable phase under thermal exposure to prevent disruption of the CMC with the volumetric change that typically accompanies a phase transformation. In the case where the formation of a thermochemically stable oxide upon oxidation of the matrix is desirable, the volume change associated with the oxide(s) formation must be sufficiently small so as to not compromise the CMC if a subsurface oxide forms. Fourthly, the matrix must be chemically compatible with SiC to avoid detrimental chemical reactions with the fibers and CVI SiC. Fifth, the matrix must possess a high melting temperature so to not limit the operating temperature of the CMC. Currently the operating temperature of SiC/SiC CMCs are limited by the melting temperature of silicon (T_m= 1414°C [32]). Lastly, the oxygen diffusivity in the matrix must be sufficiently low to limit oxidation of the CVI SiC, BN interphase and SiC fibers. An oxygen diffusivity benchmark

of $\leq 1.1 \times 10^{-11}$ cm^2/s is proposed as sufficient to protect SiC-based CMCs for service lives up to 10,000 hours. This oxygen diffusivity benchmark was calculated using Equation (1.4),

$$x^2 = Dt \qquad\qquad (1.4)$$

where x is the diffusion depth (200 µm) and t is the service life of the component (10,000 h).

Candidate matrix materials must also satisfy a number of other requirements such as resistance to calcium magnesium aluminosilicate (CMAS) [33–38], hot corrosion [24, 39–41] and erosion/ foreign object damage (FOD) [38, 42, 43] however these degradation modes are beyond the scope of this dissertation.

1.3. Matrix Material Candidates

1.3.1. Mullite and Barium Strontium Aluminosilicate

Mullite and Barium Strontium Aluminosilicate (BSAS) were used as first and second generation EBC materials and were found to exhibit good CTE matches and chemical compatibility with SiC [31, 44–46]. Additionally, the oxygen diffusivity in mullite is sufficiently low [47, 48]. However, these silicates are not sufficiently stable due to their high rates of silica volatility in high temperature water vapor environments [27, 31, 44–46, 49–51]. In addition, mullite and BSAS have a maximum use temperature of ~1300°C [44] which is lower than the desired operation temperature of SiC-based CMCs and EBCs in the next generation gas turbine engines (>1400°C) [8].

1.3.2. Rare-Earth Silicates

Rare-earth silicates are considered here as candidate matrix materials for SiC-based CMCs due to their low CTE mismatch with SiC [27, 45, 49, 52–56], relative phase stability [57] and high

melting temperatures (1720 – 1980°C) [58, 59]. Rare-earth silicate systems all contain mono and/or

disilicates the majority of which have polymorphs with transformation temperatures ranging

from ~1000 – 1600°C. However, the mono and disilicates in the Ce, Tm, Yb and Lu silicate

systems contain no polymorphs. Rare-earth silicates have the potential to be incorporated into the

CMC fiber preform via sol-gel or polymer slurry processing routes [14, 60–64].

Silica is selectively volatilized from rare-earth disilicates (RE = rare-earth element) in a

high-temperature water vapor environment to form a porous surface layer of rare-earth

monosilicate and silicon hydroxide gas (Equation (1.5)) [27, 45, 49, 50, 65–69, 60, 70]:

$$RE_2Si_2O_7 + 2H_2O \ (g) = \ RE_2SiO_5 + Si(OH)_4(g) \hspace{2cm} (1.5)$$

The silica depletion rates of rare-earth disilicates have been found to be less than those of SiO_2

and mullite and similar to BSAS. In contrast, rare-earth monosilicates (with the exception of

Sc_2SiO_5) have been found to exhibit superior thermochemical stability in high temperature water

vapor environments compared to their respective disilicates [27, 45, 49, 67, 71]. As a result, rare-earth

disilicates should exhibit superior thermochemical stability compared to BSAS over long times

since the depletion of silica from a rare-earth disilicate results in a layer of rare-earth

monosilicate that will slow the silica depletion rate from the underlying disilicate. The greater

stability of rare-earth monosilicates in high temperature water vapor can be attributed to the

lower silica activity of the $RE_2O_3 + RE_2SiO_5$ two phase mixture compared to the $RE_2SiO_5 +$

$RE_2Si_2O_7$ two phase mixture. This was demonstrated in Knudsen Effusion Mass Spectrometry

(KEMS) studies by Jacobson [72] and Costa et al. [73] for the $Y_2O_3 – SiO_2$ system and $Yb_2O_3 – SiO_2$

system respectively. Although the rare-earth monosilicates exhibit superior thermochemical

stability in high-temperature water vapor compared to their respective disilicates, the CTE

mismatch between SiC and rare-earth monosilicates is large enough to cause stresses that could

compromise the structural integrity of the CMC. Therefore, rare-earth disilicates show the most promise as a candidate matrix material for SiC-based CMCs.

There has not yet been a thorough evaluation of the thermochemical stability of a single rare-earth disilicate despite the moderate amount of high temperature water vapor studies that have been performed on rare-earth disilicates. The microstructural evolution of rare-earth disilicates and volatilization kinetics as a function of time and temperature are still unknown. In addition, the mechanism(s) that control the volatilization rate of silica from rare-earth disilicates is not understood. A full evaluation is needed to properly assess the ability of rare-earth disilicates to act as a water vapor resistant matrix for SiC-based CMCs.

1.3.3. Rare-Earth Silicides

Rare-earth silicides are also considered here as candidate matrix materials due to their potential to form oxides (RE_2O_3, RE_2SiO_5, $RE_2Si_2O_7$) that are thermochemically stable in high temperature water vapor [27, 45, 49, 50, 60, 65, 66, 68–71, 74], relative phase stability and their high melting temperatures [32, 75–85]. The Y, Nd, Sm, Gd and Ho silicide systems contain RE_3Si_5 and/or $RESi_2$ phases with α and β polymorphs [32, 78–80, 82]. In addition, most rare-earth silicides have melting temperatures that range from 1500 – 2150°C however the Sc, La, Ce, Nd, Ho and Yb silicide systems have RE_5Si_3, RE_3Si_4, RE_3Si_5 and/or $RESi_2$ phases that have melting temperatures below 1425°C [75–78, 82, 84, 85]. Rare-earth silicides have the potential to be incorporated into the CMC fiber preform via melt-infiltration (MI), similar to the Si in the matrix of current SiC/SiC CMCs.

To date there have been few studies that have investigated the oxidation behavior of rare-earth silicides at elevated temperatures (≥ 500°C) [86–88]. These studies report that RE_2O_3 and RE-Si-O form upon oxidation however they offer no information regarding the oxide microstructure

and its evolution as a function of time and temperature. A study by Poerschke [89] investigated the oxidation behavior of a densified polymer infiltration and pyrolysis (PIP) compact of SiC + YB$_2$ + Y$_5$Si$_3$ + Al$_2$O$_3$. While RE silicates were observed, the complex phase assemblage prevents determination of the fundamental oxidation mechanism(s) of RE silicides. A thorough study that investigates the high temperature oxidation behavior of a single rare-earth silicide system is needed to properly assess the ability of rare-earth silicides to act as a thermochemically stable matrix for SiC-based CMCs.

1.4. Assessing the Thermochemical Stability of Candidate Matrix Materials

One of the challenges in assessing the thermochemical stability of candidate matrix materials for SiC-based CMCs is the ability to accurately simulate the high-temperature high-velocity water vapor present in a turbine engine environment and quantitatively measure material reaction rates in reasonable test times at a reasonable cost. Laboratory furnaces, such as thermogravimetric analyzers (TGA) and cyclic furnaces, are inadequate because of the long exposure times required to achieve measurable material reaction rates at the low steam velocities that can be achieved [21, 45, 50, 60, 67, 69, 69, 70]. In addition, furnace ware components form volatile hydroxide species in the presence of water vapor at elevated temperatures (e.g. Al(OH)$_3$ (g)) which can react with the test specimen. Some rare-earth oxides and silicates have been observed to gain weight due to the volatile hydroxide species reacting/depositing during exposure [45, 60, 69]. Burner rigs, high pressure burner rigs (HPBR) and steam injection furnaces provide a means of simulating a turbine engine environment however they are expensive to build and operate [27, 29, 49, 65, 66, 68, 71]. A steam-jet furnace developed by Lucato et al. [30] provides a means of simulating a turbine engine environment and is significantly more economical to build and operate compared

to burner rigs, HPBR and steam injection furnaces. The steam-jet furnace is capable of simulating the temperatures (1000 – 1500°C) and steam velocities (up to 200 m/s) of a turbine engine operating at 10 atm total pressure with 10% water vapor. This approach of testing was adopted for this dissertation.

1.5. Dissertation Research Approach

The thermochemical stability and oxidation behavior of model rare-earth silicate and rare-earth silicide systems was investigated to determine if they possess the necessary high temperature stability to improve the water vapor resistance of SiC-based CMCs. Three matrix material concepts are described in this dissertation; a yttrium disilicate matrix, a yttrium disilicate + silicon carbide particulate matrix and a yttrium silicide matrix. The Y_2O_3 –SiO_2 (Figure 1.3) and Y – Si (Figure 1.4) systems were chosen over other rare-earths since yttrium silicates satisfy most of the criteria a matrix material must have for a CMC and that phases of the Y-Si system may oxidize to form the desired yttrium silicates. In addition, thermodynamic data are available for both the Y_2O_3 – SiO_2 [59, 90] and Y – Si systems [91] making them ideal model rare-earth silicate and silicide systems for study.

1.5.1. Y_2O_3 – SiO_2 System

There have been limited experimental determinations of the thermochemical stability of yttrium silicates in high temperature water vapor however results indicate that yttrium silicates do possess sufficient stability for use as a water vapor resistant matrix material for SiC-based CMCs [27, 45, 49, 50, 60, 67]. $Y_2Si_2O_7$ was observed to react with water vapor to form a porous Y_2SiO_5 and a volatile silicon hydroxide gas per Equation (1.5). It was found that Y_2SiO_5 exhibits

significantly greater thermochemical stability than $Y_2Si_2O_7$ in all studies with the exception of a study by Courcot et al. [67] where the opposite was found. Of these studies, only those by Fritsch [49] and Klemm [27] exposed yttrium silicates in a high-temperature (1450°C) high-velocity (100 m/s) water vapor environment representative of a turbine engine. None of the studies show the microstructural evolution of $Y_2Si_2O_7$ as a function of time or temperature after exposure to high temperature water vapor.

While Y_2SiO_5 exhibits excellent thermochemical stability in high temperature water vapor, it has a large CTE mismatch with SiC whereas $Y_2Si_2O_7$ possesses a good match to SiC (Table 1.1). Although $Y_2Si_2O_7$ does have four polymorphs (triclinic – α, monoclinic – β & γ, orthorhombic – δ) [59, 92, 93] the volume change that accompanies most polymorphic transformations is expected to be small since the density of each polymorph is similar with the exception of the α polymorph (α= 4.30, β= 4.03, γ= 4.04, δ= 4.11 g/cm^3) [93]. However, the large difference in CTE between the α, δ polymorphs and the β, γ polymorphs may lead to crack formation under thermal cycling conditions (Table 1.1) [54]. Similarly, Y_2SiO_5 possesses two polymorphs (X_1, X_2) with differences in their CTE (Table 1.1) [94]. There is controversy over the temperatures associated with the polymorphic transformations in $Y_2Si_2O_7$ and Y_2SiO_5 therefore the temperatures reported in Table 1.1 represent the widely accepted polymorphic transformation temperatures [55, 59, 92–99]. The melt temperatures of $Y_2Si_2O_7$ and Y_2SiO_5 reported in Table 1.1 are those that have been observed experimentally [92, 93, 100].

There have been limited studies that have investigated the chemical compatibility between yttrium silicates and SiC in high temperature oxidizing and water vapor environments [59, 60]. Experimental results by Liu et al. [60] show that $Y_2Si_2O_7$ does possess good chemical compatibility with SiC in high temperature water vapor whereas Y_2SiO_5 does not. A Y_2SiO_5

11

coating that was deposited on SiC was found to react with the thermally grown SiO_2 scale at the

SiC – Y_2SiO_5 interface to form $Y_2Si_2O_7$. Yttrium silicates possess sufficiently high melting

temperatures for matrix material application where $Y_2Si_2O_7$ has a melting temperature of 1775°C

and Y_2SiO_5 has a melting temperature of 1980°C (Table 1.1) [92, 93, 100]. The oxygen diffusivity in

yttrium silicates has also been scarcely studied. No oxygen diffusivity data for $Y_2Si_2O_7$ has been

reported while studies by Argirusis et al. [101, 102] have measured the oxygen diffusivity in <100>

and <010> Y_2SiO_5 single crystals at temperatures from 1100 – 1500°C (Table 1.1). The results

of these studies show promise for polycrystalline Y_2SiO_5 to have sufficiently low oxygen

diffusivities for use as a matrix material in SiC – based CMCs.
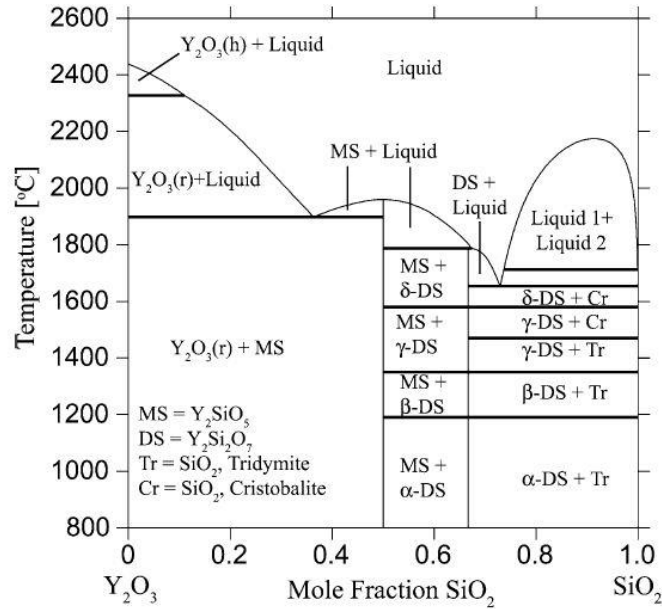
Figure 1.3. Y_2O_3 – SiO_2 system phase diagram [59]. Note the melt and polymorphic transformation temperatures for $Y_2Si_2O_7$ and Y_2SiO_5 are different than the values reported in Table 1.1.

Table 1.1. Coefficient of thermal expansion (CTE), melt/transformation temperature, and oxygen diffusivity data for SiC, Si, $Y_2Si_2O_7$, Y_2SiO_5, and Y_2O_3

Material	Crystal Structure/ Polymorph	CTE (x 10^{-6} °C^{-1})	Melt/ Transformation Temperature (°C)	Oxygen Diffusivity (cm^2/s)
SiC	Hexagonal, β	3.5 – 5.5 [27, 45, 49, 53]	2823[‡ 59]	n/a
Si	Diamond Cubic	3.4 – 4.8 [45, 52]	1414 [59]	n/a
$Y_2Si_2O_7$	Orthorhombic, α	8.0 [54]	1225 [92, 93]	Unknown
	Monoclinic, β	4.1 [54]	1445 [92, 93]	
	Monoclinic, γ	3.9 [54]	1535 [92, 93]	
	Orthorhombic, δ	8.1 [54]	1775 [92, 93, 100]	
Y_2SiO_5	Monoclinic, X1	8.7 [94]	1190 [92, 93]	~3.1 x 10^{-15} – 2 x 10^{-12} (1100 – 1500°C) [101, 102]
	Monoclinic, X2	7.8 [94]	1980 [100]	
Y_2O_3	Cubic[*], Hexagonal[†]	8.2 – 9.5 [*, 53, 103]	2410 [†, 59, 104]	~4x 10^{-9} – 1 x 10^{-8} (1000 – 1300°C)[*, 105]

[‡] SiC decomposes to liquid (~82 mol% Si) + graphite.
[*, †] denotes the cubic and hexagonal values respectively for Y_2O_3.
CTE were measured from room temperature up to 1500°C.

1.5.2. Y – Si System

The Y – Si system is comprised of the Y_5Si_3, Y_5Si_4, YSi, Y_3Si_5 and YSi_2 phases with melting temperatures that range from 1520 – 1850°C (Figure 1.4) [32]. The Y_3Si_5 and YSi_2 phases possess a low temperature (α) and a high temperature (β) polymorph. The Y_3Si_5 phase has an α polymorph with an orthorhombic structure and a β polymorph with a hexagonal structure. The opposite is true for the polymorphs of the YSi_2 phase where α is hexagonal and β is orthorhombic. The volume change that accompanies these polymorphic transformations is small

$(< \pm 1.9\%)$ since the theoretical density of each polymorph is similar (Y_3Si_5: $\alpha= 12.54$ g/cm^3, $\beta= 12.78$ g/cm^3; YSi_2: $\alpha= 4.57$ g/cm^3, $\beta= 4.53$ g/cm^3). There has been some controversy regarding the existence of the YSi_2 phase since orthorhombic $\alpha - Y_3Si_5$ and $\beta - YSi_2$ have very similar lattice parameters [32]. The CTE of the YSi_2 phase is 6.9×10^{-6} °C^{-1} which is considerably higher than that of SiC [106]. No CTE data were found in literature for other yttrium silicide phases.
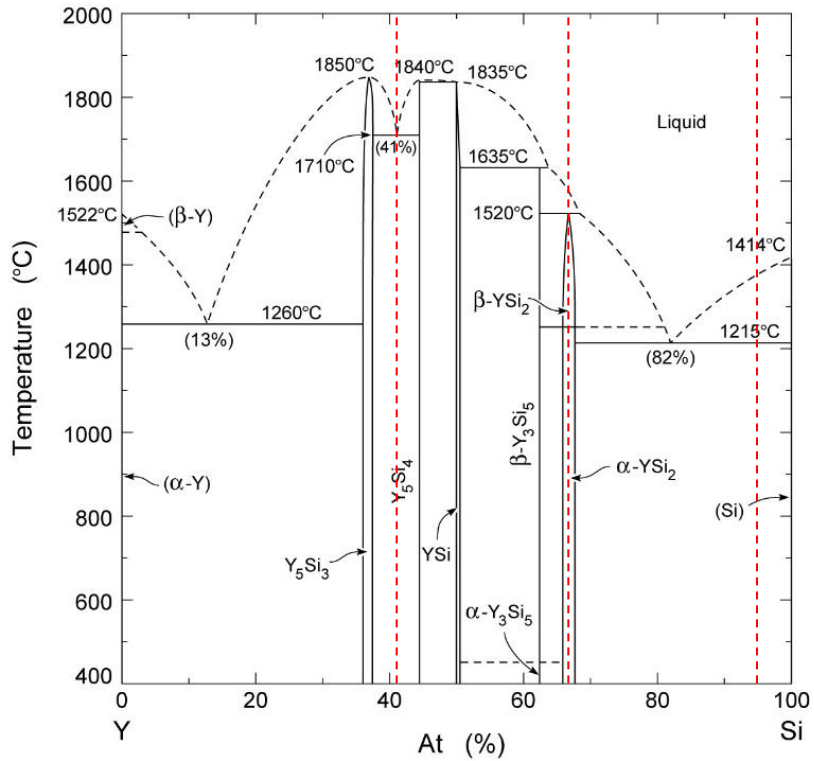
Figure 1.4. Y – Si system phase diagram (adapted from [32]). Vertical red dotted lines show the 41, 67 and 95 at% Si-Y alloy compositions studied (Chapter 7).

Oxide phases that may form during the oxidation of yttrium silicides include Y_2O_3, Y_2SiO_5, and $Y_2Si_2O_7$. The thermochemical stability in high temperature water vapor, CTE, phase stability, chemical compatibility, melting temperature and oxygen diffusivity of Y_2SiO_5 and $Y_2Si_2O_7$ were discussed in Section 1.5.1. Of the oxides that may form from yttrium silicides,

14

Y$_2$O$_3$ is the most thermochemically stable in high temperature water vapor however it has a large CTE mismatch with SiC (Table 1.1). Y$_2$O$_3$ possesses a low temperature cubic polymorph and a high temperature hexagonal polymorph with a transformation temperature of 2325°C and a melt temperature of 2410°C [59, 104] (Table 1.1). The cubic to hexagonal transformation temperature is well beyond the operating temperature of next generation gas turbine engines.

The volume change associated with the formation of oxide(s) that are thermochemically stable in high-temperature water vapor must be sufficiently small so as to not compromise the CMC when a subsurface oxide forms, as discussed in Section 1.2. The volume expansion associated with the formation of SiO$_2$ from Si and SiC is 114% and 105% respectively (Table 1.2). The volume expansion was calculated by dividing the sum of the molar volumes of the solid products by the sum of the molar volumes of the solid reactants, then subtracting 1 and multiplying by 100% (e.g. the molar volume of Si is 12.06 cm^3/mol whereas SiO$_2$ (cristobalite) is 25.77 cm^3/mol). Oxidation reactions of yttrium silicides are accompanied by the rejection of Si which is considered in the calculated volume change (Table 1.2). All yttrium silicides, with the exception of the Y$_3$Si$_5$ phase, have volume expansions that range from ~27 – 47% when oxidizing to form Y$_2$O$_3$ and Si, ~42 – 58% when oxidizing to form Y$_2$SiO$_5$ and Si and ~64 – 72% when oxidizing to form Y$_2$SiO$_7$ and Si as per the reactions in Table 1.2. The Y$_3$Si$_5$ phase has volume expansions that range from 294 – 376% when oxidizing to form Y$_2$O$_3$, Y$_2$SiO$_5$ or Y$_2$Si$_2$O$_7$ and Si (Table 1.2). The large volume change associated with the oxidation of the Y$_3$Si$_5$ phase is attributed to its larger density (α= 12.54 g/cm^3, β= 12.78 g/cm^3) compared to other yttrium silicide phases (4.52 – 4.69 g/cm^3). Although the volume expansion associated with the oxidation of most yttrium silicides are smaller than that for Si and SiC, the rate at which oxidation occurs can significantly affect the thermal stability of a CMC. Oxides that form

quickly but have a small volume expansion associated with their formation can be equally or more detrimental to the structural integrity of a CMC. The oxidation rate of Si and SiC are known to be slow at high temperatures ($\geq 1000°C$) while the oxidation rates of yttrium silicides are currently unknown [21, 107]. The oxygen diffusivity in Y_2O_3 is significantly greater than that of Y_2SiO_5 and is too high for use as a matrix material in SiC-based CMCs (Table 1.1).

Table 1.2. Specific volume change associated with the oxidation of Si, SiC and yttrium silicides.

Y – Si Phase	Oxidation Reaction	Specific Volume Change (%)
Si	$Si + O_2$ (g) $\rightarrow$ **SiO_2** (cristobalite)	+ 114
SiC	$SiC + 3/2\ O_2$ (g) $\rightarrow$ **SiO_2** (cristobalite) + CO (g)	+ 105
Y_5Si_3	$2/5\ Y_5Si_3 + 3/2\ O_2$ (g) $\rightarrow$ **Y_2O_3** + 6/5 Si	+ 27.4
	$2/5\ Y_5Si_3 + 5/2\ O_2$ (g) $\rightarrow$ **YMS** + 1/6 Si	+ 42.0
	n/a	n/a
Y_5Si_4	$2/5\ Y_5Si_4 + 3/2\ O_2$ (g) $\rightarrow$ **Y_2O_3** + 8/5 Si	+ 35.4
	$2/5\ YSi_2 + 5/2\ O_2$ (g) $\rightarrow$ **YMS** + 3/5 Si	+ 50.7
	n/a	n/a
YSi	$2YSi + 3/2\ O_2$ (g) $\rightarrow$ **Y_2O_3** + 2 Si	+ 33.6
	$2YSi + 5/2\ O_2$ (g) $\rightarrow$ **YMS** + Si	+ 47.6
	$2YSi + 7/2\ O_2$ (g) $\rightarrow$ **YDS**	+ 64.0
Y_3Si_5 - α	$2/3\ Y_3Si_5 + 3/2\ O_2$ (g) $\rightarrow$ **Y_2O_3** + 10/3 Si	+ 294
	$2/3\ Y_3Si_5 + 5/2\ O_2$ (g) $\rightarrow$ **YMS** + 7/3 Si	+ 327
	$2/3\ Y_3Si_5 + 7/2\ O_2$ (g) $\rightarrow$ **YDS** + 4/3 Si	+367
Y_3Si_5 - β	$2/3\ Y_3Si_5 + 3/2\ O_2$ (g) $\rightarrow$ **Y_2O_3** + 10/3 Si	+ 302
	$2/3\ Y_3Si_5 + 5/2\ O_2$ (g) $\rightarrow$ **YMS** + 7/3 Si	+ 336
	$2/3\ Y_3Si_5 + 7/2\ O_2$ (g) $\rightarrow$ **YDS** + 4/3 Si	+ 376
YSi_2 - α	$2\ YSi_2 + 3/2\ O_2$ (g) $\rightarrow$ **Y_2O_3** + 4 Si	+ 47.0
	$2\ YSi_2 + 5/2\ O_2$ (g) $\rightarrow$ **YMS** + 3 Si	+ 58.4
	$2\ YSi_2 + 7/2\ O_2$ (g) $\rightarrow$ **YDS** + 2 Si	+ 71.8
YSi_2 - β	$2\ YSi_2 + 3/2\ O_2$ (g) $\rightarrow$ **Y_2O_3** + 4 Si	+ 45.6
	$2\ YSi_2 + 5/2\ O_2$ (g) $\rightarrow$ **YMS** + 3 Si	+ 56.9
	$2\ YSi_2 + 7/2\ O_2$ (g) $\rightarrow$ **YDS** + 2 Si	+ 70.2

YMS = Y_2SiO_5
YDS = $Y_2Si_2O_7$

1.6. Dissertation Objectives

1.6.1. Chapter 3: Optimization and Validation of the Steam-Jet Furnace

The objectives of this chapter are to modify and optimize the steam-jet furnace design of

Lucato et al. [30] for testing of candidate matrix materials for SiC-based CMCs. In addition, the

steam-jet furnace is validated through comparison of measured to calculated SiO_2 recession

rates. The capabilities of the steam-jet furnace are demonstrated using studies of the binary metal

oxides of SiO_2, TiO_2 and Y_2O_3. Lastly, results of this work are used to resolve controversies in

the literature on the volatility of TiO_2 and Y_2O_3 in high-temperature water vapor.

1.6.2. Chapter 4: Thermochemical Stability of Y$_2$Si$_2$O$_7$

The objectives of this chapter are twofold. First, the thermochemical stability of $Y_2Si_2O_7$

is assessed in a high-temperature high-velocity water vapor environment by measuring the SiO_2

depletion as a function of time and temperature. Second, factors affecting the SiO_2 depletion

from $Y_2Si_2O_7$ are identified and discussed.

1.6.3. Chapter 5: Oxygen Diffusivity in Yttrium Silicates

The objective of this chapter is to measure the oxygen diffusivity in $Y_2Si_2O_7$ and Y_2SiO_5

using the tracer diffusion technique to assess the ability of yttrium silicates to protect SiC-based

CMCs from oxidation.

1.6.4. Chapter 6: Thermochemical Stability of SiC Particulate – Y$_2$Si$_2$O$_7$

The objectives of this chapter are threefold. First, the oxidation behavior of a SiC

particulate – $Y_2Si_2O_7$ composite is studied as a function of time and temperature in air. Oxide

morphology and kinetics are interpreted to identify the diffusion mechanism(s) that control oxide growth. Second, the thermochemical stability of the SiC particulate – $Y_2Si_2O_7$ composite is studied in a high-temperature high-velocity water vapor environment. Oxide morphology and volatilization kinetics are interpreted to identify the reactions that resulted in material recession. Finally, oxidation and volatilization kinetics of the SiC particulate – $Y_2Si_2O_7$ composite in high-temperature oxygen and water vapor containing environments are compared to those of SiC and SiO_2 to determine if a SiC – $Y_2Si_2O_7$ matrix additive improves the water vapor stability of SiC-based CMCs.

1.6.5. *Chapter 7: Thermochemical Stability of Yttrium Silicides*

The objectives of this chapter are threefold. First, the oxidation behavior of yttrium silicides is characterized as a function of alloy composition, temperature and time. Second, the oxide morphology and kinetics are interpreted to identify the diffusion mechanism(s) that control oxide growth. Finally, the suitability of RE silicides for use as MI matrix materials in SiC-based CMCs is evaluated.

2. Experimental Procedures

2.1. Materials

Test specimens of amorphous SiO_2 (99.995% pure; Quartz Scientific Inc., Fairport Harbor, OH), single crystal TiO_2 <001> (99.99% pure; MTI Corp., Richmond, CA) and polycrystalline Y_2O_3 (99.99% pure; MaTeck, Juelich, Germany) were used to validate and demonstrate the capabilities of the steam-jet furnace (Chapter 3). $Y_2Si_2O_7$ and Y_2SiO_5 specimens for steam-jet exposures (Chapter 4) and oxygen tracer diffusion studies (Chapter 5) were fabricated from powder (99.9% pure, ~ 50 µm granule size; Praxair Surface Technologies, Compton, CA). SiC powder (99.9% pure, $\leq$ 1 µm particle size; Materion, Milwaukee, WI) was mixed with $Y_2Si_2O_7$ powder at a volume ratio of 3:2 respectively to make the 60 vol% SiC particulate – 40 vol% $Y_2Si_2O_7$ matrix specimens for oxidation and steam-jet exposures (Chapter 6). Pure SiC (> 99.9995%) specimens made via Chemical Vapor Deposition (CVD; Pure SiC LR, CoorsTek, Golden, CO) were oxidized and compared to SiC particulate – $Y_2Si_2O_7$ matrix specimens. Yttrium silicides were fabricated from yttrium (99.99% pure; Stanford Advanced Materials, Irvine, CA) and silicon (99.999% pure; ESPI Metals, Ashland, OR) metal (Chapter 7).

2.2. Specimen Fabrication

2.2.1. Spark Plasma Sintering

$Y_2Si_2O_7$, Y_2SiO_5 and SiC particulate – $Y_2Si_2O_7$ powders were consolidated by Spark Plasma Sintering (SPS; Model 10-4, Thermal Technolgy LLC, Santa Rosa, CA). $Y_2Si_2O_7$ and Y_2SiO_5 powders (~10 – 20 g) were ball milled in Nalgene bottles using 12.7 mm (0.5") high density ZrO_2 beads (Glen Mills Inc., Clifton, NJ) for 21 – 27 hours to break up the large powder granules into a powder with a particle size approximately < 3 µm (Figure 2.1). SiC particulate –

$Y_2Si_2O_7$ powder was ball milled for 6 hours to ensure the powders were mixed together. After ball milling, the $Y_2Si_2O_7$, Y_2SiO_5 and SiC particulate – $Y_2Si_2O_7$ powders (10 – 20 g) were prepared for spark plasma sintering by charging the respective powders into a graphite die that was 20 mm in diameter. The SPS chamber was evacuated ($\sim$2x10^{-2} torr) and backfilled to 1 atm with argon. The SPS conditions and densities are detailed in Table 2.1. The system was heated to 600°C at which time 65 MPa pressure was applied and maintained at both peak hold temperatures and during initial stages of cooling. Hold times varied depending on the size of the charge. After cooling to 600°C, the pressure was reduced from 65 MPa to 5 MPa at a rate of 10 MPa/min. Following SPS the 20 mm diameter $Y_2Si_2O_7$, Y_2SiO_5 and SiC particulate – $Y_2Si_2O_7$ pucks (~7-11 mm in height) were sectioned using a low speed saw (Buehler, Lake Bluff, IL) into ~10 x 10 x 1.5 mm specimens. The $Y_2Si_2O_7$ and Y_2SiO_5 specimens were annealed in air at 1350°C for 24 hours to eliminate oxygen deficiencies which formed during SPS. The surface of the annealed $Y_2Si_2O_7$ and Y_2SiO_5 specimens and the as-processed SiC particulate – $Y_2Si_2O_7$ specimens were polished to a 1 µm finish with diamond (Allied High Tech Products Inc., Rancho Dominguez, CA). Additional polishing to a 0.25 µm finish with diamond and a 0.04 µm finish with colloidal silica (Struers, Cleveland, OH) was performed on $Y_2Si_2O_7$ and Y_2SiO_5 specimens that were characterized by Electron Backscatter Diffraction (EBSD) or used for the oxygen tracer diffusion studies (Chapter 5). Specimen dimensions for the oxygen tracer diffusion studies were ~ 2.5 x 2.5 x 1.5 mm. Densities of $Y_2Si_2O_7$, Y_2SiO_5 and SiC particulate – $Y_2Si_2O_7$ specimens were measured using Archimedes' Principle.
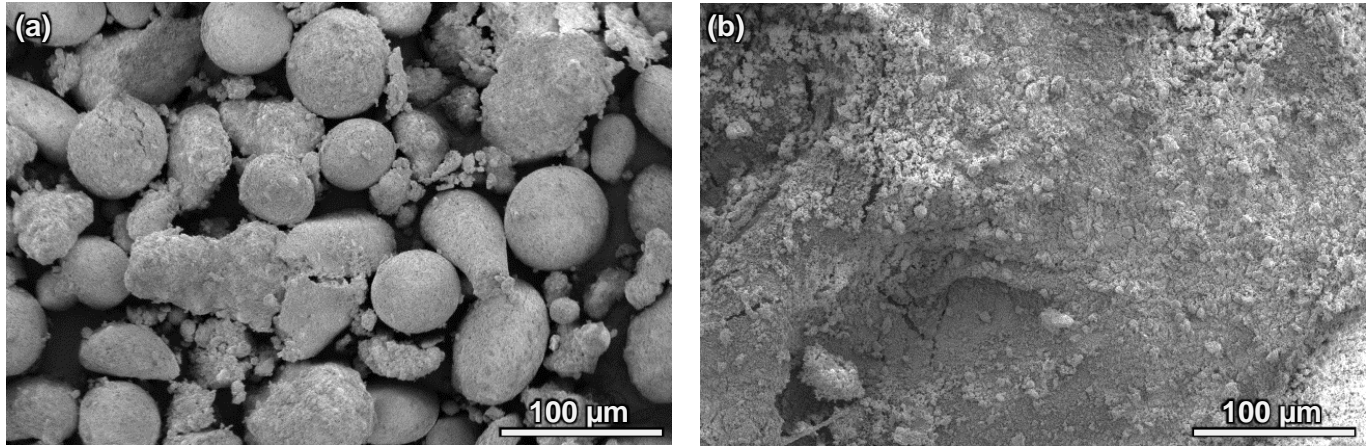
Figure 2.1. As-received $Y_2Si_2O_7$ powder before (a) and after ball milling for 21 hours (b).

Table 2.1. SPS conditions and densities for $Y_2Si_2O_7$, Y_2SiO_5 and SiC particulate – $Y_2Si_2O_7$ test specimens.

Material	Heating	Isothermal Hold	Cooling	% of Theoretical Density
$Y_2Si_2O_7$	T: 150°C/min P: 65 MPa	T: 1550°C P: 65 MPa t: 12 – 20 min	T: 75°C/min P: 65 MPa	96 – 98
Y_2SiO_5	T: 150°C/min P: 65 MPa	T: 1650°C P: 65 MPa t: 8 – 12 min	T: 10°C/min P: 65 MPa	92 – 93
SiC particulate – $Y_2Si_2O_7$	T: 150°C/min P: 65 MPa	T: 1650°C P: 65 MPa t: 15 – 17 min	T: 75°C/min P: 65 MPa	96 – 98

2.2.2. Arc melting

Yttrium silicide charges with the compositions of 41, 67 and 95 at% Si-balance Y were prepared for arc melting (Marko Materials, Inc., North Billerica, MA). Charges were prepared by weighing the appropriate amount of yttrium and silicon metal to make the desired composition. The total weight of each Y-Si charge was ~25 – 50 grams. Prior to melting, the arc melter

chamber was evacuated to 5×10^{-6} torr and back filled with Ar (25psi). A separate charge of Ti was used as an oxygen getter and was melted before an arc was struck with the Y-Si charge. The Y-Si charge was melted, forming a button which was flipped over and re-melted 2 to 3 times in attempt to create a fully alloyed button. Alloyed yttrium silicide buttons were sectioned using a low speed saw into test specimens for oxidation exposures. The surface of test specimens were polished to a 1 µm finish with diamond prior to oxidation exposures.

2.3. High-Temperature Water Vapor Exposures

The steam-jet apparatus based on a design of Lucato et al.[30] shown schematically in Figure 2.2 uses a horizontal tube furnace (Model 1730-12 HTF, CM Furnace Inc., Bloomfield, NJ) with a 1.375" inner diameter alumina tube (99.8% pure; McDanel Advanced Ceramic Technologies, Beaver Falls, PA) and an inlet stainless steel end cap (MDC Vacuum Products LLC, Hayward, CA) that accommodates feedthroughs for thermocouple, gas, and liquid water inlets.

A peristaltic pump (Reglo Analog MS 2/12, Ismatec SA, Glattburg, Switzerland) fed deionized 18.2 MΩ liquid water into the fused quartz capillary at a controlled flow rate. The liquid water was heated prior to being pumped into the capillary by flowing through copper tubing coiled in a water bath held at ~85°C. The fused quartz capillary (1 mm ID, 3 mm OD, 99.995% pure; Quartz Scientific Inc., Fairport Harbor, OH) is inserted through an ultratorr fitting (Swagelok, Solon, OH) on the end cap and extends into the center of the hot zone. A Pt-13Rh wire (0.5 mm OD) is inserted into the capillary to assist in the heating of liquid water as it travelled down the capillary. The Pt-13Rh wire is 6 – 10 cm shorter than the capillary outlet. Two smaller alumina tubes (23 mm OD) were used inside the furnace tube to support and align

the fused quartz capillary as shown in Figure 2.2. The weight of liquid water was measured throughout the experiment to determine the total amount of liquid water that was pumped into the furnace. The average mass flow rate of the liquid water for the experiment was determined by dividing the total weight of liquid water by the exposure time. Average mass flow rates ranged from 1.53 – 1.77 g/min. Liquid water evaporates as it enters the hot zone of the furnace resulting in a volume expansion forming a jet of high-temperature high-velocity steam. The steam-jet velocity was modeled by CFD analysis (ANSYS CFX, ANSYS Inc., Canonsburg, PA) (Figure 2.3). Inputs to the analysis include the mass flow rate of the liquid water, the steam-jet temperature and the geometry of the fused quartz capillary relative to the test specimen. More details about the ANSYS CFD model can be found in Appendix A. The steam-jet velocity was modeled across the surface of the specimen and the maximum calculated surface velocity was reported with the maximum material degradation depth for each exposure. A thermocouple (type R) inserted through a second inlet on the end cap extended to the center of the hot zone approximately 4 cm from the specimen and remained stationary during the experiment. Prior to each experiment, the steam-jet temperature was calibrated by placing a second thermocouple (type R) approximately 1 mm from the tip of the capillary (the same position of the specimen during the experiment) and recording the temperature of the steam-jet. Steam-jet exposure temperatures varied between 1000°C and 1400°C. This thermocouple was inserted through the open exhaust end of the alumina tube.

Test specimens were mounted in an alumina holder at a 45° angle relative to the steam-jet and held in place by platinum foil and wire. The alumina holder was pushed into the tube furnace and locked into place in front of the capillary. The capillary was adjusted to a position 1 mm away from the surface of the specimen. Experiments were conducted with no outlet endcap so

that 1 atm air was present in the tube surrounding the steam-jet. Photographs of the specimen

holder were taken before and after each experiment and were compared to confirm the specimen

did not shift during the steam-jet exposure. Further details regarding the experimental conditions

used to expose binary metal oxides (Chapter 3), $Y_2Si_2O_7$ (Chapter 4) and SiC particulates –

$Y_2Si_2O_7$ (Chapter 6) specimens in the steam-jet furnace will be provided in their respective

chapters.
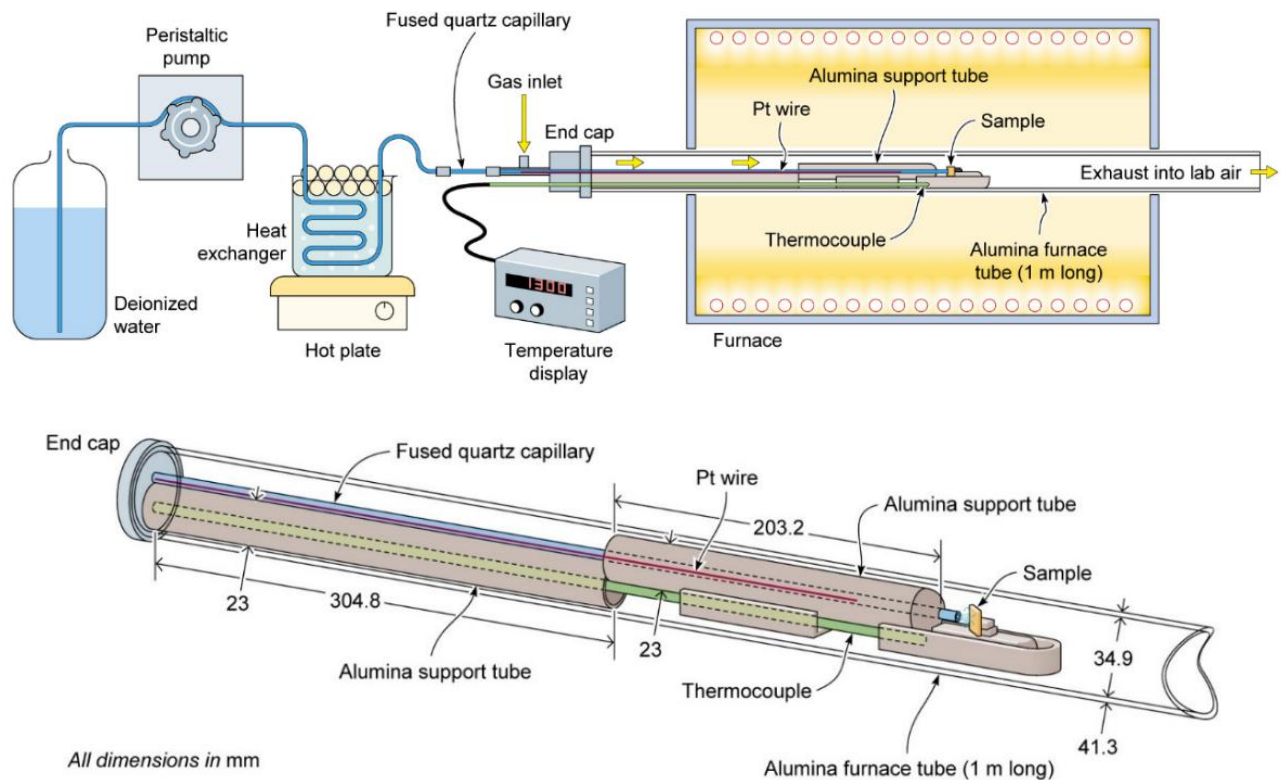
Figure 2.2. Steam-jet furnace schematic.
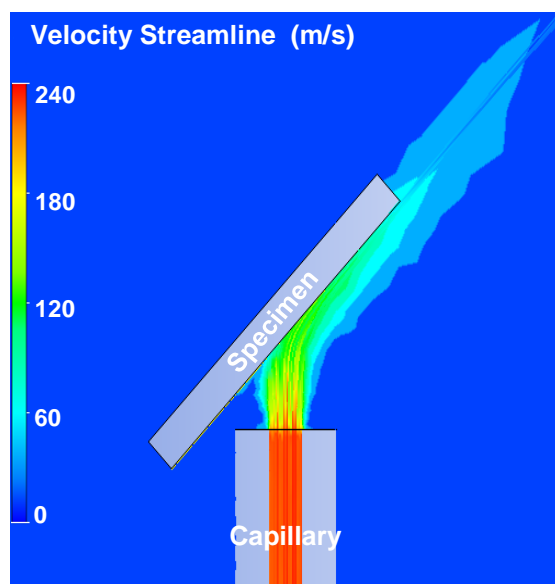
Figure 2.3. ANSYS Computational Fluid Dynamics model geometry with steam-jet velocity profile.

2.4. Oxidation Exposures

SiC particulate – $Y_2Si_2O_7$, CVD SiC and yttrium silicide specimens were oxidized in a box furnace in air (Model 1706 -FL, CM Furnace Inc., Bloomfield, NJ) at temperatures between 1000°C and 1200°C. SiC particulate – $Y_2Si_2O_7$ and CVD SiC specimens were placed on a piece of fused quartz (99.995% pure; Quartz Scientific Inc., Fairport Harbor, OH) that sat inside an alumina boat (99.8% pure, CoorsTek, Golden, CO). The fused quartz slide minimized specimen contamination from the alumina boat. Yttrium silicide specimens were placed directly in the alumina boat. The alumina boat containing the test specimen was inserted and removed from the box furnace at temperature. After removal from the furnace specimens were left to cool in ambient conditions. Further details regarding the experimental conditions used to oxidize SiC

particulates – $Y_2Si_2O_7$, CVD SiC (Chapter 6) and yttrium silicide (Chapter 7) specimens will be provided in their respective chapters.

2.5. Specimen Encapsulation and Diffusion Exposures

A system was constructed to encapsulate SPS $Y_2Si_2O_7$ and Y_2SiO_5 specimens inside a fused quartz tube (7 mm ID, 9 mm OD, 99.995% pure; Quartz Scientific Inc., Fairport Harbor, OH) in a $^{16}O_2$ (Praxair Surface Technologies, Compton, CA) or $^{18}O_2$ (97 at% ^{18}O; Sigma-Aldrich, St. Louis, MO) environment (Figure 2.4). First, the encapsulation system was pumped down to < 10 millitorr and then backfilled with $^{16}O_2$. Specimens encapsulated in a $^{16}O_2$ environment were equilibrated at temperatures from 1000 – 1300°C inside a box furnace for times much longer than the intended $^{18}O_2$ exposure as described in Section 5.4.2. Specimens were removed from the fused quartz tube and cleaned using a three step sonication process in DI water, ethanol and acetone following $^{16}O_2$ equilibration. The system was pumped down to ≤ 8 millitorr and back filled with argon (99.5% pure; Praxair Surface Technologies, Compton, CA) three times prior to encapsulating the equilibrated specimens in $^{18}O_2$. Specimens encapsulated in $^{18}O_2$ were exposed to a diffusion temperature corresponding to their prior $^{16}O_2$ equilibration temperature. The $^{18}O_2$ encapsulated specimens were quenched in water to freeze in the ^{18}O concentration profile upon removal from the furnace. Further details regarding specimen encapsulation and diffusion exposures will be provided in Chapter 5.
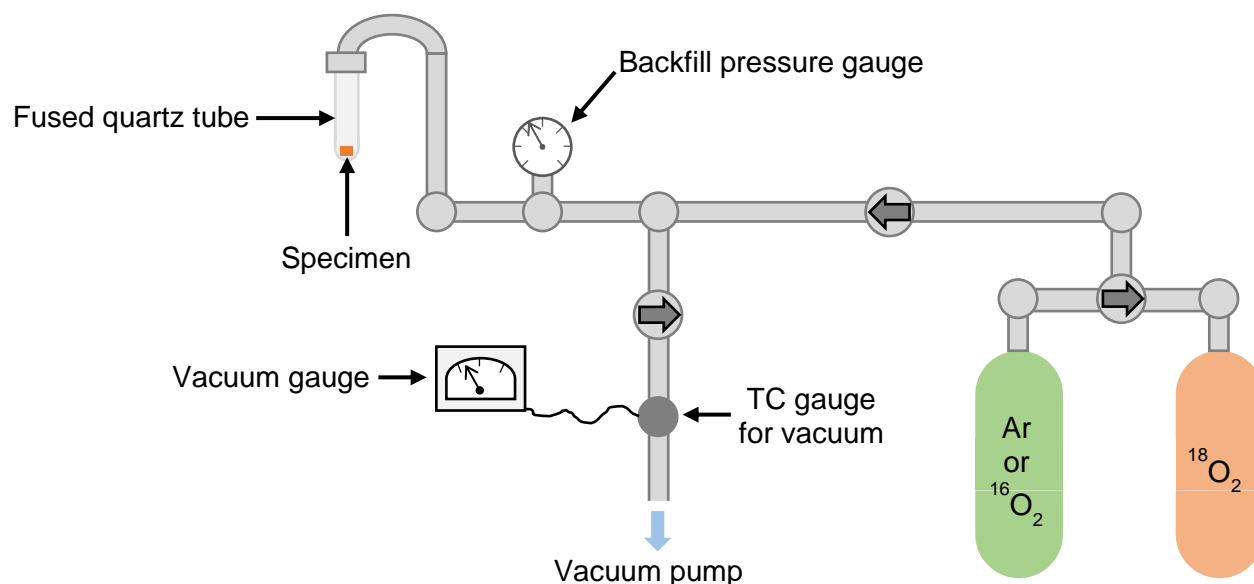
Figure 2.4. Schematic of encapsulation system.

2.6. Characterization

Weights of all specimens were measured before and after steam-jet and oxidation exposures to an accuracy of 0.05 mg (MS105DU, Mettler-Toledo, Columbus, OH). X-ray Diffraction (XRD; Panalytical X'Pert Diffractometer, Westborough, MA) was performed on specimens before and after steam-jet, oxidation and $^{18}O_2$ diffusion exposures to determine if any phase changes or new phases had formed. The recession profile of binary metal oxides and SiC particulate – $Y_2Si_2O_7$ matrix specimens after steam-jet exposures and the sputter depths of yttrium silicate oxygen tracer diffusion specimens were characterized by optical profilometry (Zygo Newview 7300, Middlefield, CT). The microstructure and composition of all specimens were characterized by Scanning Electron Microscopy (SEM; FEI Quanta 600F, Hillsboro, OR) and Energy Dispersive Spectroscopy (EDS; Oxford Instruments Aztec X-Max^N 150, Concord, MA). SEM images that were acquired using secondary electrons will be denoted as SE/SEM

images while images acquired using backscattered electrons will be denoted as BSE/SEM images. All specimens were coated with carbon, chromium or gold/palladium prior to SEM characterization to provide a conductive surface layer (Precision Etching and Coating System Model 682, Gatan Inc., Pleasanton, CA & Technics Sputter Coater). $Y_2Si_2O_7$ specimens were characterized by Electron Backscatter Diffraction (EBSD; Oxford Instruments NordlysNano, Concord, MA) after exposure in the steam-jet to identify phase and crystallographic orientation of grains in $Y_2Si_2O_7$. Time-of-Flight Secondary Ion Mass Spectrometry (ToF-SIMS: ToF-SIMS V, ION TOF, Inc., Chestnut Ridge, NY) was used to measure the ^{18}O concentration profile in ^{18}O exchanged yttrium silicate specimens. A dual beam Focused Ion Beam (FIB; FEI Quanta 3D FEG, Hillsboro, OR) was used to precisely remove a section from the $Y_2SiO_5 - Y_2Si_2O_7$ interface formed on a $Y_2Si_2O_7$ specimen during exposure in the steam-jet furnace and to remove a section of the oxide scale formed on a Y-Si specimen during oxidation. The FIB lift out specimens were characterized by Transmission Electron Microscopy (TEM; FEI Titan, Hillsboro, OR), Electron Energy Loss Spectroscopy (EELS) and Energy Filtered Transmission Electron Microscopy (EFTEM; Gatan 794 Multi-scan Camera, Pleasanton, CA). A Vickers hardness tester (MICROMET 5101, Buehler, Lake Bluff, IL) was used to indent the surface of $Y_2Si_2O_7$ specimens to mark locations of interest for future characterization after exposures to high-temperature high-velocity water vapor. Cross-sectioned TiO_2, $Y_2Si_2O_7$ and SiC particulate – $Y_2Si_2O_7$ specimens were prepared by mounting the specimen in epoxy (EpoThin ^{TM} 2, Buehler, Lake Bluff, IL), cross-sectioning the specimen with a low speed saw and polishing the cross-section to a 1 µm or 0.25 µm finish with diamond. Y_2O_3 cross-sectioned specimens were ion polished (Hitachi Ion Milling System (IM4000), Tokyo, Japan) to preserve microstructural features that would otherwise be damaged during mechanical polishing.

2.7. Thermodynamic Calculations

The partial pressure of $Si(OH)_4$ (g) from the reaction of SiO_2 and $Y_2Si_2O_7$ with water vapor, the oxide product formation from the Y_5Si_3, Y_5Si_4, YSi, Y_3Si_5 and YSi_2 phases and the reaction of Y_2O_3 and SiO_2 was predicted by thermodynamic calculations using the equilibrium module in FactSage [108]. Inputs into the equilibrium module included the SiO_2, Y_2O_3, $Y_2Si_2O_7$ or Y-Si phase of interest, H_2O (g) or O_2 (g), temperature $(100 – 1500°C)$ and the partial pressure of oxygen (1 atm). The SGPS database and custom databases for the $Y_2O_3 – SiO_2$ and $Y – Si$ systems were used for the thermodynamic calculations. Custom databases for the $Y_2O_3 – SiO_2$ and $Y – Si$ systems were made using thermodynamic data from Fabrichnaya et al. [90] and Shukla et al. [91] respectively.

3. Optimization and Validation of the Steam-Jet Furnace

3.1. Objectives

The objectives of this chapter are to modify and optimize the steam-jet furnace design of Lucato et al. [30] for testing of candidate matrix materials for SiC-based CMCs in a high-temperature high-velocity water vapor environment representative of a turbine engine. In addition, the steam-jet furnace is validated through comparison of measured to calculated SiO_2 recession. The capabilities of the steam-jet furnace are demonstrated using studies of the binary metal oxides of SiO_2, TiO_2 and Y_2O_3. Lastly, results of this work are used to resolve controversies in the literature on the volatility of TiO_2 and Y_2O_3 in high temperature water vapor.

3.2. Background: Volatility of SiO_2, TiO_2 and Y_2O_3

The volatility of SiO_2 in high-temperature water vapor by Equation (1.3) has been well studied and is known to have linear volatilization kinetics [20, 21, 29]. In addition, all available thermodynamic data for $Si(OH)_4$ (g) have been assessed by Plyasunov [109].

The volatility of TiO_2 in high-temperature water vapor is less understood. A transpiration study by Nguyen et al. [110] concluded that TiO_2 (rutile) reacts with water vapor by Equation (3.1),

$$TiO_2 + H_2O \text{ (g)} = TiO(OH)_2 \text{ (g)} \qquad (3.1)$$
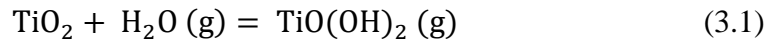
The enthalpy (247 kJ/mol) and entropy (316 kJ/mol) of reaction were also determined. Weight loss rates of TiO_2 (rutile) in high-temperature water vapor have been reported by Ueno et al. (T= 1500°C, $v_{(g)}$=4.6 x 10^{-4} m/s, P(H_2O)= 0.41 atm) [111], however they are significantly higher than the flux calculated for these test conditions using thermodynamic data of Nguyen et al. [110].

The volatility of Y_2O_3 in high-temperature water vapor is controversial. A study by Courcot et al. [112] concluded that above 1200°C, Y_2O_3 reacts with water by Equation (3.2),

$$\frac{1}{2} Y_2O_3 + \frac{3}{2} H_2O \text{ (g)} = Y(OH)_3 \text{ (g)} \qquad\qquad (3.2)$$
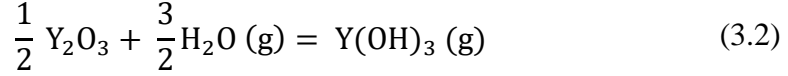
Weight loss data for Y_2O_3 in water vapor at temperatures from $1000 - 1400°C$ at 0.05 m/s linear gas velocity were reported. Thermodynamic data for $Y(OH)_3$ (g) estimated by Krikorian [113] suggest rates of $Y(OH)_3$(g) formation should be orders of magnitude lower than those observed by Courcot et al.

3.3. Experimental

3.3.1. High-Temperature Water Vapor Exposures

The steam-jet apparatus described in Section 2.3 was used to expose SiO_2, TiO_2 and Y_2O_3 in a high-temperature high-velocity water vapor environment. Experiments were performed at $1200 - 1400°C$ for $20 - 192$ hours, steam-jet velocities of $158 - 190$ m/s and 1 atm H_2O pressure. Although the steam-jet furnace is based on a design of Lucato et al. [30] several modifications have been made in this study. Firstly, the specimen orientation and geometry has been modified in this study as shown in Figure 2.2. Lucato et al. directed their steam-jet onto the leading edge of sharp wedge shaped specimens whereas this study directed the steam-jet onto a polished flat face of all test specimens which were orientated at a 45° relative to the steam-jet. This configuration allows for testing of a variety of coupon shapes as well as coated coupons. Secondly, in this study efforts were made to ensure complete vaporization of water. The liquid water was preheated prior to entering the capillary. In addition, a Pt-13Rh wire was inserted into the capillary to assist in the heating of the liquid water as it travelled through the capillary. Thirdly, Lucato et al. flowed argon gas through their mullite furnace tube whereas no argon and an alumina tube were used in this study. Finally, the argon gas and water vapor were extracted

through an exhaust endcap in the study by Lucato et al. whereas no exhaust endcap was used in this study.

3.3.2. Characterization

Weights of all specimens were measured before and after steam-jet exposures to an accuracy of 0.05 mg. X-ray Diffraction (XRD) analysis was performed on specimens before and after steam-jet exposures to determine if any polymorph/phase changes occurred during exposure. Specimen microstructure and composition were characterized by Scanning Electron Microscopy (SEM) and Energy Dispersive Spectroscopy (EDS). SEM images that were acquired using secondary electrons are denoted as SE/SEM images while images acquired using backscattered electrons are denoted as BSE/SEM images. Optical profilometry was used to characterize specimen recession profiles after steam-jet exposures.

3.4. Theory: Gas Boundary Layer Limited Volatility

The volatility rate of an oxide depends on the gas velocity, total pressure, temperature and the partial pressure of water vapor assuming the flux of volatile gas species is limited by diffusion through a gas boundary layer. For a flat plate geometry the Sherwood number, Sh, can be calculated using the following relationship [114]:

$$Sh_l = \frac{k_c L}{D_{AB}} = 0.664 Re^{1/2} Sc^{1/3} \quad (Re < 2 \times 10^5) \quad\quad (3.3)$$

$$Sh_t = \frac{k_c L}{D_{AB}} = 0.0365 Re^{0.8} Sc^{1/3} \quad (Re > 2 \times 10^5) \quad\quad (3.4)$$

where Sh_l and Sh_t are the Sherwood numbers for laminar and turbulent flow respectively, k_c is the convective mass transfer coefficient, L is the characteristic length, D_{AB} is the interdiffusion

coefficient for the volatile species in the gas boundary layer, Re is the Reynolds number and Sc is the Schmidt number describing gas boundary layer properties. The mass flux, J, can be calculated by the following relationship [114]:

$$J = k_c \rho' \tag{3.5}$$

where ρ' is the equilibrium concentration of the volatile species at the oxide – gas interface. Substituting Equations (3.3) & (3.4) into Equation (3.5) and expanding the Reynolds and Schmidt numbers results in,

$$J_l = 0.664 \left(\frac{\rho \upsilon L}{\mu}\right)^{1/2} \left(\frac{\mu}{\rho D_{AB}}\right)^{1/3} \frac{D_{AB} \rho'}{L} \tag{3.6}$$

$$J_t = 0.0365 \left(\frac{\rho \upsilon L}{\mu}\right)^{0.8} \left(\frac{\mu}{\rho D_{AB}}\right)^{1/3} \frac{D_{AB}}{L} \tag{3.7}$$

where J_l and J_t are the mass fluxes for laminar and turbulent flow respectively, ρ is the concentration of the major gas species in the boundary layer, υ is the gas velocity and μ is the gas viscosity. The gas concentrations, ρ and ρ', are calculated using the ideal gas law. Partial pressures of $Si(OH)_4$ (g), $TiO(OH)_2$ (g) and $Y(OH)_3$ (g) were calculated using data from Plyasunov [109], Nguyen et al. [110] and Krikorian [113] respectively. The gas velocity was modeled using ANSYS CFX as described in Section 2.3. The gas viscosity was obtained from work by Svehla [115]. The interdiffusion coefficient was calculated using the Chapman-Enskog equation [116], using tabulated values for the collision diameter, σ, force constant, ε/k, and the collision integral, Ω, of the appropriate gas mixtures [115, 117]. Since these parameters are not available for $Si(OH)_4$ (g), $TiO(OH)_2$ (g) and $Y(OH)_3$ (g), values for SiF_4, $SiCl_4$ and AlF_3 were used respectively as an approximation. Krikorian notes that hydroxides act as pseudo halides suggesting these approximations are reasonable [113]. Representative values for the terms in Equations (3.6) & (3.7) can be seen in Table 3.1 for SiO_2, TiO_2 and Y_2O_3 specimens exposed at 1240°C and 1300°C.

Note that the characteristic length, L, for each test specimen was taken to be the distance from the impingement site to the downstream edge of the specimen.

Table 3.1. Representative values for terms in Equations (3.6) & (3.7).

	SiO_2 ($T_{steam}=1300°C$)	TiO_2 ($T_{steam}=1240°C$)	Y_2O_3 ($T_{steam}=1300°C$)
$\rho(T)$	1.40×10^{-4} g/cm^3	1.45×10^{-4} g/cm^3	1.40×10^{-4} g/cm^3
ν	176 m/s	176 m/s	173 m/s
L	0.75 cm	0.93 cm	0.50 cm
$\mu(T)$	5.44×10^{-4} g/cm·s	5.26×10^{-4} g/cm·s	5.44×10^{-4} g/cm·s
$D_{AB}(T)$	2.41 cm^2/s	1.54 cm^2/s	1.94 cm^2/s
$\rho'(T)$	3.70×10^{-9} g/cm^3	2.23×10^{-11} g/cm^3	2.75×10^{-12} g/cm^3
σ_{H2O}	2.641 Å	2.641 Å	2.641 Å
σ_{gas}	4.880 Å (SiF$_4$)	5.977 Å (SiCl$_4$)	4.198 Å (AlFl$_3$)
ε_{H2O}/k	809.1 K	809.1 K	809.1 K
ε_{gas}/k	171.9 (SiF$_4$)	390.2 K (SiCl$_4$)	1846 K (AlFl$_3$)
Ω	0.8732	0.9778	1.279

Tabulated values with (T) indicates there is a temperature dependence.

3.5.   Results

3.5.1.   Steam-Jet Furnace

The flow within the capillary and along the specimen surface (flat plate) can be characterized by the Reynolds number, $Re_{d, L}$ [114, 118]:

$$Re_{d,L} = \frac{\rho \upsilon x}{\mu} \qquad (3.8)$$

where ρ is the density of steam ($\sim 1.4 \times 10^{-4}$ g/cc), ν is the velocity of the steam-jet, *x* is the inner diameter of the capillary (1mm) or the specimen length from the impingement site to the downstream edge of the specimen, μ is the viscosity of the fluid ($\sim 5 \times 10^{-4}$ g/cm·s) and the subscripts of d and L represent flow in a tube of diameter d or a flat plate of characteristic length

L. For flow within the capillary the onset of turbulence occurs when $Re_d = 2300$ and becomes fully developed turbulent flow when $Re_d > 10,000$ while for flow on a flat plate (specimen surface) the onset of turbulence occurs when $Re_L \sim 500,000$ and becomes fully developed turbulent flow when $Re_L > 1,000,000$ [118]. For all experimental conditions used in this study the maximum $Re_{d, L}$ reached for flow within the capillary and on a flat plate was equal to 486 and 4520 respectively. Therefore the flow at the exit of the capillary and the specimen surface are assumed to be laminar.

At temperatures from $1200 - 1400°C$ the jet of steam was observed to pulse at a frequency of ~ 2 pulses/s while measuring the steam-jet temperature prior to starting an experiment. Large pulses in the steam-jet generally corresponded to a decrease in the steam-jet temperature ($\sim 10 - 50°C$) which in turn reduces the flux of volatile species by a maximum factor of ~ 1.2. While not explicitly quantified, small droplets of liquid water were observed exiting the capillary about once per minute in the larger pulses. The amount of liquid water that did not vaporize inside the furnace was minimized by preheating the liquid water prior to entering the capillary and using a Pt-13Rh wire inside the capillary. In addition, it was observed that not all of the liquid water was vaporized when flow rates exceeded 1.8 mL/min. The length of the capillary in the hot zone of the furnace is not sufficient to allow equilibration of the water vapor and the furnace atmosphere, thus the temperature of the steam-jet is lower than the furnace set temperature by $\sim 40 - 80°C$. An estimate of the position at which the liquid water vaporized could be obtained from the onset of discoloration visible on the inside of the fused quartz capillary after each exposure (Figure 3.1). The discoloration is presumed to come from trace amounts of contaminants in the water. The distance from the location of liquid water

vaporization to the exit of the capillary ranged from ~23 – 33 cm depending on the exposure

temperature and liquid water flow rate.
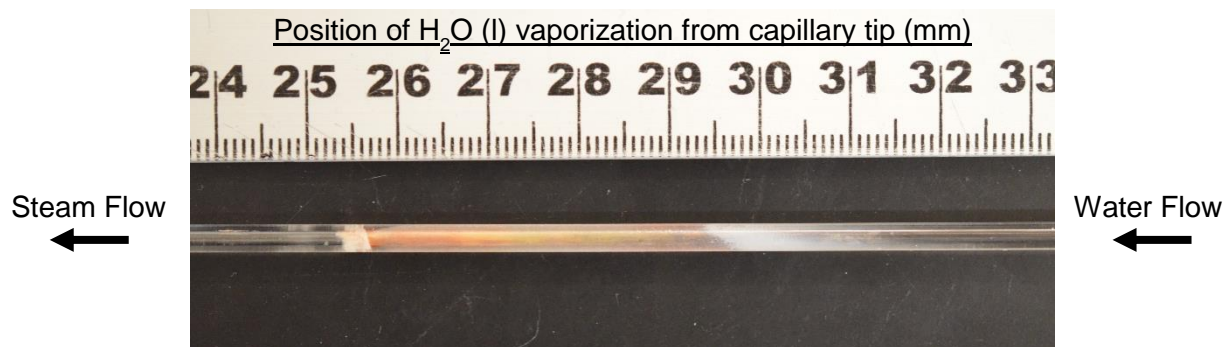
Figure 3.1. Fused quartz capillary after steam-jet exposure showing the discoloration resulting from the vaporization of liquid water.

The change in the inner diameter (ID) of the fused quartz capillary was measured in

cross-section by SEM at several locations along the capillary following steam-jet exposures at

1200 – 1400°C for 50 – 192 hours with steam-jet velocities of 149 – 190 m/s (Table 3.2). Note

the total length of the capillary is 73 cm. The ID of fused quartz capillaries increased within the

region where the liquid water vaporized to form steam with the largest increase occurring at the

capillary exit (Figure 3.2). The increase in the capillary ID presumably occurred due to a reaction

of the capillary with the steam via Equation (1.3).

Table 3.2. Capillary inner diameter (ID) recession rates. Measurements made at 1400°C were performed by Cory Parker (University of Virginia).

Temperature (°C)	Location (cm)	Capillary ID Recession Rate (µm/h)
	0	0
1200	57	0.026
	73	0.25
	0	0
1300	46.5	0.12
	73	0.81
	0	0
1400	33	0
	73	1.7

Figure 3.2. Change in capillary ID as a function of steam temperature and position along capillary. t = 50 – 192 h, $v_{(g)}$= 149 – 190 m/s, $P(H_2O)$= 1 atm. Measurements made at 1400°C were performed by Cory Parker (University of Virginia).

The total volume of SiO_2 that volatilized from the capillary was calculated assuming that

SiO_2 loss from the capillary ID increased linearly from the location of liquid water vaporization

38

to the capillary exit (Figure 3.3). The partial pressure of $Si(OH)_4$ (g) in the steam-jet was calculated at each temperature by dividing the total moles of volatilized SiO_2 (mol SiO_2 = mol $Si(OH)_4$ (g)) by the total moles of liquid water used during exposure (Figure 3.4). The measured partial pressure of $Si(OH)_4$ (g) is lower than the calculated equilibrium partial pressure for SiO_2 [109] with an activity of 1 and 0.4 (representative SiO_2 activity of Y_2SiO_5 + $Y_2Si_2O_7$, important for Chapter 4 [72]) at 1200°C and 1300°C. The measured partial pressure of $Si(OH)_4$ (g) is close to that of SiO_2 with an activity of 0.4 at 1400°C.
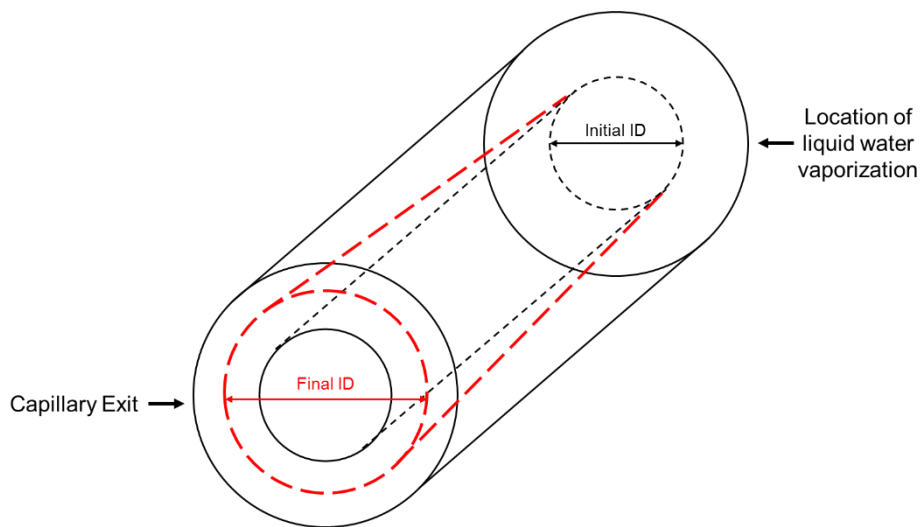
Figure 3.3. Illustration of assumed geometry for capillary inner diameter (ID) increase.
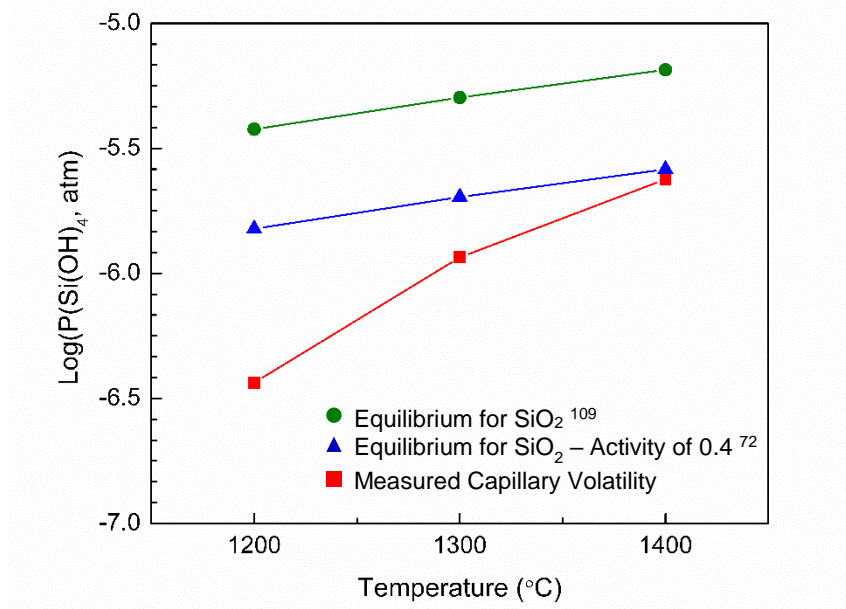
Figure 3.4. Partial pressure of Si(OH)$_4$ (g) vs. temperature for measured capillary volatility and calculated equilibrium partial pressure for SiO$_2$ and SiO$_2$ with an activity of 0.4. Measurements made at 1400°C were performed by Cory Parker (University of Virginia).

3.5.2. Maximum Recession Calculations

The flux of volatile gas species, J, assuming laminar flow and the maximum steam-jet velocity was calculated using Equation (3.6). The oxide mass flux, J_{ox}, was calculated using the following relationship:

$$J_{ox} = J \cdot \left(\frac{M_{ox}}{M_{gas}}\right) \tag{3.9}$$

where M_{ox} is the atomic mass of the oxide and M_{gas} is the atomic mass of the volatile gas species. The maximum recession rate, r_{max}, of the oxide was calculated by,

$$r_{max} = \frac{J_{ox}}{\rho''} \tag{3.10}$$

40

where ρ'' is the density of the oxide. These calculated values can then be compared to measured recession values to validate the use of quantitative measured recession obtained in the steam-jet furnace exposures.

3.5.3. SiO₂

Three SiO_2 specimens were exposed in the steam-jet furnace to confirm linear volatilization kinetics and determine the recession rate of silica in high-temperature high-velocity water vapor environments. These experiments were conducted at a steam-jet temperature of 1300°C for times of 20 – 75 h, a steam-jet velocity of 170 – 174 m/s and at 1 atm H_2O. One of the experiments consisted of three 25 h steam-jet exposures where a single specimen was exposed for 25 h, removed from the furnace, weighed, and then put back in the furnace for further exposures. Linear weight loss rates were observed which is consistent with known SiO_2 volatilization kinetics and Equation (3.6) (Figure 3.5) [20, 21, 29]. The magnitude of the weight loss, however, cannot be easily converted to a flux since the gas velocity varies across the SiO_2 surface.
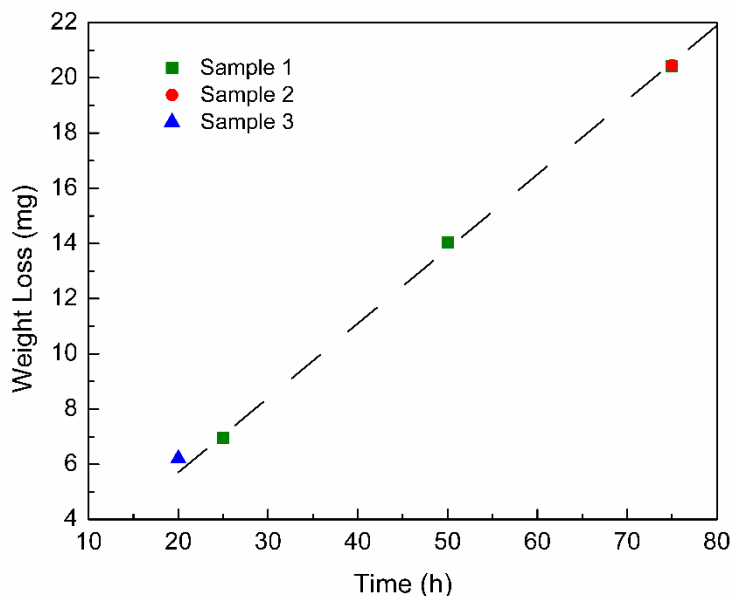
Figure 3.5. SiO$_2$ weight loss vs. exposure time data for steam-jet exposures at 1300°C, v$_{(g)}$ = 170 – 174 m/s and P(H$_2$O) = 1 atm.

Additional specimens were exposed in the steam-jet furnace at 1200°C – 1400°C for 20 –

50 h with a steam-jet velocity of 161 – 195 m/s at 1 atm H$_2$O. XRD results show that the as-

received SiO$_2$ specimens were amorphous and all specimens transformed to cristobalite during

exposure in the steam-jet furnace, as expected. After steam-jet exposure the steam-jet

impingement site can be seen on each specimen after they were coated with platinum (Figure

3.6). Water vapor has also reacted with the area that appears to be bounded by a "curved"

interface that starts slightly behind the steam-jet impingement site and extends downstream of

the impingement site. The platinum foil used to secure the specimen in the sample holder has

disturbed the flow of water vapor outside of the impingement site and has created the surface

features seen near the bottom edge of the specimen in Figure 3.6b, d.
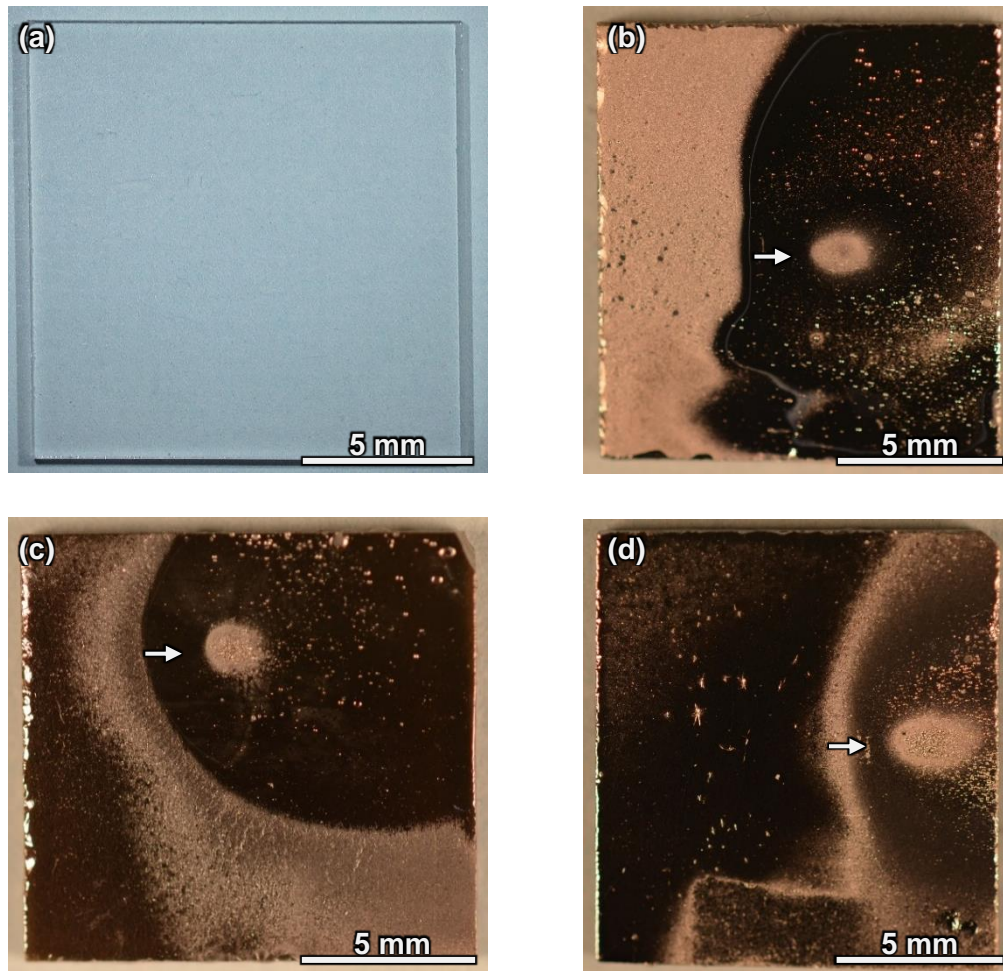
Figure 3.6. SiO$_2$ as-received specimen (a) and after steam-jet exposure at 1200°C (b), 1300°C (c) and 1400°C (d). t = 20 – 50 h, v$_{(g)}$= 164 – 195 m/s, P(H$_2$O)= 1 atm. Arrow ($\rightarrow$) indicates the direction of the steam-jet. Exposed specimens have been coated with platinum to visualize the steam-jet impingement site.

The maximum recession was measured on each specimen using an optical profilometer (Figure 3.7 & Figure 3.8) and the corresponding recession rates were determined (Table 3.3). The surface roughness outside of the steam-jet impingement site is attributed to the β → α cristobalite transformation that occurs during cooling and will be discussed in Section 3.6.2.

These recession rates were in reasonable agreement with calculated recession rates based on assessed data for Si(OH)$_4$ (g) [109] and assuming laminar flow. The enthalpy of reaction (ΔH_{rxn}; Equation (1.3)) from this study was calculated to be 120 kJ/mol which is a factor of ~2.1 greater than the calculated ΔH_{rxn} (56 kJ/mol) using data by Plyasunov [109] (Figure 3.9). It should be acknowledged that there is a large uncertainty associated with the calculated ΔH_{rxn} in this study due to the minimal data used in its determination. It is important to note that several repeat experiments were performed at each exposure temperature however recession measurements from specimens with good initial surface baselines are reported here.
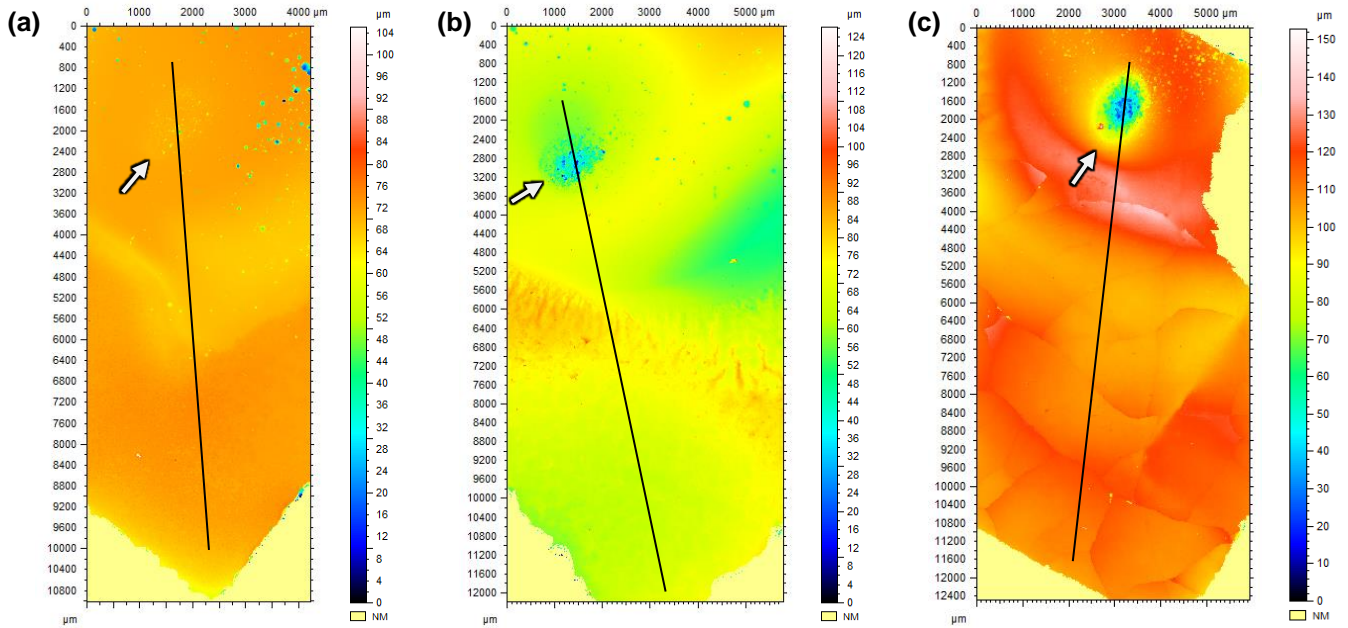
Figure 3.7. 3D surface profile of SiO$_2$ specimens after exposure at 1200°C (a), 1300°C (b) and 1400°C (c). t = 20 – 24 h, v$_{(g)}$= 164 – 195 m/s, P(H$_2$O)= 1 atm. Arrow (→) indicates the direction of the steam-jet and the black line represents the location of the 2D recession profile seen in Figure 3.8.
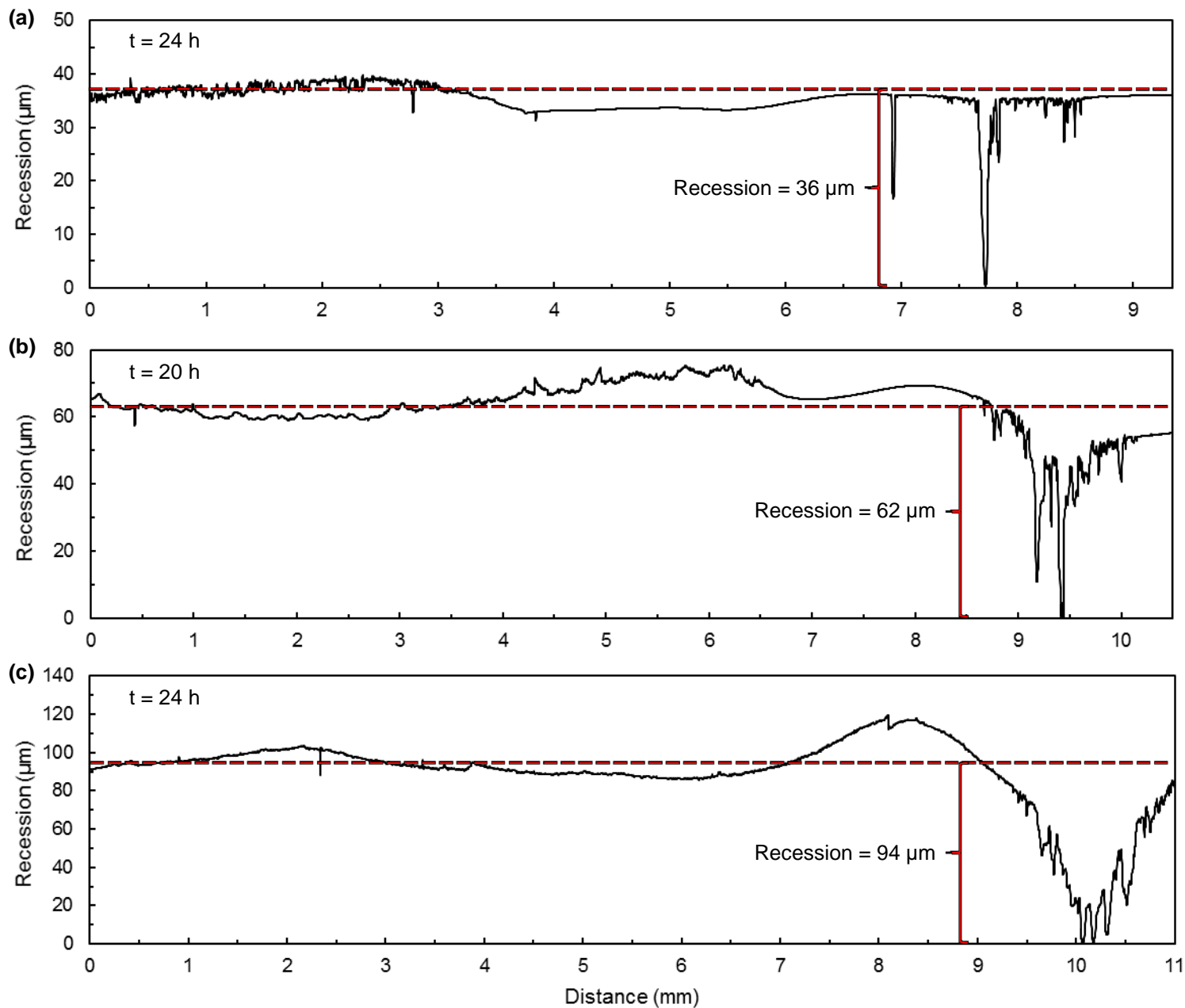
Figure 3.8. Corresponding 2D line profiles from optical profilometer measurements of SiO_2 specimens after exposure at 1200°C (a), 1300°C (b) and 1400°C (c). t = 20 – 24 h, $v_{(g)}$= 164 – 195 m/s, $P(H_2O)$= 1 atm. Red dotted line indicates where the baseline measurements were made.

Table 3.3. Experimental conditions, measured and calculated recession measurements for SiO_2.

Temperature (°C)	Other Experimental Conditions	Measured Recession Rate (µm/h)	Calculated Recession Rate (µm/h)
1200	t= 50 h, $v_{(g)}$ = 161 m/s, L = 0.4 cm	1.1	5.2
	t= 24 h, $v_{(g)}$ = 164 m/s, L = 0.5 cm	1.5	4.7
1300	t= 20 h, $v_{(g)}$ = 176 m/s, L = 0.7 cm	3.1	5.2
1400	t= 24 h, $v_{(g)}$ = 195 m/s, L = 0.35 cm	3.9	10.3
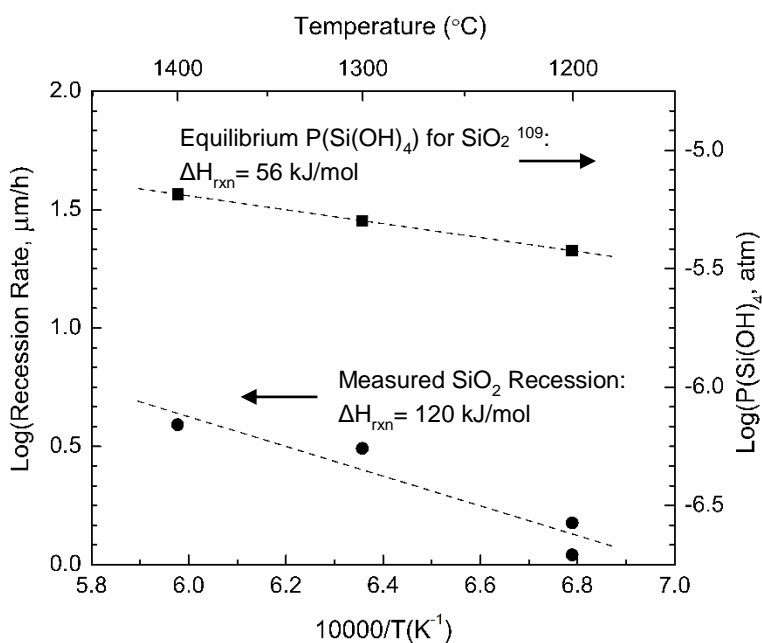
Figure 3.9. Measured SiO_2 recession rate and calculated $P(Si(OH)_4$ (g)) vs. inverse temperature for the reaction of SiO_2 and water vapor (Equation (1.3)). Measured and calculated enthalpies of reaction (ΔH_{rxn}) are shown.

3.5.4. TiO_2

Single crystal TiO_2 <001> specimens were exposed in the steam-jet furnace at 1240 –

1300°C for 48 – 100 h with a steam-jet velocity of 167 – 176 m/s at 1 atm H_2O. The steam-jet

impingement site can be clearly seen on a TiO_2 specimen after exposure (Figure 3.10). The specimen gained weight after the steam-jet exposure likely due to contamination from volatile species inside the steam-jet furnace and platinum from the specimen holder. Platinum foil used to secure the specimen in the specimen holder adhered to parts of the specimen after the steam-jet exposure. Removing the Pt foil resulted in the rough surface appearance along the bottom center to bottom right corner of the specimen (Figure 3.10b). In addition, weight change due to oxygen nonstoichiometry in TiO_{2-x} may confound weight loss due to volatilization. As confirmation of the importance of oxygen nonstoichiometry, a TiO_2 <001> specimen that was exposed in air for 10 min at 1400°C and a total pressure of 1 atm was found to undergo a color change from transparent to light blue with a corresponding weight loss of 0.72 mg, an ∼0.17% change. XRD results show that as-received TiO_2 <001> single crystals were of the rutile phase. No phase change was observed to occur after the high-temperature exposure in air and after steam-jet exposures.
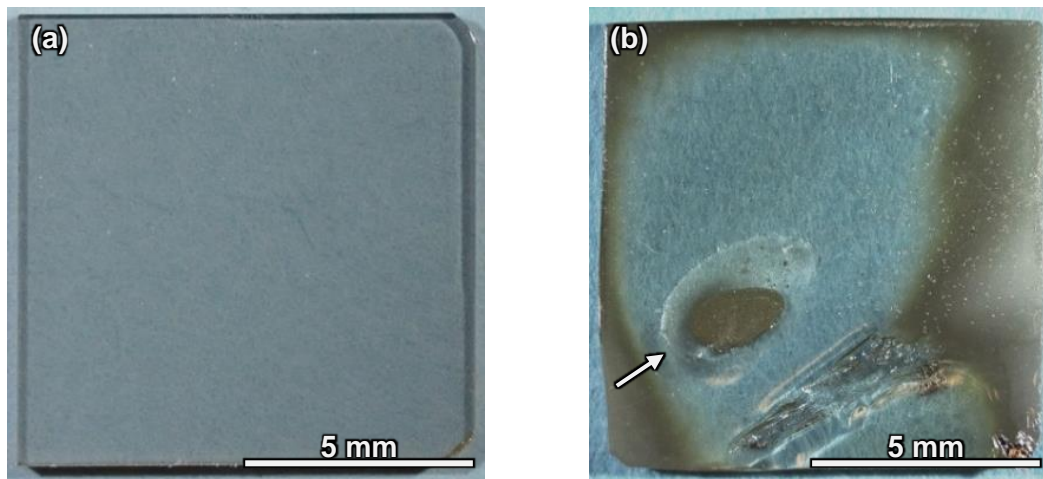
Figure 3.10. TiO_2 <001> single crystal as-received specimen (a) and after steam-jet exposure (b). T_{steam}= 1240°C, t = 100 h, $v_{(g)}$ = 176 m/s, P(H_2O)= 1 atm. Arrow (→) indicates the direction of the steam-jet.

A cross section of the specimen viewed under SEM after exposure (Figure 3.11) shows a smoothly varying recession profile which is consistent with the optical profilometer recession profile (Figure 3.12) and the velocity distribution of the steam-jet (Figure 2.3). Note that in Figure 3.11 the scale in the x and y directions are different and the location of the cross-section does not correspond to the same location of the 2D recession profile shown in Figure 3.12b. Facets were also observed by SEM at the impingement site of a specimen exposed for 48 hours at 1300°C (Figure 3.13), consistent with results of Ueno et al. [111]. This observation suggests that water vapor volatilized TiO_2 resulting in the formation of low surface energy step edges. A maximum recession of 92 µm after a 100 h exposure in the steam-jet was measured using an optical profilometer (Figure 3.12). The corresponding recession rate of 0.92 µm/h is considerably higher than the calculated recession rate of 0.016 µm/h based on data for $TiO(OH)_2$ (g) obtained by the transpiration technique [110] and assuming laminar flow (Table 3.4).
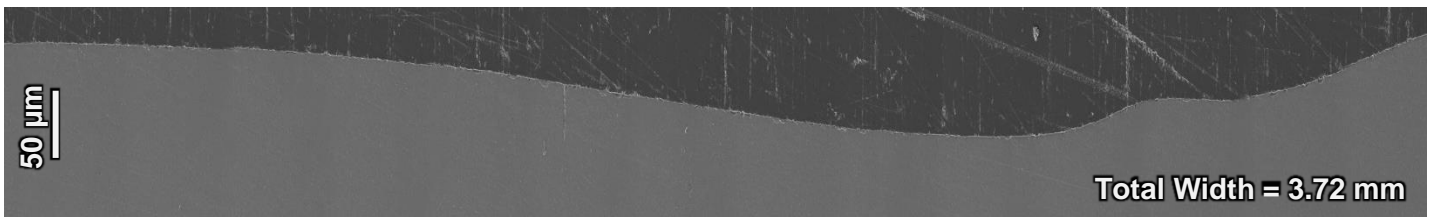
Figure 3.11. SE/SEM cross-section of TiO_2 <001> single crystal after exposure. T_{steam}= 1240°C, t = 100 h, $v_{(g)}$= 176 m/s, $P(H_2O)$= 1 atm.
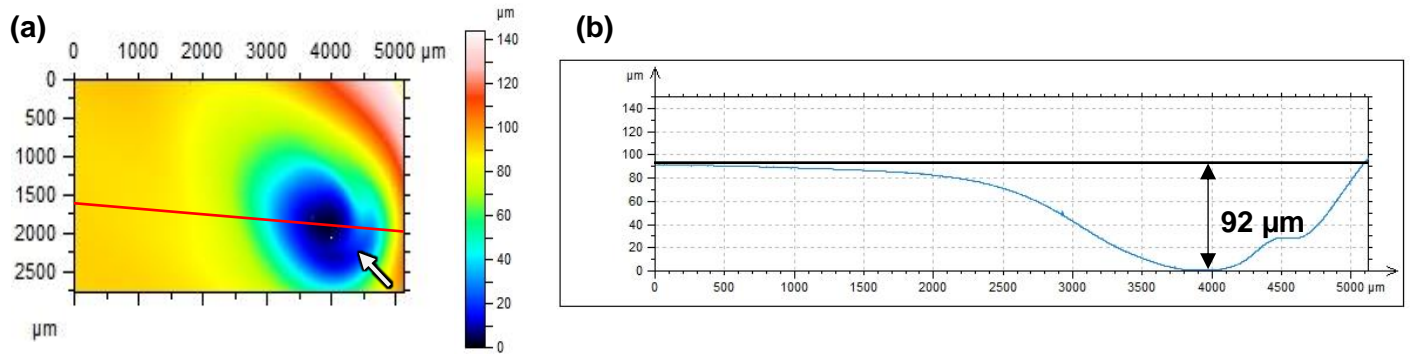
Figure 3.12. 3D surface profile of TiO_2 <001> single crystal after exposure (a) and the corresponding 2D recession profile (b). T_{steam}= 1240°C, t = 100 h, $v_{(g)}$= 176 m/s, $P(H_2O)$ = 1 atm. Arrow (→) indicates the direction of the steam-jet and the red line represents the location of the 2D recession profile.
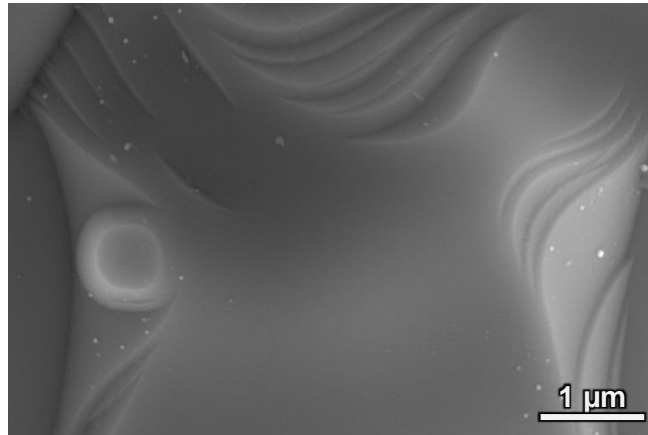
Figure 3.13. SE/SEM image showing surface faceting at the impingement site of a TiO_2 <001> specimen exposed in the steam-jet. T_{steam}= 1240°C, t = 100 h, $v_{(g)}$= 176 m/s, $P(H_2O)$ = 1 atm.

49

Table 3.4. Experimental conditions, volatility/recession measurements and calculated $M_x(OH)_y$ partial pressures of various studies. Agreement between studies is made by comparing shaded cells.

Author	Material	Experimental Conditions	I. Measured Volatility/ Recession Rate	II. Calculated $M_x(OH)_y$ Partial Pressure	Recession Rate Extrapolated from I or II to experimental conditions of this study [b]
This Study	SiO_2	T=1300°C, v=176 m/s, P(H_2O)= 1 atm, L=0.75 cm	3.1 µm/h	n/a	
Lucato et al. [30]	SiC	T=1350°C, v=160 m/s, P(H_2O)= 1 atm, L=0.75 cm	0.97 µm/h [a]	n/a	1.1 µm/h
Plyasunov [109]	SiO_2	n/a	n/a	P(Si(OH)$_4$) = 4.97 x 10^{-6} atm at 1300°C, 1 atm H_2O from $\Delta H^{\circ}_{f,298}$, ΔS°_{298} and C_p	5.2 µm/h
This Study		T=1240°C, v=176 m/s, P(H_2O)= 1 atm, L=0.93 cm	0.92 µm/h	n/a	
Ueno et al. [111]	TiO_2	T=1500°C, v=4.6 x 10^{-4} m/s, P(H_2O)= 0.41 atm, L= 2.553 cm	2.2 x 10^{-5} g/cm^{2}h	n/a	4.4 µm/h
Nguyen et al. [110]		n/a	n/a	P(TiO(OH)$_2$) = 3.02 x 10^{-8} atm at 1240°C, 1 atm H_2O from experimentally determined k_{eq}	0.016 µm/h
This Study		T=1300°C, v= 169 m/s, P(H_2O)= 1 atm, L=0.5 cm	≤ 0.01 µm/h	n/a	
Courcot et al. [112]	Y_2O_3	T=1300°C, v=0.05 m/s, P(H_2O)= 0.493 atm, L=1 cm	0.051 mg/cm^{2}h	n/a	16.9 µm/h
Krikorian [113]		n/a	n/a	P(Y(OH)$_3$) = 2.52 x 10^{-9} atm at 1300°C, 1 atm H_2O from $\Delta H^{\circ}_{f,298}$ and ΔS°_{298}	0.0048 µm/h

[a] Measured recession of SiC has been converted to SiO_2
[b] Equation (3.11) was used to extrapolate I and II to the experimental conditions of this study where n = 2 for SiO_2, n = 1 for TiO_2 and n = 3/2 for Y_2O_3.

3.5.5. Y_2O_3

Y_2O_3 specimens were exposed in the steam-jet furnace at 1300°C for 100 h with a steam-jet velocity of 169 – 173 m/s at 1 atm H_2O. All specimens gained weight after steam-jet exposures (Appendix B). After steam-jet exposures, XRD results indicated the starting phase, Y_2O_3 (cubic), was still predominant, but additional minor phases of Y_2SiO_5 and $Y_4Al_2O_9$ were also detected (Figure 3.14). After steam-jet exposures the steam-jet impingement site cannot be clearly seen on the specimen surface (Figure 3.15a). SEM of an as received specimen shows the presence of large pores on the specimen surface (Figure 3.15b). After the steam-jet exposure a uniform distribution of small pores (< 1.5 µm) is present at the steam-jet impingement site (Figure 3.15c). In addition, some small cracks were also observed.
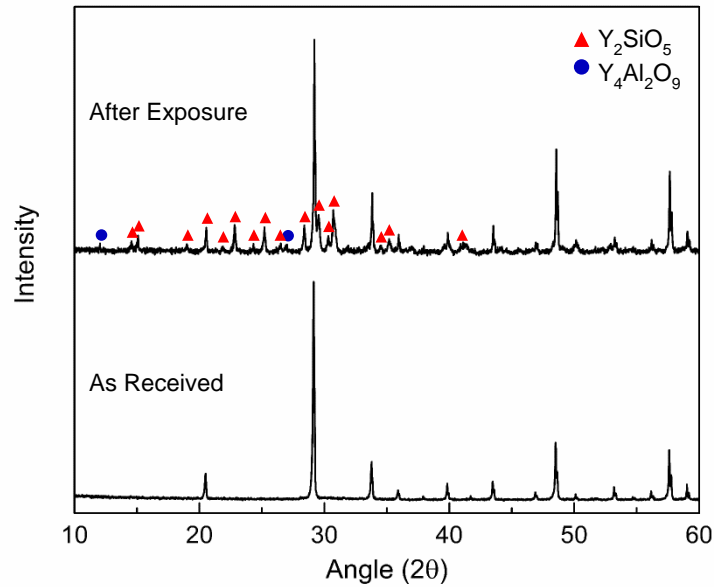
Figure 3.14. XRD patterns for Y_2O_3 before and after exposure in the steam-jet. T_{steam}= 1300°C, t = 100 h, $v_{(g)}$= 169 m/s, $P(H_2O)$= 1 atm.
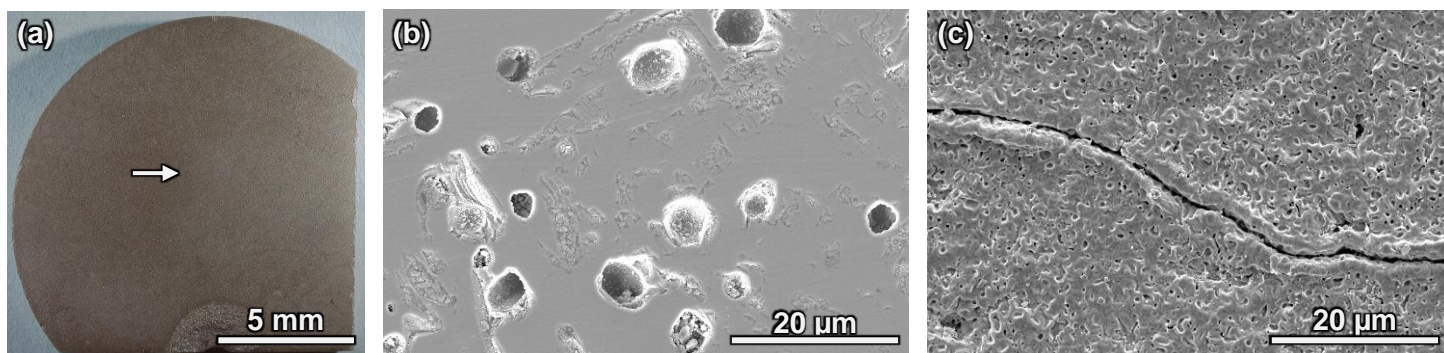
Figure 3.15. Optical microscope image of a Y_2O_3 specimen after steam-jet exposure (a), SE/SEM of as-received surface (b) and at steam-jet impingement site after exposure (c). T_{steam}= 1300°C, t = 100 h, $v_{(g)}$= 169 m/s, $P(H_2O)$= 1 atm. Arrow ($\rightarrow$) indicates the direction of the steam-jet.

Trace amounts of Al and Si contamination were detected by EDS upstream of the steam-impingement site. At the steam-jet impingement site Si contamination was also detected by EDS. The EDS and XRD results suggest that the observed weight gain can be attributed to volatile aluminum and silicon hydroxide species reacting with Y_2O_3. The volatile hydroxide species formed as a result of water vapor reacting with the alumina furnace ware and the fused quartz capillary. SEM of a cross-section through the impingement site of a specimen exposed in the steam-jet shows that a thin porous layer (3.2 $\pm$ 1.8 µm) is present at the surface of the specimen and is of a different phase than the underlying Y_2O_3 (Figure 3.16). EDS of the cross-section suggests that the thin porous layer is Y_2SiO_5 based on the Y:Si ratio of approximately 2:1 which is consistent with the findings of XRD where Y_2SiO_5 was detected. A thin porous layer was also observed downstream of the impingement site and was about half the thickness (1.7 $\pm$ 0.5 µm) of the porous layer formed at the impingement site.
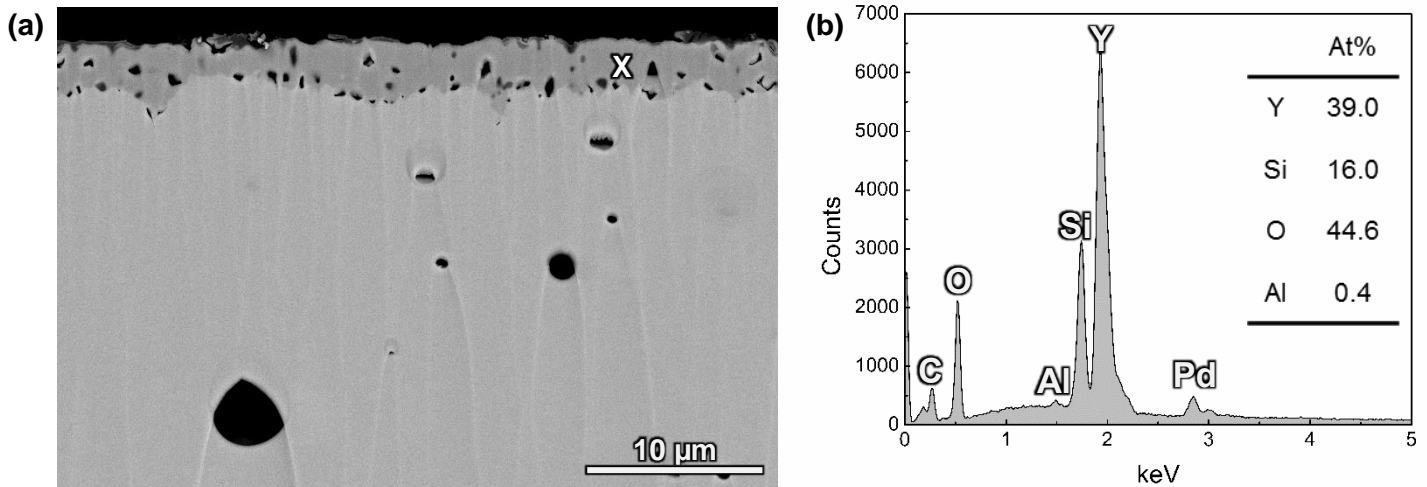
Figure 3.16. BSE/SEM cross-section image of Y_2O_3 after steam-jet exposure at the impingement site (a) and corresponding EDS spectrum acquired at the white X (b). T_{steam}= 1300°C, t = 100 h, $v_{(g)}$ = 169 m/s, $P(H_2O)$ = 1 atm.

Optical profilometry measurements were obtained on the surface of the specimen before and after a steam-jet exposure (Figure 3.17 & Figure 3.18). No clear impingement site can be seen within the roughness of the specimen surface in the 2D line profile (Figure 3.18). Given that no impingement site was observed in the surface profilometry measurements and the Y_2SiO_5 layer formed on the specimen surface from steam-jet impingement to downstream of the impingement site, we use the roughness of the specimen to bound the maximum amount of Y_2O_3 volatilization that may have occurred. The roughness of the specimen surface after the steam-jet exposure is on the order of ~1 µm thus any Y_2O_3 recession due to volatilization was assumed to be less than or equal to 1 µm. This value corresponds to a maximum recession rate of ≤ 0.01 µm/h which is in reasonable agreement with the calculated recession rate of 0.0047 µm/h based on estimated thermodynamic data for $Y(OH)_3$ (g) [113] and assuming laminar flow (Table 3.4).
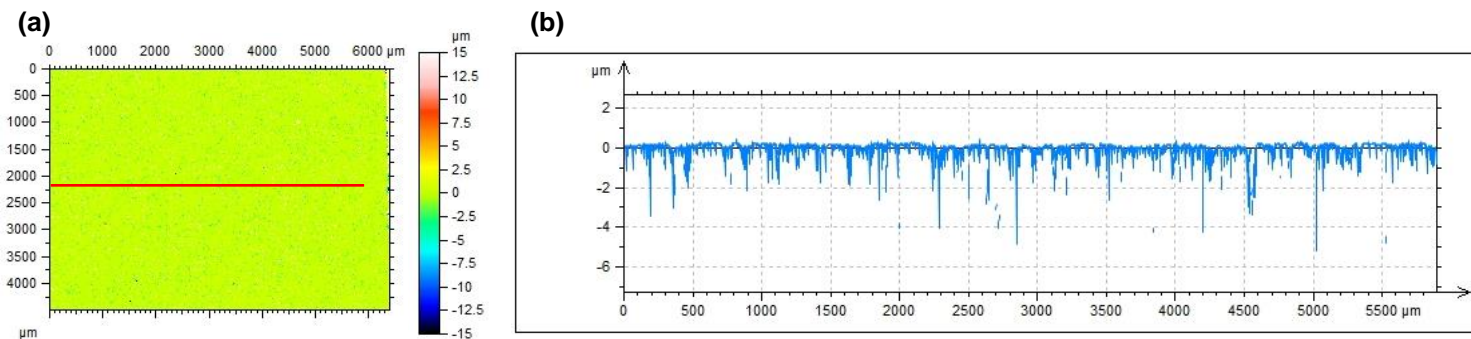
Figure 3.17. 3D surface profile of Y_2O_3 before exposure (a) and 2D line profile (b). Red line represents the location of the 2D line profile.
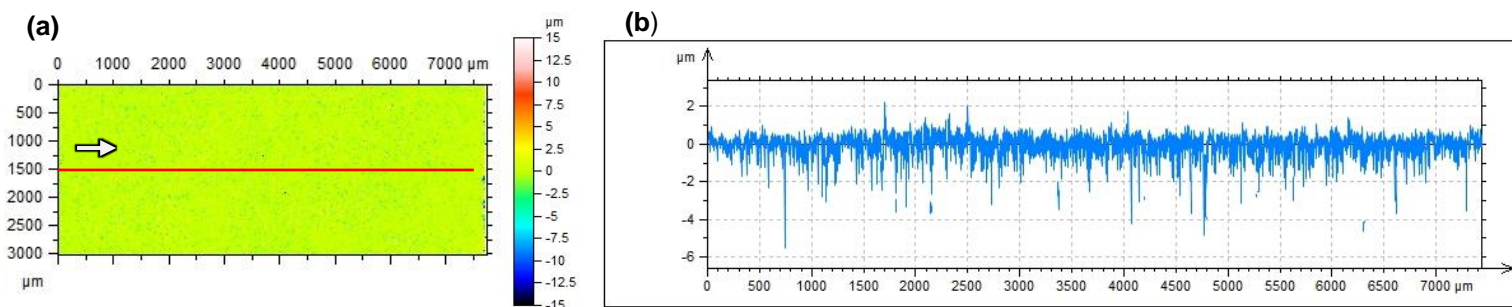
Figure 3.18. 3D surface profile of Y_2O_3 after exposure (a) and 2D line profile (b). $T_{steam}=$ 1300°C, t = 100 h, $v_{(g)} =$169 m/s, $P(H_2O)=$ 1 atm. Arrow ($\rightarrow$) indicates the direction of the steam-jet and the red line represents the location of the 2D line profile.

3.6. Discussion

3.6.1. Steam-Jet Furnace Limitations and Advantages

3.6.1.1. Capillary Volatility

Volatilization of the capillary during steam-jet exposure results in the formation of $Si(OH)_4$ (g) (Figure 3.4) and an increase in the ID of the capillary (Figure 3.2). The $Si(OH)_4$ (g) in the water vapor can react with some test specimens, as demonstrated with the Y_2O_3 specimen in this study (Figure 3.16). The volatility of oxides that do not readily form silicon containing

oxides or have high silica activities can be accurately assessed using the steam-jet furnace. At temperatures of 1300°C and 1400°C the partial pressure of $Si(OH)_4$ (g) in the water vapor from the fused quartz capillary is high enough that it approaches equilibrium values saturating the gas stream and limiting SiO_2 volatility from reduced SiO_2 activity materials such as rare-earth silicates [72, 73] (Figure 3.4). Therefore, a capillary made of a material that does not react with high temperature water vapor (e.g. Platinum [119]) is needed to test the volatility of oxides that can form silicon containing oxides and test oxides with reduced SiO_2 activity at temperatures greater than 1200°C. In addition, the increase in the ID of the fused quartz capillary with exposure time results in a decrease of the steam-jet velocity and change in Re_d for flow within the capillary. The maximum decrease in steam-jet velocity during all exposures was less than 30 m/s and Re_d was < 800, thus the flow at the capillary exit remained laminar.

3.6.1.2. Volatilization Reaction vs. Erosion

A volatilization reaction is one where the high-velocity water vapor chemically reacts with the specimen to form a volatile gas species and/or a new phase whereas erosion is when the high-velocity water vapor mechanically removes material from the specimen without any chemical reaction taking place. Measurable oxide recession in this study can be attributed to a volatilization reaction between the oxide and water vapor and should not be confused with an erosion mechanism. To demonstrate this, a SiO_2 specimen (25.4 x 25.4 x 1 mm) was exposed in the steam-jet (T_{steam}=1240°C, t=170 h, $v_{(g)}$= 177 m/s, $P(H_2O)$= 1 atm) orientated so that its leading edge was perpendicular to the jet of steam. The steam-jet flow should stagnate at the impingement site for this orientation, resulting in an area of low recession surrounded by measureable recession. This stagnation point was observed as shown in Figure 3.19, which is

55

consistent with a volatility reaction rather than erosion. Similar observations were made by Lucato et al. [30]. In contrast, if the observed recession was due to an erosion mechanism a depression or hole is expected since erosion rates of brittle materials like oxides reach a maximum at the impingement point when the specimen orientation is perpendicular to the flow of steam [120]. The smoothly varying recession observed in the cross-section of a steam-jet exposed TiO_2 <001> specimen shown in Figure 3.11 is consistent with the velocity distribution of the steam-jet (Figure 2.3). This smooth recession profile is better explained by a surface volatilization reaction of TiO_2 than by mechanical erosion. The oxide recession profile would appear as a rough scalloped surface if the recession was caused by an erosion mechanism [120]. In addition, no impingement site was observed on Y_2O_3 specimens after they were exposed in the steam-jet indicating that no erosion took place. In fact, a thin porous layer of Y_2SiO_5 had formed along the surface of Y_2O_3 due to a chemical reaction with $Si(OH)_4$ (g) present in the steam.
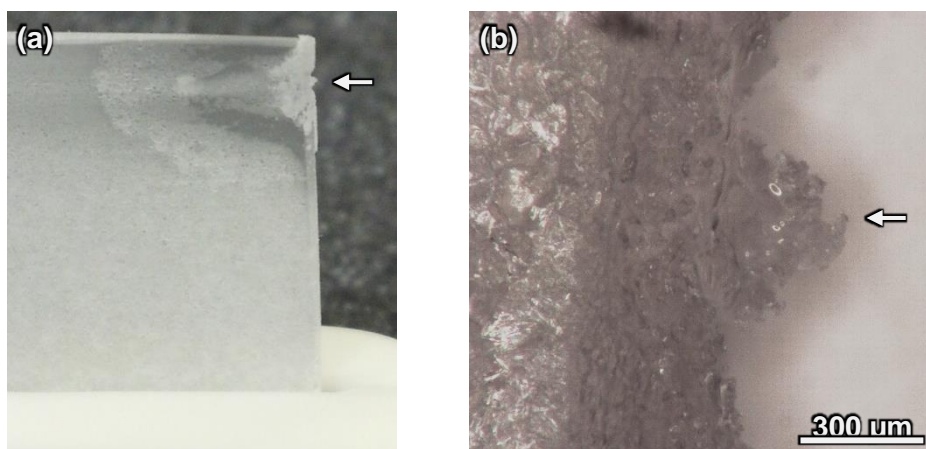
Figure 3.19. SiO_2 specimen after steam-jet exposure with leading edge oriented perpendicular to the steam-jet (a) and the steam-jet impingement site at higher magnification (b). T_{steam}= 1240°C, t = 170 h, $v_{(g)}$= 177 m/s, $P(H_2O)$= 1 atm. Arrow ($\leftarrow$) indicates the direction of the steam-jet. This study was performed by Jack Valentine (now at Bain and Company).

3.6.1.3. Comparison of the Steam-Jet with Other Laboratory Tests

The steam-jet furnace is able to achieve significantly higher gaseous metal hydroxide volatility rates compared to other laboratory testing capabilities. This is shown in Table 3.5, where the calculated volatility rate of SiO_2 in the steam-jet, burner rig [27], high pressure burner rig (HPBR) [29] and TGA [21] is compared. The linear volatility rate, k_l, of each test rig was calculated using the following equation normalized to the steam-jet furnace test conditions:

$$k_l \propto \exp\left(\frac{-\Delta H_r}{RT}\right) \cdot \frac{P(H_2O)^n \cdot v^{1/2}}{P_{total}^{1/2}} \tag{3.11}$$

where ΔH_r is the enthalpy of the volatilization reaction, R is the universal gas constant, T is the temperature, $P(H_2O)$ is the partial pressure of water vapor, n is the number of moles of H_2O for the gaseous hydroxide formation reaction (n= 2 for SiO_2), v is the gas velocity and P_{total} is the total pressure. Equation (3.11) is derived from the parametric dependence of the gaseous flux given by Equation (3.6). The steam-jet is capable of achieving volatility rates a factor of ~17 to 250 greater than other laboratory test capabilities. This enables the steam-jet to create measurable material recession in shorter test times compared to the other laboratory tests.

Table 3.5. Comparison of SiO_2 volatility in the steam-jet furnace to other laboratory tests.

	Total pressure (atm)	P(H$_2$O) (atm)	Gas velocity (m/s)	Normalized Recession Rate
Steam-jet	1	1	175	100
Burner rig [27]	1	0.28	100	6
HPBR [29]	6	0.6	20	5
TGA [21]	1	0.5	0.04	0.4

3.6.1.4. Steam-Jet Modifications

The specimen configuration used in this study, a coupon placed at 45° to the steam injection capillary, has several advantages over the wedge specimen used in the study by Lucato et al. [30]. Firstly, there is minimal specimen preparation required since the steam-jet impinges on only one side of the specimen. Therefore the leading edge of the specimen does not need to be polished into a sharp wedge. Secondly, the specimen can be easily positioned in front of the steam-jet because the impingement site can be located at any position on the specimen surface. Finally, this configuration enables the easy testing of thermal sprayed EBCs since only one side of the substrate material needs to be coated. The preheating of the liquid water prior to entering the capillary and the addition of a Pt-13Rh wire inserted into the capillary minimized the amount of liquid water that did not vaporize in the furnace during large pulses in the steam-jet. As a result, the difference between the furnace set temperature and the temperature of the steam-jet of this study ($\sim 40 - 80°C$) is lower than that measured in the study by Lucato et al. [30] ($\sim 150°C$).

3.6.2. SiO$_2$

The observed linear weight loss kinetics is consistent with the known rate law for SiO$_2$ volatilization [20, 21, 29]. The maximum recession was determined by measuring the difference between the height of the average roughness baseline prior to the impingement site and the maximum recession (Figure 3.7 & Figure 3.8). The cause of the rough surface outside of the impingement site is due to the formation of small cracks that form as a result of a $\sim 3 - 7\%$ volume change when β cristobalite transforms to α cristobalite at $\sim 220 - 270°C$ [121–123]. These small cracks began to form in the top left corner of specimen during cooling (Figure 3.20). As the specimen continued to cool, the β → α transformation front moved across the specimen

towards the bottom right corner. The cracking associated with the $\beta \rightarrow \alpha$ transformation made the selection of an average roughness baseline not possible on many specimens exposed in the steam-jet furnace. In fact, the cracking was so severe on some specimens that they completely broke apart on cooling. The severity of the cracking and specimens breaking apart was observed to increase with increasing exposure temperature.
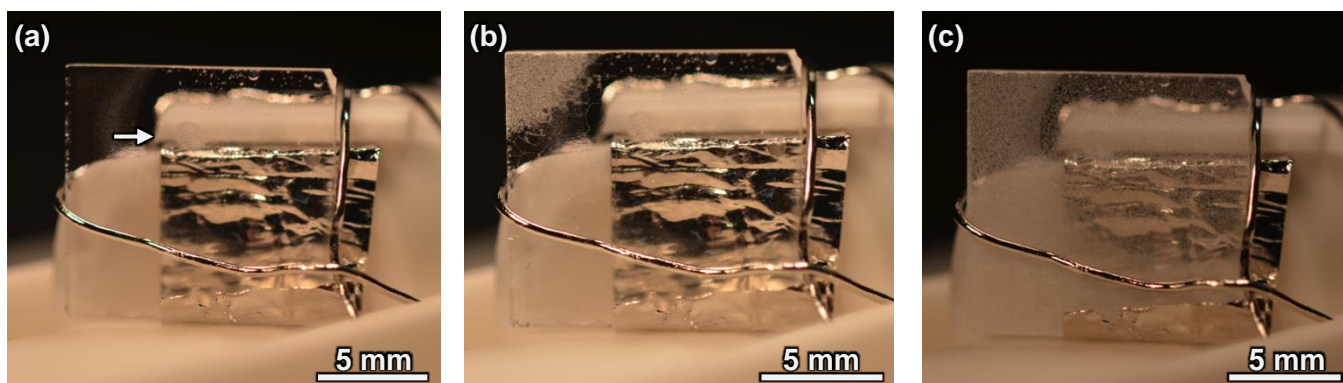
Figure 3.20. SiO_2 specimen after steam-jet exposure just after removal from the furnace (a) and during cooling (b,c). (T_{steam}=1300°C, t=20 h, $v_{(g)}$= 176 m/s, $P(H_2O)$= 1 atm). Arrow ($\rightarrow$) indicates the direction of the steam-jet.

The measured recession rates at 1200 – 1400°C were smaller by a factor of ~ 1.7 – 4.7 than the calculated recession values. Several factors may have contributed to the lower measured recession and ΔH_{rxn} values compared to those calculated based on assessed data for $Si(OH)_4$ (g) [109]. The ID of the capillary increases during exposure resulting in a decrease in the steam-jet velocity which reduces the SiO_2 volatility rate. The maximum decrease in steam-jet velocity for all exposures was less than 30 m/s which corresponds to a maximum reduction of flux by a factor of 0.9. The calculated recession rate does not take this into account since the maximum steam-jet velocity (present at short times) is used in the calculation. In addition, the presence of $Si(OH)_4$ (g) in the steam-jet would act to retard the volatilization reaction that occurs on the

specimen surface. Finally, the specimen is not being continuously exposed to a single steam

temperature due to the pulsing of the steam-jet. As a result, the flux of volatile species decreased

during the pulse however this effect is not expected to be significant as already described in

Section 3.4. In the study by Lucato et al. [30], a recession rate of 0.6 – 0.7 μm/h was measured on a

SiC test specimen exposed at 1350°C with a steam-jet velocity of 160 m/s. Converting the

measured SiC recession to SiO_2 recession via the density ratio between SiC (3.21 g/cc) and SiO_2

(cristobalite = 2.32 g/cc), a SiO_2 recession rate of 0.97 μm/h is found. Using the SiO_2 recession

rate obtained under the experimental conditions of Lucato et al. and ΔH_{rxn} from assessed

thermodynamic data by Plyasunov [109], the SiO_2 recession rate of Lucato et al. can be calculated

at the experimental conditions of this study at 1300°C. A recession rate of 1.1 μm/h was

calculated which is in fair agreement with the recession rate of 3.1 μm/h measured in this study

(Table 3.4).

Two major differences between the Lucato et al. work and this study were investigated to

determine if they contributed to the difference in measured recession rates. Firstly, the way in

which the steam-jet velocity was estimated in each study was different, however both methods

were found to agree with one another as shown in Table 3.6 and thus did not contribute to the

difference in measured recession rates. In this study, the steam-jet velocity was estimated using

the CFD model described in Section 2.3 while Lucato et al. estimated the steam-jet velocity

using the ideal gas law,

$$v_{av} = \frac{\dot{m} \, R \, T}{A \, MW \, P} \tag{3.12}$$

where v_{av} is the estimated average steam-jet velocity at the capillary exit, $\dot{m}$ is the mass flow

rate, R is the universal gas constant, T is the temperature of the steam-jet, A is the cross-section

area of the capillary, MW is the molecular weight of water, and P is the pressure at the exit of the

capillary. The pressure at the exit of the capillary (1 atm) was confirmed to be accurate within <0.2% from CFD analysis [30]. There is reasonable agreement between the steam-jet velocity at the capillary exit estimated by the CFD model and Equation (3.12), however, as the mass flow rate increases this agreement decreases.

Table 3.6. Comparison of steam-jet velocities estimated by CFD model and Equation (3.12).

Author	CFD Estimated Steam-Jet Velocity	Equation (3.12) Estimated Steam-Jet Velocity
This Study ($\dot{m}$= 0.028 g/s, T=1300°C)	Impingement site: 176 m/s Capillary exit: 262 m/s	256 m/s
Lucato et al. ($\dot{m}$= 0.017 g/s, T=1350°C)	Impingement site: 156 m/s Capillary exit: 167 m/s	160 m/s

Secondly, the specimens in this study were orientated at 45° relative to the steam-jet while Lucato et al. orientated a sharp wedge specimen so that it was parallel to the steam-jet. Lucato et al. also exposed specimens at 45° relative to the steam-jet and observed pitted surfaces similar to wedge specimens exposed directly in the steam-jet, however, no recession rates were reported. A study by Robinson et al. [29] measured the SiC recession rates of specimens after they were exposed parallel and 45° to the gas flow in a HPBR. Their study concluded that the specimen orientation had no significant effect on the measured recession rate. Therefore it is also unlikely that the specimen orientation contributed to the difference in measured recession between Lucato et al. and this study. The cause of this difference in measured recession rates remains unknown.

3.6.3. TiO₂

A comparison between the TiO$_2$ recession rate calculated using thermodynamic data for

TiO(OH)$_2$ (g) from Nguyen et al. [110] and the measured recession rate of this study are shown in

Table 3.4. Limitations of the transpiration experimental technique may contribute to the

discrepancy with the measured TiO$_2$ recession rate of this study. Nguyen et al. reported that a

portion of the material collected in their transpiration study was insoluble and thus could not be

analyzed by inductively coupled plasma atomic emission spectroscopy (ICP-AES). Therefore

there is uncertainty as to whether all of the Ti was collected. If the insoluble material did in fact

contain some Ti, the thermodynamic data of Nguyen et al. would result in under predictions of

TiO$_2$ recession, consistent with the observations of this study. In addition, the amount of Ti

collected during the transpiration studies was very small (9 – 262 μg) thus it would require only

a minimal amount of uncollected Ti to introduce significant error into the measurements.

The study conducted by Ueno et al. [111] was performed on a polycrystalline TiO$_2$ (rutile)

specimen using a Corrosion Testing Machine in 30 wt% water vapor (air:H$_2$O = 70:30 (wt%),

P(H$_2$O) = 0.41 atm) at 1500°C with a gas flow rate of 4.6×10^{-4} m/s. The experimental weight

loss technique utilized by Ueno et al. also has some uncertainty. Ueno et al. reported that a

weight decrease was observed during the corrosion test which corresponded to a volatility rate of

2.2 x 10^{-5} g/cm^2 h, however, effects of changes in oxygen stoichiometry have not been

considered. The measured recession rate of Ueno et al. extrapolated to the experimental

conditions of this study using Equation (3.11) can be seen in Table 3.4. The measured recession

rate of Ueno et al. is in fair agreement with the measured recession rate of this study however

these results suggest that Ueno et al. over predict TiO$_2$ volatility. The direct measurement of

TiO_2 recession in this study is considered the most reliable measurement of TiO_2 volatility in high-temperature water vapor.

3.6.4. Y_2O_3

The formation of Y_2SiO_5 at and downstream of the steam-jet impingement site presumably occurred due to a reaction of Y_2O_3 with $Si(OH)_4$ (g) given by Equation (3.13).

$$Y_2O_3 + Si(OH)_4 \text{ (g)} = Y_2SiO_5 + 2H_2O \text{ (g)} \qquad (3.13)$$
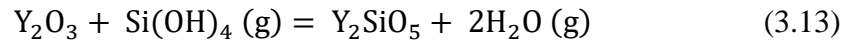
The $Si(OH)_4$ (g) present in the jet of steam is due to a reaction of water vapor with the fused quartz capillary given by Equation (1.3). Similar observations were made in a study by Fritsch et al. [46] where YAG ($Y_3Al_5O_{12}$) decomposed to $Y_2O_3 + Al(OH)_3$ (g) in the presence of water vapor which in turn reacted with $Si(OH)_4$ (g) to form Y_2SiO_5.

A recession rate of 0.0048 µm/h was calculated using estimated thermodynamic data for $Y(OH)_3$(g) from Krikorian [113] assuming laminar flow (Table 3.4) which shows fair agreement with the assumed recession rate of this study. These results suggests that Krikorian provided a good estimate of the thermodynamic data for $Y(OH)_3$ (g). However, more definitive steam-jet exposures of Y_2O_3 conducted with a non-reactive capillary are needed to confirm this conclusion. Courcot et al. [112] report the volatilization rate of Y_2O_3 at 1300°C ($P(H_2O)$ = 50 kPa, $v_{(g)}$= 0.05 m/s) to be 0.051 mg/cm²h. Converting this volatilization rate to a maximum recession rate using Equation (3.10) and extrapolating to the experimental conditions of this study using Equation (3.11), a recession rate of 16.9 µm/h was found (Table 3.4). The results of this study and the calculated recession using estimated thermodynamic data by Krikorian [113] are not in agreement with the results of the study by Courcot et al. [112]. These findings suggest that the volatility rate of Y_2O_3 reported by Courcot et al. is unreasonably high. In addition to these

results, another study by Courcot et al. [124] on the Y_2O_3–SiO_2 system concluded that at 1300°C, the partial pressures of the $Y(OH)_3$ (g) and $Si(OH)_4$ (g) species derived from weight loss experiments suggest that SiO_2 is only a factor of ~1.1 more volatile than Y_2O_3. The high Y_2O_3 volatility rates observed by Courcot et al. [112, 124] are not consistent with findings in the literature and this study where Y_2O_3 was more than two orders of magnitude more stable than SiO_2. For example, Y_2O_3 showed no weight loss when exposed in a burner rig for 109 h at 1450°C with a combustion gas at $P(H_2O) = 0.28$ bar flowing at 100 m/s [49]. In fact, a small weight gain was reported due to the transport of SiO_2 vapor to the Y_2O_3 specimens. Similarly, Y_2O_3 was observed to gain weight due to reaction with volatile aluminum hydroxide species after exposure for 400 h at 1400°C with a gas at $P(H_2O) = 0.5$ atm flowing at 1×10^{-3} m/s [60]. These observations are consistent with the weight gain observed in the current study, where volatile silicon and aluminum hydroxide species reacted with Y_2O_3 at and outside of the steam-jet impingement site. In addition, no destabilization of yttria-stabilized zirconia (YSZ, ZrO_2–8 wt% Y_2O_3) was observed in simulated combustion environments [31, 46, 125, 126]. This again provides evidence that Y_2O_3 is more stable than SiO_2 in high-temperature water vapor. This is relevant for rare-earth silicates in which silica is shown to be selectively volatilized in high-temperature high-velocity water vapor (Chapter 4).

3.7. Conclusions

SiO_2 specimens were exposed in the steam-jet furnace and linear volatilization kinetics was observed. The measured recession rate of SiO_2 in this study was in reasonable agreement with prior studies. TiO_2 was found to have measurable recession rates whereas Y_2O_3 was stable in the high-temperature high-velocity water vapor environment. Controversies in literature for

TiO(OH)$_2$ (g) formation from TiO$_2$ and Y(OH)$_3$ (g) formation from Y$_2$O$_3$ were addressed. The results of this study demonstrate that the steam-jet furnace is an effective laboratory test that is capable of simulating a turbine engine environment and enables quantitative determination of material stability toward gaseous metal hydroxide formation in reasonable test times at a reasonable cost. The steam-jet provides for direct measurement of sample recession rather than indirect methods of material loss rates by weight change or volatilization – condensation. The fused quartz capillary limits materials that can be tested and is not suitable for those that readily form silicon containing oxides (e.g. Y$_2$O$_3$) or have low SiO$_2$ activities (e.g. Y$_2$SiO$_5$ + Y$_2$Si$_2$O$_7$). Finally, the specimen configuration used in this study requires no elaborate specimen preparation, enables the testing of coated specimens and allows for easy specimen insertion.

3.8.   Recommendations for Future Work

To enable steam-jet testing of materials that have reduced SiO$_2$ activity, such as rare-earth silicates [72, 73], the fused quartz capillary must be replaced with a material that does not react with high-temperature water vapor. The success of the Pt/Rh wire used inside the fused quartz capillary to assist in the heating of the liquid water suggests that this material may be suitable for use as a non-reactive capillary. A Pt/Rh capillary of the same length and ID to the fused quartz capillary should be installed and validated at 1200 – 1400°C using SiO$_2$, Y$_2$O$_3$ and rare-earth silicates.

4.   Thermochemical Stability of $Y_2Si_2O_7$

4.1.   Objective

The objective of this chapter is to assess the thermochemical stability of $Y_2Si_2O_7$ in a high-temperature high-velocity water vapor environment by measuring the SiO_2 depletion rate as a function of time and temperature. Factors effecting the SiO_2 depletion from $Y_2Si_2O_7$ are identified and discussed.

4.2.   Experimental

4.2.1.   *Materials and Preparation*

$Y_2Si_2O_7$ powder was consolidated into a dense puck using Spark Plasma Sintering (SPS) as described in Section 2.2.1 and sectioned into ~10 x 10 x 1.5 mm test specimens. Specimens were annealed in air at 1350°C for 24 hours to eliminate oxygen deficiencies which formed during SPS. The as-annealed specimens were polished to a 1 µm finish with diamond. Specimens for EBSD characterization were polished to a 0.25 µm finish with diamond and then vibratory polished with 0.04 µm colloidal silica for 5 – 6 hours. After vibratory polishing the coupons were sonicated in soapy water to remove any remaining colloidal silica and then cleaned by a three step sonication in DI water, ethanol and acetone.

4.2.2.   *High-Temperature Water Vapor Exposures*

The steam-jet apparatus described in Section 2.3 was used to expose test specimens in a high-temperature high-velocity water vapor environment. Experiments were performed at 1000 – 1400°C for 6 – 250 hours, steam-jet velocities of 130 – 186 m/s and at 1 atm H_2O pressure. During steam-jet exposures that were 250 hours the fused quartz capillary was changed after 125

hours to limit the decrease in steam-jet velocity the specimen would experience throughout the duration of exposure. The decrease in steam-jet velocity results from the increase in the inner diameter of the capillary due to reaction with water vapor as discussed in Section 3.5.1. A single specimen was used to characterize the microstructural evolution with time (Section 4.3.4) and was exposed in the steam-jet at 1200°C for time intervals between 3 and 125 hours, slowly removed from the furnace (~ 12 minutes) at temperature and left to cool in ambient conditions. The specimen experienced a cooling rate of ~100°C/min. After removal from the furnace the specimen was characterized by weight change, XRD, SEM and EDS and then was inserted back into the steam-jet furnace at temperature for further exposure. This process was repeated until the total exposure time reached 250 hours. Throughout the entire experiment all steam-jet furnace hardware, with the exception of the fused quartz capillary, remained in place so that the impingement site on the specimen would be at the same location for every exposure. Fused quartz capillaries were changed after total exposure times of 24, 48, 60 and 125 hours to minimize the velocity decrease resulting from an increase in the capillary ID. In addition, capillaries were frequently changed because they have been observed to break during testing after being cycled at temperature running with and without steam.

4.2.3. Characterization

Weights of all specimens were measured before and after exposure to an accuracy of 0.05 mg. X-ray Diffraction (XRD) was performed on specimens before and after steam-jet exposure to determine if any polymorph/phase changes occurred during exposure. Specimen microstructure and composition were characterized by Scanning Electron Microscopy (SEM), Transmission Electron Microscopy (TEM) and Energy Dispersive Spectroscopy (EDS). SEM

images that were acquired using secondary electrons are denoted as SE/SEM images while images acquired using backscattered electrons are denoted as BSE/SEM images. The pore surface area was quantified by image analysis using ImageJ software. Electron Backscatter Diffraction (EBSD) was used to characterize phase and crystallographic orientation of grains in $Y_2Si_2O_7$ specimens after steam-jet exposure at 1300°C.

A Vickers hardness tester was used to indent the specimen surface utilized for the microstructural evolution study at locations 3 mm downstream of the impingement site so that the microstructure and phase evolution near the indent could be repeatedly found and characterized as a function of exposure time. The specimen used to characterize the microstructural evolution with time was coated with carbon before SEM and EDS characterization to reduce specimen charging. The carbon coating was baked off in a box furnace at 500°C for 30 minutes before the specimen was weighed and put back into the steam-jet furnace for further exposure.

4.2.4. *Cross-Sectioning Procedure and SiO₂ Depletion Measurements*

Specimens were mounted in epoxy, cross-sectioned and polished to a 1 µm finish with diamond for SEM and EDS characterization once the XRD analysis and surface characterization by SEM and EDS was complete. The specimen was carefully ground and polished so a total of ~150 – 200 µm of material was removed once the steam-jet impingement site was identified in cross-section by SEM. The specimen was then characterized again by SEM and EDS. This process was repeated ~5 – 8 times for every specimen that was exposed in the steam-jet furnace until the entire impingement site had been characterized (polished through). SiO_2 depletion measurements were made using ImageJ software from the BSE/SEM images taken at each cross-

section. SiO_2 depletion depths were measured at ~10 µm intervals across the entire impingement site on each cross-section. The cross-section from each specimen that had the greatest average SiO_2 depletion depth was used to represent the site at which the steam-jet velocity and SiO_2 volatility was the greatest.

4.3. Results

4.3.1. As-Processed Specimen

XRD analysis of as-processed specimens identified the β, γ and δ polymorphs as major and minor polytypes (Appendix C). A single low intensity peak for ZrO_2 (tetragonal) was also identified. Optical and SEM images of the surface of an as-processed specimen can be seen in Figure 4.1. The BSE/SEM image shows the specimen is dense and contains some surface cracks and ZrO_2 impurities (Figure 4.1b). The cracks originated during processing and will be discussed in more detail in Sections 4.4.1 & 4.4.2. The ZrO_2 impurities originated from the ZrO_2 beads used during ball milling of the as-received powder prior to consolidation by SPS. The initial grain size was measured to be 11.8 ± 3.8 µm.
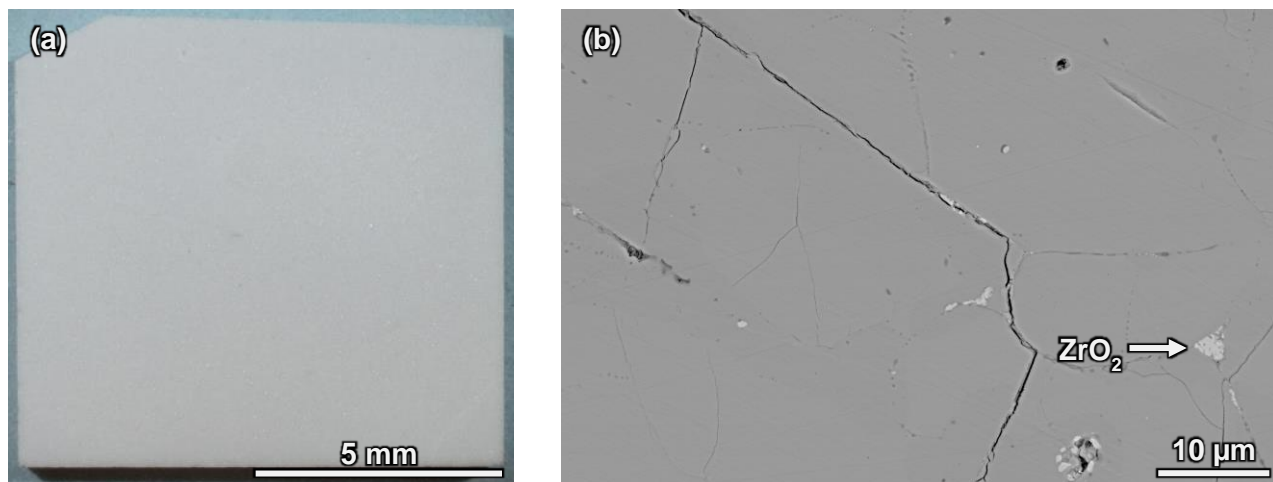
Figure 4.1. Optical (a) and BSE/SEM image (b) of the surface of an as-processed $Y_2Si_2O_7$ specimen showing cracks and ZrO_2 impurities from processing.

4.3.2. Time Dependence for SiO_2 Depletion from $Y_2Si_2O_7$

Specimens were exposed in the steam-jet for 60, 125 and 250 hours at 1200°C, a steam-jet velocity of 158 – 174 m/s and at 1 atm H_2O partial pressure. All specimens lost weight during steam-jet exposures (Appendix D). Although the weight loss of each specimen cannot be compared to one another since the area exposed to the steam-jet was different on each specimen, these results indicate that a volatilization reaction took place. After steam-jet exposures the β, γ and δ polymorphs were identified as major and minor polytypes (Appendix C). No correlation between the presence of major/minor polytypes and exposure time in the steam-jet were observed. The X2 polymorph of Y_2SiO_5 was also identified after steam-jet exposures indicating that SiO_2 had preferentially volatilized from $Y_2Si_2O_7$. The contrast observed in low magnification BSE/SEM images of the steam-jet impingement site on the specimen surface after exposure indicates that a different phase is present in the areas exposed to high-temperature water vapor (lighter region) (Figure 4.2). The darker $Y_2Si_2O_7$ regions found on the left side of the

images have not been exposed to high-velocity water vapor. Surface cracks that presumably

formed during exposure were also visible at the steam-jet impingement site. EDS acquired

outside of the area exposed to high-velocity water vapor shows there is a Y:Si ratio of ~1:1

which is consistent with $Y_2Si_2O_7$ (Figure 4.3a). EDS acquired at the steam-jet impingement site

shows there is a Y:Si ratio of ~2:1 indicating that SiO_2 had volatilized from $Y_2Si_2O_7$ to form

Y_2SiO_5 (Figure 4.3b), consistent with findings from the XRD analysis . Higher magnification

SE/SEM and BSE/SEM images of the steam-jet impingement site show the presence of a fine

grained (< 2 µm) Y_2SiO_5 that contains pores and surface cracks (Figure 4.4 – Figure 4.6).
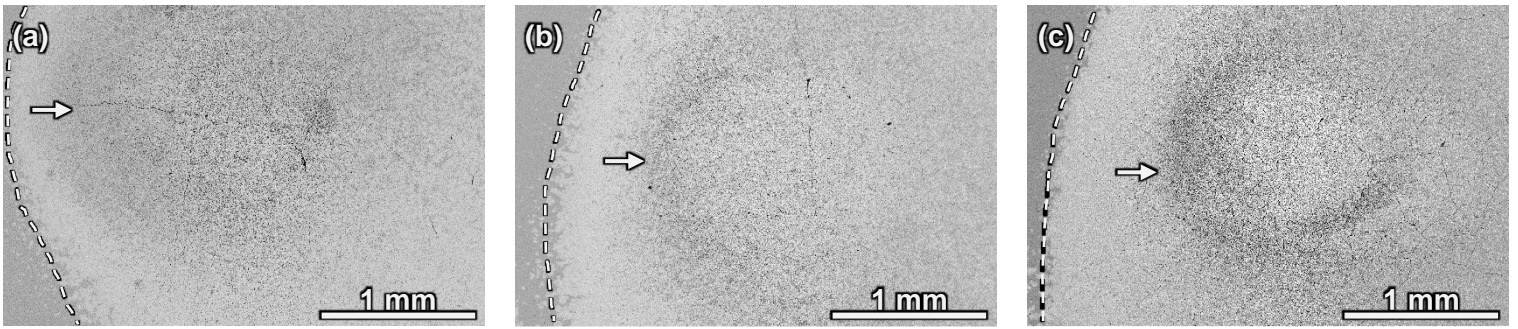
Figure 4.2. Plan view BSE/SEM images of the steam-jet impingements site on $Y_2Si_2O_7$ specimens after exposure for 60 (a), 125 (b) and 250 hours (c) at 1200°C. $v_{(g)}$= 169 – 171 m/s, $P(H_2O)$= 1 atm. Arrow ($\rightarrow$) indicates direction of steam-jet. Dashed lines indicate boundary between $Y_2Si_2O_7$ (dark) and Y_2SiO_5 (light).
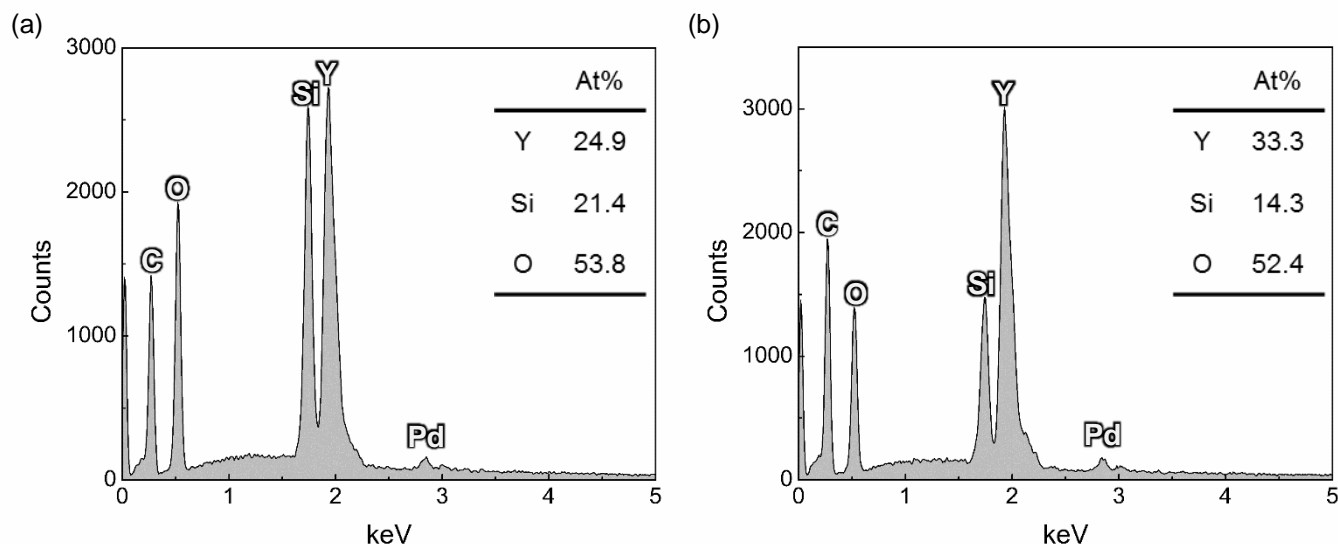
Figure 4.3. EDS analysis of $Y_2Si_2O_7$ after exposure in the steam-jet furnace for 250 hours at 1200°C, $v_{(g)}$= 171 m/s and $P(H_2O)$= 1 atm. Area upstream of the high-velocity water vapor exposure (a) and at the impingement site (b). The EDS was conducted using an accelerating voltage of 10kV. Quantification of carbon was excluded from the analysis.
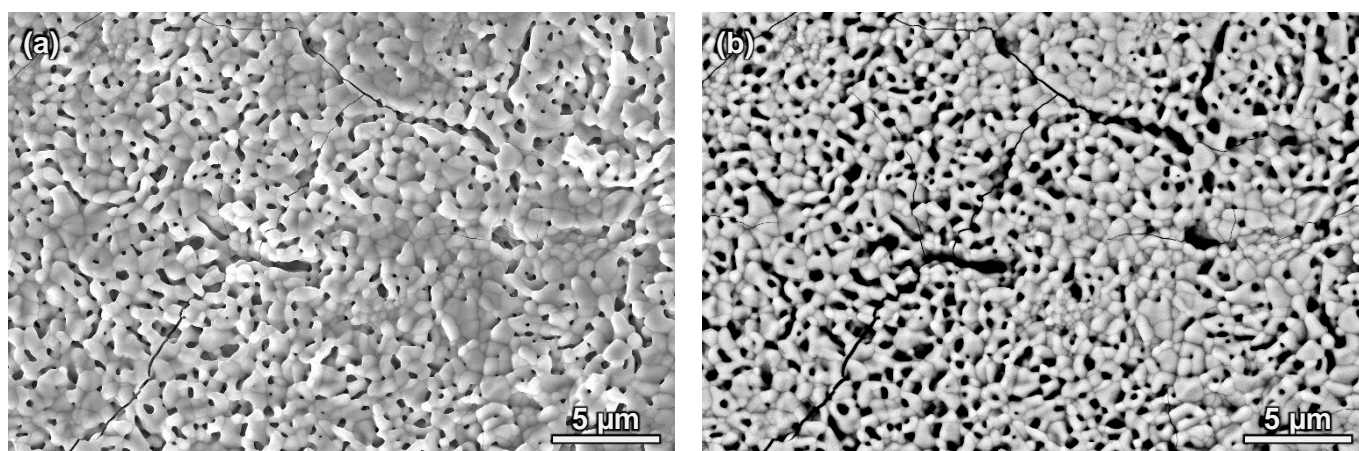
Figure 4.4. Plan view SE/SEM (a) and BSE/SEM (b) images of the steam-jet impingement site on a $Y_2Si_2O_7$ specimen after exposure for 60 hours at 1200°C showing porous Y_2SiO_5 surface. $v_{(g)}$= 170 m/s, $P(H_2O)$= 1 atm.
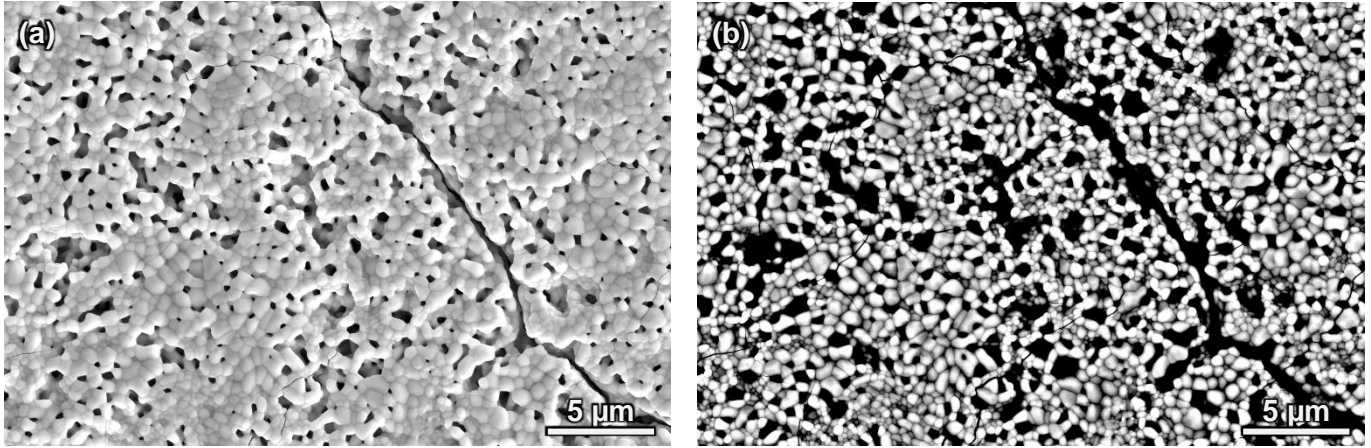
Figure 4.5. Plan view SE/SEM (a) and BSE/SEM (b) images of the steam-jet impingement site on a $Y_2Si_2O_7$ specimen after exposure for 125 hours at 1200°C showing porous Y_2SiO_5 surface. $v_{(g)}$= 169 m/s, $P(H_2O)$= 1 atm.
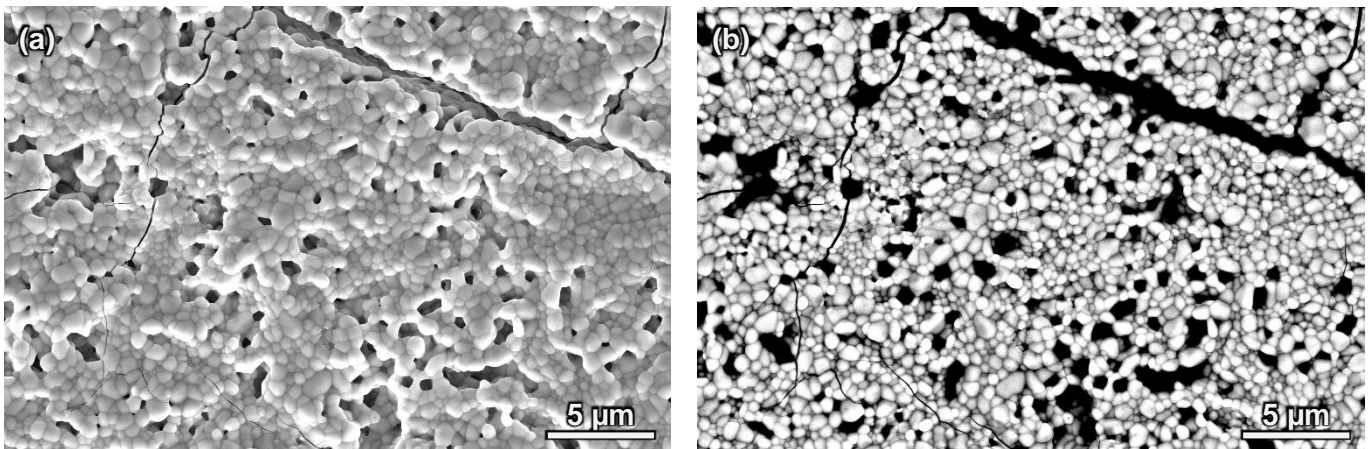
Figure 4.6. Plan view SE/SEM (a) and BSE/SEM (b) images of the steam-jet impingement site on a $Y_2Si_2O_7$ specimen after exposure for 250 hours at 1200°C showing porous Y_2SiO_5 surface. $v_{(g)}$= 171 m/s, $P(H_2O)$= 1 atm.

BSE/SEM characterization of cross-sections through the impingement site show that a fairly uniform porous depletion layer is present for all exposure times (Figure 4.7). The thickness of the porous depletion layer increases with time. EDS point analysis shows that the porous depletion layer has a Y:Si ratio of ~2:1 indicating that SiO_2 had volatilized from $Y_2Si_2O_7$ to form

Y_2SiO_5 (Figure 4.8), consistent with findings from XRD analysis and the EDS point analysis acquired in plan view at the specimen surface. EDS acquired on the base material below the porous depletion layer shows there is a Y:Si ratio of ~1:1 which is consistent with $Y_2Si_2O_7$. EDS maps of Y, Si and O acquired at the cross-section shown in Figure 4.8 show that the porous layer is depleted in Si and O (Figure 4.9). TEM characterization of a $Y_2Si_2O_7$ specimen exposed in the steam-jet for 125 hours showed there was no SiO_2 present along the $Y_2SiO_5 - Y_2Si_2O_7$ interface, inside Y_2SiO_5 pores or at grain boundaries (Figure 4.10)

Figure 4.7. BSE/SEM images of cross-sections through the steam-jet impingement site on $Y_2Si_2O_7$ specimens exposed for 60 (a), 125 (b) and 250 hours (c) at 1200°C showing porous Y_2SiO_5 surface layer. $v_{(g)}$= 169 – 171 m/s, $P(H_2O)$= 1 atm.
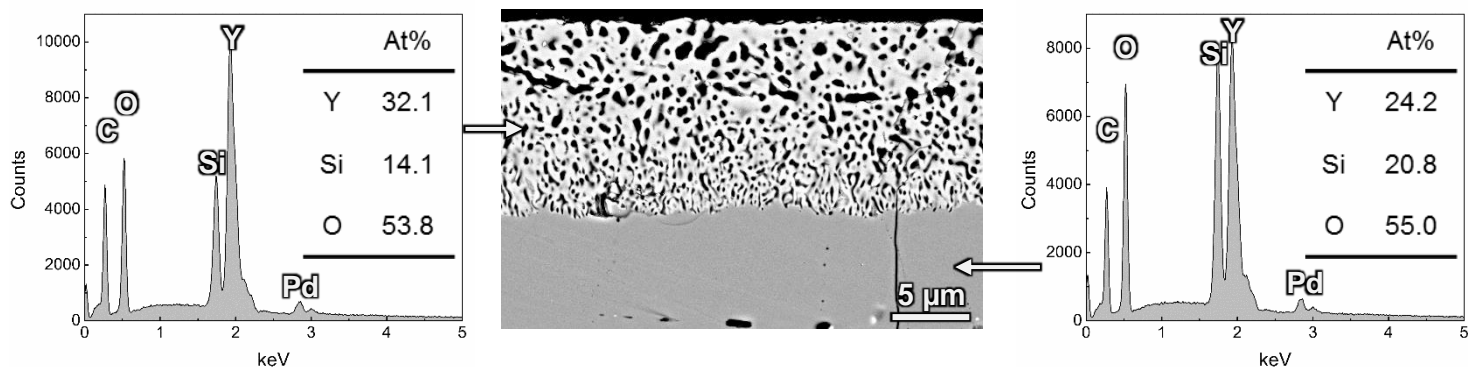
Figure 4.8. EDS analysis of a cross-section through a $Y_2Si_2O_7$ specimen after exposure in the steam-jet furnace for 250 hours at 1200°C, $v_{(g)}$= 164 m/s and $P(H_2O)$= 1 atm. Porous Y_2SiO_5 layer (left) and base $Y_2Si_2O_7$ (right). The EDS was conducted using an accelerating voltage of 10kV. Quantification of carbon was excluded from the analysis.
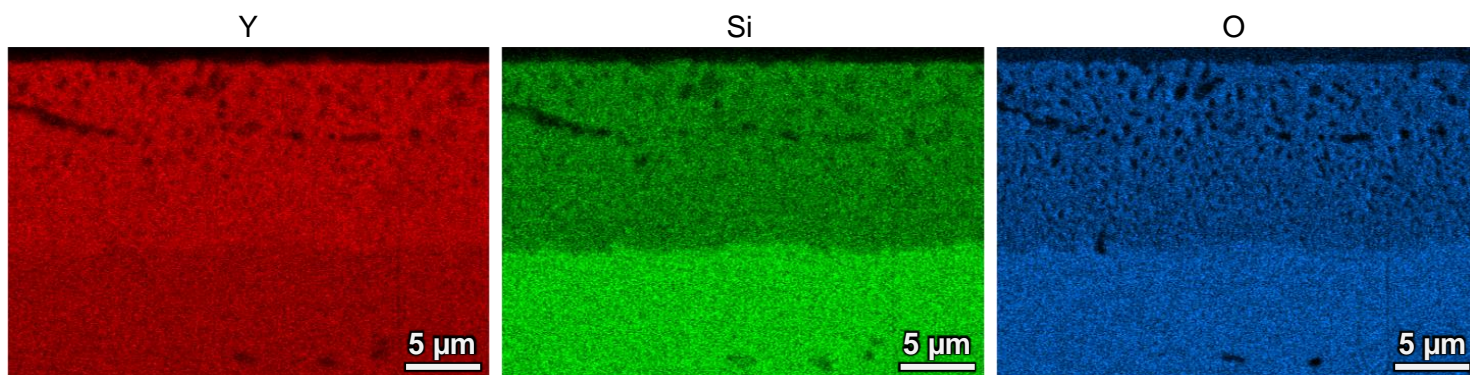
Figure 4.9. EDS maps of Y, Si and O acquired for the cross-section shown in Figure 4.8 showing Si and O depletion and Y enrichment of the porous surface layer. $Y_2Si_2O_7$ specimen was exposed in the steam-jet for 250 hours at 1200°C, $v_{(g)}$= 164 m/s and $P(H_2O)$= 1 atm. EDS maps were acquired using an accelerating voltage of 10kV.
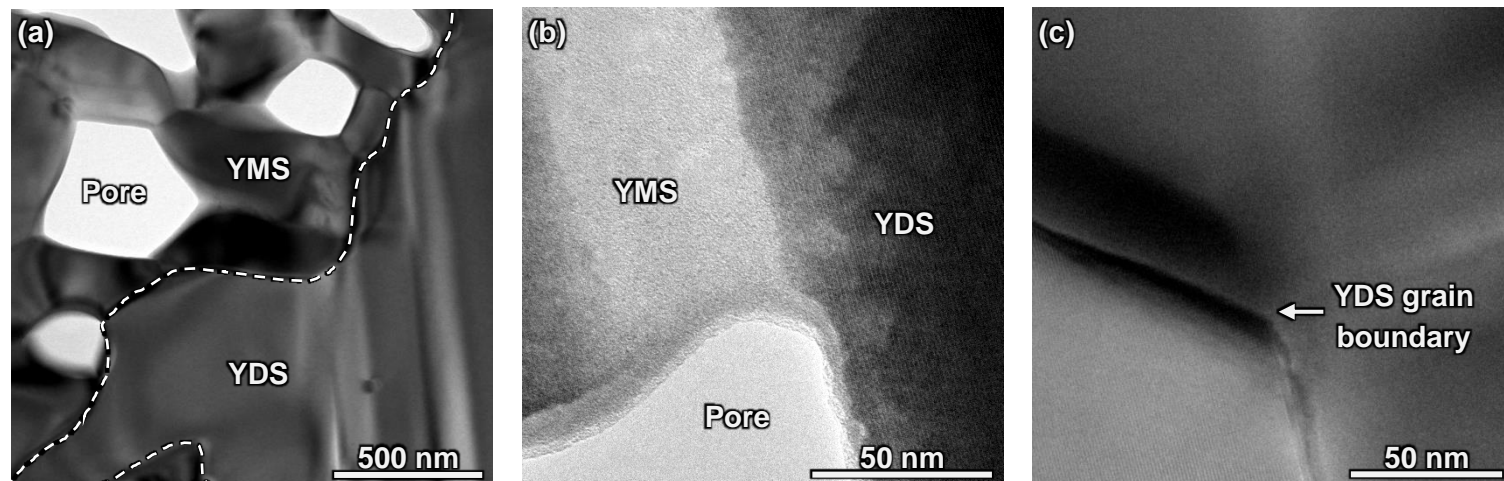
Figure 4.10. TEM images showing there is no SiO_2 at the Y_2SiO_5 (YMS) – $Y_2Si_2O_7$ (YDS) interface (a,b) and at a YDS grain boundary (c) in a YDS specimen exposed in the steam-jet for 125 hours at 1200°C. $v_{(g)}$= 165 m/s, $P(H_2O)$= 1 atm.

The average SiO_2 depletion depths measured from cross-sections at each exposure time are shown in Table 4.1 and plotted vs. $time^{1/2}$ in Figure 4.11. SiO_2 volatility from $Y_2Si_2O_7$ appears to follow parabolic kinetics based on the reasonable agreement of the measured SiO_2 depletion data to the linear fit (Figure 4.11), however, there is a large scatter associated with the average SiO_2 depletion depth measured for each exposure time. Although the variation in SiO_2 depletion depth for a single specimen was relatively small ($\pm$ 0.7 to $\pm$ 1.9) the variation in SiO_2 depletion from specimen to specimen was large (e.g. 6.1 $\pm$ 1.2 to 17.5 $\pm$ 1.2 for 250 h) which contributes to the large observed scatter. The average SiO_2 depletion depth measured for all specimens in this study can be found in Appendix E. No correlation between the average SiO_2 depletion depth and the specimen processing batch was observed.

Table 4.1. Average SiO_2 depletion depths for $Y_2Si_2O_7$ specimens exposed in the steam-jet for 60, 125 and 250 hours at 1200°C. $v_{(g)}$= 158 – 174 m/s, $P(H_2O)$= 1 atm.

Exposure Time (h)	Average SiO_2 Depletion Depth (µm)
60	4.47 ± 2.06
125	5.81 ± 2.37
250	10.1 ± 4.26
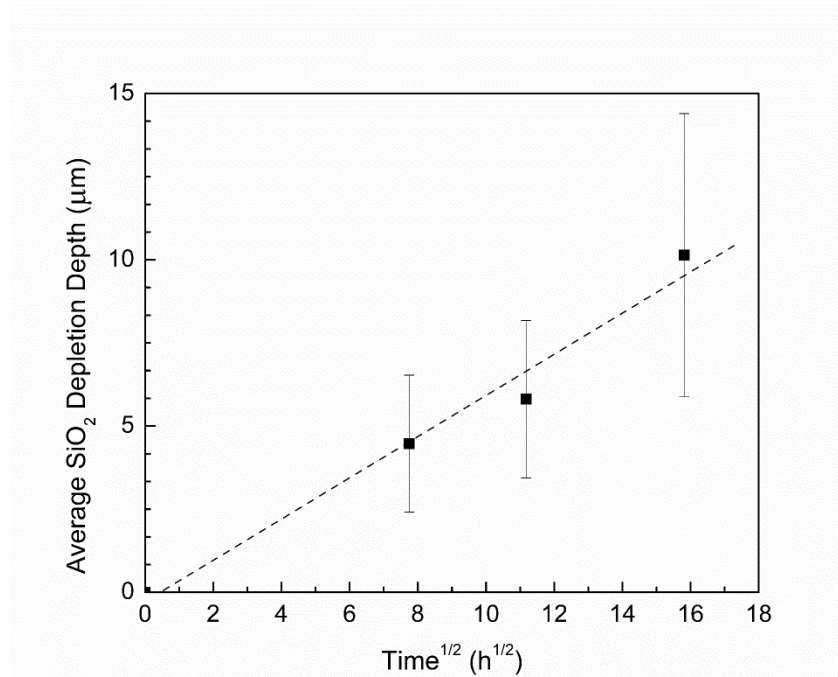
Figure 4.11. Plot of the average SiO_2 depletion depth vs. time $^{1/2}$ measured from $Y_2Si_2O_7$ specimens exposed in the steam-jet for 60, 125, and 250 hours at 1200°C. Linear fit indicates parabolic kinetics. $v_{(g)}$= 158 – 174 m/s, $P(H_2O)$= 1 atm.

4.3.3. *Temperature Dependence for SiO_2 depletion from $Y_2Si_2O_7$*

Specimens were exposed in the steam-jet for 125 hours at 1000 – 1400°C, a steam-jet velocity of 130 – 186 m/s and at 1 atm H_2O partial pressure. All specimens lost weight during steam-jet exposures (Appendix D) indicating that a volatilization reaction took place. After steam-jet exposures the β, γ and δ polymorphs were identified as major and minor polytypes

(Appendix C). No correlation between the presence of major/minor polytypes and the exposure temperature of the steam-jet were observed. The X2 polymorph of Y_2SiO_5 was also identified on some specimens after steam-jet exposures. The contrast observed in low magnification BSE/SEM images of the steam-jet impingement site on the specimen surface after exposure at $1000 - 1200°C$ indicates that a different phase is present in the areas exposed to high-velocity water vapor (lighter region) (Figure 4.12). The darker regions found on the left side of the images have not been exposed to high-velocity water vapor. Surface cracks that presumably formed during exposure were also visible at the steam-jet impingement site. EDS acquired outside of the area exposed to high-velocity water vapor shows there is a Y:Si ratio of ~1:1, consistent with $Y_2Si_2O_7$, whereas a Y:Si ratio of ~2:1 was found at the steam-jet impingement site indicating the formation of Y_2SiO_5. These results are consistent with the EDS results from specimens exposed for $60 - 250$ hours at $1200°C$ (Figure 4.3). Higher magnification SE/SEM and BSE/SEM images of the steam-jet impingement site show the presence of fine grained (≤ 2 µm) Y_2SiO_5 that contains pores and surface cracks (Figure 4.5, Figure 4.13, Figure 4.14). Most pores are seen to take on a "rectangular" like appearance on the specimen exposed at $1000°C$ whereas specimens exposed at $1100°C$ and $1200°C$ have pores that are round. In some areas the "rectangular" pores appear to be oriented in a particular direction indicating there is a possible crystallographic orientation dependence related to their formation.
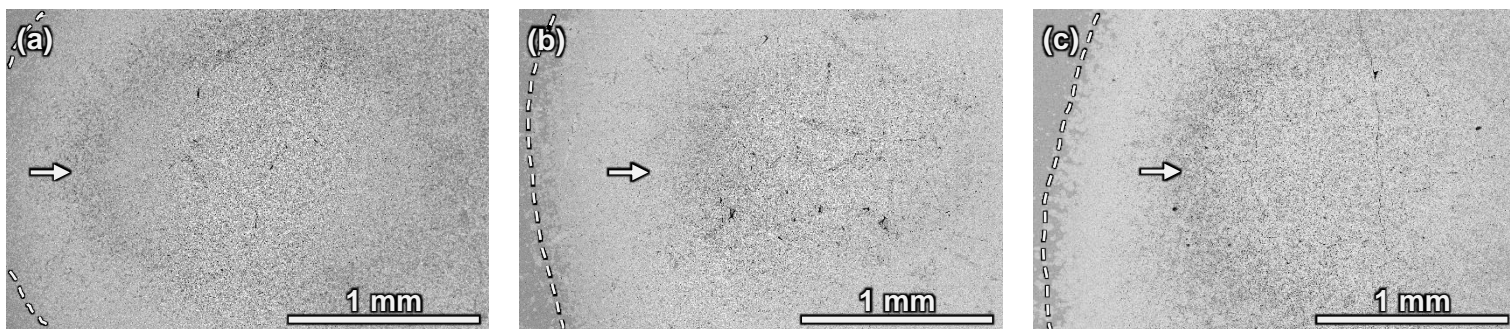
Figure 4.12. Plan view BSE/SEM images of the steam-jet impingements site on $Y_2Si_2O_7$ specimens after exposure for 125 hours at 1000°C (a), 1100°C (b) and 1200°C (c). $v_{(g)}$= 130 – 169 m/s, P(H_2O)= 1 atm. Arrow ($\rightarrow$) indicates direction of steam-jet. Dashed lines indicate boundary between $Y_2Si_2O_7$ (dark) and Y_2SiO_5 (light).
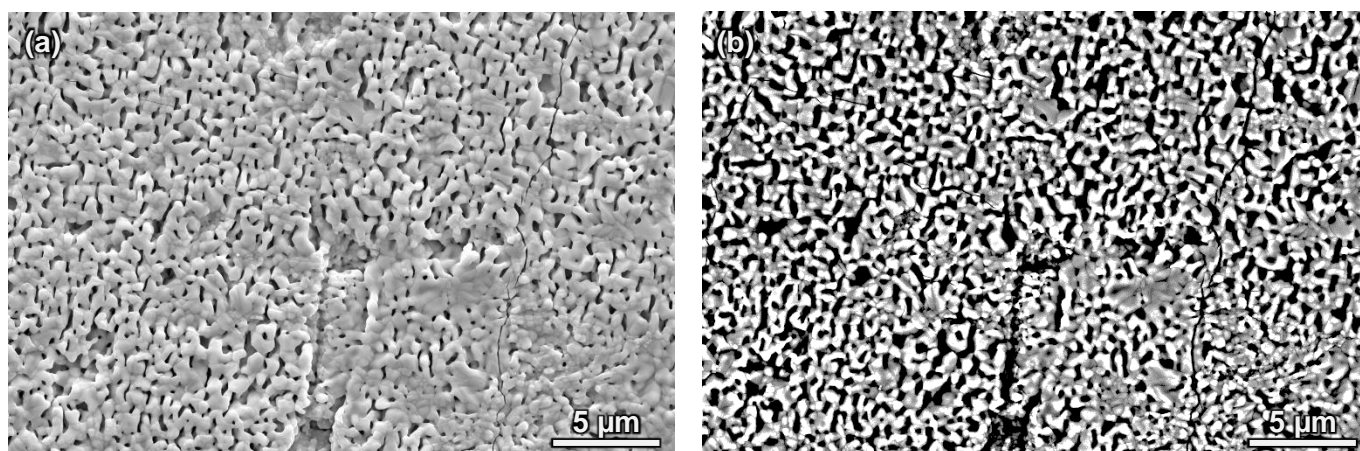
Figure 4.13. Plan view SE/SEM (a) and BSE/SEM (b) images of the steam-jet impingement site on a $Y_2Si_2O_7$ specimen after exposure for 125 hours at 1000°C showing porous Y_2SiO_5 surface. $v_{(g)}$= 130 m/s, P(H_2O)= 1 atm.
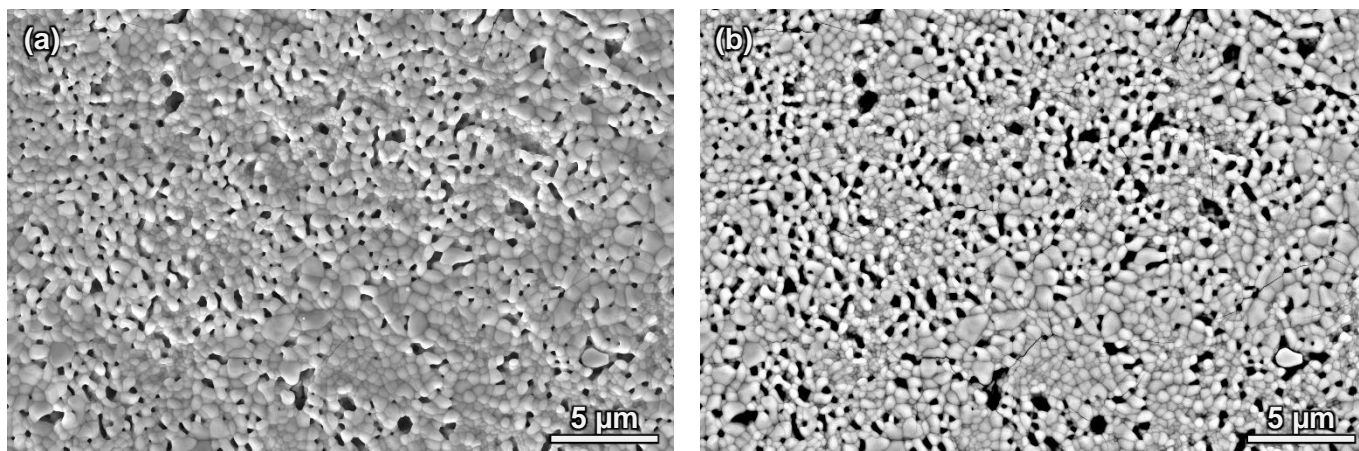
Figure 4.14. Plan view SE/SEM (a) and BSE/SEM (b) images of the steam-jet impingement site on a $Y_2Si_2O_7$ specimen after exposure for 125 hours at 1100°C showing porous Y_2SiO_5 surface. $v_{(g)}$= 149 m/s, P(H_2O)= 1 atm.

SE/SEM images of the steam-jet impingement site on the specimen surface after exposure at 1300°C and 1400°C shows the presence of faceted grains and some porosity. Different grains have undergone faceting with different orientation and spacing. Specimens exposed at 1400°C were observed to have less porosity than those exposed at 1000 – 1300°C. EDS acquired at the steam-jet impingement site shows there is a Y:Si ratio of ~1:1 which is consistent with $Y_2Si_2O_7$.
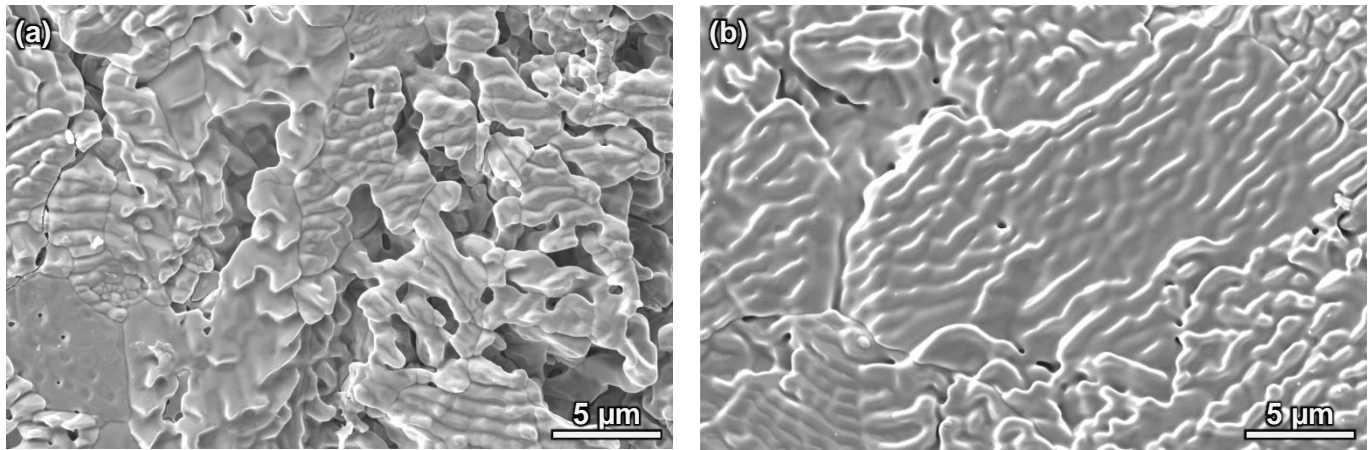
Figure 4.15. Plan view SE/SEM images of the steam-jet impingement site on a $Y_2Si_2O_7$ specimen after exposure for 125 hours at 1300°C (a) and 1400°C (b) showing faceted surface. $v_{(g)}$= 174 – 186 m/s, $P(H_2O)$= 1 atm.

BSE/SEM characterization of cross-sections through the impingement site on specimens exposed in the steam-jet at 1000 – 1200°C show that a fairly uniform porous depletion layer is present (Figure 4.16). The thickness of the porous depletion layer is similar at 1000°C and 1100°C whereas it is considerably larger at 1200°C. The pores in the depletion layer at 1000°C are small and elongated toward the specimen surface while at 1100°C a mix between elongated and round pores is observed. At 1200°C all pores are round. Cross-sections through the impingement site on specimens exposed in the steam-jet at 1300°C and 1400°C show that a non-uniform porous depletion layer is present (Figure 4.17). The porous depletion layer was observed to predominantly form at cracks on specimen exposed at 1300°C and only formed at cracks on specimens exposed at 1400°C. EDS point analysis indicates that the porous depletion layer is Y_2SiO_5 based on the Y:Si ratio of ~2:1. This is not consistent with the results from the EDS analysis acquired in plan view at the specimen surface. Given the non-uniformity of the SiO_2 depletion layer at these temperatures the plan view EDS point analysis may have been acquired

81

in regions where there was no SiO_2 depletion layer or it was very thin. The average SiO_2

depletion depths measured from cross-sections at each exposure temperature are shown in Table

4.2 and plotted in Figure 4.18. The average SiO_2 depletion depth could not be measured on

specimens exposed at 1300°C and 1400°C due to the non-uniformity of the SiO_2 depletion layer

and because SiO_2 predominantly depleted at defects such as cracks. SiO_2 volatility from $Y_2Si_2O_7$

is the same at 1000°C and 1100°C and a factor of ~4 greater at 1200°C. The temperature

dependence activation energy for SiO_2 volatilization from $Y_2Si_2O_7$ could not be described with

an Arrhenius relationship since the average SiO_2 depletion was the same at 1000°C and 1100°C

and much greater at 1200°C. This indicates there is a possible change in volatilization

mechanism between 1000°C and 1100°C or there are several contributing mechanisms that affect

the SiO_2 volatility from $Y_2Si_2O_7$.
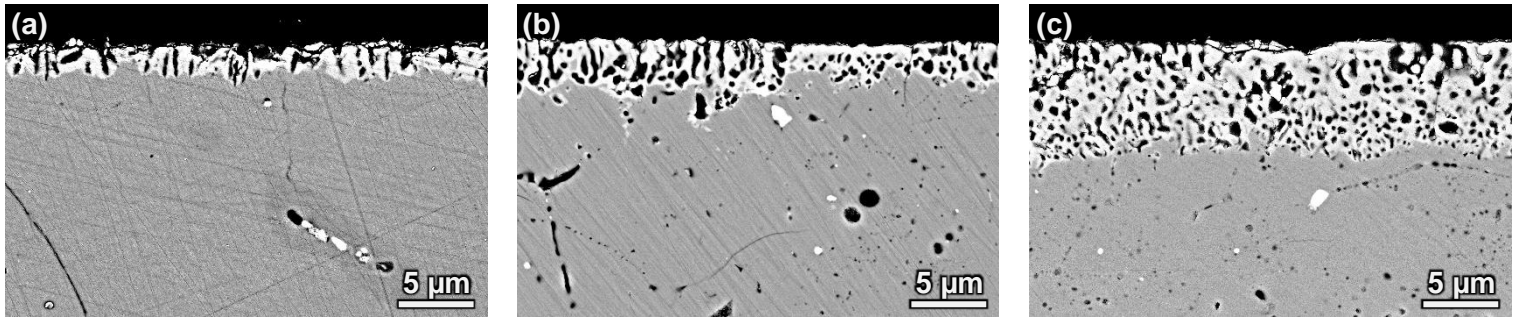
Figure 4.16. BSE/SEM images of cross-sections through the steam-jet impingement site on $Y_2Si_2O_7$ specimens exposed for 125 hours at 1000°C (a), 1100°C (b) and 1200°C (c) showing porous Y_2SiO_5 surface layer. $v_{(g)}$= 130 – 169 m/s, $P(H_2O)$= 1 atm.
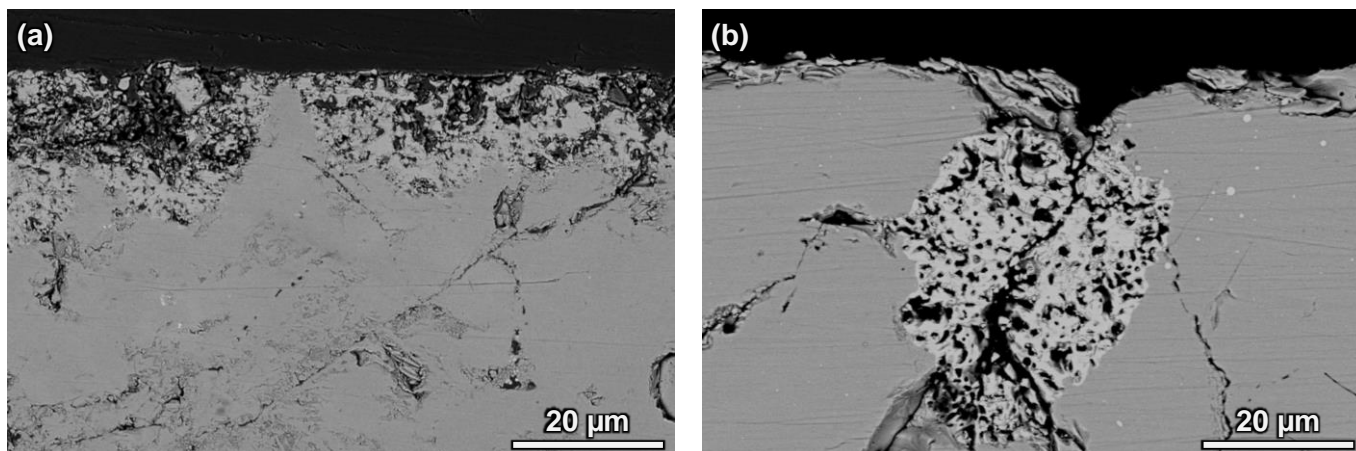
Figure 4.17. BSE/SEM images of cross-sections through the steam-jet impingement site on $Y_2Si_2O_7$ specimens exposed for 125 hours at 1300°C (a) and 1400°C (c). $v_{(g)}= 174 – 186$ m/s, $P(H_2O)= 1$ atm.

Table 4.2. Average SiO_2 depletion depths for $Y_2Si_2O_7$ specimens exposed in the steam-jet for 125 hours at 1000°C – 1400°C. $v_{(g)}= 130 – 186$ m/s, $P(H_2O)= 1$ atm.

Exposure Temperature (°C)	Average SiO_2 Depletion Depth (µm)
1000	1.41 ± 0.64
1100	1.42 ± 0.66
1200	5.81 ± 2.37
1300	n/a
1400	n/a
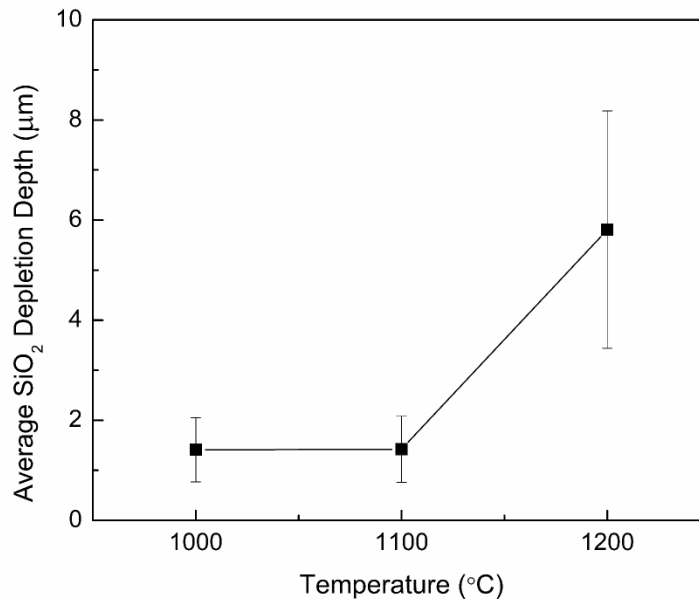
Figure 4.18. Plot of the average SiO_2 depletion depth vs. temperature measured from $Y_2Si_2O_7$ specimens exposed in the steam-jet for 125 hours at 1000°C, 1100°C and 1200°C. $v_{(g)}$= 130 – 170 m/s, $P(H_2O)$= 1 atm.

4.3.4. Microstructural Evolution

A single specimen was exposed in the steam-jet at 1200°C for multiple times between 3 and 125 hours to understand the sequence in which the microstructure evolves with time as SiO_2 is depleted from $Y_2Si_2O_7$. The specimen was removed from the furnace after the desired exposure time, characterized by weight change, XRD, SEM and EDS and then inserted back into the steam-jet furnace for further exposure. This process was repeated until the total exposure time reached 250 hours.

The measured specimen weight loss increased with exposure time and is plotted vs. time$^{1/2}$ in Figure 4.19 . The weight loss due to SiO_2 volatility from $Y_2Si_2O_7$ follows parabolic kinetics based on the good agreement of the measured weight loss data to the linear fit. The red

dotted lines indicate when a new fused quartz capillary was inserted. XRD analysis of as-processed specimens identified the δ polymorph as the major polytype and the β polymorph as the minor polytype (Appendix F). As the total steam-jet exposure time increased the peaks corresponding to the δ polymorph were observed to decrease while the peaks corresponding to the β polymorph increased. After a total steam-jet exposure time of 60 hours the intensity of the main peak for the β polymorph surpassed that of the δ polymorph. The X2 polymorph of Y_2SiO_5 was identified after 30 hours of exposure.
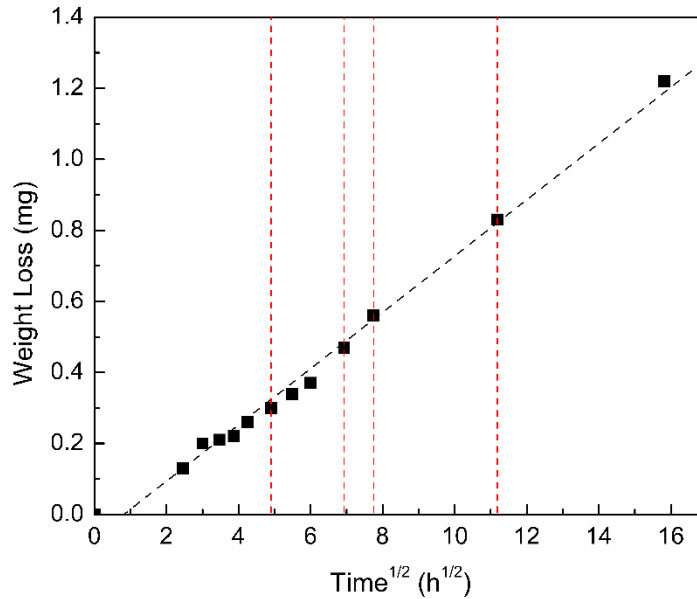
Figure 4.19. Plot of weight loss vs. time $^{1/2}$ measured from a $Y_2Si_2O_7$ specimen exposed in the steam-jet for up to 250 hours at 1200°C. Specimen was intermittently removed from the steam-jet furnace during exposure to be weighed. Linear fit indicates parabolic kinetics. $v_{(g)}$= 164 m/s, $P(H_2O)$= 1 atm. The red dotted lines indicate when a new fused quartz capillary was inserted.

4.3.4.1. Microstructural Evolution of $Y_2Si_2O_7$ at the Impingement Site

BSE/SEM and EDS characterization of the steam-jet impingement site after exposure for 6 hours at 1200°C shows that the majority of the surface is depleted in SiO_2 and very few $Y_2Si_2O_7$ grains remain (Figure 4.20). The SiO_2 depleted microstructure contains significant porosity where the majority of the pores take on an elongated "rectangular" appearance and appear to be oriented in specific directions. Some round pores were also observed. The initial rate at which SiO_2 is depleted from $Y_2Si_2O_7$ is fast, making it difficult to characterize the initiation and evolution of the SiO_2 depleted microstructure at the steam-jet impingement site. Therefore, characterization of the initiation and evolution of the SiO_2 depleted microstructure was made downstream of the impingement site as described in the next section.
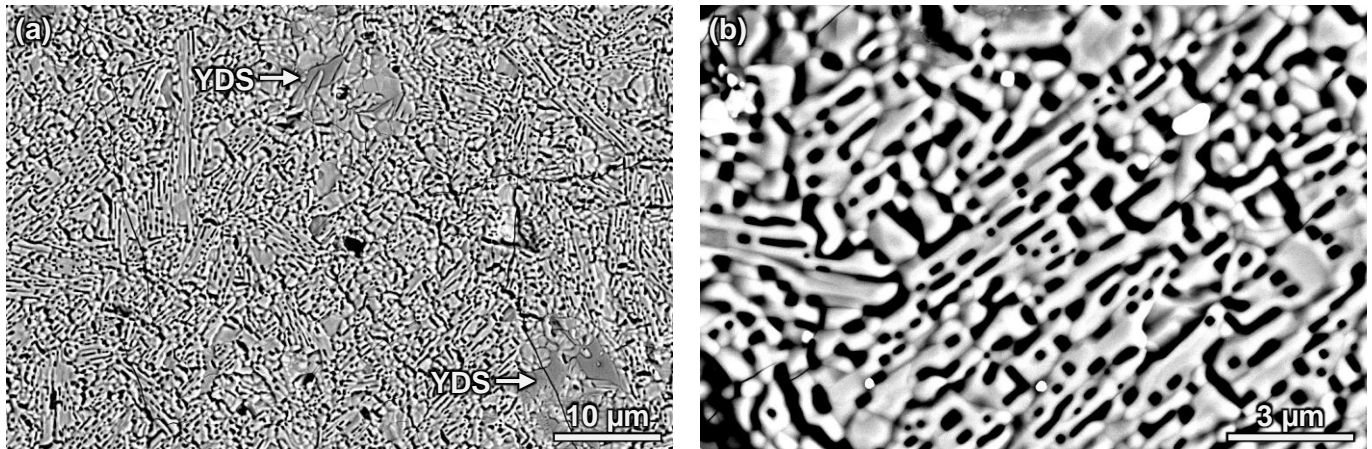
Figure 4.20. Plan view BSE/SEM images of the steam-jet impingement site on a $Y_2Si_2O_7$ (YDS) specimen after exposure for 6 hours at 1200°C showing rapid formation of Y_2SiO_5 + oriented pores. $v_{(g)}$= 164 m/s, $P(H_2O)$= 1 atm.

4.3.4.2. Microstructural Evolution of $Y_2Si_2O_7$ Downstream of the Impingement Site

The initiation and evolution of the SiO_2 depleted microstructure was characterized 3 mm downstream of the steam-jet impingement site where the rate of SiO_2 depletion from $Y_2Si_2O_7$

was slower than the impingement site. The steam-jet velocity 3 mm downstream of the impingement site was determined to be 79 m/s from the ANSYS CFD model described in Appendix A. The reduced velocity 3 mm downstream is a factor of ~2.1 less than at the steam-jet impingement site resulting in a factor of ~1.4 less flux of volatile gas species as shown by Equation (3.6).

BSE/SEM and EDS characterization of the initiation and evolution of the SiO_2 depleted microstructure can be seen in Figure 4.21. After 6 hours of exposure the initiation of SiO_2 depletion was observed to occur inside grains, at grain boundaries and surface cracks resulting in the formation of both porous and faceted regions of Y_2SiO_5 (Figure 4.21b). Pores with a "rectangular" appearance were typically observed at sites where SiO_2 depletion was first initiated. Red arrows in Figure 4.21b indicate initiation sites for SiO_2 depletion. The SiO_2 depletion fronts spread out from sites where SiO_2 was initially depleted. The newly formed SiO_2 depleted regions were comprised of small grains ($< 1\ \mu m$) and very few pores. After $12 - 36$ hours of exposure the SiO_2 depletion front continued to spread and consumed all remaining $Y_2Si_2O_7$ grains (Figure 4.21c, d, e, f). Round pores formed and coarsened in the regions already depleted in SiO_2. Grain growth and the formation of cracks were also observed. After $60 - 250$ hours of exposure the pores and grains of the SiO_2 depleted microstructure continued to coarsen (Figure 4.21g, h, i). Pre-existing cracks were observed to self-heal while new cracks were observed to form.
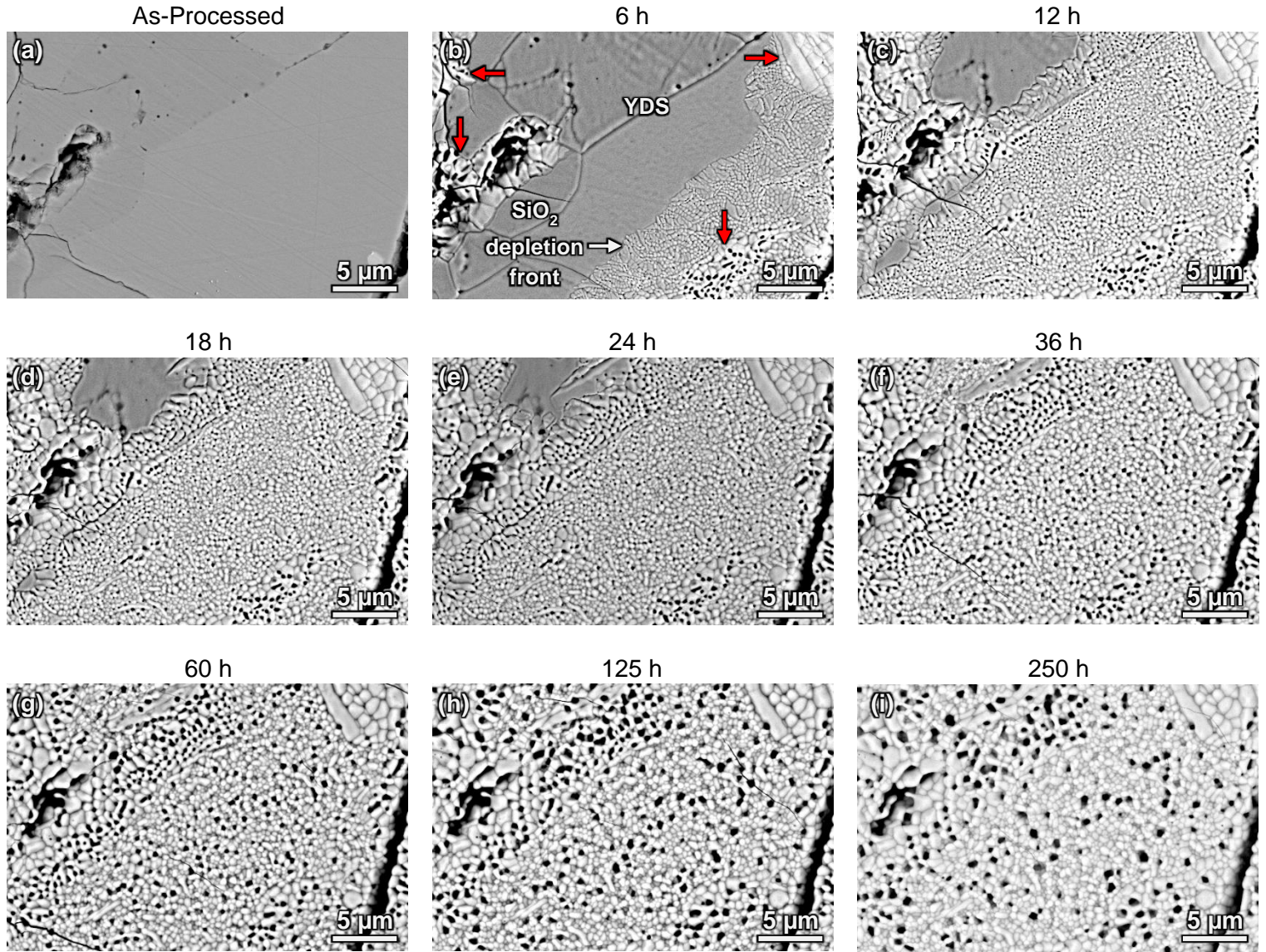
Figure 4.21. Plan view BSE/SEM images 3 mm downstream of the steam-jet impingement site on a $Y_2Si_2O_7$ (YDS) specimen after intermittent removal and exposure for up to 250 hours at 1200°C. Sequence shows SiO_2 depletion was initiated at some locations (red arrows) and the SiO_2 depletion front spreads (white arrow) while grains and pores coarsen with time. $v_{(g)}= 79$ m/s, $P(H_2O)= 1$ atm.

Image analysis was used to quantify the average pore size and total pore area fraction after steam-jet exposures from 12 – 250 hours (Figure 4.22). BSE/SEM images used for the image analysis are shown in Appendix G. The average pore size was seen to increase with exposure time at a decreasing rate, consistent with BSE/SEM observations. The total pore area fraction generally increased for times up to 125 hours of exposure. After 250 hours of exposure the total pore area fraction decreased.
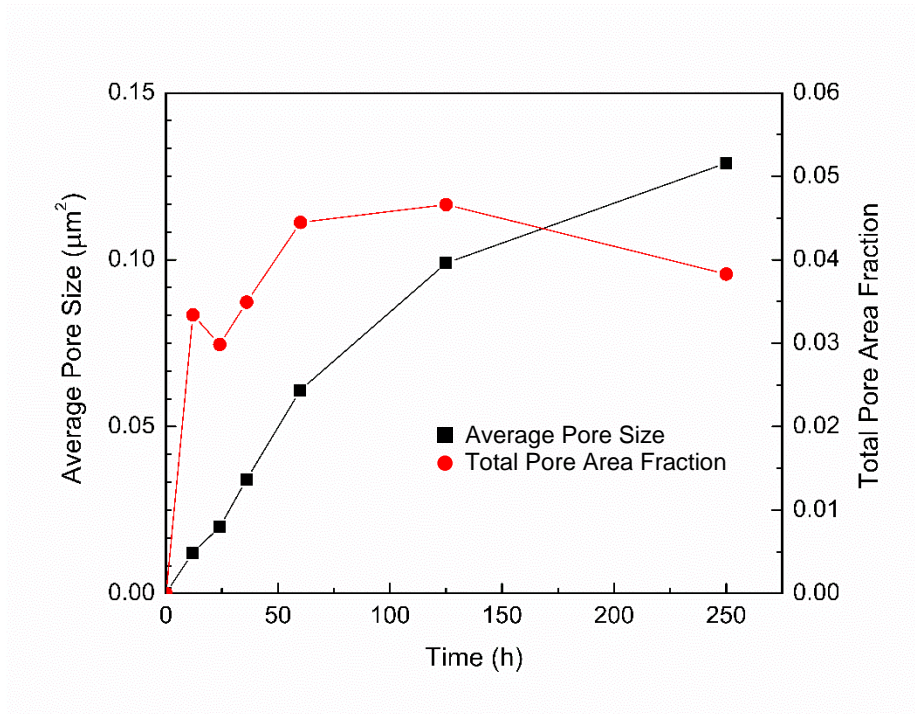
Figure 4.22. Plot of the average pore size and total pore area fraction vs. exposure time showing coarsening of pores and reduction of pore area fraction. Measurements are from BSE/SEM images 3 mm downstream of the steam-jet impingement site on a $Y_2Si_2O_7$ (YDS) specimen after intermittent removal and exposure for up to 250 hours at 1200°C. $v_{(g)}$= 79 m/s, P(H_2O)= 1 atm.

A cross-section 3 mm downstream of the impingement site of a $Y_2Si_2O_7$ specimen exposed in the steam-jet for 12 hours at 1200°C shows that elongated rectangular pores form perpendicular to the specimen surface (Figure 4.23). It is hypothesized that right of the dotted

line shows the initiation site for SiO_2 depletion with "rectangular" pores and left of the dotted line shows where the SiO_2 depletion front may have spread from to form Y_2SiO_5 with small circular pores. This pore microstructure is very different to that seen in cross-section after exposure for 60 – 250 hours at 1200°C (Figure 4.7). Specimens exposed for 125 hours at 1000°C and 1100°C showed the presence of some small elongated pores (Figure 4.16).
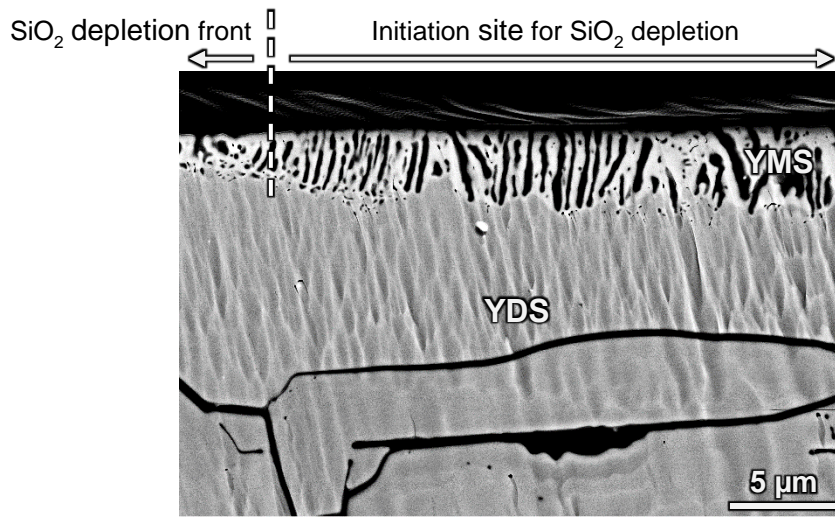
Figure 4.23. BSE/SEM image of a cross-section 3 mm downstream of the steam-jet impingement site on $Y_2Si_2O_7$ (YDS) specimen exposed for 12 hours at 1200°C. $v_{(g)}$= 158 m/s, P(H_2O)= 1 atm. Right of the dotted line shows the initiation site for SiO_2 depletion with "rectangular" pores and left of the dotted line shows where the SiO_2 depletion front spread from with circular pores.

4.3.5. Non-Uniform SiO₂ Depletion

The uniformity of the SiO_2 depletion layer is highly dependent on specimen microstructure and defects such as cracks, pores and grain fallout. Grain fallout refers to the process when a porous Y_2SiO_5 surface layer is formed and breaks off the specimen leaving underlying $Y_2Si_2O_7$ exposed to high-temperature water vapor. The presence of cracks, porosity and grain fallout provide fast pathways for water vapor to penetrate below the specimen surface

90

and react with underlying $Y_2Si_2O_7$. This results in a non-uniform SiO_2 depletion layer like that shown in Figure 4.24, where the red arrows show SiO_2 depletion along cracks and the green arrows show SiO_2 depletion in regions that experienced grain fallout. This was also observed in specimens exposed in the steam-jet at 1300°C and 1400°C (Figure 4.17). In regions that do not have any defects, like the one on the right side of Figure 4.24, a uniform SiO_2 depletion layer is observed. For the purposes of determining the SiO_2 volatilization kinetics from $Y_2Si_2O_7$, only regions of SiO_2 depletion that are unaffected by defects were reported in Sections 4.3.2 & 4.3.3. The formation of cracks in $Y_2Si_2O_7$ and Y_2SiO_5 will be discussed in Sections 4.4.1 & 4.4.2.
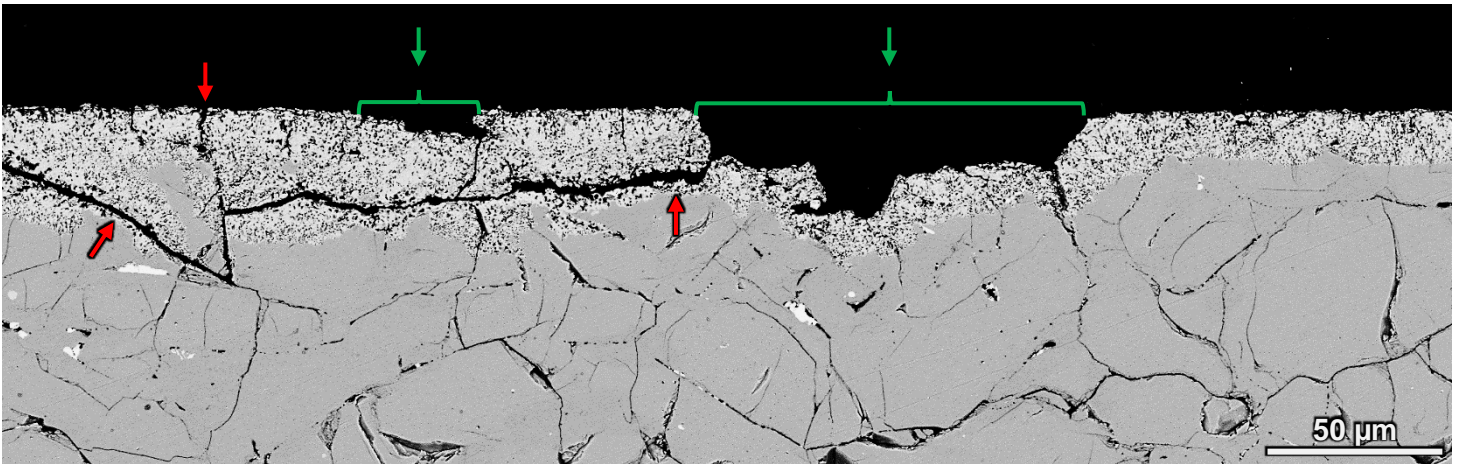
Figure 4.24. BSE/SEM image of a cross-section through the steam-jet impingement site on a $Y_2Si_2O_7$ specimen exposed for 250 hours at 1000°C (a), 1100°C (b) and 1200°C (c). $v_{(g)}$= 163 m/s, P(H_2O)= 1 atm. Red arrows show SiO_2 depletion along cracks and green arrows show regions of grain fallout.

4.4. Discussion

4.4.1. As-Processed Specimens

SEM characterization of the surface of as-processed specimens showed that they are dense and contain some surface cracks and ZrO_2 impurities (Figure 4.1b). The exact cause

leading to crack formation during processing is unknown, however, the multiple polymorphs present in the specimens after processing (Appendix C) have the potential to induce cracking from the volume changes associated with their transformation and differences in their CTE. The volume reduction associated with the transformation of the β polymorph (as-received powder) to the γ and δ polymorphs is less than 1.3% and is therefore unlikely to be the cause of the observed cracks in the as-processed material. The CTE of the β (4.1×10^{-6} °C^{-1}) and γ (3.9×10^{-6} °C^{-1}) polymorphs are very similar while the δ (8.1×10^{-6} °C^{-1}) polymorph has a much larger CTE (Table 1.1) [54]. Such large differences in CTE could lead to crack formation during SPS processing and is thus the likely cause of the observed cracks.

The presence of the β, γ and δ polymorphs after processing is to be expected since the as-received $Y_2Si_2O_7$ is mainly comprised of the β polymorph and the SPS hold temperature (1550°C) is very close to the γ → δ transformation temperature (Table 1.1) [92, 93]. There is controversy over the temperatures associated with the polymorphic transformations since many authors have observed polymorphs well outside of their supposed temperature region of stability [55, 59, 92–99]. This indicates that under certain circumstances the polymorphic transformations in $Y_2Si_2O_7$ can be sluggish and the presence of multiple polymorphs at any time are not uncommon. In the majority of cases the δ polymorph was identified as either a major or minor polymorph present after SPS and annealing (Appendix C). The δ polymorph was not present after processing batch #3 and #15 specimens and was identified after some steam-jet exposures as a minor polymorph. SEM characterization of cross-sections from batch #3 and #15 specimens after steam-jet exposure showed that they contained very few or no subsurface cracks whereas specimens from other batches were always found to contain cracks. These observations support the notion that the CTE differences between the δ and β/γ polymorphs could be the cause for the

cracks observed after processing and exposure. It is currently unknown why batches #3 and #15 did not contain the δ polymorph.

The ZrO_2 impurities observed in the specimen after processing originated from the ZrO_2 beads used to ball mill the as-received $Y_2Si_2O_7$ powder prior to consolidation by SPS. ZrO_2 (10.6 x 10^{-6} $°C^{-1}$) [127] does have a large CTE difference from the β and γ polymorphs of $Y_2Si_2O_7$ however it was present as small particles and as a small volume fraction, so it is not expected to create significant CTE mismatch stresses that would lead to crack formation. In addition, no cracks originating from ZrO_2 impurities were observed by SEM. The presence of the ZrO_2 impurities had no significant effect on the SiO_2 depletion from $Y_2Si_2O_7$. ZrO_2 is known to be significantly more thermochemically stable in high temperature water vapor than $Y_2Si_2O_7$ [27, 128–130] and was observed to remain in the porous Y_2SiO_5 layer after SiO_2 had volatilized from $Y_2Si_2O_7$ (Figure 4.25).
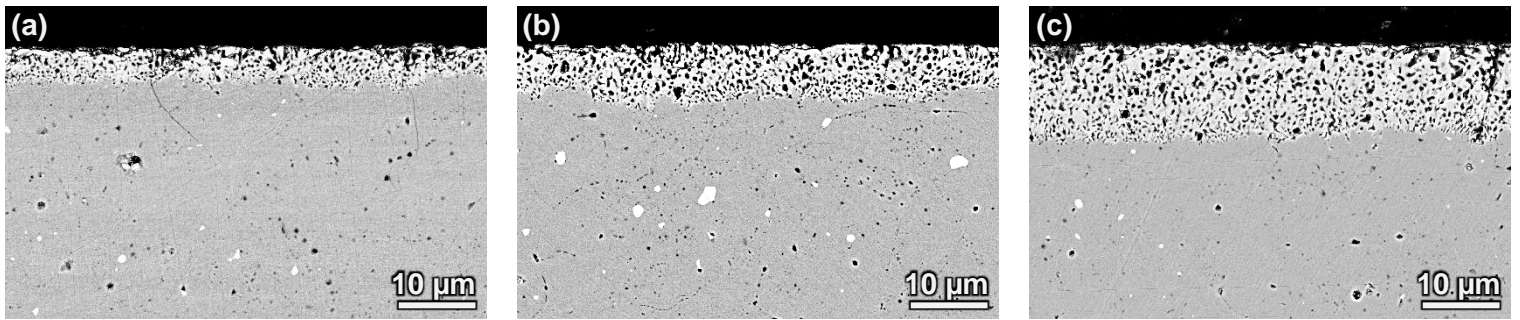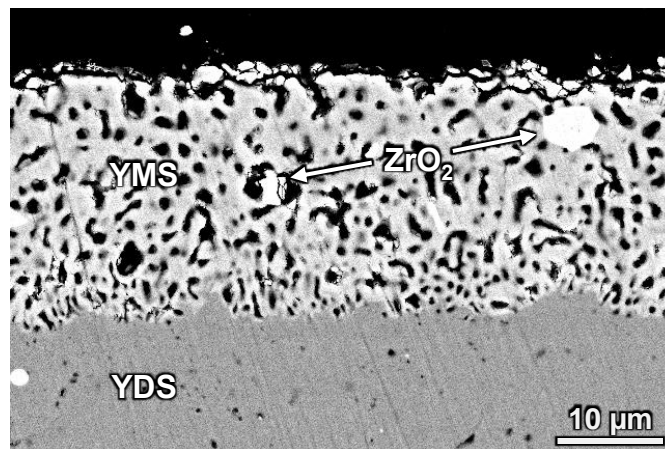

Figure 4.25. BSE/SEM image of a cross-section through the steam-jet impingement site on a $Y_2Si_2O_7$ specimen exposed for 250 hours at 1200°C. $v_{(g)}$= 171 m/s, $P(H_2O)$= 1 atm. Arrows are pointing to ZrO_2 impurities that did not volatilize during exposure.

4.4.2. SiO₂ Volatility from Y₂Si₂O₇

Characterization by weight change, XRD, SEM, EDS and TEM showed that the exposure of $Y_2Si_2O_7$ to a high-temperature high-velocity water vapor environment resulted in the selective volatilization of SiO_2 to form a silicon hydroxide gas and a porous surface layer of Y_2SiO_5 (Equation (4.1)).

$$Y_2Si_2O_7 + 2H_2O \text{ (g)} = Y_2SiO_5 + Si(OH)_4 \text{(g)} \tag{4.1}$$
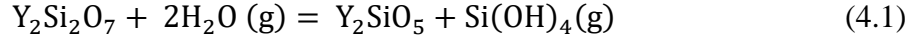
This result is consistent with other studies that investigated the thermochemical stability of $Y_2Si_2O_7$ in high temperature water vapor [27, 45, 49, 50, 60]. Specimens that did not show the presence of Y_2SiO_5 in the XRD analysis (Appendix C) after steam-jet exposures at $1000 – 1200°C$ likely had Y_2SiO_5 layers that were very thin (significantly less than the penetration depth of the x-rays) and/or a significant portion of the area analyzed by XRD was not exposed to high-velocity water vapor. Either of these scenarios could lead to Y_2SiO_5 diffraction peaks that have intensities too low to be identified during analysis. Prior TEM studies showed the presence of a glassy SiO_2 rich phase along grain boundaries of $Y_2Si_2O_7$ which volatilized in high temperature water vapor, resulting in the formation of large voids between grains for water vapor to penetrate below the surface [131, 132]. TEM characterization of $Y_2Si_2O_7$ specimens in this study showed there was no SiO_2 present along grain boundaries (Figure 4.10) indicating that water vapor diffused through pores, along grain boundaries or cracks to react with $Y_2Si_2O_7$. The origin of the porosity in the Y_2SiO_5 surface layer is attributed to the 25% volume reduction associated with the transformation of $Y_2Si_2O_7$ to Y_2SiO_5. Because the Y_2SiO_5 surface layer is laterally constrained, it is under a state of biaxial tension which may have caused cracks to form during steam-jet exposures or upon cooling. In addition, crack formation at the steam-jet impingement site may

have formed upon cooling due to the CTE mismatch between the Y_2SiO_5 (X2 = 7.8 x 10^{-6} °C^{-1}) surface layer and $Y_2Si_2O_7$ (β, γ = ~4 x 10^{-6} °C^{-1}) (Table 1.1).

4.4.2.1. Kinetics

SiO_2 volatilization kinetics from $Y_2Si_2O_7$ at 1200°C were determined using the average SiO_2 depletion depths from specimens exposed for 60, 125 and 250 hours and using weight change measurements from a single specimen intermittently exposed and removed from the steam-jet for a total of 250 hours. SiO_2 volatility appeared to follow parabolic kinetics based on the reasonable agreement of the measured SiO_2 depletion depth data to the linear fit (Figure 4.11), however, it is difficult to conclude the exact volatilization kinetics based solely on this result due to the large scatter in the measured data. Factors attributing to the large scatter in the measured SiO_2 depletion data will be discussed in Section 4.4.6. The weight loss due to SiO_2 volatility of a single specimen was also found to exhibit parabolic kinetics based on the good agreement of the measured weight loss data to the linear fit (Figure 4.19). Note the linear fit does not go through the origin indicating there is an incubation time of ~1 hour before significant volatility begins. Although no specimens were characterized after 1 hour of exposure, observations of the microstructural evolution with time would suggest that after 1 hour only certain initiation sites would be depleted in SiO_2 whereas as the rest of the specimen would not. The exposure time is also short enough that any SiO_2 depletion front has not had time to spread a considerable distance. The long rectangular pores seen in cross-section of a $Y_2Si_2O_7$ specimen exposed in the steam-jet for 12 hours at 1200°C allow for fast transport of water vapor inward and $Si(OH)_4$ (g) outward (Figure 4.23) which is not indicative of parabolic SiO_2 volatilization kinetics, however, gas phase transport can be parabolic if the diffusion path length increases. In

addition, the pore size ($< 0.5 \, \mu m$) at these times indicate Knudsen diffusion plays a role in gas phase diffusion which will reduce the overall flux of $Si(OH)_4$ (g). Weight loss measurements following steam-jet exposures are not typically used to determine volatilization kinetics since the location of the impingement site and the area exposed to high velocity water vapor is not the same on each specimen. During this experiment, however, all steam-jet furnace hardware, with the exception of the fused quartz capillary, remained in place throughout the entire experiment making the location of the steam-jet impingement site and the area exposed to high velocity water vapor the same for each exposure. This experimental method was validated using the SiO_2 system as discussed in Section 3.6.2. Since the SiO_2 depletion depth and weight loss measurements were in agreement it can be concluded that the SiO_2 volatilization from $Y_2Si_2O_7$ exhibits parabolic kinetics, representative of a diffusion limited process.

The results of this study are consistent with the parabolic weight loss kinetics measured by Klemm [27] and Fritsch [49] for $Y_2Si_2O_7$ exposed in a high-temperature high-velocity water vapor environment (T= 1450°C, t= 100 – 700 h, $v_{(g)}$= 100 m/s, $P(H_2O)$= 0.28 bar). Conversely, a study by Courcot et al. [67] found that $Y_2Si_2O_7$ exhibited linear weight loss kinetics when exposed in high-temperature water vapor (T= 1200 – 1400°C, t= up to 25 h, $v_{(g)}$= 5 cm/s, $P(H_2O)$= 50kPa). The validity of Courcot et al. results are questionable since the exposure times were short and the water vapor velocity was very low. In addition, Courcot et al. study showed that $Y_2Si_2O_7$ exhibited greater thermochemical stability than Y_2SiO_5 while SiO_2 was more thermochemically stable than Y_2O_3 which is contrary to the results of this study (and that of Chapter 3) and other studies in literature [27, 45, 49, 60].

4.4.3. Suppression of SiO₂ Volatility

The microstructure and SiO_2 depletion behavior of specimens exposed in the steam-jet for 125 hours at 1300°C and 1400°C were very different from those exposed at 1000 – 1200°C. The decrease in SiO_2 volatility and the formation of a non-uniform SiO_2 depletion layer at 1300°C and 1400°C can be attributed to the high partial pressure of $Si(OH)_4$ (g) already present in the water vapor from the fused quartz capillary. Comparison of the measured capillary volatility to the equilibrium $P(Si(OH)_4)$ for rare-earth disilicates (Section 3.5.1, Figure 3.4) showed that at 1300°C and 1400°C the $P(Si(OH)_4)$ in the water vapor approaches equilibrium values for rare-earth disilicates therefore suppressing the volatility of SiO_2. At 1300°C the $P(Si(OH)_4)$ in the water vapor is low enough that some non-uniform SiO_2 depletion is observed whereas SiO_2 volatility is almost completely suppressed at 1400°C. In fact, SiO_2 was only observed to be depleted at 1400°C along subsurface cracks. SiO_2 depletion along subsurface cracks will be discussed in Section 4.4.7.

4.4.4. Microstructural Evolution

SiO_2 depletion from $Y_2Si_2O_7$ initiated inside grains, at grain boundaries and surface cracks forming porous and faceted Y_2SiO_5. The initiation of SiO_2 depletion along a grain boundary or crack is expected since they offer fast transport for water vapor to simultaneously react with material at the grain boundary or crack interface and at the specimen surface. The cause for the initiation of SiO_2 depletion at a single point inside a grain is less understood since the grain has a single orientation and the activation energy for the volatilization reaction to take place should be the same everywhere in the grain. It is hypothesized that the initiation of SiO_2 depletion inside a grain may occur at high energy sites such as defects or impurity particles,

97

although not confirmed with this study. Once the initiation of SiO_2 depletion has occurred a SiO_2 depletion front spreads outward from the initial SiO_2 depleted sites (Figure 4.21). This indicates that it is energetically favorable for Y_2SiO_5 to continue to nucleate at the interface between $Y_2Si_2O_7$ and the initial SiO_2 depletion front. As the exposure time increases pores and grains are observed to coarsen to lower the interfacial free energy of the system (Figure 4.22).

SiO_2 was quickly depleted from $Y_2Si_2O_7$ at the steam-jet impingement site to form Y_2SiO_5 that contained rectangular and round pores (Figure 4.20). The rectangular pores appear to be oriented in specific directions indicating there may be a preferred crystallographic orientation related to their formation. Some $Y_2Si_2O_7$ grains were still present at the impingement site which also indicates there may be possible crystallographic orientation/polymorph effects related to the SiO_2 volatility from $Y_2Si_2O_7$. Microstructural features observed on a $Y_2Si_2O_7$ specimen 1 mm downstream of the steam-jet impingement site after exposure for 125 hours at 1000°C are used to inform a hypothesis as to how the rectangular pore structure formed (Figure 4.26). Figure 4.26a shows that Y_2SiO_5 has nucleated within $Y_2Si_2O_7$ grains and at grain boundaries, consistent with prior observations at 1200°C (Figure 4.21). At higher magnification some $Y_2Si_2O_7$ grains (of a given orientation) nucleate cuboidal Y_2SiO_5 grains while other $Y_2Si_2O_7$ grains (possibly of a different orientation) nucleate rounded Y_2SiO_5 grains (Figure 4.26b). It is hypothesized that the coarsening of the cuboidal Y_2SiO_5 grains (shown by the white double sided arrows) results in the formation of the observed rectangular pore structure.
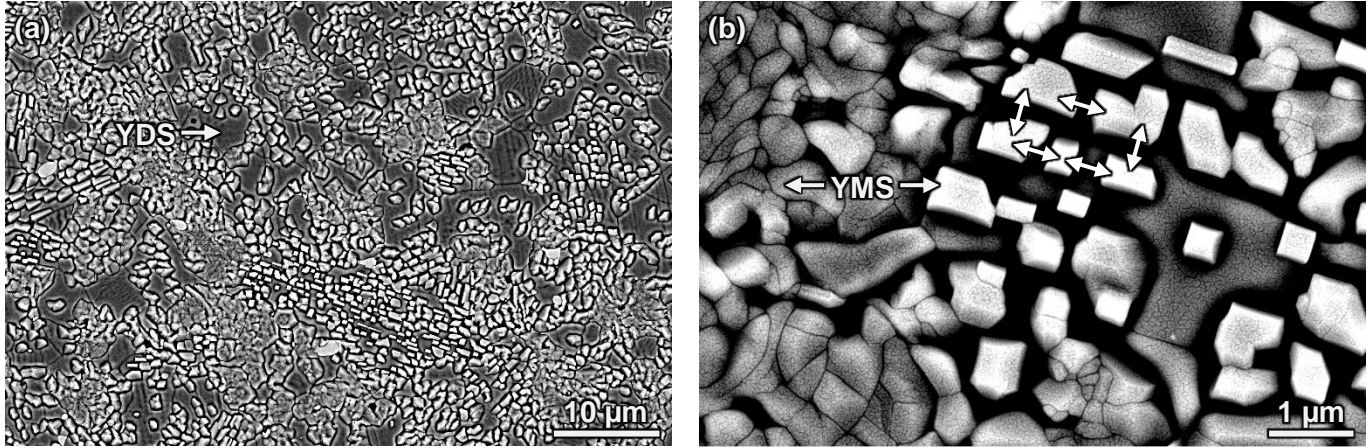
Figure 4.26. Plan view BSE/SEM image 1 mm downstream of the steam-jet impingement site on a $Y_2Si_2O_7$ (YDS) specimen after exposure for 125 hours at 1000°C showing the nucleation of Y_2SiO_5 (YMS) within YDS grains. $v_{(g)}$= 131 m/s, $P(H_2O)$= 1 atm. White double sided arrows ($\leftrightarrow$) in (b) indicate hypothesized directions for YMS coarsening to form "rectangular" pores.

The microstructural evolution observed at the specimen surface may be used to explain the porous Y_2SiO_5 microstructure seen in cross-section after exposure. The elongated rectangular Y_2SiO_5 pore microstructure seen in cross-section after 12 hours of exposure (Figure 4.23) is very different to that of specimens exposed for 60 – 250 hours at 1200°C (Figure 4.7). The pores near the surface of the Y_2SiO_5 shown in cross-section on a $Y_2Si_2O_7$ specimen after steam-jet exposure for 250 hours at 1200°C (Figure 4.27) are large, consistent with the pore coarsening observed on the surface with increasing exposure time (Figure 4.21). A region with medium sized pores is observed below the surface region containing large pores. The pores in this region have had less time to coarsen since the Y_2SiO_5 in this region formed after the Y_2SiO_5 at the surface. The pore size in this region is similar to those seen on the surface after 60 and 125 hours of exposure. Finally, the new pores forming at the $Y_2Si_2O_7 – Y_2SiO_5$ interface are small and elongated, similar to those observed at short times at the specimen surface and in cross-section. These

findings demonstrate that coarsening of the pores and grains in the Y_2SiO_5 layer control the evolution of the SiO_2 depleted microstructure.
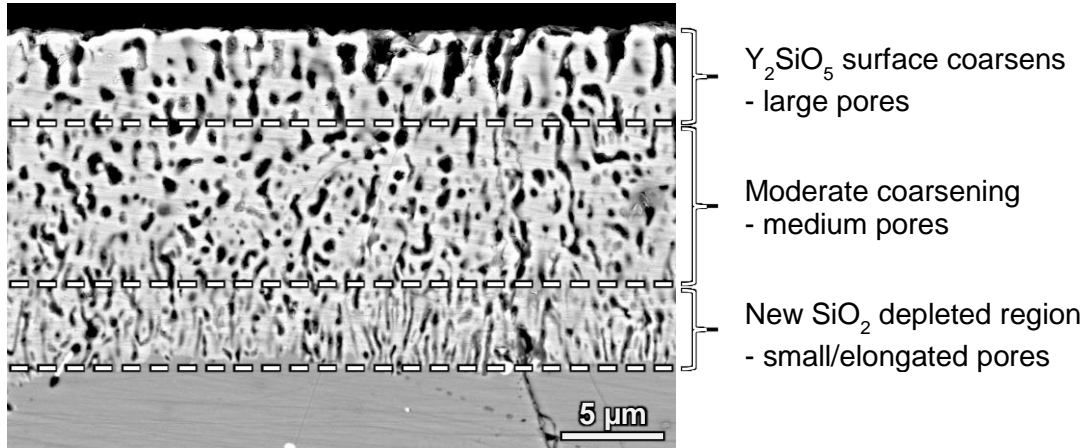
Figure 4.27. BSE/SEM image of a cross-section through the steam-jet impingement site on $Y_2Si_2O_7$ specimen exposed for 250 hours at 1200°C showing the change in pore size through the Y_2SiO_5 layer. $v_{(g)}= 158$ m/s, $P(H_2O)= 1$ atm.

4.4.5. *Mechanisms Affecting SiO$_2$ Volatility from Y$_2$Si$_2$O$_7$*

Characterization of the SiO_2 depletion depth and the microstructural evolution as a function of time and temperature allows for identification of the mechanism(s) that control the rate of SiO_2 volatility from $Y_2Si_2O_7$. Possible mechanisms are shown in Table 4.3 and include the equilibrium formation $Si(OH)_4$ (g), Y_2SiO_5 coarsening, the development of tortuosity in the pore network and diffusion of H_2O (g) and $Si(OH)_4$ (g) through pores by molecular diffusion and/or Knudsen diffusion.

SiO_2 depletion from $Y_2Si_2O_7$ was found to follow parabolic kinetics in the time dependent study at 1200°C (Section 4.3.2) which indicates a diffusional process is rate limiting. Therefore, the surface volatilization reaction (linear kinetics) can not be rate controlling (I-Table

4.3). Coarsening of Y_2SiO_5 and concomitant increases in tortuosity occur by mass transport of the solid phase. Coarsening can occur by lattice diffusion, grain boundary diffusion, surface diffusion and evaporation/condensation [133]. These are all activated processes as given by Equation II-i in Table 4.3, however, the enthalpies of these mass transport processes are unknown. Some lattice and grain boundary diffusion must be occurring at 1200°C since densification (decrease in pore area fraction) of Y_2SiO_5 is observed (Figure 4.22). This may exhibit parabolic kinetics since the path length for diffusion increases as the particle size increases, however, there is a small change in path length (~100 nm) so this is unlikely. The coarsening is accompanied by increases in tortuosity which will then affect gas phase transport in the Y_2SiO_5 reaction layer (II-ii Table 4.3).

Finally, gas phase diffusion processes through the growing porous layer of Y_2SiO_5 could be a rate controlling mechanism for SiO_2 depletion from $Y_2Si_2O_7$. For all exposures, gas phase diffusion in pores is expected to occur by both molecular and Knudsen diffusion since pore sizes are below the critical pore diameter ($< 12\ \mu m$ for H_2O (g), $< 3.4\ \mu m$ for $Si(OH)_4$ (g)) for Knudsen diffusion to contribute (Appendix I). The temperature dependence of these mechanisms are reported in Equations III-i and III-ii in Table 4.3 while the pressure dependence has been neglected since all experiments were performed at 1 atm. The diffusion of H_2O (g) inward and $Si(OH)_4$ (g) outward increases with temperature proportional to $T^{3/2}$ and $T^{1/2}$ for molecular and Knudsen diffusion respectively. Consider two cases. First, if SiO_2 depletion from $Y_2Si_2O_7$ were limited by the flux of H_2O (g) inward then the temperature dependence of D_M and D_K would be observed. The dc/dx term in Equations III-i and III-ii in Table 4.3 will not significantly change with temperature because H_2O (g) saturates the pore network. In the second case, if SiO_2 depletion from $Y_2Si_2O_7$ were limited by the outward flux of $Si(OH)_4$ (g) the dc/dx

term will be proportional to $\exp\left(\frac{-\Delta H_1}{RT}\right)$ since the equilibrium $Si(OH)_4$ (g) concentration

boundary condition at the $Y_2SiO_5/Y_2Si_2O_7$ interface increases according to this relation. This

exponential dependence dominates over the temperature contributions from D_M and D_K.

Identification of the rate controlling mechanism for SiO_2 depletion from $Y_2Si_2O_7$ was not

possible due to the change in temperature dependence over the range of 1000°C to 1200°C

(Figure 4.18) and the lack of SiO_2 depletion data collected above 1200°C where SiO_2 depletion

rates are easily measured. Operating the steam-jet above 1200°C using a non-reactive capillary

and/or testing a silicate, such as $HfSiO_4$, that will deplete in SiO_2 and form a product that will not

coarsen/sinter may be used to identify the rate controlling mechanism.

Table 4.3. Mechanisms affecting SiO_2 volatility from $Y_2Si_2O_7$.

	Process	Mechanism	Flux/Diffusion	Comment
I.	Surface Reaction	$Y_2Si_2O_7 + 2H_2O$ (g) $= Y_2SiO_5 + Si(OH)_4(g)$	$J \propto P(Si(OH)_4) \propto \exp\left(\frac{-\Delta H_1}{RT}\right)$	Derived from parametric dependence of the gaseous flux given by Equation (3.6), $\Delta H_1 = 62.7$ kJ/mol at 1100°C [†]
II.	Solid State Diffusion	(i) Coarsening	$D = D_o \exp\left(\frac{-\Delta H_2}{RT}\right)$	ΔH_2 is unknown
		(ii) Tortuosity	$J_{M,K} \propto \frac{-D_{M,K}}{\tau^2}\frac{dc}{dx}$	Also changes with coarsening, Reference [134]
III.	Gas Phase Diffusion in Pores	(i) Molecular Diffusion	$D_M \propto T^{3/2}$ $J_M \propto -D_M \frac{dc}{dx}$	Reference [114]
		(ii) Knudsen Diffusion	$D_K \propto T^{1/2}$ $J_K \propto -D_K \frac{dc}{dx}$	Applies up to a critical pore size, Reference [114]

[†] calculated from FactSage reaction module using SGPS database.

4.4.6. *Variability in Measured SiO₂ Depletion Depths*

The large scatter in the measured SiO_2 depletion depths (Table 4.1 & Table 4.2) can be attributed to the variability in the SiO_2 depletion from specimen to specimen exposed under the same testing conditions (Appendix E). The exact cause of this variability is currently unknown however factors such as the processing batch of the specimen, polymorphs and steam-jet velocity can be ruled out. The density of all specimens were very similar (96-98% of theoretical density) regardless of what batch they were processed from. Varying amounts of cracks were observed from batch to batch however all SiO_2 depletion measurements were made in defect free zones. Specimens from the same batch that were exposed under the same testing conditions were seen in some instances to have very different amounts of SiO_2 depletion (e.g. #18-2 & #18-3, #15-3 & 15-5 in Appendix E) while in other instances have similar depletion (e.g. #16-5 & #16-6, #15-1 & 15-4 in Appendix E). In nearly all the instances mentioned above the same $Y_2Si_2O_7$ polymorphs were identified by XRD analysis thus eliminating the effects of polymorphs as a cause for the observed variability. The steam-jet velocity did not significantly vary from exposure to exposure at a given temperature and time (Appendix D & E). Since the flux of the volatile species has a $v^{1/2}$ dependence (Equation (3.6)) the small change in steam-jet velocity resulted a 0.4 – 5% change in the flux of $Si(OH)_4$ (g) from specimen to specimen.

On several occasions it was observed in plan view that some $Y_2Si_2O_7$ grains experienced no SiO_2 depletion whereas neighboring grains did (Figure 4.20, Figure 4.21, Figure 4.26). This indicates there may be crystallographic orientation effects on SiO_2 depletion from $Y_2Si_2O_7$ which could cause variability in SiO_2 depletion from specimens exposed under the same conditions. EBSD characterization of $Y_2Si_2O_7$ specimens exposed in the steam-jet at 1300°C showed that there was no distinct texturing of grains and thus the orientation of grains in all specimens should

be completely random (Appendix H). EBSD did show that grain faceting resulting from specimen exposure to high temperature water vapor at 1300°C correlates with crystallographic orientation. Whether grain faceting relates to SiO_2 volatilization is currently unknown. Another possible cause of variation in SiO_2 depletion is the degree to which some specimen surfaces sintered. Unlike coarsening where pores and grains are getting larger with exposure time, sintering closes off porosity at the surface without a significant increase in the pore and grain size. This behavior can be seen in Figure 4.28 where there is less porosity at the surface compared to a specimen exposed under the same experimental conditions (Figure 4.6). The average SiO_2 depletion depth for the specimen in Figure 4.28 was 6.1 ± 1.2 µm compared to 12.0 ± 1.3 µm for the specimen shown in Figure 4.6. The cause of the observed sintering behavior for some specimens is currently unknown.
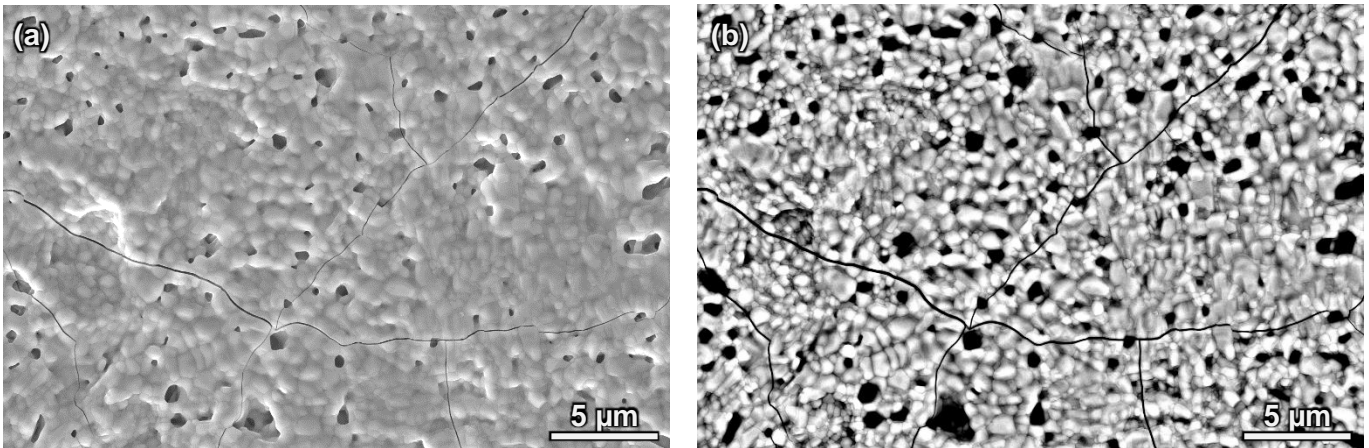
Figure 4.28. Plan view SE/SEM (a) and BSE/SEM (b) images of the steam-jet impingement site on a $Y_2Si_2O_7$ specimen after exposure for 250 hours at 1200°C showing porous Y_2SiO_5 that has sintered. $v_{(g)} = 169$ m/s, $P(H_2O) = 1$ atm.

4.4.7. Effects of Defects on SiO$_2$ Depletion from Y$_2$Si$_2$O$_7$

A fairly uniform SiO$_2$ depletion layer was observed to form in defect free regions on dense Y$_2$Si$_2$O$_7$ specimens (Figure 4.7 & Figure 4.16) whereas non-uniform SiO$_2$ depletion was observed in regions that contained defects (Figure 4.24). For the purposes of this study only defect free regions with SiO$_2$ depletion were measured to identify the SiO$_2$ volatilization kinetics from Y$_2$Si$_2$O$_7$ however defects such as cracks and grain fallout were found to provide fast pathways for water vapor to penetrate below the surface and react with Y$_2$Si$_2$O$_7$. As a matrix and/or EBC material Y$_2$Si$_2$O$_7$ will inevitably contain some defects from processing and also form defects during service, therefore defects should be considered in determining the lifetime of a component. SiO$_2$ volatility along subsurface cracks can be as great or greater than at the specimen surface (Figure 4.17 & Figure 4.24). This result is not expected since the volatility of SiO$_2$ has a $v^{1/2}$ dependence (Equation (3.6)) and the velocity of the water vapor is expected to be significantly reduced deeper in a crack. Therefore there must be some other factor leading to the high rates of SiO$_2$ depletion in cracks that are currently not understood.

4.4.8. Implications for Y$_2$Si$_2$O$_7$ as a Matrix in SiC-based CMCs

Y$_2$Si$_2$O$_7$ exhibited good thermochemical stability in high-velocity water vapor at temperatures of 1000 – 1200°C for up to 250 hours demonstrating it can protect the SiC fibers in a CMC from oxidation/volatilization. The slowing SiO$_2$ volatilization kinetics of Y$_2$Si$_2$O$_7$ with time at 1200°C are desirable for gas turbine engine components that can have service lives on the order of 10,000 hours. It is expected that the Y$_2$SiO$_5$ coarsening and increasing tortuosity of the pore network will continue to slow SiO$_2$ volatilization with time. In addition, the porous Y$_2$SiO$_5$ surface layer is significantly more thermochemically stable than Y$_2$Si$_2$O$_7$ (SiO$_2$ activity of Y$_2$O$_3$

+ Y_2SiO_5 = 0.002 vs. SiO_2 activity of Y_2SiO_5 + $Y_2Si_2O_7$ = 0.4) [72] in high-temperature water vapor and should remain as a semi-protective layer on top of $Y_2Si_2O_7$ for a considerable amount of a component's service life. This assumes that other factors such as coefficient of thermal expansion (CTE) mismatch and foreign object damage (FOD) do not cause the Y_2SiO_5 to spall off from $Y_2Si_2O_7$.

The CTE of β and γ – $Y_2Si_2O_7$ have a good CTE match to SiC whereas δ – $Y_2Si_2O_7$ and Y_2SiO_5 do not (Table 1.1). If a significant amount of Y_2SiO_5 formed in the matrix the CTE mismatch stresses could lead to crack formation and compromise the CMC. CTE mismatch stresses between $Y_2Si_2O_7$ and Y_2SiO_5 may also lead to crack formation in the Y_2SiO_5 which will provide fast pathways for water vapor to react with the underlying $Y_2Si_2O_7$.

$Y_2Si_2O_7$ displayed poor phase stability during exposures in high-temperature water vapor as polymorphic transformations between the β, γ and δ polymorphs were observed. Polymorphic transformations can also be expected to occur during service in a gas turbine engine. The volumetric change that accompanies these polymorphic transformations is small ($< 1.3\%$) and is unlikely to lead to crack formation that could compromise the CMC. However, the CTE mismatch between the β/γ and δ polymorphs is large and is believed to be the cause of crack formation during processing of $Y_2Si_2O_7$ specimens. This CTE mismatch between SiC, β/γ – $Y_2Si_2O_7$ and δ – $Y_2Si_2O_7$ could lead to crack formation that could compromise the CMC. Therefore a rare-earth disilicate, such as $Yb_2Si_2O_7$, that possesses similar thermochemical stability in high-temperature water vapor to $Y_2Si_2O_7$, has a good CTE match to SiC and does not have any polymorphs would be better suited as a water vapor resistant matrix material for SiC-based CMCs.

4.5. Conclusions

The thermochemical stability of $Y_2Si_2O_7$ in high-temperature high-velocity water vapor was assessed at temperatures from $1000 - 1400°C$ and times of $6 - 250$ hours. SiO_2 depletion from $Y_2Si_2O_7$ results in the formation of porous Y_2SiO_5 and $Si(OH)_4$ (g). SiO_2 depletion was found to follow parabolic volatilization kinetics at $1200°C$ indicating the reaction is limited by a diffusion process. Characterization of the SiO_2 depleted microstructure with time identified that mechanisms such as the $P(Si(OH)_4)$ formation reaction, H_2O (g) and $Si(OH)_4$ (g) diffusion through pores by molecular and/or Knudsen diffusion, Y_2SiO_5 coarsening kinetics and the tortuosity changes of the pore network can affect SiO_2 depletion from $Y_2Si_2O_7$. Formation of cracks in $Y_2Si_2O_7$ specimens after processing and steam-jet exposures can likely be attributed to the CTE mismatch between the β/γ and $\delta - Y_2Si_2O_7$ polymorphs. The low SiO_2 depletion at $1000 - 1200°C$ and the slowing SiO_2 volatilization kinetics with time at $1200°C$ shows that $Y_2Si_2O_7$ possesses sufficient thermochemical stability to be a water vapor resistant matrix material for SiC-based CMCs. However, the CTE mismatch stresses that would accompany a polymorphic transformation during thermal cycling of a gas turbine engine may lead to crack formation in the CMC. Therefore other rare-earth disilicates that possesses similar thermochemical stability in high-temperature water vapor to $Y_2Si_2O_7$, have a good CTE match to SiC and do not have any polymorphs would be best suited as a water vapor resistant matrix material for SiC-based CMCs.

4.6. Recommendations for Future Work

The exact mechanism controlling the SiO_2 depletion from $Y_2Si_2O_7$ could not be identified due to the several factors that affect SiO_2 depletion from $Y_2Si_2O_7$ as well as the inability to test SiO_2 volatility at temperatures greater than $1200°C$. A silicate that will deplete in SiO_2 and form

a product that will not coarsen/sinter can be used to identify the mechanism controlling the SiO_2 volatility from $Y_2Si_2O_7$. $HfSiO_4$ is a promising candidate material for this study because it should volatilize SiO_2 to form porous HfO_2 that will not coarsen/sinter at the steam-jet test temperatures [135]. Sintering additives to incorporate into the starting material may be explored to create a self-healing water vapor resistant matrix and/or EBC.

Higher temperature exposures of $Y_2Si_2O_7$ should be completed to assess its thermochemical stability at the desired operating temperatures of next generation gas turbine engines. To perform steam-jet experiments at higher temperatures the fused quartz capillary must be replaced with a nonreactive capillary, as discussed in Section 3.8.

EBSD may be used to characterize the orientation of grains in a given region before exposure in the steam-jet furnace to understand if the crystallographic orientation of grains effect SiO_2 depletion from $Y_2Si_2O_7$. Following the steam-jet exposure for a short time (~3 – 12 hours) the region previously characterized by EBSD can be characterized by SEM and EDS to determine which orientation of grains have been depleted in SiO_2.

$Y_2Si_2O_7$ applied to a CMC component using a thermal spray process may have very different thermochemical stability in high temperature water vapor relative to the SPS $Y_2Si_2O_7$ specimens tested in this study. Thermal spray in a non-equilibrium process and results in a coating with multiple phases ($Y_2Si_2O_7$, Y_2SiO_5, Y_2O_3) and a very different microstructure compared to the homogeneous specimens used in this study. Thermal sprayed $Y_2Si_2O_7$ should be exposed in the steam-jet under the same experimental conditions used in this study so a direct comparison between the thermochemical stability of SPS and thermal sprayed $Y_2Si_2O_7$ can be made.

5. Oxygen Diffusivity in Yttrium Silicates

5.1. Objective

The objective of this chapter is to measure the oxygen diffusivity in $Y_2Si_2O_7$ and Y_2SiO_5 using the tracer diffusion technique to assess the ability of yttrium silicates to protect SiC-based CMCs from oxidation.

5.2. Diffusion Theory

Oxygen tracer diffusion experiments are an effective method of measuring the oxygen diffusivity in ceramic materials. These experiments involve exposing a test specimen at elevated temperatures in an environment containing a tracer gas, typically $^{18}O_2$. The $^{18}O_2$ exchanges with ^{16}O in the lattice of the material as expressed by the overall reaction in Equation (5.1).

$$\frac{1}{2} \, ^{18}O_2 \text{ (g)} + \, ^{16}O_{lattice} \rightarrow \, ^{18}O_{lattice} + \frac{1}{2} \, ^{16}O_2 \text{ (g)} \tag{5.1}$$
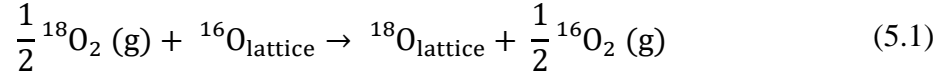
The stable isotope ^{18}O is ideal for tracer diffusion experiments because its natural abundance is very low (0.2%) and it can be easily distinguished from ^{16}O when characterized by Secondary Ion Mass Spectrometry (SIMS) techniques [136, 137].

Under the experimental conditions used for the ^{18}O exchange, the diffusion equation is solved for transport in a semi-infinite medium while the boundary conditions are chosen to describe transfer of ^{18}O across the gas/solid interface [136, 137]. The assumption is made that the diffusion rate is proportional to the difference between the ^{18}O concentration in the gas and the ^{18}O concentration at the surface at any time. This boundary condition is expressed by,

$$-D_b \left(\frac{dC}{dx}\right)_{x=0} = k_s \, (C_g - C_s) \tag{5.2}$$

where D_b is the bulk oxygen tracer diffusion coefficient, k_s is the oxygen tracer surface exchange coefficient, C_g is the ^{18}O isotope concentration of the gas and C_s is the ^{18}O isotope concentration at the surface. The solution to the diffusion equation for a semi-infinite medium with the boundary conditions given by Equation (5.2) has been described by Crank [138]:

$$C'(x,t) = \frac{C(x,t) - C_o}{C_g - C_o} = \text{erfc}\left(\frac{x}{2\sqrt{D_b t}}\right) - \exp\left(\frac{k_s x}{D_b} + \frac{k_s^2 t}{D_b}\right) \cdot \text{erfc}\left(\frac{x}{2\sqrt{D_b t}} + k_s\sqrt{\frac{t}{D_b}}\right) \quad (5.3)$$

where $C(x,t)$ is the isotopic concentration of ^{18}O at depth x, C_o is the background ^{18}O concentration (0.2% natural abundance), C_g is the isotopic concertation of ^{18}O in the gas, D_b is the bulk diffusion coefficient, t is time and k_s is the surface exchange coefficient. D_b and k_s are determined by fitting Equation (5.3) to the ^{18}O concentration profile measured by SIMS.

5.3. Diffusion Considerations for Polycrystalline Yttrium Silicates

Diffusion of ^{18}O may vary as a function of the crystallographic direction because of the symmetry of the atomic structure of materials (diffusion is a 2nd rank tensor). Therefore materials whose crystal structure is not cubic, such as monoclinic β and γ – $Y_2Si_2O_7$ (Figure 5.1) and X2 – Y_2SiO_5 (Figure 5.2), may exhibit anisotropic diffusion behavior. Polycrystalline materials that display no distinct texturing will be comprised of grains that have random orientations and thus different ^{18}O diffusion rates. In this scenario, the measured oxygen diffusion coefficient is an average of the diffusivities for every grain orientation in the volume of material that was measured.

Defects such as grain boundaries and pores can provide fast (short circuit) diffusion pathways for ^{18}O in polycrystalline materials. In tracer diffusion experiments, short circuit diffusion occurs in addition to bulk diffusion which is significantly slower. Short circuit

diffusion can be recognized by a long "tail" in the diffusion profile which extends to considerable distances in the specimen [137]. Since polycrystalline materials contain grains with random orientations and short circuit diffusion pathways the oxygen diffusion coefficient is often higher than it is for a single crystal of the same material.
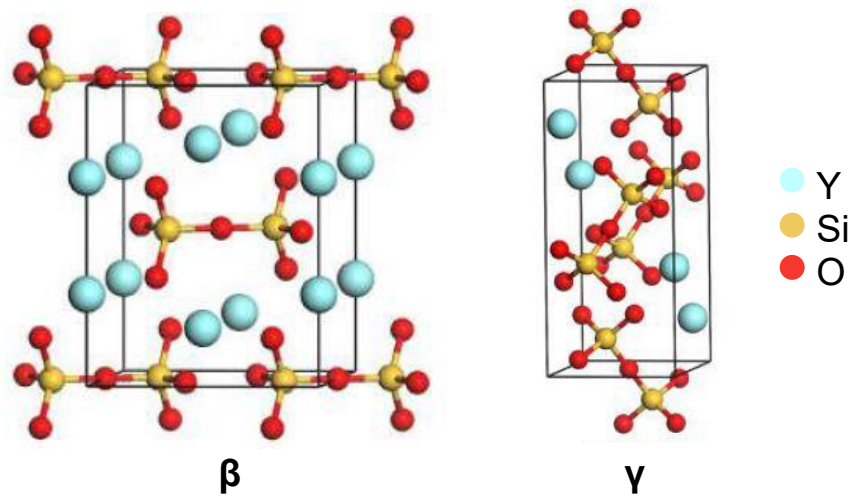
Figure 5.1. Monoclinic crystal structures of β and γ – $Y_2Si_2O_7$ [131].
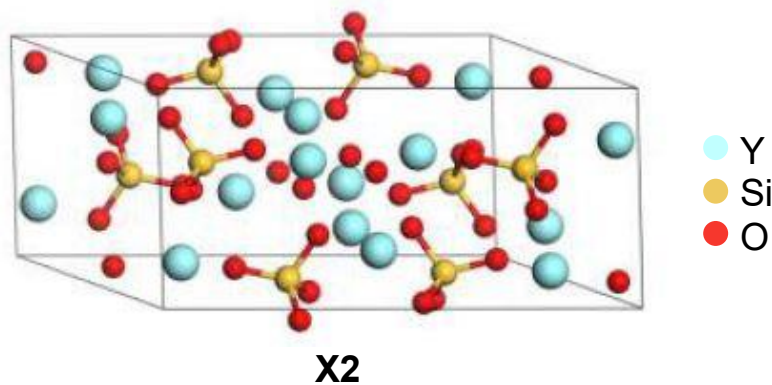
Figure 5.2. Monoclinic crystal structure of X2 – Y_2SiO_5 [131].

5.4.   Experimental

5.4.1. Materials Fabrication and Preparation

Y$_2$Si$_2$O$_7$ and Y$_2$SiO$_5$ powders were consolidated into a dense puck using Spark Plasma

Sintering (SPS) as described in Section 2.2.1 and sectioned into ~10 x 10 x 1.5 mm coupons.

Coupons were polished to a 0.25 µm finish with diamond and then vibratory polished with 0.04

µm colloidal silica for 5 – 6 hours. The coupons were sonicated in soapy water to remove any

remaining colloidal silica after vibratory polishing. The coupons were then sectioned into ~2.5 x

2.5 x 1.5 mm test specimens. The final sectioning to obtain test specimens took place following

the polishing procedure to ensure that every test specimen had an identical surface finish.

Specimens were then cleaned by a three step sonication in DI water, ethanol and acetone.

Following the cleaning procedure, specimens were annealed in air at 1350°C to relieve surface

stresses caused by the specimen preparation procedure that might lead to artifacts in the oxygen

diffusion measurements.

5.4.2. Specimen Encapsulation and Diffusion Exposures

A system was constructed to encapsulate Y$_2$Si$_2$O$_7$ and Y$_2$SiO$_5$ specimens inside a fused

quartz tube (7 cm length, 7 mm ID, 9 mm OD, 99.995% pure) in a ^{16}O$_2$ or ^{18}O$_2$ (97 at% ^{18}O)

environment. A schematic of the encapsulation system is shown in Figure 2.4. First, specimens

were encapsulated in a ^{16}O$_2$ environment and equilibrated at each diffusion temperature in a box

furnace for 48 – 201 hours to ensure a uniform chemical potential of ^{16}O in the material (Table

5.1). Specimen equilibration also allows time to further reduce any remaining surface stresses

created during polishing as near surface damage can significantly affect the shape of the ^{18}O

diffusion profile [136, 139]. The encapsulation system was pumped down to < 10 millitorr before

backfilling with $^{16}O_2$. The $^{16}O_2$ backfill pressures were set so the $^{16}O_2$ pressure inside the fused quartz tube would be ~1.2 atm at the equilibration temperature (Appendix J). This was done to reduce the likelihood that the fused quartz tube would slump at high temperatures and make contact with the polished specimen surface. Encapsulated specimens were removed from the furnace and were left to cool to room temperature (RT) following $^{16}O_2$ equilibration. Equilibrated specimens were removed from the fused quartz tube and again cleaned by a three step sonication in DI water, ethanol and acetone. Specimens were next encapsulated in an $^{18}O_2$ environment. The encapsulation system was pumped down to $\leq$ 8 millitorr and back filled with argon (99.5% pure) three times prior to backfilling with $^{18}O_2$. The $^{18}O_2$ backfill pressures were set so the pressure inside the fused quartz tube would be ~1.3 atm at the equilibration temperature (Appendix J). $^{18}O_2$ backfill pressures that would yield a pressure of 1 atm at each diffusion temperature were increased by 30% to account for any loss of $^{18}O_2$ to the walls of the fused quartz encapsulation tube and to reduce the likelihood that the fused quartz tube would slump and make contact with the polished specimen surface. The specimens were exposed at each diffusion temperature in a box furnace for 0.167 – 2.5 hours (Table 5.1). Note the exchange times are significantly shorter than the $^{16}O_2$ equilibrium times. All specimens were inserted and removed from the box furnace at temperature. The furnace temperature was observed to drop 10 – 56°C and ramp back to the furnace set temperature in 35 – 60 seconds after opening and closing the box furnace door to insert the encapsulated specimen into the furnace. Encapsulated specimens were quenched in water to freeze in the ^{18}O concentration profile upon removal from the furnace.

Table 5.1. Diffusion temperatures, $^{16}O_2$ equilibration times and ^{18}O diffusion times for $Y_2Si_2O_7$ and Y_2SiO_5.

Material	Diffusion Temperature (°C)	$^{16}O_2$ Equilibration Time (h)	^{18}O Diffusion Time (h)
	1100	201	2.5
$Y_2Si_2O_7$	1200	168	1.25
	1300	48	0.167
	1000	168	2
Y_2SiO_5	1100	145	1.5
	1200	72	0.75

5.4.3. Characterization

Time-of-Flight Secondary Ion Mass Spectrometry (ToF-SIMS) was used to measure the ^{18}O concentration profiles in ^{18}O exchanged $Y_2Si_2O_7$ and Y_2SiO_5 specimens. The ToF-SIMS was equipped with a Bi liquid metal ion gun for imaging and a Cs ion gun for sputtering. The analysis chamber pressure was maintained to pressures $\leq 5 \times 10^{-9}$ mbar. Optical profilometry was used to measure the depth of the crater formed from the Cs ion beam. The data obtained from the ToF-SIMS can be calibrated to depth data using the results from optical profilometry assuming a constant sputter rate during the ToF-SIMS measurements. Concentration profiles were fit to a solution of the diffusion equation for a semi-infinite medium (Equation (5.3)) using an application called TraceX [140] that was built into MatLab. This application returns the bulk tracer diffusion coefficient (D_b), the surface exchange coefficient (k_s) and the goodness of fit (R^2). X-ray Diffraction (XRD) and Scanning Electron Microscopy (SEM) were used to characterize the phase and microstructure of specimens before and after ^{18}O exchange. A summary of all specimens for this study can be found in Appendix K. Results and discussion focus on those specimens in which the concentration profiles had the best fit to the diffusion equation (Equation

(5.3)). Average grain size measurements were made using the line – intercept method. The pore

area fraction was determined by image analysis using ImageJ. The average pore size was

calculated from the average pore area fraction and number of pores assuming pores were

circular.

5.5. Results

5.5.1. $Y_2Si_2O_7$

The β and γ polymorphs of $Y_2Si_2O_7$ were identified by XRD analysis before and after ^{18}O

exchanges. SEM characterization of the specimen surface showed there was minor porosity (pore

area fraction = 0.0051 ± 0.0027) within grains and along the grain boundaries. The grain

boundaries were well defined and the average grain size was measured to be 5.7 ± 1.4 µm.

Similar porosity and minor surface roughening were observed at the bottom of the sputter crater

after ToF-SIMS analysis. SEM images showing a representative specimen surface and the

surface at the bottom of a sputter crater following ToF-SIMS analysis are shown in Figure 5.3.
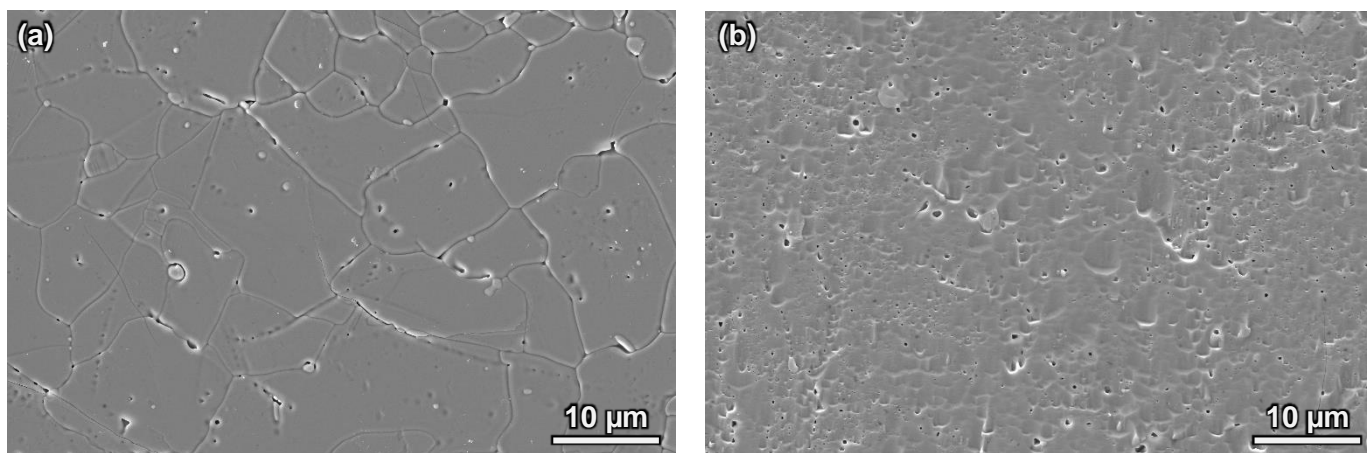
Figure 5.3. SE/SEM images of $Y_2Si_2O_7$ surface after ^{18}O exchange at 1300°C for 0.167 h (a) and
the surface at the bottom of the ToF-SIMS sputter crater (b).

The ^{18}O concentration profiles for $Y_2Si_2O_7$ exchanged at $1100 - 1300°C$ are shown in Figure 5.4. Surface isotopic concentrations ranged from $17 - 51\%$ which is significantly lower than the ^{18}O concentration in the gas phase (97%). The ^{18}O concentration profiles for specimens exchanged at $1100°C$ and $1300°C$ reached isotopic ratios of $0.5 - 0.7\%$ at diffusion depths greater than 2.5 µm which is close to the natural abundance of ^{18}O (0.2%). The specimen exchanged at $1200°C$ reached an isotopic ratio of 2.8% at diffusion depths greater than 2.5 µm which is an order of magnitude greater than the natural abundance of $^{18}O_2$. Sputter depths ranged from $3.16 - 3.82$ µm. Note the measured concentration data are not plotted for the entire depth that was sputtered.

There is good agreement between the measured ^{18}O concentration data and the fit to the diffusion equation (Equation (5.3)) at each diffusion temperature. Oxygen diffusion coefficients ranged from 2.96×10^{-13} to 1.22×10^{-12} cm^2/s and surface exchange coefficients ranged from 1.96×10^{-9} to 4.1×10^{-8} cm/s (Table 5.2). Measured values for the oxygen diffusion coefficients are plotted against inverse temperature in Figure 5.5. The activation energy for oxygen diffusion was 129 kJ/mol however there is large uncertainty associated with this value due to the limited data used to calculate it.
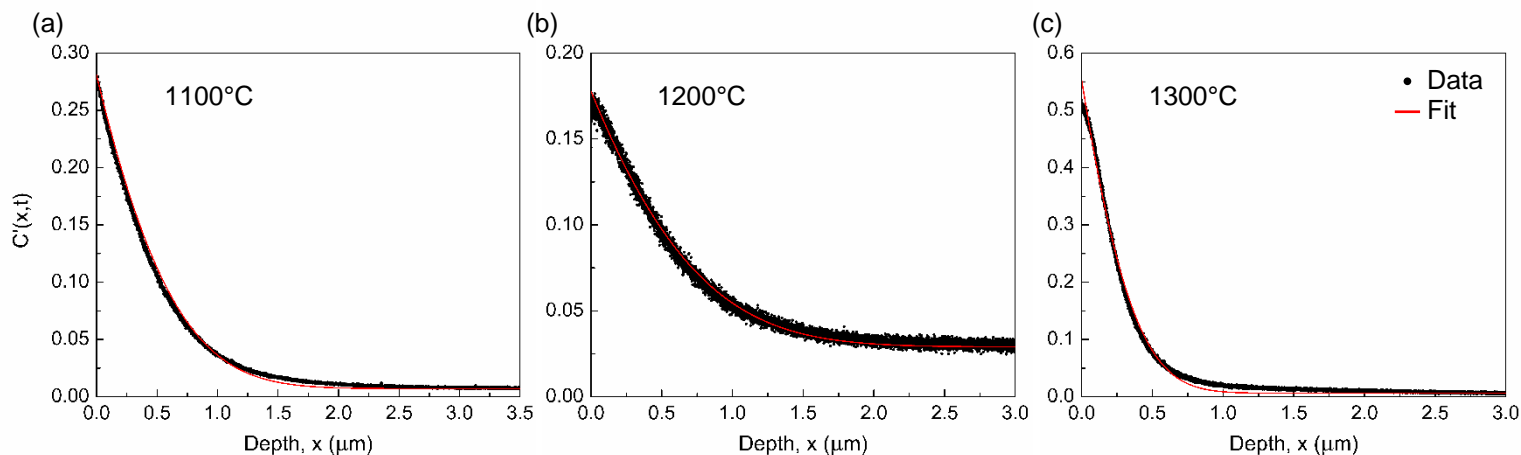
Figure 5.4. ^{18}O concentration profiles for $Y_2Si_2O_7$ exchanged at 1100°C (a), 1200°C (b) and 1300°C (c). Note the measured concentration data are not plotted for the entire sputter depth.

Table 5.2. Summary of oxygen tracer diffusion data measured for $Y_2Si_2O_7$ specimens that were exchanged at 1100 – 1300°C.

Diffusion Temperature (°C)	D_b (cm^2/s)	k_s (cm/s)
1100	2.96 x 10^{-13}	1.96 x 10^{-9}
1200	8.85 x 10^{-13}	2.1 x 10^{-9}
1300	1.22 x 10^{-12}	4.1 x 10^{-8}
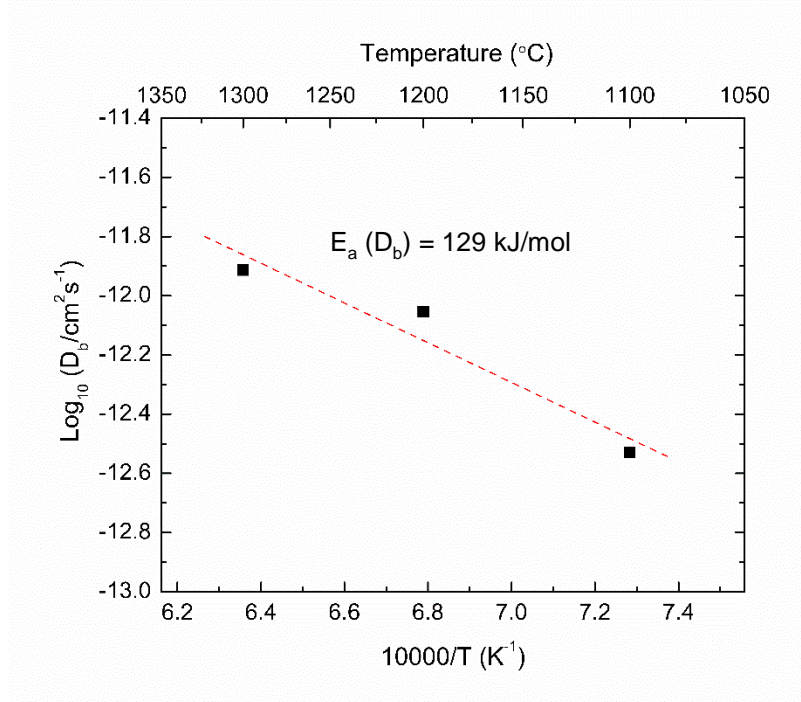
Figure 5.5. Arrhenius plot of measured oxygen diffusion coefficients for $Y_2Si_2O_7$.

[18]O concentration maps as a function of diffusion depth are shown in Figure 5.6 – Figure 5.8 for specimens exchanged at 1100 – 1300°C. Note the brighter color/greater intensity corresponds to a higher concentration of [18]O and the brightness/intensity cannot be used to compare [18]O concentrations between different specimens. The [18]O concentration at the surface appears to be fairly uniform for all specimens. Some grains contain more [18]O than others at diffusion depths up to 0.5 µm indicating possible anisotropic diffusion behavior. This behavior is still visible up to a diffusion depth of 1 µm in the specimen exchanged at 1100°C. An example showing the difference in [18]O concentration between two neighboring grains is highlighted in Figure 5.6 at a diffusion depth on 0.5 µm. High concentrations of [18]O are present along some grain boundaries at diffusion depths $\geq$ 0.5 µm. As the diffusion depth continues to increases, the highest concentrations of [18]O are observed along grain boundaries. The specimen exchanged at

1200°C was found to have significantly more ^{18}O present at grain boundaries compared to specimens exchanged at 1100°C and 1300°C. A 3D rendition of the ^{18}O concentration found throughout the entire volume of $Y_2Si_2O_7$ that was sputtered can be seen in Figure 5.9 illustrating the compilation of results shown in Figure 5.6 – Figure 5.8. ^{18}O concentration maps showing the summation of the ^{18}O concentration found throughout the entire volume $Y_2Si_2O_7$ that was sputtered can be seen in Figure 5.10. These maps clearly show that some grains contain more ^{18}O than others and high concentrations of ^{18}O are present along some grain boundaries.
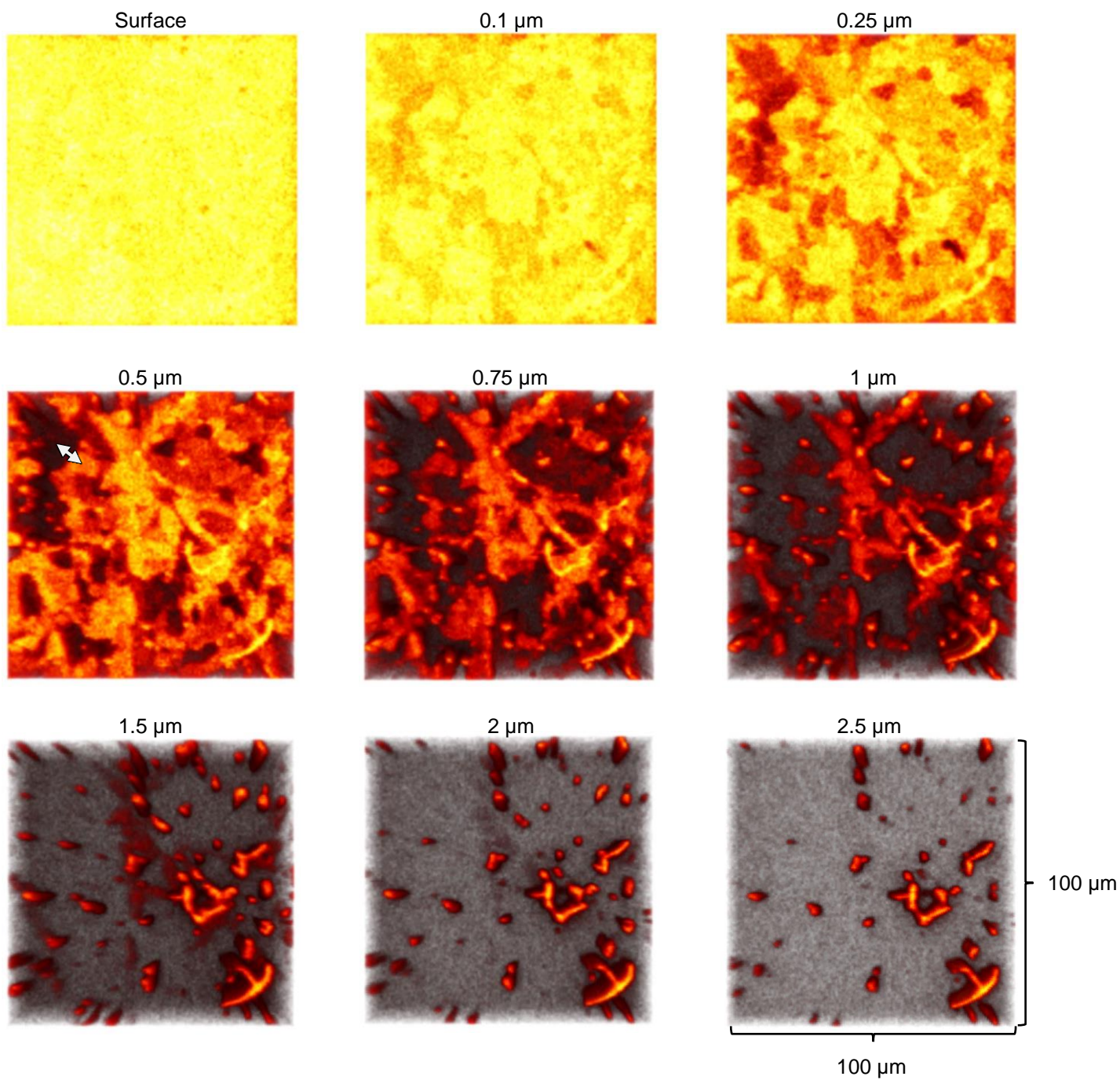
Figure 5.6. ^{18}O concentration maps as a function of diffusion depth for a $Y_2Si_2O_7$ specimen exchanged at 1100°C. Greater intensity represents a higher concentration of ^{18}O. White arrow at a diffusion depth of 0.5 µm highlights the ^{18}O concentration difference between neighboring grains.

120
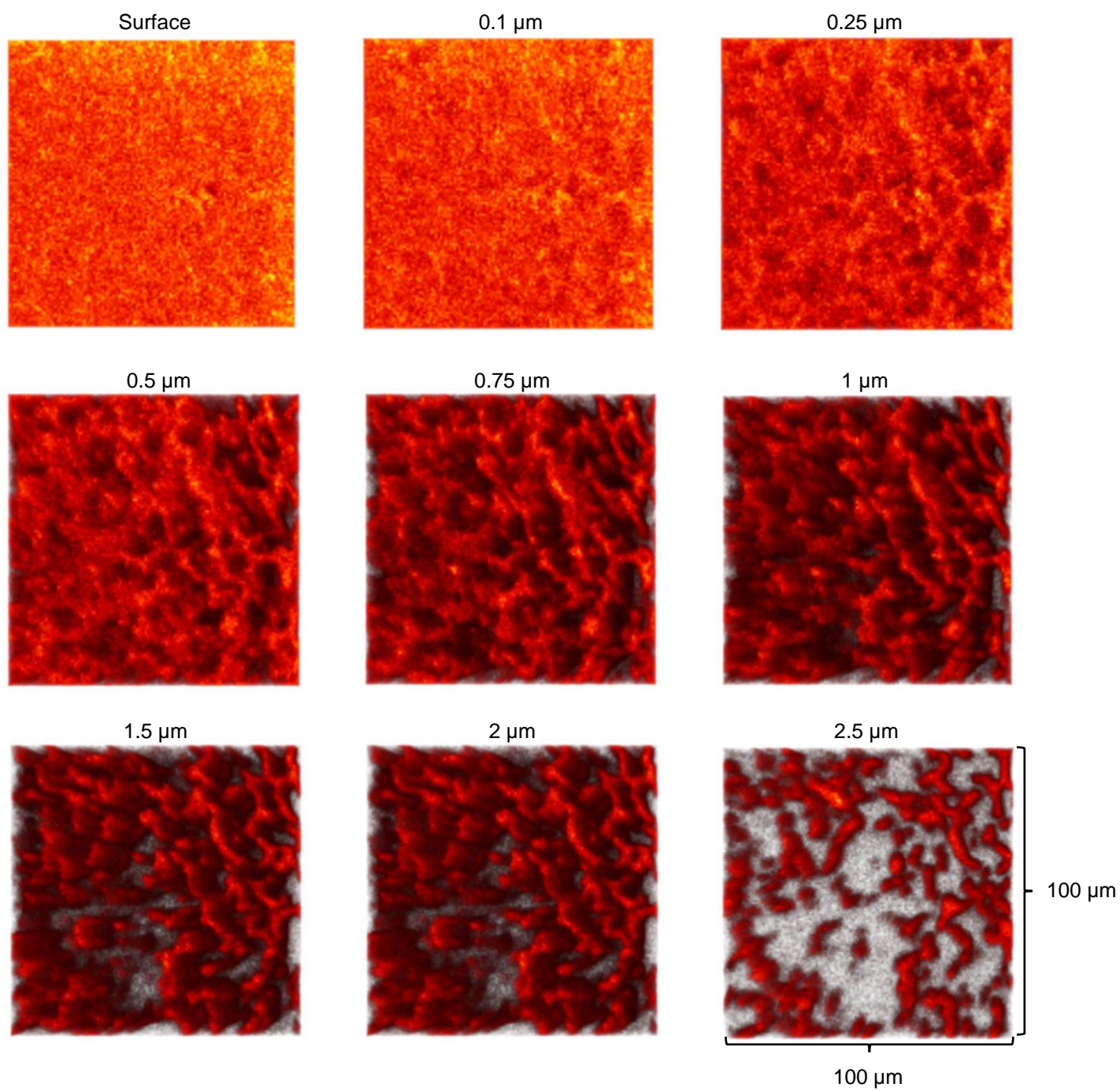
Figure 5.7. ^{18}O concentration maps as a function of diffusion depth for a $Y_2Si_2O_7$ specimen exchanged at 1200°C. Greater intensity represents a higher concentration of ^{18}O.
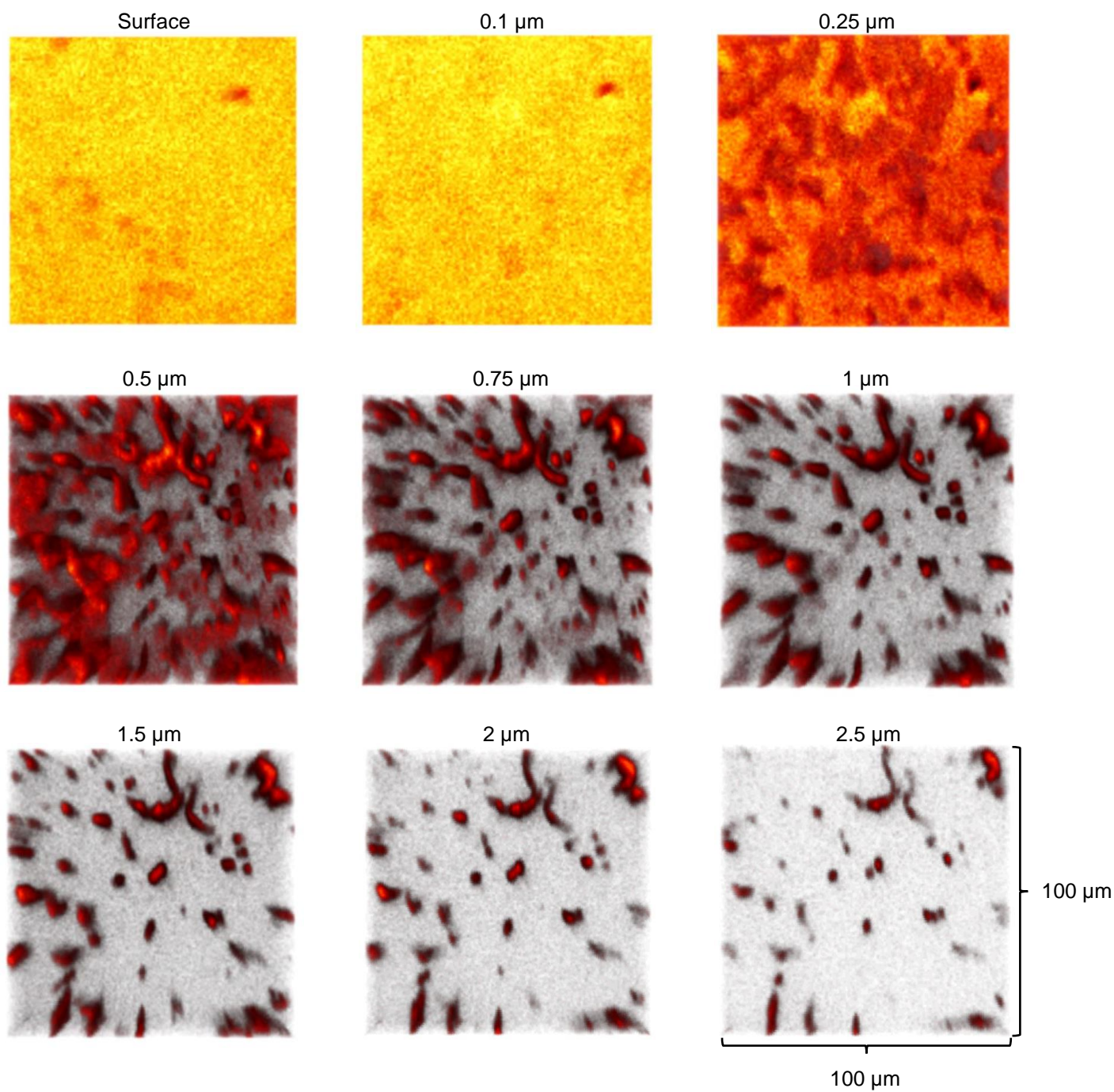
Figure 5.8. ^{18}O concentration maps as a function of diffusion depth for a $Y_2Si_2O_7$ specimen exchanged at 1300°C. Greater intensity represents a higher concentration of ^{18}O.
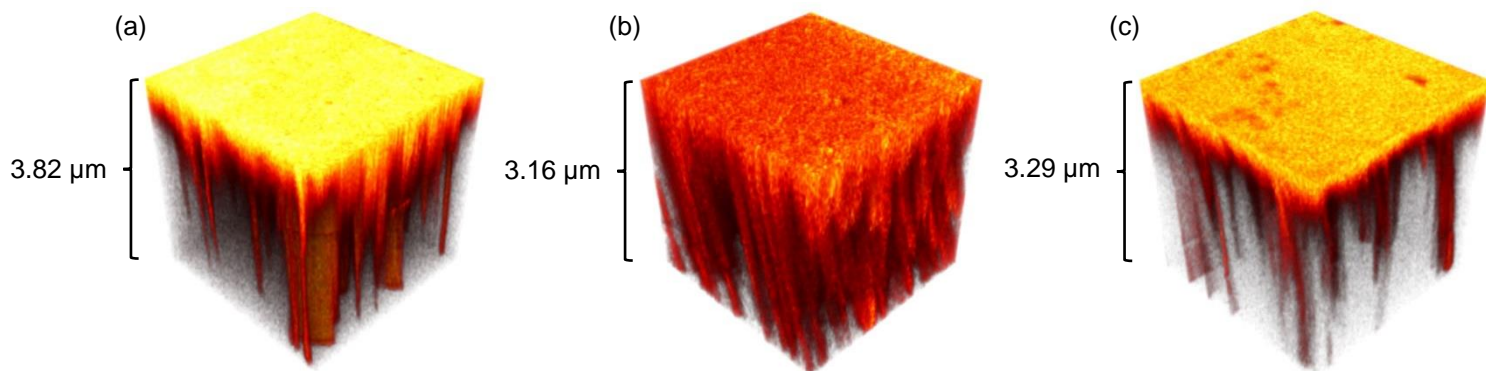
Figure 5.9. 3D rendition of the ^{18}O concentration found throughout the entire volume of $Y_2Si_2O_7$ that was sputtered and analyzed after exchange at 1100°C (a), 1200°C (b) and 1300°C (c). The total sputter depths are shown to the left of each figure. Greater intensity represents a higher concentration of ^{18}O but the intensities cannot be used to compare the ^{18}O concentrations from one specimen to another.
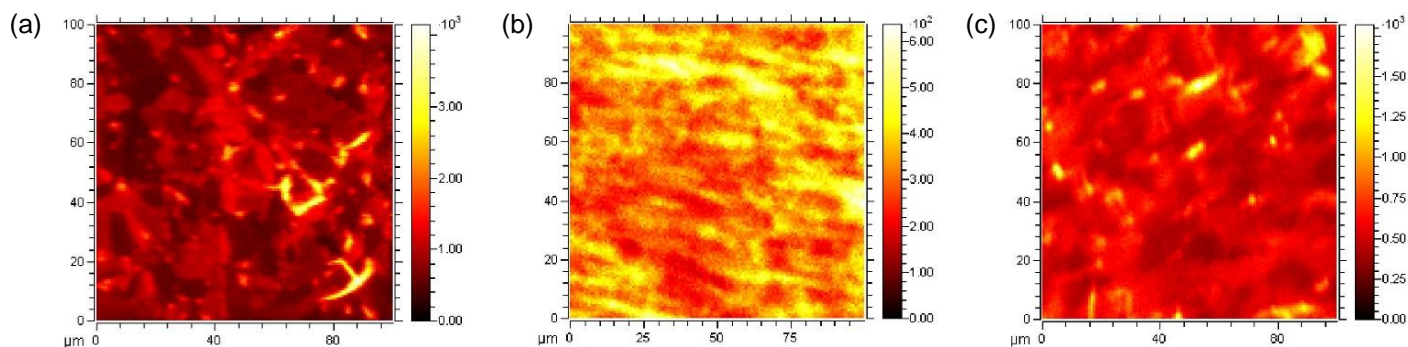
Figure 5.10. ^{18}O concentration maps showing the summation of the ^{18}O concentration found throughout the entire volume $Y_2Si_2O_7$ that was sputtered from specimens exchanged at 1100°C (a), 1200°C (b) and 1300°C (c). High concentration of ^{18}O can be seen in some grains and along some grain boundaries.

5.5.2. Y_2SiO_5

The X2 polymorph of Y_2SiO_5 was identified by XRD analysis before and after ^{18}O exchanges. SEM characterization of the specimen surface showed there was minor porosity (pore area fraction $= 0.016 \pm 0.009$) within grains and along the grain boundaries. The grain boundaries are visible however they are not as well defined as those for $Y_2Si_2O_7$ specimens (Figure 5.3a). The average grain size was measured to be 7.0 ± 1.7 µm. Porosity and surface roughening were observed at the bottom of the sputter crater after ToF-SIMS analysis. SEM images showing a representative specimen surface and the surface at the bottom of a sputter crater following ToF-SIMS analysis are shown in Figure 5.11. The amount of porosity has increased from the surface (pore area fraction $= 0.005$) to the bottom of the sputter crater (pore area fraction $= 0.021$) on this particular specimen.

The ^{18}O concentration profiles for Y_2SiO_5 exchanged at $1000 - 1200°C$ are shown in Figure 5.12. Surface isotopic concentrations ranged from $8.5 - 38\%$ which is significantly lower than the ^{18}O concentration in the gas phase (97%). All ^{18}O concentration profiles reached isotopic ratios of $0.3 - 0.8\%$ at diffusion depths greater than 1 µm which is close to the natural abundance of ^{18}O (0.2%). Sputter depths ranged from $1.42 - 4.11$ µm. Note the measured concentration data are not plotted for the entire depth that was sputtered.
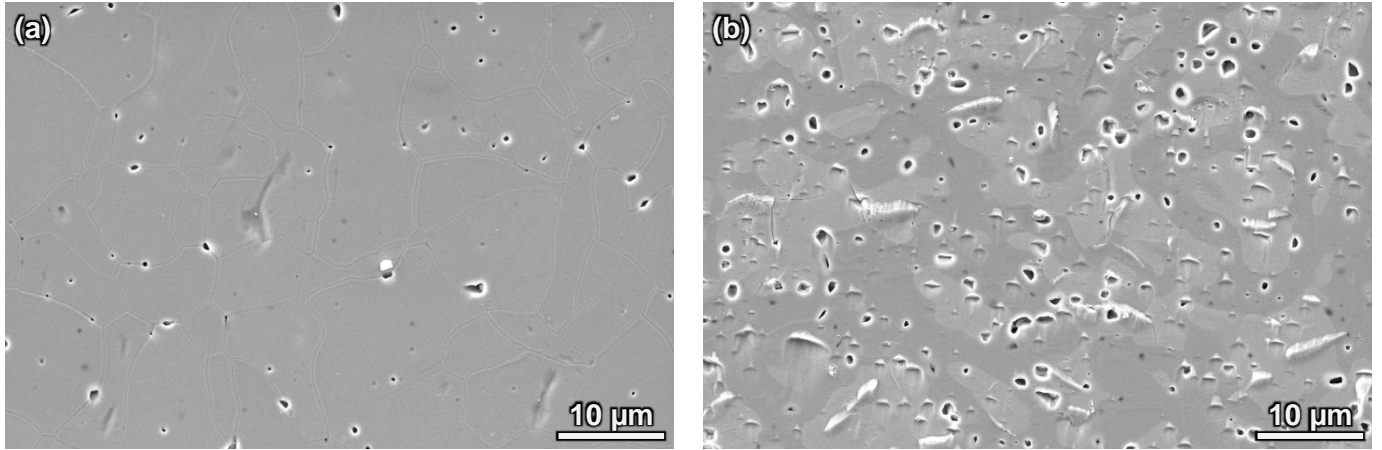
Figure 5.11. SE/SEM images of Y_2SiO_5 surface after ^{18}O exchange at 1100°C for 1.5 h (a) and the surface at the bottom of the ToF-SIMS sputter crater (b).
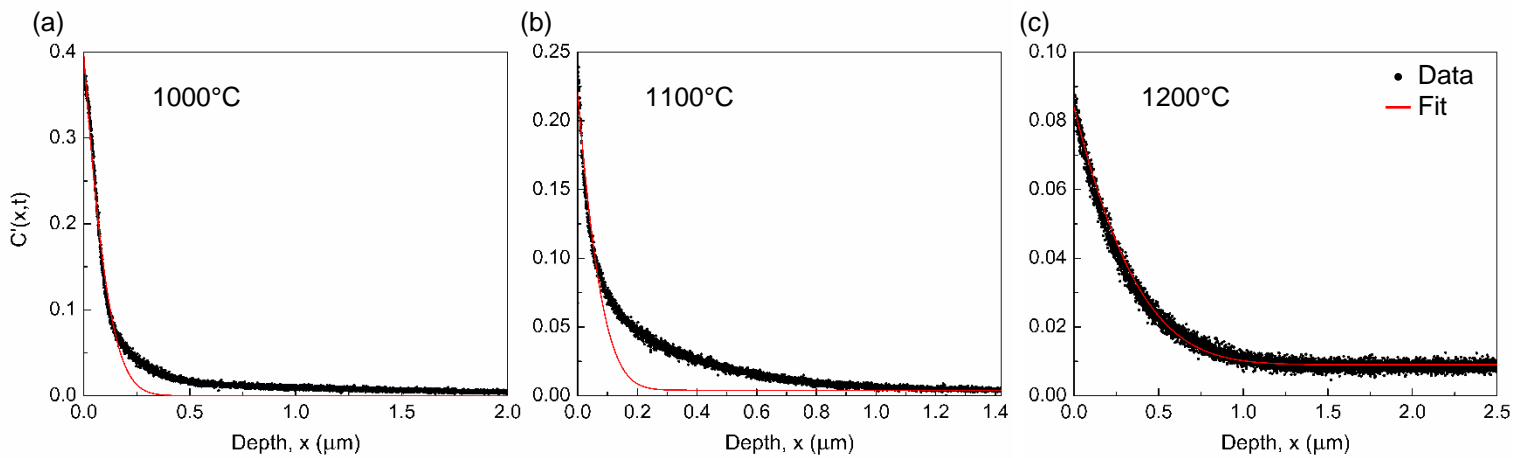
Figure 5.12. ^{18}O concentration profiles for Y_2SiO_5 exchanged at 1000°C (a), 1100°C (b) and 1200°C (c). Note the measured concentration data are not plotted for the entire sputter depth.

The specimen exchanged at 1200°C had a good fit of the measured ^{18}O concentration data and to the diffusion equation (Equation (5.3)) whereas the agreement was not as good for specimens exchanged at 1000°C and 1100°C. There is a reasonable fit of the data to the diffusion equation in the initial region (C'(x,t)= 0.38 to 0.1) on the specimen exchanged at 1000°C, thus the oxygen diffusion and surface exchange coefficients could be determined. The TraceX

application was not able to fit the diffusion equation to the measured ^{18}O concentration data for

the specimen exchanged at 1100°C thus an oxygen diffusion and surface exchange coefficient

could not be determined. The fit to the diffusion equation shown in Figure 5.12 is a forced fit to

the initial region (C'(x,t)= 0.24 to 0.1) of the ^{18}O concentration profile.

Oxygen diffusion coefficients ranged from 1.2×10^{-14} to 4.12×10^{-13} cm^2/s and surface

exchange coefficients ranged from 6.75×10^{-10} to 8.73×10^{-10} cm/s (Table 5.3). Measured values

for the oxygen diffusion coefficients are plotted against inverse temperature in Figure 5.13. The

activation energy for oxygen diffusion was 275 kJ/mol however there is significant uncertainty

associated with this value due to the limited data used to calculate it.

Table 5.3. Summary of oxygen tracer diffusion data measured for Y_2SiO_5 specimens that were
exchanged at 1000 – 1200°C.

Diffusion Temperature (°C)	D_b (cm^2/s)	k_s (cm/s)
1000	1.20×10^{-14}	6.75×10^{-10}
1100	n/a	n/a
1200	4.12×10^{-13}	8.73×10^{-10}
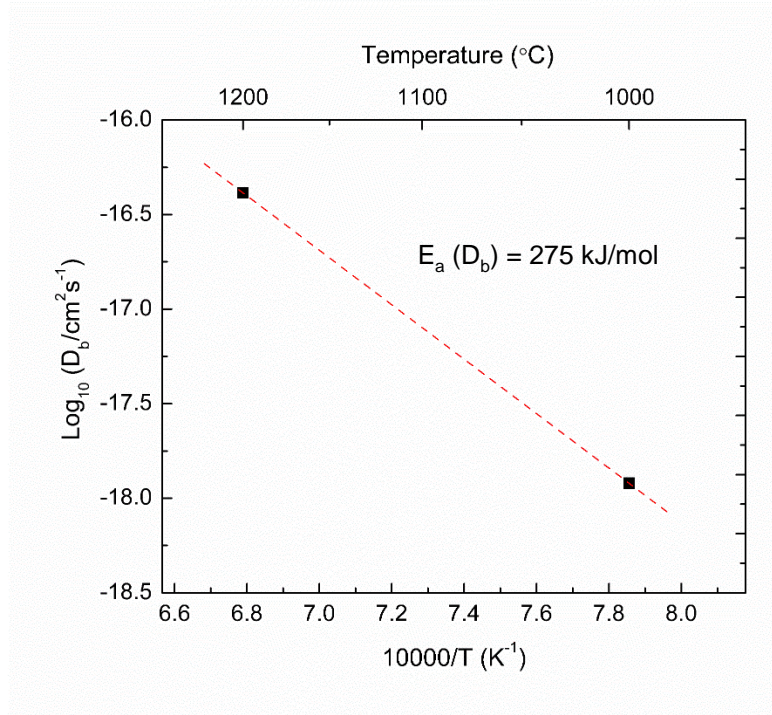
Figure 5.13. Arrhenius plot of measured oxygen diffusion coefficients for Y_2SiO_5.

^{18}O concentration maps as a function of diffusion depth are shown in Figure 5.14 –
Figure 5.16 for specimens exchanged at 1000 – 1200°C. Note the brightness/intensity cannot be
used to compare ^{18}O concentrations between different specimens. The ^{18}O concentration at the
surface appears to be fairly uniform on the specimen exchanged at 1000°C while specimens
exchanged at 1100°C and 1200°C have some grains that contain more ^{18}O than others indicating
possible anisotropic diffusion behavior. ^{18}O was observed along some grain boundaries up to
0.25 µm below the surface on the specimens exchanged at 1100°C and 1200°C. As the diffusion
depth increases, the highest concentrations of ^{18}O were observed only within some grains and/or
on grain boundaries/surrounding pores. The ^{18}O concentration surrounding a pore appear as a
circle on the ^{18}O concentration map. The concentration of ^{18}O along grain boundaries was
significantly lower in Y_2SiO_5 compared to $Y_2Si_2O_7$ (Figure 5.6 – Figure 5.8). A 3D rendition of

127

the ^{18}O concentration found throughout the entire volume of Y_2SiO_5 that was sputtered can be seen in Figure 5.17 illustrating the compilation of results shown in Figure 5.14 – Figure 5.16. ^{18}O concentration maps showing the summation of the ^{18}O concentration found throughout the entire volume Y_2SiO_5 that was sputtered can be seen in Figure 5.18. These maps clearly show that some grains contain more ^{18}O than others.

It is important to note that it appears the specimen exchanged at 1000°C (Figure 5.17a) has a much thinner ^{18}O concentration near the surface compared to specimens exchanged at 1100°C and 1200°C. We know this is not the case since we can see from the ^{18}O concentration profiles (Figure 5.12) that the ^{18}O concentration in all specimens approaches background levels (0.2%) at similar diffusion depths (0.5 – 1 µm). The ToF-SIMS analysis on the specimen exchanged at 1000°C was too long resulting in a much larger analysis depth compared to specimens exchanged at 1100°C and 1200°C, thus giving the appearance of a thinner layer of ^{18}O near the surface.
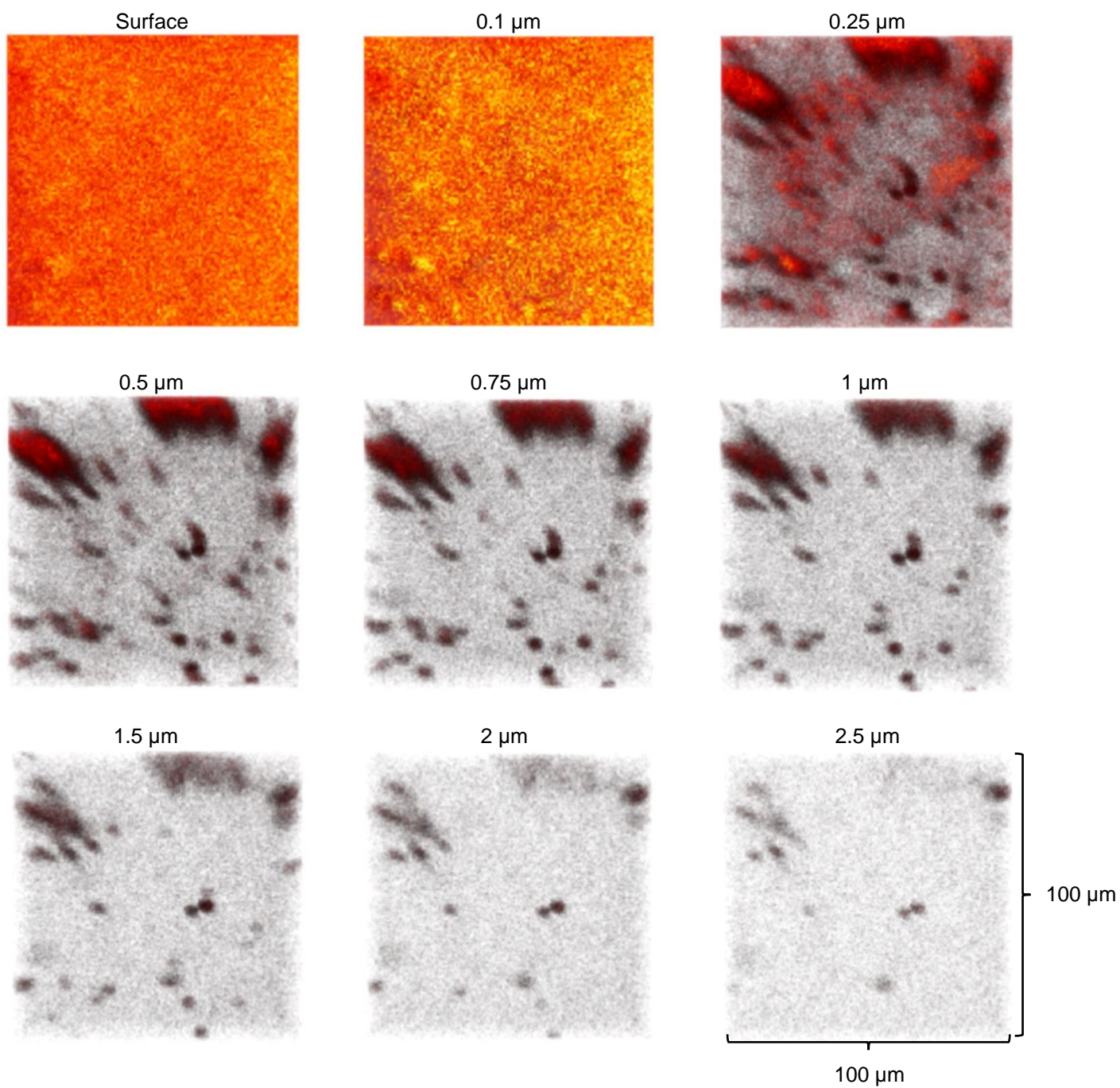
Figure 5.14. ^{18}O concentration maps as a function of diffusion depth for a Y_2SiO_5 specimen exchanged at 1000°C. Greater intensity represents a higher concentration of ^{18}O.

129
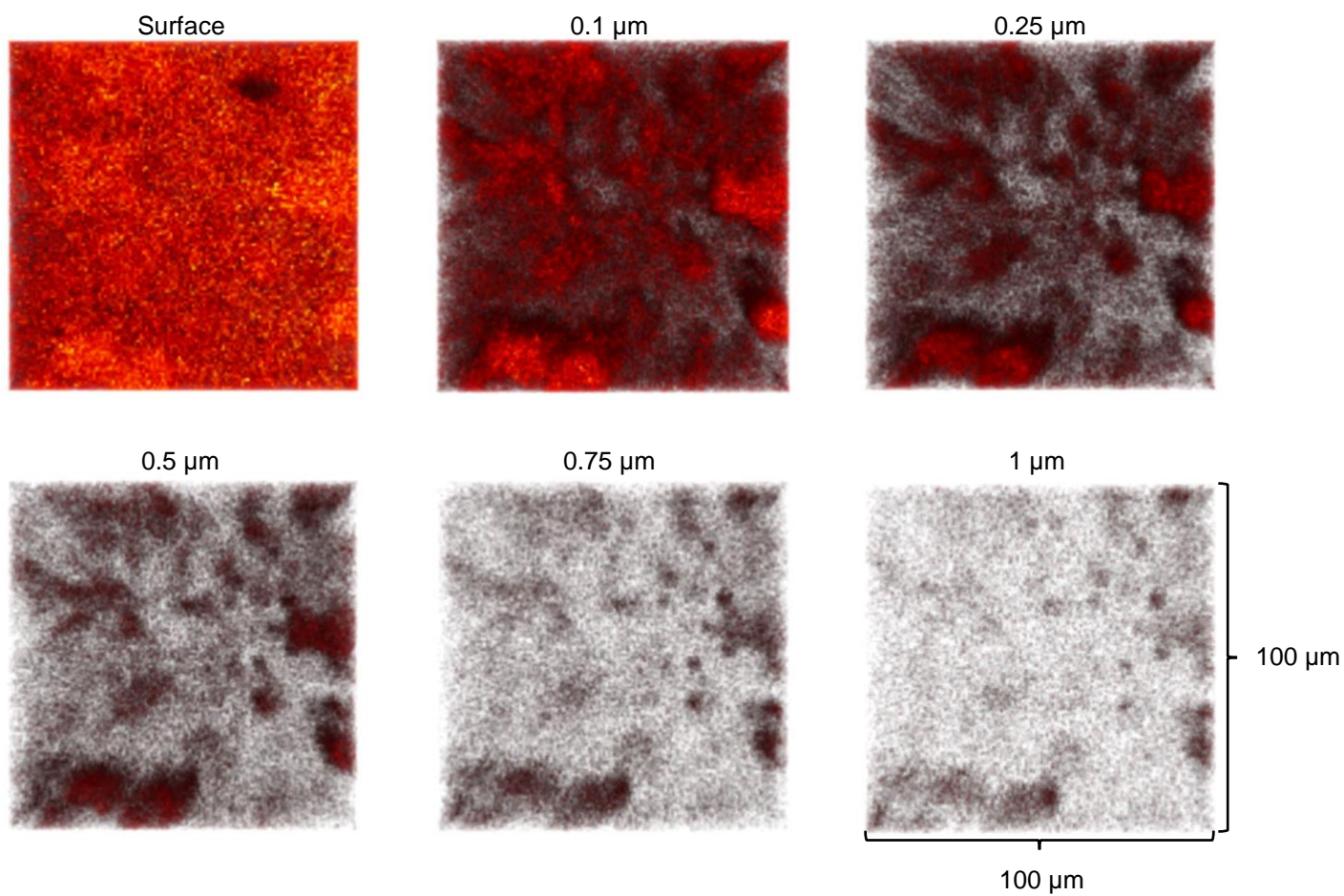
Figure 5.15. ^{18}O concentration maps as a function of diffusion depth for a Y$_2$SiO$_5$ specimen exchanged at 1100°C. Greater intensity represents a higher concentration of ^{18}O.

Figure 5.16. ^{18}O concentration maps as a function of diffusion depth for a Y_2SiO_5 specimen exchanged at 1200°C. Greater intensity represents a higher concentration of ^{18}O.

131

Figure 5.17. 3D rendition of the ^{18}O concentration found throughout the entire volume of Y_2SiO_5 that was sputtered and analyzed after exchange at 1100°C (a), 1200°C (b) and 1300°C (c). The total sputter depths are shown to the left of each figure. Greater intensity represents a higher concentration of ^{18}O but the intensities cannot be used to compare the ^{18}O concentrations from one specimen to another.

Figure 5.18. ^{18}O concentration maps showing the summation of the ^{18}O concentration found throughout the entire volume Y_2SiO_5 that was sputtered from specimens exchanged at 1000°C (a), 1100°C (b) and 1200°C (c). High concentration of ^{18}O can be seen in some grains and along some grain boundaries.

132

5.6. Discussion

5.6.1. ^{18}O Exchange Method

5.6.1.1. $^{18}O_2$ Concentration Boundary Condition

The encapsulation method offers an easy way to expose a test specimen in a controlled environment however this method has the potential to introduce error into the values of D_b and k_s and should be discussed. It is assumed that the boundary conditions (Equation (5.2)) remain constant throughout the entire ^{18}O exchange when fitting the measured ^{18}O concentration profile to the solution of the diffusion equation for a semi-infinite medium (Equation (5.3)). The volume of the tracer gas, which contains 97 at% ^{18}O, does not change as the exchange proceeds since it is confined to the inside of the tube however the $^{18}O_2$ concentration in the tracer gas may change. Three contributions to $^{18}O_2$ loss are considered. Two sources of ^{18}O loss arise from the tracer gas exchanging with (i) ^{16}O in the specimen and (ii) ^{16}O in the fused quartz tube. The decrease of ^{18}O results in an equal increase of ^{16}O in the tracer as the exchange proceeds. The third source of $^{18}O_2$ loss arises from $^{18}O_2$ permeation through the fused quartz tube resulting in only a loss of the tracer gas since the wall thickness of the fused quartz tube (2 mm) is well beyond the estimated diffusion distance for $^{16}O_2$ to permeate through the tube from the outside air. Each of these sources of $^{18}O_2/^{18}O$ loss will be considered separately in the following paragraphs.

First, the change in the $^{18}O_2$ concentration in the tracer gas resulting from exchange with the test specimen can be estimated in the following manner. The moles of ^{18}O that exchanged with the specimen in the volume of material that was analyzed can be calculated by taking a summation of the measured ^{18}O counts (number of ^{18}O atoms analyzed) and dividing it by Avogadro's number. The total moles of ^{18}O that exchanged with the specimen can then be estimated by multiplying the total surface area of the specimen by the number of moles of ^{18}O

133

per surface area that was analyzed by ToF-SIMS (~100 µm x 100 µm). This assumes that the ^{18}O exchange behavior is consistent on all areas of the specimen. The moles of $^{18}O_2$ in the encapsulation tube at the start of the experiment were estimated using the fused quartz tube dimensions and the tracer gas backfill pressures (Appendix J). It was found that the concentration of ^{18}O that exchanged with each specimen was on the order of $10^{-13} – 10^{-15}$ mol while the moles of ^{18}O in the tracer gas at the start of the experiment was ~1.5 x 10^{-5} mol. Although the ^{18}O that diffused beyond the depth analyzed by ToF-SIMS was not accounted for in this estimation, its concentration will be very low since all specimens (with the exception of the $Y_2Si_2O_7$ specimen exchanged at 1200°C) had ^{18}O concentrations approaching the natural abundance (0.2%) at the time the ToF-SIMS analysis stopped. Therefore the change in the concentration of $^{18}O_2$ in the tracer gas resulting from the loss of ^{18}O to the test specimen during the exchange is negligible.

Next, the change in the $^{18}O_2$ concentration in the tracer gas resulting from the loss of ^{18}O to the fused quartz tube via network exchange with ^{16}O can be estimated using Equation (1.4) to solve for the diffusion distance. Values for D_b (network exchange) have been published by Cawley et al. [141] (~$10^{-15} – 10^{-18}$ cm^2/s from 900 – 1200°C, replotted by Kalen et al. [142]). The estimated diffusion distances are very small (<0.02 µm) since the values of D_b are so low and the volume of the fused quartz tube exchanged with ^{18}O is very small as well. Therefore the change in the concentration of ^{18}O in the tracer gas resulting from ^{18}O network exchange with the fused quartz tube is negligible.

Finally, the change in the $^{18}O_2$ concentration in the tracer gas resulting from the loss of $^{18}O_2$ to the fused quartz tube via permeation can also be estimated using Equation (1.4) to solve for the diffusion distance. Values for D_b (permeation) have been published by Norton [143] (~2 x

$10^{-9} - 2 \times 10^{-8}$ cm^2/s from 900 – 1200°C, replotted by Kalen et al. [142]). For all specimens exchanged in this study the diffusion distances for permeation were < 100 µm. The moles of $^{18}O_2$ lost to the fused quartz tube can be estimated by multiplying the volume of the tube that was permeated with $^{18}O_2$ by the solubility of $^{18}O_2$ in SiO$_2$ (5.5 x 10^{16} cm^{-3} at 1000°C) [107, 143] and dividing by Avogadro's number. The concentration of $^{18}O_2$ that was lost to the quartz tube was < 10^{-8} mol while the moles of $^{18}O_2$ in the tracer gas at the start of the experiment was ~3 x 10^{-5} mol. Therefore the change in the concentration of $^{18}O_2$ in the tracer gas resulting from the loss of $^{18}O_2$ to the fused quartz tube during the exchange is also negligible.

5.6.1.2. Transient Heating

The transient heating time may introduce error to the values of D_b and k_s as the specimens are inserted into the furnace. The temperature decrease was small (10 – 56°C) and the furnace quickly got back to temperature (35 – 60 seconds) after opening and closing the box furnace door to insert the encapsulated specimen into the furnace. Given the small size of the encapsulation tube and specimen, it is expected that the time it took for the specimen to reach the exchange temperature was short (on the order of 1 – 2 minutes) relative to the total exchange times for most specimens. Therefore it is not expected that the transient time associated with heating the specimen will introduce significant error to the values of D_b and k_s. The measured D_b and k_s Y$_2$Si$_2$O$_7$ specimen exchanged for 10 minutes at 1300°C is the most affected by error from transient heating.

5.6.2. ^{18}O Concentration Profiles and Maps

The initial region that corresponds to a large decrease in C'(x,t) with x (large slope) in each ^{18}O concentration profile can be attributed to bulk diffusion whereas the regions where C'(x,t) slowly decreases with x (small slope) can be attributed to grain boundary diffusion [136, 137, 144] (Figure 5.4 & Figure 5.12). The ^{18}O concentration profiles seen in Figure 5.4 & Figure 5.12 all contain extended "tails" which suggest there are short circuit diffusion pathways present in each material, however, sputter crater base roughening, crater wall effects and pores can produce artifacts that may be mistaken for short circuit diffusion paths [136, 137, 145]. Optical profilometry showed there was minor roughening of the crater walls and base on all specimens, therefore artifacts from crater base roughening and crater wall effects can be ruled out. Optical profilometer images and line profiles showing the sputter crater of representative $Y_2Si_2O_7$ and Y_2SiO_5 specimens after ^{18}O exchange are shown in Figure 5.19 & Figure 5.20. The minimal porosity observed for $Y_2Si_2O_7$ specimens (pore area fraction = 0.0051 $\pm$ 0.0027) rules out the contribution of diffusion in pores to artifacts in the ^{18}O concentration profiles (Figure 5.4). It is important to note that the $Y_2Si_2O_7$ specimen exchanged at 1200°C contained the greatest amount of porosity at grain boundaries which may explain why it had the highest concentration of ^{18}O along its grain boundaries (Figure 5.7) and a higher concentration of ^{18}O at long sputter depths (Figure 5.4b). The greater porosity observed in the Y_2SiO_5 specimens (pore area fraction = 0.016 $\pm$ 0.009) has the potential to produce measurable short circuit diffusion. The average pore size was calculated to be 0.27 $\pm$ 0.017 µm however some pores were observed to be greater than 1 µm in size. Pores greater than 1 µm are short circuit diffusion paths and introduce uncertainty in the determination of D_b from the diffusion profile since they are on the same order as the measured diffusion depths. It should be noted that the pores in $Y_2Si_2O_7$ and Y_2SiO_5 specimens

appeared to be unconnected so ^{18}O diffusion from the sides or bottom of the specimen should not influence the measured ^{18}O concentration profile. The extended "tails" seen in all ^{18}O concentration profiles and the enrichment of ^{18}O along grain boundaries and pores in the ^{18}O concentration maps can therefore be are attributed to short circuit diffusion.
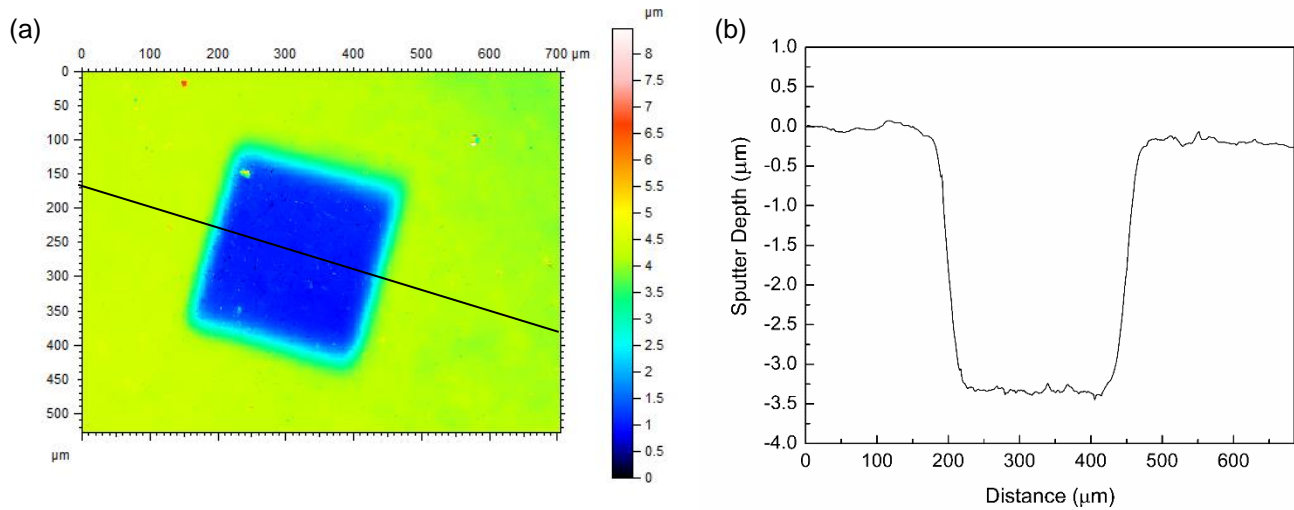
Figure 5.19. 3D surface profile of a sputter crater on a $Y_2Si_2O_7$ specimen exchanged at 1300°C (a) and the corresponding 2D line profile (b). Black line in (a) represents the location of the 2D line profile.
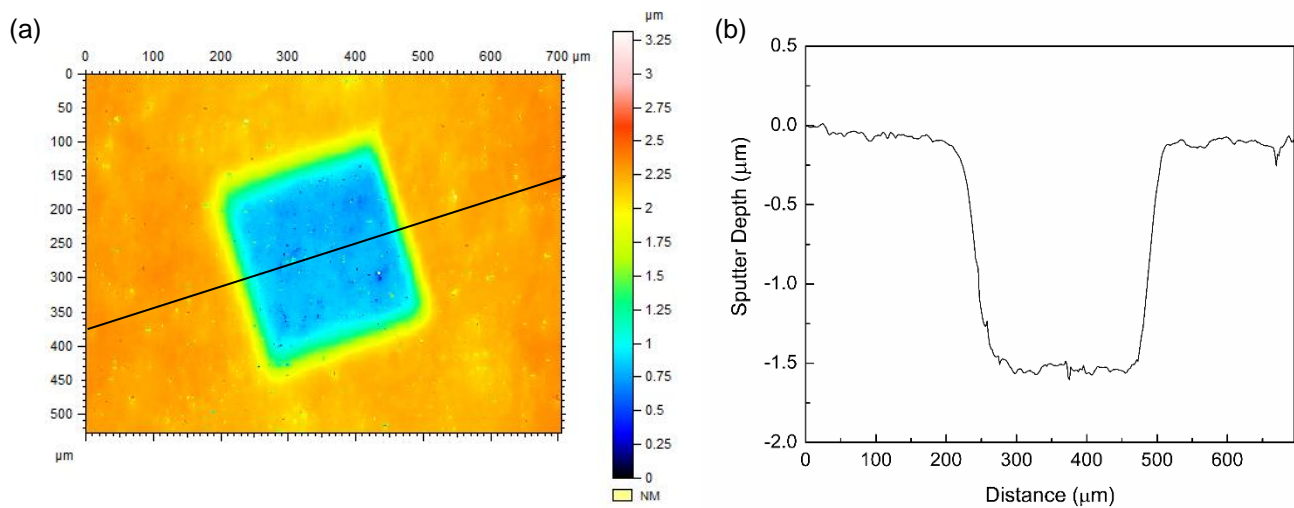
Figure 5.20. 3D surface profile of a sputter crater on a Y_2SiO_5 specimen exchanged at 1100°C (a) and the corresponding 2D line profile (b). Black line in (a) represents the location of the 2D line profile.

There are two indications that the measured diffusion coefficient is a good representation of the bulk diffusion coefficient despite that there is short circuit diffusion occurring. Firstly, there is a good fit of the diffusion equation (Equation (5.3)) to the initial region of all ^{18}O concentration profiles (with the exception of the Y_2SiO_5 specimen exchanged at 1100°C). Secondly, the contribution of bulk and short circuit diffusion to the ^{18}O concentration profiles can be seen by plotting the measured ^{18}O concentration data (C'(x,t)) as ln[C'(x,t)] vs. $\eta^{6/5}$ (Figure 5.21 & Figure 5.22) where η is a dimensionless parameter that represents coordinates perpendicular to the boundary and is given by [146–148],

$$\eta = \frac{x}{\sqrt{D_b t}} \tag{5.4}$$

The grain bulk and short curcuit components can be easily distinguished in each profile. The initial region that is fit to the diffusion equation (Equation (5.3)) represents the contribution of bulk diffusion while the region where the slope of the data changes represents the contribution of short circuit diffusion.
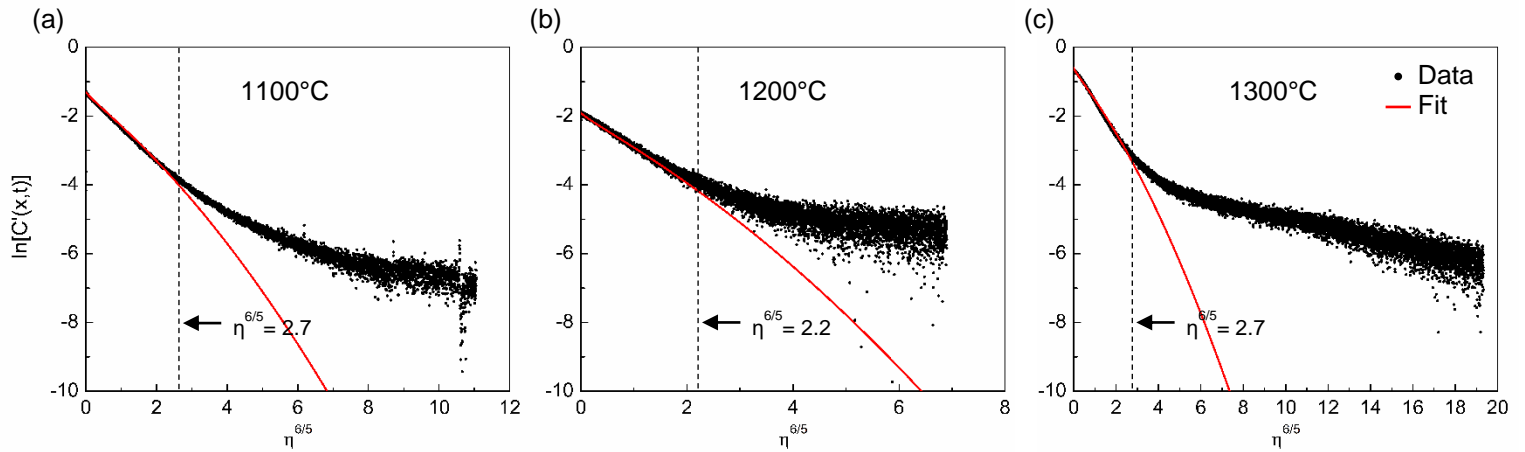
Figure 5.21. ^{18}O concentration profiles plotted as ln [C'(x,t)] vs. $\eta^{6/5}$ for $Y_2Si_2O_7$ specimens exchanged at 1100°C (a), 1200°C (b) and 1300°C (c). In each plot the contribution from bulk diffusion is shown by the fit of the diffusion equation (red line) to the ^{18}O concentration data.
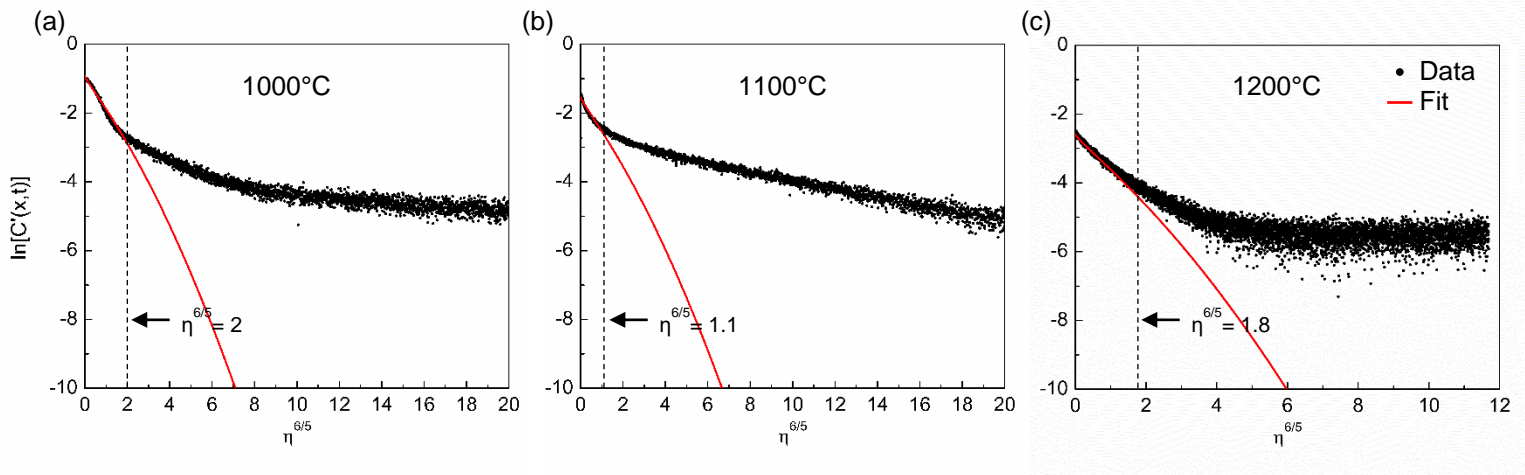
Figure 5.22. ^{18}O concentration profiles plotted as ln [C'(x,t)] vs. $\eta^{6/5}$ for Y_2SiO_5 specimens exchanged at 1000°C (a), 1100°C (b) and 1200°C (c). In each plot the contribution from bulk diffusion is shown by the fit of the diffusion equation (red line) to the ^{18}O concentration data.

Y_2SiO_5 specimens exchanged at 1000°C and 1100°C exhibited the largest diffusion "tails" resulting in a deviation of the ^{18}O concentration profile from the fit to the bulk diffusion equation (Figure 5.6a, b). The ^{18}O concentration maps did show the presence of ^{18}O along some

grain boundaries however it was significantly less than that of the $Y_2Si_2O_7$ specimens (Figure 5.6 – Figure 5.8 & Figure 5.14 – Figure 5.16), all of which had good fits of the bulk diffusion equation. This suggests that the large pores observed in Y_2SiO_5 specimens were partially responsible for the deviation of the fit to the diffusion equation to the measures ^{18}O concentration profile.

5.6.3. Anisotropic Diffusion Behavior

The ^{18}O concentration maps showed that some grains in $Y_2Si_2O_7$ and Y_2SiO_5 contained higher concentration of ^{18}O than others (Figure 5.10 & Figure 5.18). This anisotropic bulk diffusion behavior may be expected since the crystal structures of the β & γ – $Y_2Si_2O_7$ polymorph and the X2 – Y_2SiO_5 polymorph are monoclinic. These observation are consistent with those suggested by Liu et al. [149] based on first-principal calculations of activation energies for vacancy-mediated oxygen diffusion in Y_2SiO_5. In addition, oxygen tracer diffusion studies performed on <100> and <010> Y_2SiO_5 single crystals also found bulk diffusion to be anisotropic [101, 102]. Unfortunately the studies of the <100> and <010> single crystals were performed at different temperatures so a direct measure of anisotropy is unavailable. Since the $Y_2Si_2O_7$ specimens were comprised of the β & γ polymorphs it is also possible that anisotropic diffusion behavior observed in the ^{18}O concentration maps could be attributed to the differences in bulk diffusion between the two polymorphs. However, the β & γ – $Y_2Si_2O_7$ polymorphs are both monoclinic with similar densities (β= 4.03, γ= 4.04 g/cm^3) [93] and with similar bonding of SiO_4 tetrahedra in their crystal structure (Figure 5.1). Therefore it is still likely that differences in ^{18}O concentrations in different grains of $Y_2Si_2O_7$ can be attributed to anisotropic bulk diffusion

rather than polymorph variations. EBSD analysis would confirm this, but requires identification of the same grains in EBSD and ToF-SIMS, an experiment beyond the scope of this work.

5.6.4. *Activation Energy for Oxygen Diffusion*

The activation energy for oxygen diffusion (E_a (D_b)) in $Y_2Si_2O_7$ and Y_2SiO_5 was calculated to be 129 kJ/mol and 275 kJ/mol respectively however it must be noted that there is large uncertainty, especially for Y_2SiO_5, associated with this value due to the limited data used to calculate it (Figure 5.5). There have been no oxygen diffusivity studies on $Y_2Si_2O_7$ reported in literature therefore no direct comparison can be made to assess the validity of these results. The activation energy for oxygen diffusion in Y_2SiO_5 single crystals was found to be 267 kJ/mol [101] which is in good agreement with the activation energy calculated in this study for Y_2SiO_5. This demonstrates that the value for the activation energy calculated in this study for Y_2SiO_5 is reasonable (note there is significant uncertainty associated with this value) while the value calculated for $Y_2Si_2O_7$ is low for a network diffusion exchange process.

Several factors that can affect the measured oxygen diffusivity and thus the calculated activation energy in this study are short circuit diffusion, anisotropic diffusion, β & γ polymorphs of $Y_2Si_2O_7$ and transient heating at the start of ^{18}O exchanges. It has been discussed in Section 5.6.2. that the measured oxygen diffusion coefficient (D_b) should represent bulk diffusion only however some minor contribution of short circuit diffusion to D_b and E_a (D_b) is expected. The anisotropic diffusion behavior can potentially have a significant effect on E_a (D_b) as first – principal calculations by Liu et al. [149] for the vacancy-mediated oxygen diffusion in Y_2SiO_5 show that the E_a (D_b) can range from 231 – 379 kJ/mol depending on the crystallographic orientation of the diffusion path. In addition, the β & γ polymorphs of $Y_2Si_2O_7$ could have considerable

differences between their values for D_b which will result in different E_a (D_b), however, this is unlikely given their similar densities and bonding of their crystal structures as discussed in Section 5.6.3. Transient time to heat the specimen after insertion into the box furnace may also effect the measured D_b, however, this is not expected to significantly affect E_a (D_b) for most specimens in this study as discussed in Section 5.6.1.2.

5.6.5. *Comparison of Oxygen Diffusivities in Other Oxides*

The measured oxygen diffusivities in polycrystalline $Y_2Si_2O_7$ and Y_2SiO_5 were similar in magnitude (Figure 5.23). The oxygen diffusivities in yttrium silicates from $1000 - 1300°C$ were just below the oxygen diffusivity benchmark of 1.1×10^{-11} cm^2/s demonstrating that yttrium silicates are adequate oxygen barriers to protect SiC-based CMCs from oxidation for lifetimes of 10,000 hours, assuming an EBC thickness of 200 µm. The measured oxygen diffusivity in polycrystalline Y_2SiO_5 in this study was $1 - 2$ order of magnitude greater than those measured for <010> Y_2SiO_5 single crystals [101]. This result is expected as short circuit diffusion and anisotropic diffusion behavior can contribute to D_b in polycrystalline materials as discussed in Section 5.6.4. Similar differences between the oxygen diffusivity in single crystal and polycrystalline Al_2O_3 have been observed [145]. $Y_2Si_2O_7$ and Y_2SiO_5 have a lower oxygen diffusivity than SiO_2 (permeation) [143] and single crystal Y_2O_3 [105], constituents of $Y_2Si_2O_7$ and Y_2SiO_5, and a greater oxygen diffusivity than SiO_2 (network) [141] and single crystal 3:2 mullite [48], a first generation EBC material. Oxygen diffusivity results from kinetic Monte Carlo (kMC) simulations for $Yb_2Si_2O_7$ [150, 151] were ~4 orders of magnitude lower than the values obtained here for $Y_2Si_2O_7$. It is likely the results from the kMC simulation underestimate the oxygen diffusivity

in polycrystalline $Yb_2Si_2O_7$ given that $Yb_2Si_2O_7$ and $\beta - Y_2Si_2O_7$ have the same crystal structure, space group and very similar lattice parameters.

An estimated oxygen diffusion coefficient of 2.03 x 10^{-8} cm^2/s at 1316°C was reported for $Yb_2Si_2O_7$ by Richards et al. [70] which is ~4 – 8 orders of magnitude greater than the values obtained here for $Y_2Si_2O_7$ and from the kMC simulation for $Yb_2Si_2O_7$. The oxygen diffusion coefficient was estimated from the thickness of the SiO_2 thermally grown oxide (TGO) that formed on the Si bond coat at the bond coat/$Yb_2Si_2O_7$ EBC interface. Similar oxygen diffusion coefficients between $\beta/\gamma - Y_2Si_2O_7$ measured in this study and $Yb_2Si_2O_7$ are expected given the similarities in their crystal structures, as discussed above and in Section 5.6.3. There are two factors that could contribute to the large difference between the diffusion coefficient for $Y_2Si_2O_7$ measured in this study and the diffusion coefficient for $Yb_2Si_2O_7$ estimated by Richards et al. First, oxygen diffusion occurred by random exchange between ^{18}O and ^{16}O in this study since there was a uniform oxygen chemical potential whereas there was an oxygen chemical potential gradient that was the driving force for oxygen diffusion in the study by Richards et al., similar to the experimental conditions of an oxygen permeability study. Second, the $Yb_2Si_2O_7$ was an air plasma sprayed (APS) EBC which has a very different microstructure than the homogeneous specimens used in this study. The $Yb_2Si_2O_7$ EBC had a fine grain size (several hundred nanometers after deposition to ~5 µm after environmental exposure) and secondary phases of Yb_2SiO_5 and Yb_2O_3. It is likely there was significant oxygen diffusion along grain boundaries given the small initial grain size and it is currently unknown what affects the secondary phases may have on the rate of oxygen diffusion through the EBC.
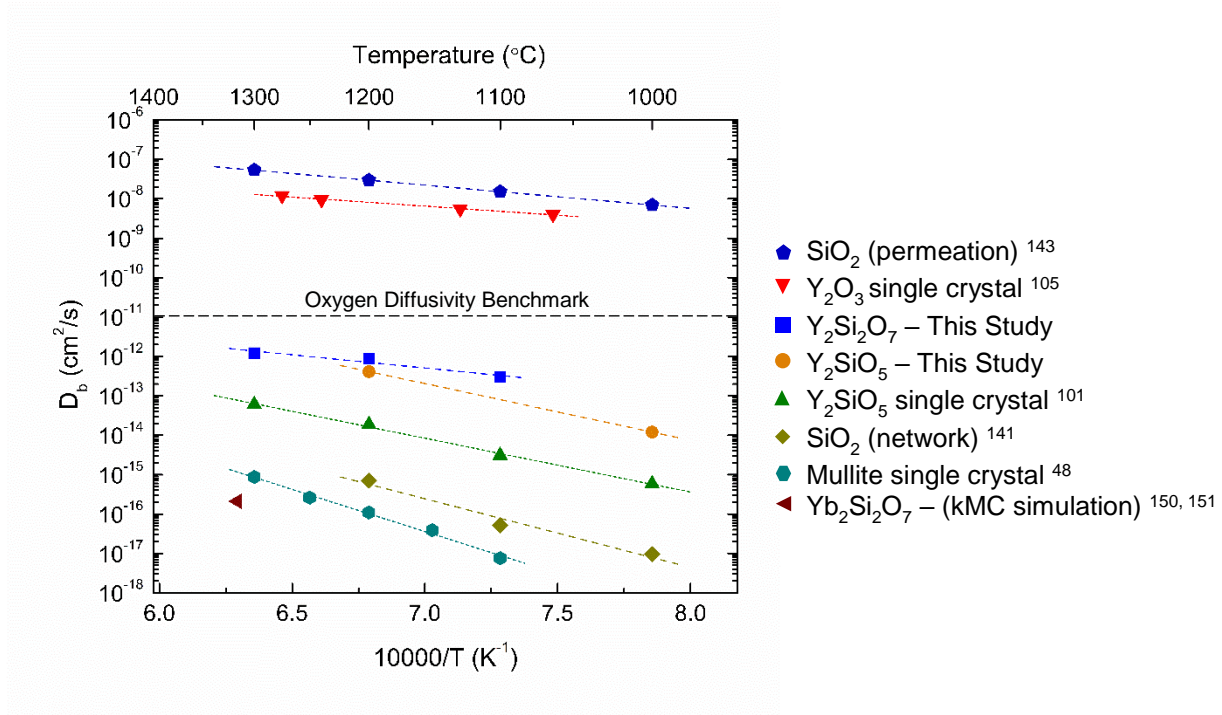
Figure 5.23. Plot of oxygen diffusivity vs. inverse temperature for different oxides

5.7. Conclusions

The oxygen diffusion coefficients for polycrystalline $Y_2Si_2O_7$ and Y_2SiO_5 were measured at temperatures from 1000 – 1300°C. The measured oxygen diffusivities in $Y_2Si_2O_7$ were not significantly different from those of Y_2SiO_5. High concentrations of ^{18}O along grain boundaries, pores and in some grain orientations (anisotropic diffusion) were observed. Uncertainty in the activation energy for oxygen diffusion in polycrystalline $Y_2Si_2O_7$ and Y_2SiO_5 was attributed to the small amount of data obtained as well as to possible effects of short circuit diffusion pathways and anisotropic diffusion. The oxygen diffusivities for polycrystalline $Y_2Si_2O_7$ and Y_2SiO_5 were all below the oxygen diffusivity benchmark of 1.1 x 10^{-11} cm^2/s in the temperature range of 1000 – 1300°C demonstrating that yttrium silicates are adequate oxygen barriers to protect SiC-based CMCs from oxidation. These new data now enable the estimation of oxygen

diffusion rates through yttrium silicate EBCs and ceramic composite matrices, critical for life prediction of engine components that require service lives $\geq$ 10,000 hours.

5.8. Recommendations for Future Work

The grain boundary diffusion coefficient (D_{gb}) can be determined from the experimental data of this work. Measured ^{18}O concentration profiles can be fit to the semi-infinite solution of the diffusion equation (Equation (5.3)) that includes the grain boundary tailing function parameters, A_{gb} and Z_{gb} (Equation (5.5)) [137, 146–148].

$$C'(x,t) = \frac{C(x,t) - C_o}{C_g - C_o} = \text{erfc}\left(\frac{x}{2\sqrt{D_b t}}\right) - \exp\left(\frac{k_s x}{D_b} + \frac{k_s^2 t}{D_b}\right) \cdot \text{erfc}\left(\frac{x}{2\sqrt{D_b t}} + k_s\sqrt{\frac{t}{D_b}}\right)$$

$$+ A_{gb}\exp\left(-Z_{gb}x^{6/5}\right) \tag{5.5}$$

The grain boundary diffusion product can be obtained using the Le Claire relation [147] or the relation developed by Chung and Wuensch [148]. The validity of applying each relation to the results of this work must be explored.

Additional ^{18}O tracer diffusion studies should be performed to determine the reproducibility of results obtained using polycrystalline $Y_2Si_2O_7$ and Y_2SiO_5 specimens. Prior to ^{18}O exchange Electron Backscatter Diffraction (EBSD) may be used to characterize the crystallographic orientation and polymorph of grains at the site that will be analyzed by ToF-SIMS. After ^{18}O exchange, the crystallographic orientation and polymorph of grains that contain higher concentrations of ^{18}O can be identified.

Yttrium silicates are candidate materials for application as EBCs for SiC-based CMCs and would likely be deposited onto the CMC using a thermal spray process. Thermal spray is a non-equilibrium process and results in a coating with multiple phases ($RE_2Si_2O_7$, RE_2SiO_5,

RE$_2$O$_3$) and a very different microstructure than the homogeneous specimens used in this study. Oxygen tracer diffusion experiments performed on thermal spray yttrium silicates could be used to identify the effects that phase and microstructure have the on oxygen diffusivity in these materials. An assessment can then be made whether the oxygen diffusivity in a homogeneous rare-earth silicate specimen accurately represents the diffusivity values for a coating that would be on a gas turbine engine component.

6. Thermochemical Stability of SiC Particulate – $Y_2Si_2O_7$

6.1. Objective

The objectives of this chapter are threefold. First, the oxidation behavior of a SiC particulate – $Y_2Si_2O_7$ composite is studied as a function of time and temperature in air. Oxide morphology and kinetics are interpreted to identify the diffusion mechanism(s) that control oxide growth. Second, the thermochemical stability of the SiC particulate – $Y_2Si_2O_7$ composite is studied in a high-temperature high-velocity water vapor environment. Oxide morphology and volatilization kinetics are interpreted to identify the reactions that resulted in material recession. Finally, oxidation and volatilization kinetics of the SiC particulate – $Y_2Si_2O_7$ composite in high-temperature oxygen and water vapor containing environments are compared to those of SiC and SiO_2 to determine if a SiC – $Y_2Si_2O_7$ matrix additive improves the water vapor stability of SiC-based CMCs.

6.2. Experimental

6.2.1. Materials and Preparation

60 vol% SiC particulate – 40 vol% $Y_2Si_2O_7$ (SiC particulate – $Y_2Si_2O_7$) specimens were prepared by Spark Plasma Sintering (SPS) as described in Section 2.2.1 and sectioned into test specimens of various sizes with surface areas of 1.681 cm^2 to 3.887 cm^2. The starting particle sizes were ≤ 1 µm and < 3 µm for SiC and $Y_2Si_2O_7$ respectively. The 60 vol% SiC particulate – 40 vol% $Y_2Si_2O_7$ composition was chosen based on the maximum amount of $Y_2Si_2O_7$ that could be incorporated into the matrix of a CMC by Rolls-Royce Corporation processing routes in 2014. Pure SiC ($> 99.9995\%$) baseline specimens made via Chemical Vapor Deposition (CVD) were

~12.6 x 12.6 x 3 mm. All specimens were polished to a 1 µm finish with diamond before oxidation or steam-jet exposures.

6.2.2. Oxidation Exposures

SiC particulate – $Y_2Si_2O_7$ and CVD SiC specimens were oxidized in air for $60 – 250$ hours at $1000 – 1200°C$ using a box furnace. Specimens were placed on a piece of fused quartz that sat inside an alumina boat. The fused quartz slide minimized contamination from the alumina boat that is known to occur for SiC oxidation [152]. The alumina boat containing the test specimen was inserted and removed from the box furnace at temperature. Three SiC particulate – $Y_2Si_2O_7$ and/or CVD SiC specimens in three separate alumina boats were inserted into the furnace at the same time. A single specimen was removed at temperature after 60, 125 and 250 hours during the time dependence study at $1200°C$. The temperature of the box furnace was observed to drop $45 – 116°C$ when inserting and/or removing a specimen and returned to the set temperature in < 1 minute. After removal from the furnace all specimens were left to cool in ambient conditions.

6.2.3. High-Temperature Water Vapor Exposures

The steam-jet apparatus described in Section 2.3 was used to expose SiC particulate – $Y_2Si_2O_7$ specimens in a high-temperature high-velocity water vapor environment. Experiments were performed at $1200°C$ for 60 hours, steam-jet velocities of $160 – 164$ m/s and at 1 atm H_2O pressure.

6.2.4. Characterization

Weights of all specimens were measured before and after oxidation and steam-jet exposures to an accuracy of 0.05 mg. The surface area of specimens used in oxidation experiments were calculated using dimensions that were measured by a micrometer prior to oxidation. X-ray Diffraction (XRD) analysis was performed on specimens before and after oxidation and steam-jet exposures to determine if any polymorph/phase changes occurred during exposure. Specimen microstructure and composition were characterized by Scanning Electron Microscopy (SEM) and Energy Dispersive Spectroscopy (EDS). All SEM images were acquired using backscattered electrons and are denoted as BSE/SEM images. The recession profile of SiC particulate – $Y_2Si_2O_7$ specimens after steam-jet exposure were characterized by optical profilometry.

6.3. Results

6.3.1. As-Processed SiC Particulate – $Y_2Si_2O_7$ and CVD SiC Specimens

XRD analysis of as-processed SiC particulate – $Y_2Si_2O_7$ specimens identified α – SiC and γ – $Y_2Si_2O_7$ as major phases/polymorphs and β – $Y_2Si_2O_7$ as the minor phase/polymorph. Optical and BSE/SEM images of the surface of an as-processed specimen can be seen in Figure 6.1. The BSE/SEM image shows the specimen contains minor porosity and is comprised of SiC particulates (dark phase) that are surrounded by $Y_2Si_2O_7$ (bright phase). Some surface cracks were also observed. XRD analysis of as-received CVD SiC specimens identified β-SiC as the only phase/polymorph. CVD SiC specimens were nearly completely dense.
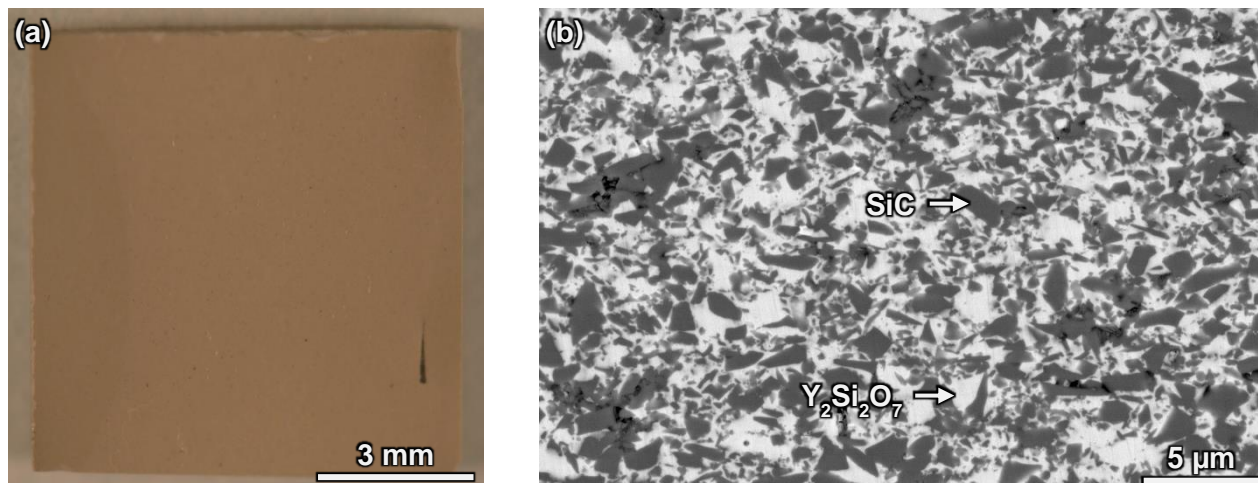
Figure 6.1. Optical (a) and BSE/SEM image (b) of the surface of an as-processed SiC particulate – $Y_2Si_2O_7$ specimen.

6.3.2. Time Dependence for the Oxidation of SiC Particulate – $Y_2Si_2O_7$ and CVD SiC

SiC particulate – $Y_2Si_2O_7$ and CVD SiC specimens were oxidized in air for 60, 125 and

250 hours at 1200°C. XRD analysis of the SiC particulate – $Y_2Si_2O_7$ specimens identified

α – SiC and γ – $Y_2Si_2O_7$ as major phases/polymorphs and α and β – cristobalite as the minor

phases/polymorphs following oxidation. XRD analysis of the CVD SiC specimens identified

β – SiC and α – cristobalite as the major and minor phases/polymorphs respectively after

oxidation. SEM characterization of the surface of SiC particulate – $Y_2Si_2O_7$ specimens after

oxidation shows that a non-uniform multiphase oxide scale has formed (Figure 6.2). Some

porosity and cracks were observed in the oxide scale. EDS analysis shows that the light grey

phase has a Y:Si ratio of ~ 1:1 indicating the presence of $Y_2Si_2O_7$ whereas Si and O were

detected in the dark grey/black phase indicating the presence of SiO_2. The $Y_2Si_2O_7$ in the oxide

scale appears different than it does in the as-processed specimen indicating that it grew on the

surface during oxidation. Small facets can be seen in the SiO_2 regions indicating that it is crystalline. These results are consistent with the findings from the XRD analysis.
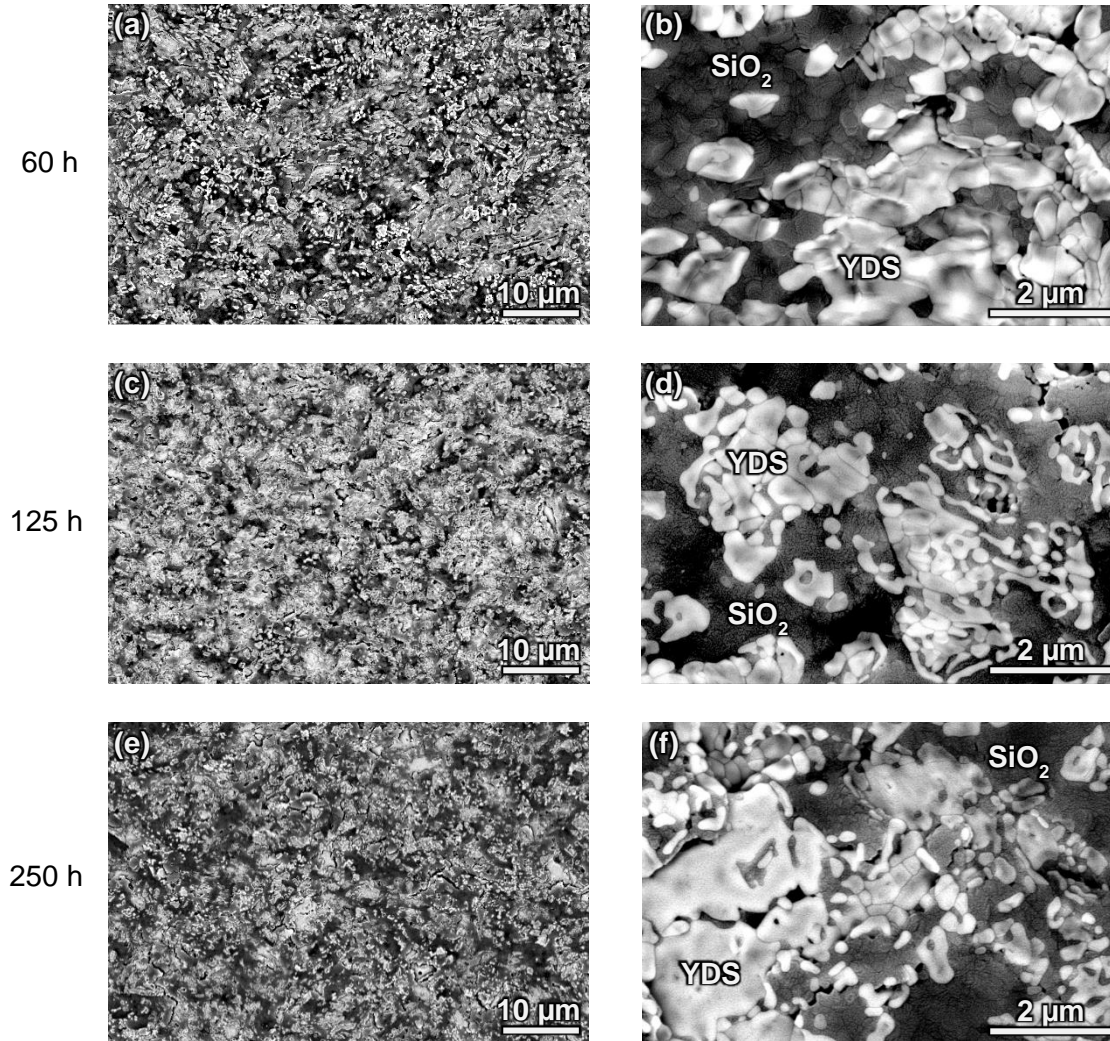
Figure 6.2. Plan view BSE/SEM images SiC particulate – $Y_2Si_2O_7$ specimens after oxidation in air for 60 (a,b), 125 (c,d) and 250 hours (e,f) at 1200°C.

SEM characterization of cross-sections of SiC particulate – $Y_2Si_2O_7$ specimens after oxidation shows that the oxide/substrate interface is not well defined (Figure 6.3). EDS analysis indicates that SiO_2 and $Y_2Si_2O_7$ were present at the specimen surface, consistent with results

from surface EDS analysis and XRD. All SiC particulates that were at the specimen surface have oxidized to form SiO_2. Some SiC particulates below the specimen surface have formed an external SiO_2 scale indicating there is inward oxygen transport. These observations are consistent with those in the EDS elemental maps for the specimen oxidized for 125 hours where the near surface regions are saturated with oxygen and depleted in carbon (Figure 6.4). The depletion of carbon results from the oxidation of SiC to form SiO_2 and CO (g) per Equation (1.1). SiO_2 formation appears to have increased with increasing exposure time. No SiO_2 scale thickness measurements were made due to the absence of a well-defined scale. No reactions were observed between subsurface SiC and $Y_2Si_2O_7$.
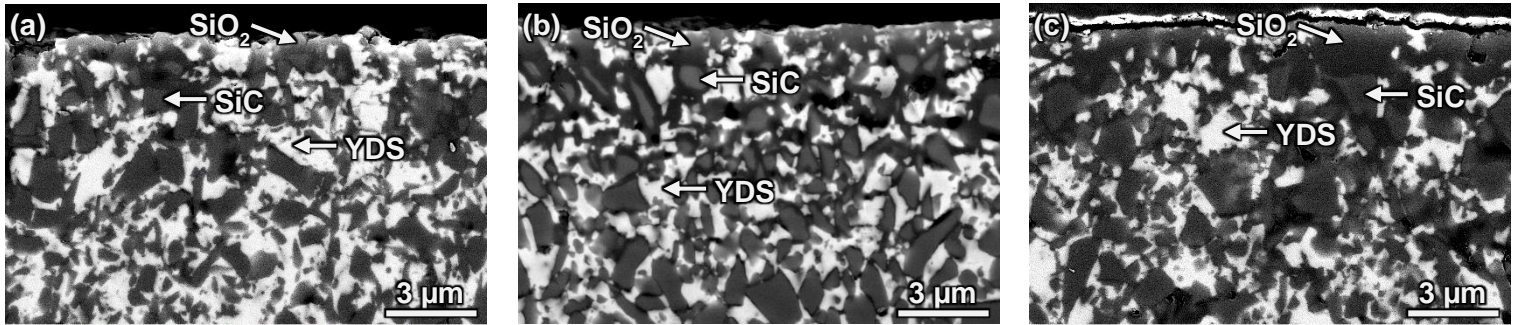
Figure 6.3. BSE/SEM images of cross-sections on SiC particulate – $Y_2Si_2O_7$ specimens after oxidation in air for 60 (a), 125 (b) and 250 hours (c) at 1200°C.

The measured specific weight change increased during oxidation at 1200°C and was greater for the SiC particulate – $Y_2Si_2O_7$ specimens than the CVD SiC specimens (Table 6.1). The average specific weight change has been plotted vs. time$^{1/2}$ in Figure 6.5. The oxidation of SiC particulate – $Y_2Si_2O_7$ is consistent with parabolic oxidation kinetics whereas it is clear that CVD SiC exhibits parabolic oxidation kinetics. The parabolic oxidation rate constants

152

determined from specific weight change measurements were 1.44 x 10^{-3} mg^2/cm^4 h and 5.05 x

10^{-5} mg^2/cm^4 h for SiC particulate – Y$_2$Si$_2$O$_7$ and CVD SiC respectively. Specific weight changes

for all SiC particulate – Y$_2$Si$_2$O$_7$ and CVD SiC specimens in this study can be found in Appendix

L & M.
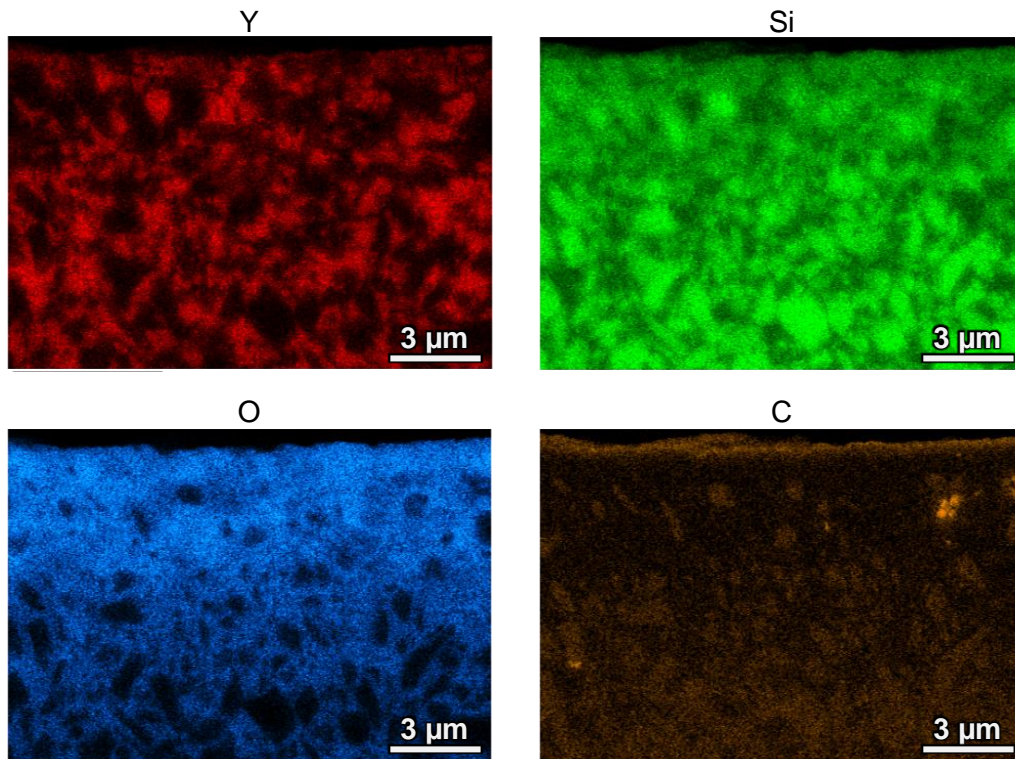
Figure 6.4. EDS elemental maps for Y, Si, O and C corresponding to the SiC particulate – Y$_2$Si$_2$O$_7$ specimen cross-section shown in Figure 6.3b. Specimen was oxidized in air for 125 hours at 1200°C.

Table 6.1. Average specific weight change for SiC particulate – $Y_2Si_2O_7$ and CVD SiC specimens oxidized in air for 60 – 250 hours at 1200°C. A minimum of two specimens were oxidized at each test condition.

Material	Time (h)	Average Specific Weight Change (mg/cm^2)
SiC particulate – $Y_2Si_2O_7$	60	0.298 ± 0.053
	125	0.469 ± 0.063
	250	0.583 ± 0.11
CVD SiC	60	$0.055 \pm 5E\text{-}5$
	125	$0.079 \pm 9E\text{-}4$
	250	0.112 ± 0.011
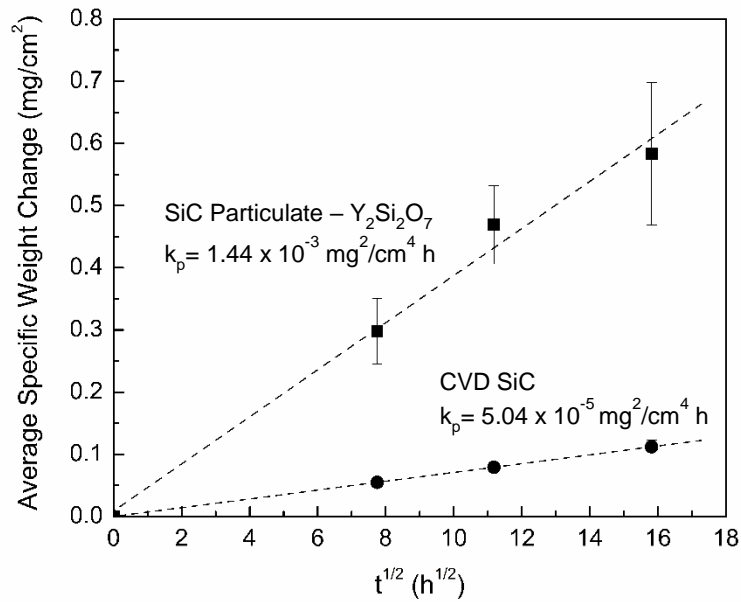
Figure 6.5. Plot of average specific weight change vs. time $^{1/2}$ measured from SiC particulate – $Y_2Si_2O_7$ and CVD SiC specimens after oxidation in air for 60 – 250 hours at 1200°C.

Temperature Dependence for the Oxidation of SiC Particulate – $Y_2Si_2O_7$ and CVD SiC

SiC particulate – $Y_2Si_2O_7$ and CVD SiC specimens were oxidized in air for 125 hours at 1000°C, 1100°C and 1200°C. XRD analysis of the SiC particulate – $Y_2Si_2O_7$ specimens identified α – SiC and γ – $Y_2Si_2O_7$ as major phases/polymorphs and α and β – cristobalite as the minor phases/polymorphs following oxidation. XRD analysis of the CVD SiC specimens identified β – SiC as the major phase/polymorph after oxidation at all temperatures while α – cristobalite was identified as the minor phase/polymorph after oxidation at 1200°C. No SiO_2 phases were identified after oxidation at 1000°C and 1100°C. SEM characterization of the surface of SiC particulate – $Y_2Si_2O_7$ specimens after oxidation shows that a non-uniform multiphase oxide scale has formed (Figure 6.6). Porosity and cracks were observed in the oxide scale at all temperatures however a greater amount was observed on specimens oxidized at 1000°C. The $Y_2Si_2O_7$ in the oxide scale appears different than it does in the as-processed specimen indicating that it grew on the surface during oxidation. EDS analysis shows that the light grey phase has a Y:Si ratio of ~ 1:1 indicating the presence of $Y_2Si_2O_7$ whereas Si and O were detected in the dark grey/black phase indicating the presence of SiO_2. Small facets can be seen in the SiO_2 regions on specimens oxidized at 1100°C and 1200°C indicating that it is crystalline. These results are consistent with the findings from the XRD analysis.
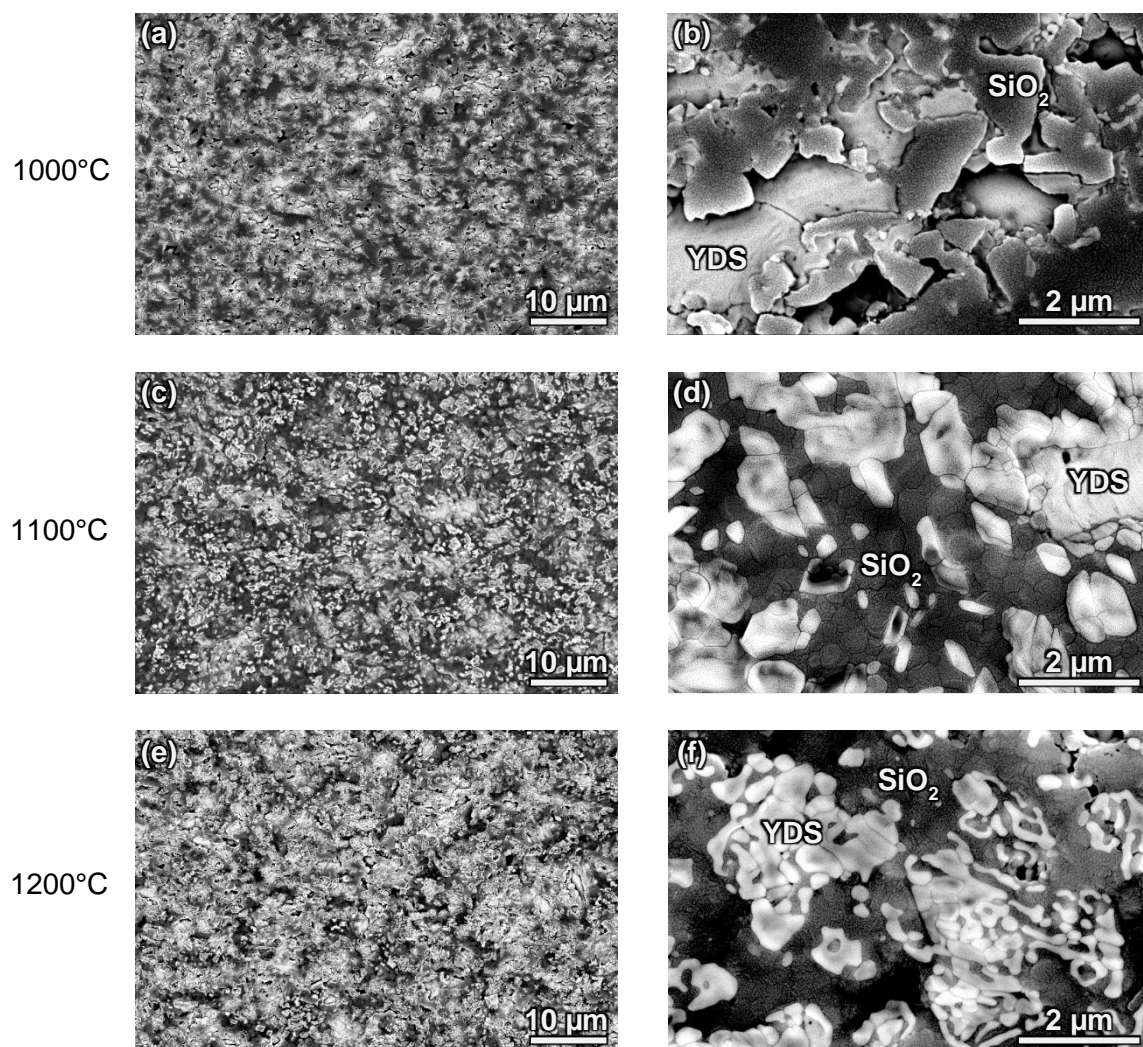
Figure 6.6. Plan view BSE/SEM images SiC particulate – $Y_2Si_2O_7$ specimens after oxidation in air for 125 hours at 1000°C (a,b), 1100°C (c,d) and 1200°C hours (e,f).

SEM characterization of cross-sections of SiC particulate – $Y_2Si_2O_7$ specimens after oxidation shows that the oxide/substrate interface is not well defined (Figure 6.7). EDS analysis indicates that SiO_2 and $Y_2Si_2O_7$ were present at the specimen surface, consistent with results from surface EDS analysis and XRD. All SiC particulates that were at the specimen surface have oxidized to form SiO_2. Some SiC particulates below the specimen surface have formed an

external SiO$_2$ scale on specimens oxidized at 1100°C and 1200°C indicating there is inward oxygen transport. SiO$_2$ formation appears to have increased with increasing temperature. No SiO$_2$ scale thickness measurements were made due to the absence of a well-defined scale. No reactions were observed between subsurface SiC and Y$_2$Si$_2$O$_7$.
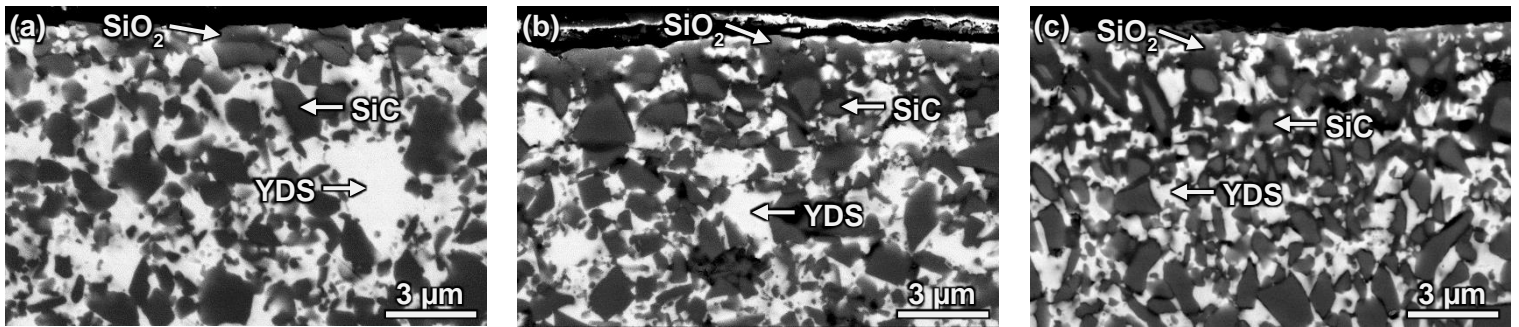
Figure 6.7. BSE/SEM images of cross-sections on SiC particulate – Y$_2$Si$_2$O$_7$ specimens after oxidation in air for 125 hours at 1000°C (a), 1100°C (b) and 1200°C (c).

The measured specific weight change was greatest after oxidation at 1000°C for the SiC particulate – Y$_2$Si$_2$O$_7$ specimens whereas the specific weight change was found to increase with increasing temperature for CVD SiC specimens (Table 6.2, Figure 6.8). Specific weight change of SiC particulate – Y$_2$Si$_2$O$_7$ specimens was an order of magnitude greater than CVD SiC specimens at each oxidation temperature. No oxidation activation energy for SiC particulate – Y$_2$Si$_2$O$_7$ was calculated due to the high specific weight change measured on specimens oxidized at 1000°C. Parabolic rate constants have been calculated from specific weight change measurements made for CVD SiC specimens and have been plotted against inverse temperature in Figure 6.9. An activation energy of 217 kJ/mol was obtained for the oxidation of CVD SiC.

Specific weight changes for all SiC particulate – $Y_2Si_2O_7$ and CVD SiC specimens in this study

can be found in Appendix L & M.

Table 6.2. Average specific weight change for SiC particulate – $Y_2Si_2O_7$ and CVD SiC specimens oxidized in air for 125 hours at 1000 – 1200°C. A minimum of two specimens were oxidized at each test condition.

Material	Temperature (°C)	Average Specific Weight Change (mg/cm^2)
SiC particulate – $Y_2Si_2O_7$	1000	0.785 ± 0.41
	1100	0.244 ± 0.019
	1200	0.469 ± 0.063
CVD SiC	1000	0.02 ± 0.003
	1100	0.056 ± 0.001
	1200	0.079 ± 0.001
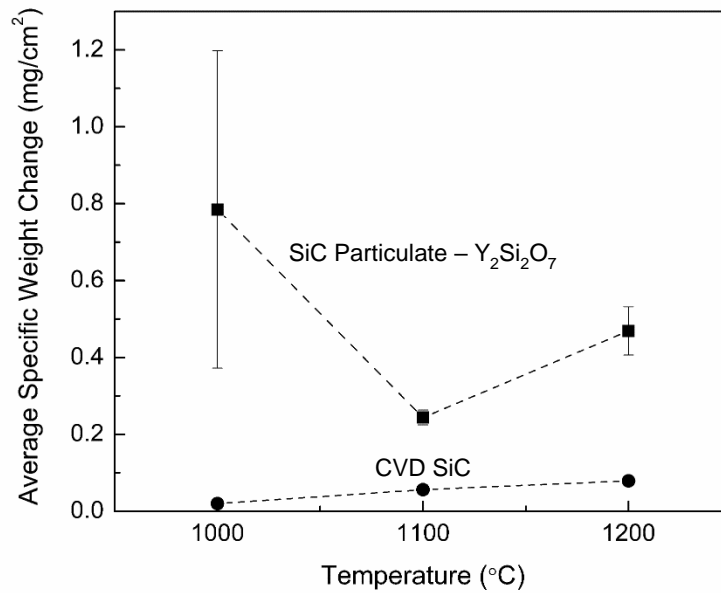
Figure 6.8. Plot of average specific weight change vs. temperature measured from SiC particulate – $Y_2Si_2O_7$ and CVD SiC specimens after oxidation in air for 125 hours at 1000 – 1200°C.
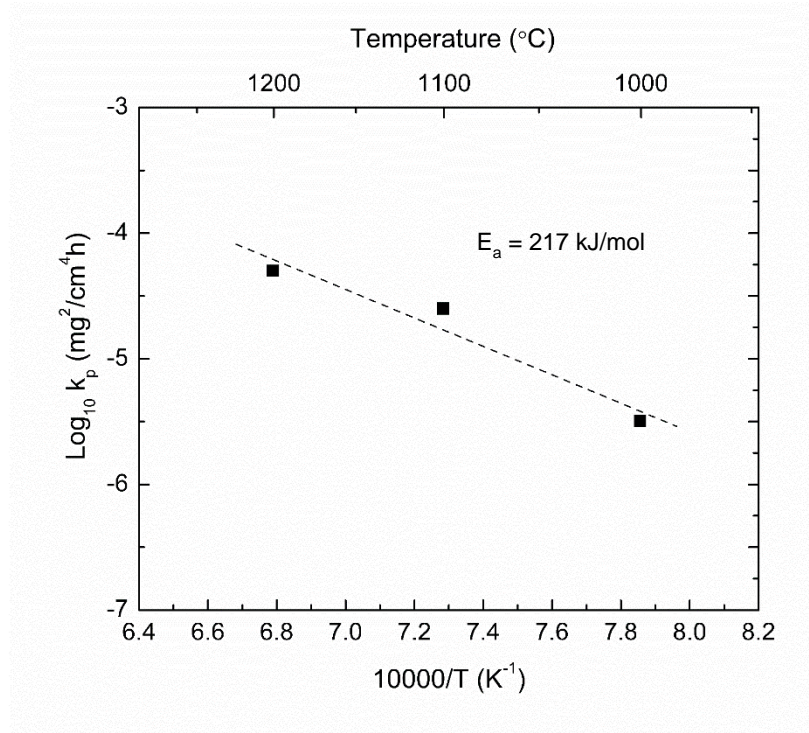
Figure 6.9. Arrhenius plot of parabolic rate constants for oxidation of CVD SiC.

6.3.4. *Thermochemical Stability of SiC Particulate – $Y_2Si_2O_7$ in High-Temperature High-Velocity Water Vapor*

Specimens were exposed in the steam-jet for 60 hours at 1200°C, steam-jet velocities of 160 – 164 m/s and at 1 atm H_2O pressure. All specimens lost weight during steam-jet exposures (Appendix N). After steam-jet exposure XRD analysis identified γ – $Y_2Si_2O_7$ and α – cristobalite as major phases/polymorphs and α – SiC and β – $Y_2Si_2O_7$ as the minor phases/polymorphs. An optical image shows that the steam-jet impingement site is visible on the specimen after exposure and that the specimen changed color from beige (Figure 6.1) to white (Figure 6.10). A maximum recession of 208 µm was measured using an optical profilometer which corresponds to a recession rate of 3.5 µm/h (Figure 6.11).

159
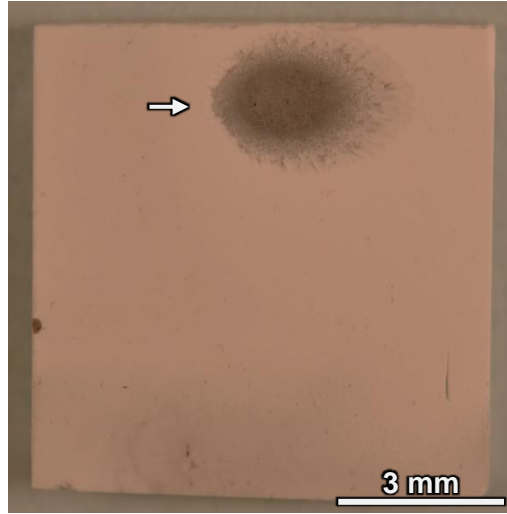
Figure 6.10. Optical image of a SiC particulate – $Y_2Si_2O_7$ specimen after steam-jet exposure for 60 hours at 1200°C. $v_{(g)}$= 164 m/s, $P(H_2O)$= 1 atm. Arrow ($\rightarrow$) indicates direction of steam-jet.
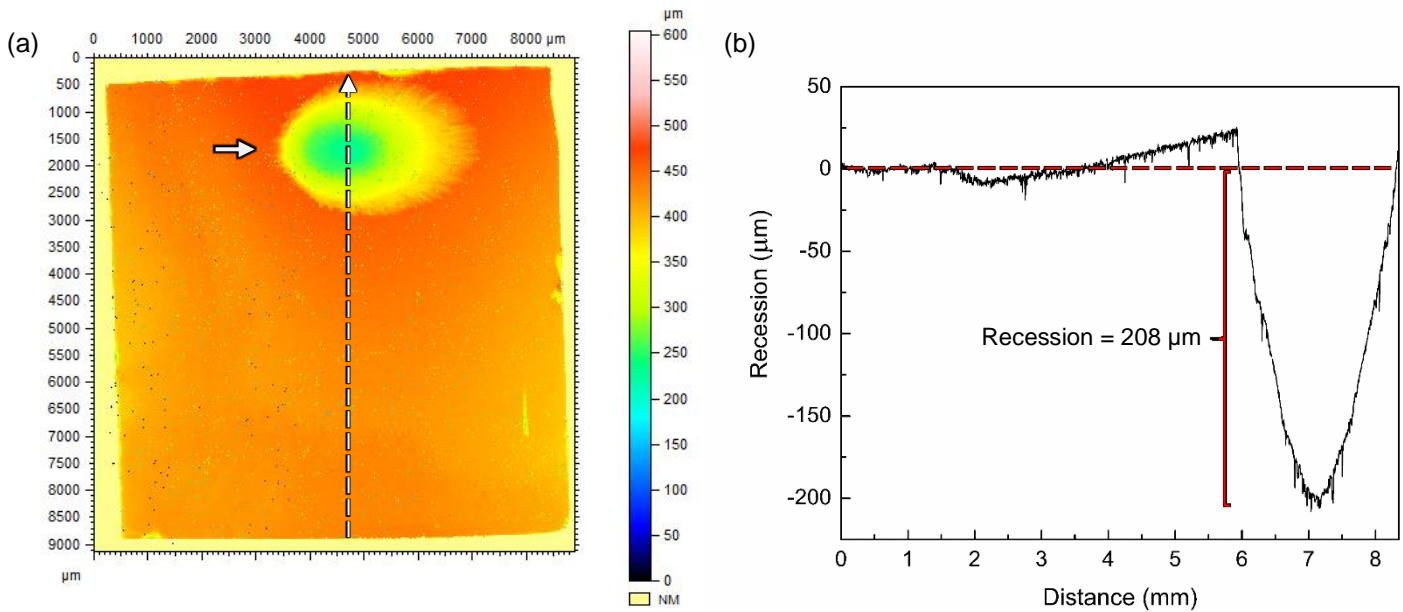
Figure 6.11. 3D surface profile of a SiC particulate – $Y_2Si_2O_7$ specimen after steam-jet exposure (a) and the corresponding 2D recession profile (b). T_{steam}= 1200°C, t= 60 h, $v_{(g)}$= 164 m/s, $P(H_2O)$= 1 atm. Solid arrow ($\rightarrow$) indicates direction of steam-jet, dotted arrow in (a) represents the location of the 2D recession profile and the dotted line in (b) shows the surface baseline used for the recession measurement.

160

SEM and EDS characterization at the steam-jet impingement site shows that the surface has roughened and contains $Y_2Si_2O_7$ and SiO_2 (Figure 6.12a), consistent with the results from the XRD analysis. Porous $Y_2Si_2O_7$ was observed upstream of the steam-jet impingement site (Figure 6.12b). A cross-section through the specimen shows there is significant material loss at the steam-jet impingement site and the presence of a porous surface layer in the areas that were not exposed to high-velocity water vapor, such as near the bottom edge of the specimen (Figure 6.13). The porous surface layer was also observed to form along a subsurface crack. Note the location of the cross-section may not correspond to the location of maximum recession. The orientation of the cross-section shown in Figure 6.13 is the same as that for the 2D recession profile shown in Figure 6.11b where the left side of the cross-section/recession profile is near the bottom edge of the specimen.
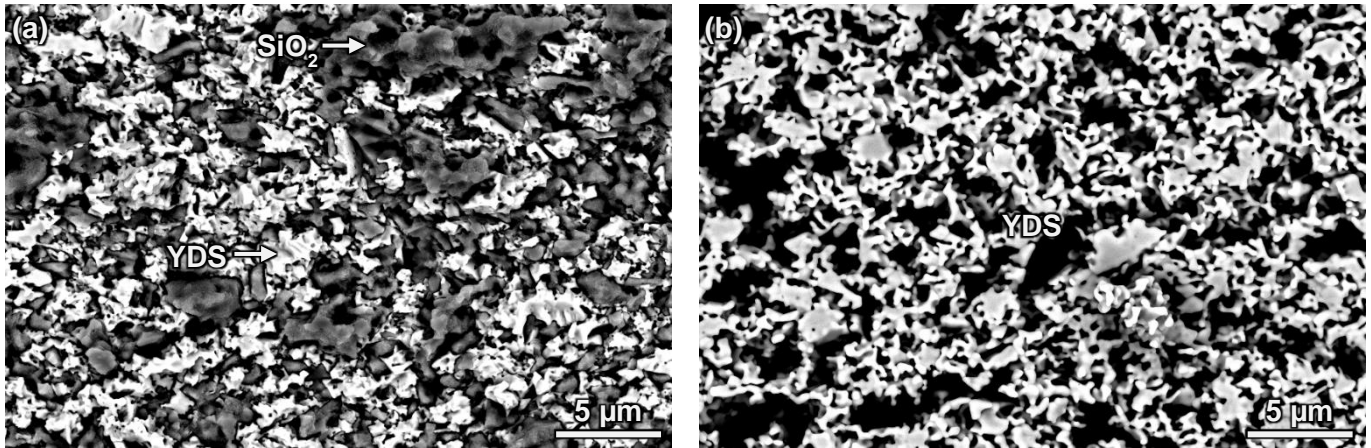
Figure 6.12. Plan view BSE/SEM images at the steam-jet impingement site (a) and upstream of the impingement site (b) on a SiC particulate – $Y_2Si_2O_7$ specimen after steam-jet exposure for 60 hours at 1200°C. $v_{(g)}$= 160 m/s, $P(H_2O)$= 1 atm.
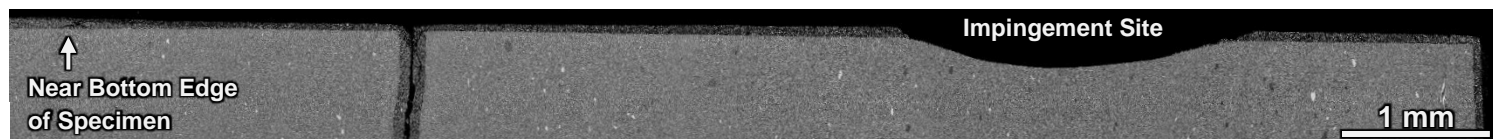
Figure 6.13. BSE/SEM image of a cross-section through a SiC particulate – $Y_2Si_2O_7$ specimen after steam-jet exposure for 60 hours at 1200°C. $v_{(g)}$= 160 m/s, $P(H_2O)$= 1 atm.

Higher magnification BSE/SEM images in cross-section show that the impingement site is rough and contains $Y_2Si_2O_7$ and a thin layer of SiO_2 (Figure 6.14a) as determined by EDS point analysis where Si and O were detected in addition to areas that had a Y:Si ratio of ~ 1:1. These results are consistent with SEM, EDS and XRD characterization performed on the surface. A layered structure containing a surface layer of porous $Y_2Si_2O_7$ and an intermediate layer of SiO_2 + $Y_2Si_2O_7$ had formed on the SiC particulate – $Y_2Si_2O_7$ substrate near the bottom edge of the specimen (Figure 6.13 & Figure 6.14b). EDS elemental maps for the region near the bottom edge of the specimen show that the top surface layer is depleted of Si and O (SiO_2) compared to the intermediate layer below (Figure 6.15), consistent with results from EDS point analysis. In addition, EDS maps show that a thin oxide layer has formed at the interface between SiO_2 + $Y_2Si_2O_7$ and the SiC particulate – $Y_2Si_2O_7$ substrate.
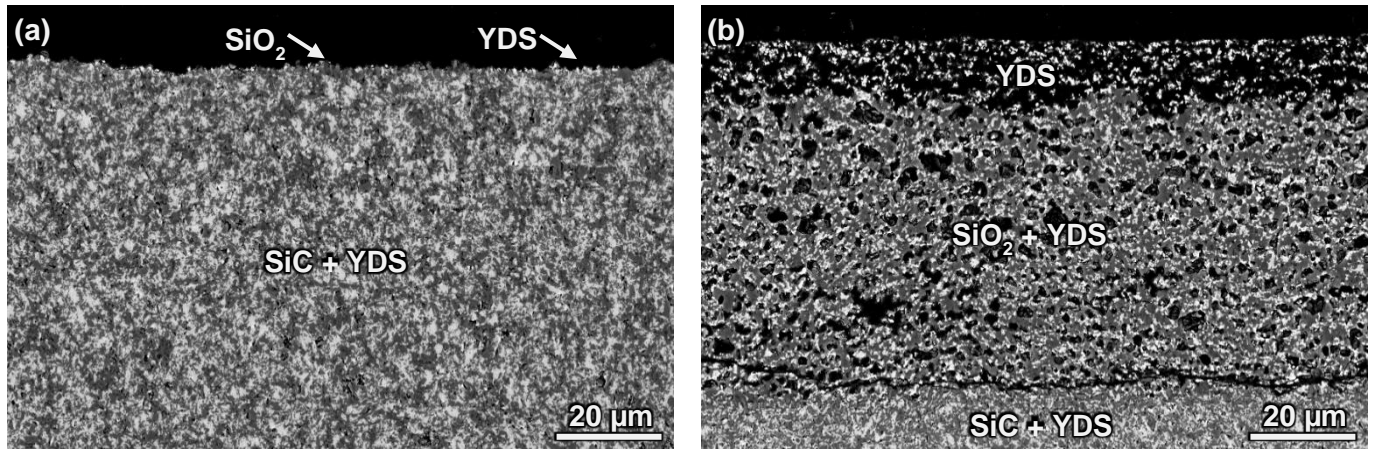
Figure 6.14. BSE/SEM images of a cross-section through the steam-jet impingement site (a) and near the bottom edge (b) on a SiC particulate – $Y_2Si_2O_7$ specimen after steam-jet exposure for 60 hours at 1200°C. $v_{(g)}$= 160 m/s, $P(H_2O)$= 1 atm.
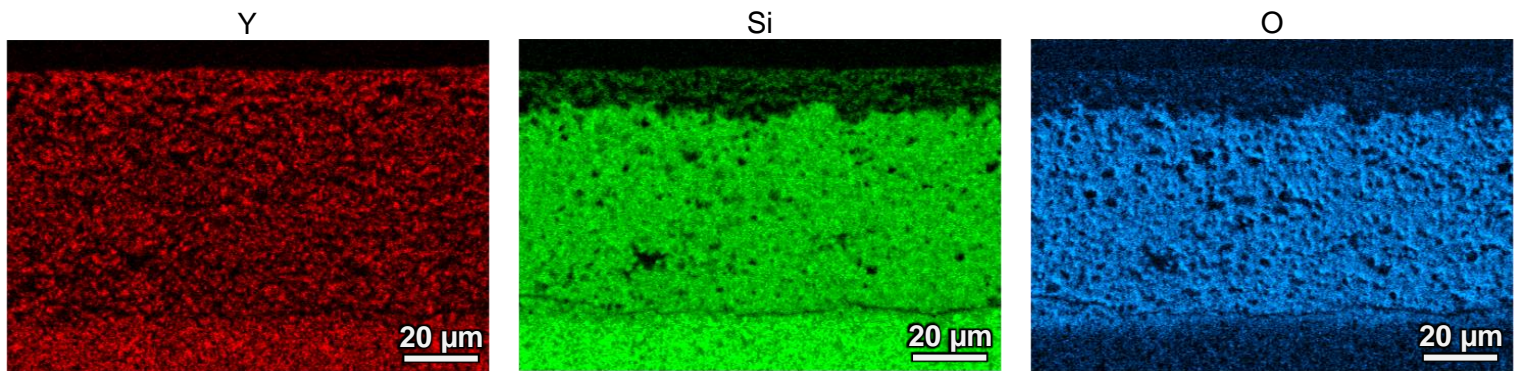
Figure 6.15. EDS elemental maps for Y, Si and O corresponding to the SiC particulate – $Y_2Si_2O_7$ specimen cross-section shown in Figure 6.14b. Specimen was exposed in the steam-jet furnace for 60 hours at 1200°C.

163

6.4.   Discussion

6.4.1. Oxidation Kinetics

Oxidation of SiC particulate – $Y_2Si_2O_7$ specimens resulted in the formation of a non-uniform multiphase oxide scale upon oxidation consisting of SiO_2 and $Y_2Si_2O_7$. Some porosity and surface cracks were also observed. SEM and EDS characterization of cross-sections showed that the SiC particulates at and below the specimen surface oxidized to form SiO_2 by Equation (1.1) (Figure 6.3, Figure 6.4, Figure 6.7). These results indicate that the oxidation rate of SiC particulate – $Y_2Si_2O_7$ is limited by the oxidation of SiC and thus the diffusion of oxygen through SiO_2. The oxidation of SiC exhibits parabolic oxidation kinetics [18, 19, 21–23] which is consistent with the oxidation kinetics at 1200°C determined for SiC particulate – $Y_2Si_2O_7$ and CVD SiC in this study (Figure 6.5).

The significantly larger parabolic rate constant (k_p) for SiC particulate – $Y_2Si_2O_7$ compared to CVD SiC can be attributed to the non-protective nature of the multiphase oxide scale that formed on the SiC particulate – $Y_2Si_2O_7$ specimens. Pores and cracks at the specimen surface offer fast diffusion pathways for oxygen to penetrate below the surface and oxidize SiC. In addition, impurities in the SiO_2 scale introduced from the starting SiC powder could break up the SiO_2 network thereby creating larger pathways for molecular oxygen to diffuse through. The effect of impurities in SiO_2 on the oxidation of SiC will be discussed in Section 6.4.4.

The k_p for CVD SiC at 1200°C (5.04 x 10^{-5} mg^2/cm^4 h) determined from specific weight change measurements in this study was a factor of ~2.2 greater than the k_p determined by Ogbuji et al. (2.29 x 10^{-5} mg^2/cm^4 h) [18]. Note the k_p value determined from oxide thickness by Ogbuji et al. for CVD SiC oxidized at 1200°C in O_2 has been converted to a specific weight change rate

constant at a $P(O_2)= 0.21$ atm (air). Possible causes leading to this discrepancy will be discussed in Section 6.4.4.

6.4.2. Temperature Dependence for the Oxidation of SiC Particulate – $Y_2Si_2O_7$ and CVD SiC

The measured specific weight change for SiC particulate – $Y_2Si_2O_7$ specimens was greatest after oxidation at 1000°C and was found to increase from 1100°C to 1200°C (Figure 6.8). The slower oxide growth at 1000°C prevented the rapid sealing of pores and cracks that were present in the as-processed specimen. This allows oxygen to penetrate far below the specimen surface and internally oxidize the SiC particulates. In addition, the multiphase oxide scale contained large pores at 1000°C which again provides fast pathways for oxygen transport below the specimen surface (Figure 6.6a).

The measured specific weight change for SiC particulate – $Y_2Si_2O_7$ was an order of magnitude greater than that for CVD SiC at all temperatures. Causes for the greater specific weight change of the SiC particulate – $Y_2Si_2O_7$ specimens was discussed above and in Section 6.4.1. The measured specific weight change of CVD SiC increased with increasing temperature. Reasonable agreement was found between the parabolic rate constants determined from specific weight change measurements in this study and the results of Ramberg et al. [19], Ogbuji et al. [18] and Costello et al. [153] (Table 6.3). The activation energy for the oxidation of CVD SiC determined in this study (217 kJ/mol) was higher than activation energies obtained by Ogbuji et al. [18] (118 kJ/mol) for the oxidation of CVD SiC and Deal and Grove [107] (119 kJ/mol) for the oxidation of Si. The activation energy determined in this study was in reasonable agreement with those determined by Costello et al. [153] (134 – 389 kJ/mol) for the oxidation of α – SiC. Costello

et al. contributes their high activation energy, relative to Ogbuji et al. and Deal and Grove, to the

effects that impurities in the SiO_2 scale have on the oxidation rate of SiC. The effect of

impurities on the oxidation of SiC will be discussed in Section 6.4.4.

Table 6.3. Comparison of parabolic rate constants (k_p) for the oxidation of CVD SiC and α – SiC in air.

	Temperature (°C)	k_p (mg^2/cm^4 h)
This Study	1000	3.20×10^{-6}
	1100	2.51×10^{-5}
	1200	5.04×10^{-5}
Ramberg et al. [19]	1000	8.78×10^{-6}
	1100	1.53×10^{-5}
Ogbuji et al. [18]	1200	2.29×10^{-5}
Costello et al. [153]	1200	3.10×10^{-5}

k_p values determined from oxide thickness by Ramberg et al. and Ogbuji et al. for CVD SiC oxidized at 1000 – 1200°C in O_2 have been converted to a specific weight change rate constant using the density of amorphous SiO_2 (2.2 g/cm^3) and cristobalite (2.32 g/cm^3) respectively at a P(O_2)= 0.21 atm (air). k_p value determined by Costello et al. [153] from oxide thickness for α-SiC oxidized at 1200°C in air has also been converted to a specific weight change rate constant using the density of cristobalite.

6.4.3. Formation of $Y_2Si_2O_7$ in the Oxide Scale

The microstructure of the $Y_2Si_2O_7$ in the oxide scale is considerably different than that in

the as-processed SiC particulate – $Y_2Si_2O_7$ specimen. This indicates that $Y_2Si_2O_7$ is growing

from the SiO_2 at the specimen surface upon oxidation. Similar observations of $Y_2Si_2O_7$ growth

from SiO_2 have been made in oxidation studies of Si_3N_4 that contained Y_2O_3 sintering additives

which created a Y rich glassy intergranular phase [154–156]. The thermodynamic mechanism for

cation diffusion through an amorphous intergranular phase in Si_3N_4 developed by Clarke [157] was

166

used to explain the transport of yttrium to the surface. The presence of dissolved Y creates a chemical potential gradient between the yttrium-rich amorphous SiO_2 phase boundary and the pure SiO_2 which forms on the surface during oxidation of the Si regions. The chemical potential gradient results in the diffusion of yttrium to the surface SiO_2 scale until the yttrium concentration is constant in both the phase boundary and at the surface. This situation cannot be achieved since SiO_2 is continually being formed at or below the surface. Finally, a crystalline yttrium containing oxide phase forms on the surface of the SiO_2 possibly due to the reduction in free energy resulting from the formation of a more stable crystalline phase from an amorphous phase.

Although the oxidation of SiC particulate – $Y_2Si_2O_7$ results in the creation of phase boundaries between SiO_2 and bulk $Y_2Si_2O_7$, they should be in equilibrium with one another (Figure 1.3) and thus there would be no driving force for Y in the bulk $Y_2Si_2O_7$ to diffuse to the surface [156]. It is clear that Y is diffusing from bulk $Y_2Si_2O_7$ to the surface however the cause for the disturbance in equilibrium between SiO_2 and bulk $Y_2Si_2O_7$ is unknown. It is hypothesized that an intergranular glassy phase may form containing impurities from the SiC (such as Al and Fe) or impurities from the box furnace which initiates diffusion of Y from bulk $Y_2Si_2O_7$. In addition, oxidation studies of yttrium silicides have shown that Y will dissolve in SiO_2 and diffuse to the surface when SiO_2 is in equilibrium with $Y_2Si_2O_7$ (Chapter 7).

6.4.4. *Factors Affecting the Oxidation of SiC Particulate – $Y_2Si_2O_7$ and CVD SiC*

Some microstructural features that can introduce scatter to specific weight change measurements for SiC particulate – $Y_2Si_2O_7$ and CVD SiC specimens are pores, cracks and phase boundaries since they provide fast diffusion pathways for oxygen to oxidize material

below the specimen surface, as discussed in Section 6.4.1. It is expected that these microstructural features have largely been the cause of the scatter in specific weight change measurements for SiC particulate – $Y_2Si_2O_7$ specimens since they possess all these features in the as-processed material whereas CVD SiC specimens are homogenous throughout and are nearly completely dense.

The presence of impurities in the air from the box furnace insulation can also affect measured specific weight change values. A study that compared oxidation of CVD SiC (100 h, 1300°C in O_2) in Al_2O_3 and fused quartz furnace tubes found that more rapid oxidation kinetics resulted when specimens were oxidized in the Al_2O_3 tube [158]. It was found that Na impurities from the Al_2O_3 tube accelerates the oxidation of SiC due to increased permeation of molecular oxygen through the oxide. The increased oxygen permeability was attributed to the formation of non-bridging oxygens. The presence of Na impurities increased the specific weight change by a factor of ~2.7 relative to a specimen oxidized in high purity fused quartz furnace tubes. No Na was detected by EDS in the SiO_2 scale of the specimens in this study however the concentration may be below the limit of the detector (~1 at%). Sodium concentration less than 1 at% can still have a large effect of the oxidation kinetics of SiC as shown by Zheng et al. [159] where 50 ppm Na increased the oxide scale thickness by a factor of 1.2 after a 3 hour exposure at 1200°C in O_2.

The presence of small concentrations of Y and other impurities from the starting SiC powder in the SiO_2 scale on the SiC particulate – $Y_2Si_2O_7$ specimens may also increase the diffusion of oxygen through SiO_2. Oxidation studies of CVD SiC by Ogbuji et al. [18] and Ramberg et al. [19] were performed in a much "cleaner" environment where they used dry O_2 and furnace tubes made of high purity fused quartz or mullite that has been cleaned with HF to remove impurities by surface segregation and etching.

6.4.5. *Thermochemical Stability of SiC Particulate – $Y_2Si_2O_7$ in High-Temperature High-Velocity Water Vapor*

The exposure of SiC particulate – $Y_2Si_2O_7$ specimen to high-temperature high-velocity water vapor resulted in significant material loss. A recession rate of 3.5 µm/h was measured which is a factor of ~2 – 18 greater than that for SiO_2 (1.5 µm/h) (Chapter 3) and SiC (> 0.2 µm/h) [20, 27–30] when exposed under the same or harsher conditions.

SEM and EDS characterization near the bottom edge of the specimen where the water vapor velocity was low provided insight into the possible oxidation/volatilization reactions which lead to the material loss observed at the impingement site. Near the bottom edge of the specimen a layered structure containing a surface layer of porous $Y_2Si_2O_7$ and an intermediate layer of $SiO_2 + Y_2Si_2O_7$ had formed on the SiC particulate – $Y_2Si_2O_7$ substrate (Figure 6.14b). This microstructure could have formed from the following oxidation/volatilization reactions;

$$SiC + Y_2Si_2O_7 + 3H_2O \text{ (g)} \rightarrow SiO_2 + Y_2Si_2O_7 + CO \text{ (g)} + 3H_2 \text{ (g)} \qquad (6.1)$$

$$SiO_2 + Y_2Si_2O_7 + 2H_2O \text{ (g)} \rightarrow Si(OH)_4\text{(g)} + \text{ pores} + Y_2Si_2O_7 \qquad (6.2)$$
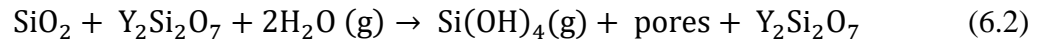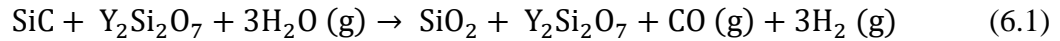
First, the water vapor oxidized SiC to form SiO_2 and volatile CO (g) and H_2 (g) while the $Y_2Si_2O_7$ remained unaffected due to its superior thermochemical stability in water vapor compared to SiO_2. This resulted in a microstructure consisting of $SiO_2 + Y_2Si_2O_7$. Second, the SiO_2 closest to the surface reacted with water vapor to form a volatile $Si(OH)_4$ (g) leaving behind pores + $Y_2Si_2O_7$, as seen in Figure 6.14b. The same oxidation/volatilization reactions would have taken place at the steam-jet impingement site however the oxidation/volatilization rates would have been much greater due to the increased velocity of the water vapor. At the impingement site the fragile porous $Y_2Si_2O_7$ region that remains after SiO_2 had been volatilized is mechanically eroded by the high-velocity water vapor leaving behind the rough surface observed at the

impingement site. Since SiO_2 is volatilizing nearly as fast as it forms from the oxidation of SiC at the impingement site there was only a thin surface layer of SiO_2 present after exposure.

The region near the bottom edge of the specimen highlights the severity of the SiC oxidation in water vapor compared to air. In water vapor that was approximately stagnant SiC was observed to oxidize as far as ~70 µm below the initial specimen surface (Figure 6.14b) whereas in air SiC oxidized < 5 µm below the initial specimen surface (Figure 6.3a) after exposure at 1200°C for 60 hours. The accelerated SiC oxidation in water vapor is consistent with results found in literature [21–23, 26].

6.4.6. *Implications for SiC Particulate – $Y_2Si_2O_7$ as a Matrix for SiC CMCs*

The oxidation of SiC particulate – $Y_2Si_2O_7$ for up to 250 hours at 1000 – 1200°C in air resulted in the formation of a non-protective multiphase oxide scale consisting of SiO_2 and $Y_2Si_2O_7$. The non-protective nature of the oxide scale was demonstrated when specific weight change measurements for SiC particulate – $Y_2Si_2O_7$ specimens were an order of magnitude greater than that for CVD SiC. In addition, the poor oxidation resistance of the SiC particulate – $Y_2Si_2O_7$ specimens at 1000°C indicates that the oxidation behavior of this material would be problematic during thermal cycling events in a turbine engine.

In high-temperature high-velocity water vapor SiC particulate – $Y_2Si_2O_7$ suffered from significant material loss due to the preferential oxidation/volatilization of SiC and erosion of the remaining porous structure of $Y_2Si_2O_7$. The thermochemical stability/erosion resistance of SiC particulate – $Y_2Si_2O_7$ was found to be worse than that for SiO_2 measured in this study (Chapter 3) and for SiC exposed under similar or worse conditions [20, 27–30]. The results of this study show that

replacing the Si/SiC matrix with a SiC particulate – $Y_2Si_2O_7$ matrix would significantly reduce the oxidation and water vapor resistance of a CMC.

6.5. Conclusions

The oxidation behavior and thermochemical stability in water vapor was assessed for SiC particulate – $Y_2Si_2O_7$ at temperatures from $1000 – 1200°C$ and times of $60 – 250$ hours. Oxidation in air resulted in the formation of a non-protective multiphase oxide scale consisting of SiO_2 and $Y_2Si_2O_7$. SiC particulate – $Y_2Si_2O_7$ specimens exhibited parabolic oxidation kinetics at $1200°C$ indicating the oxidation rate was controlled by the diffusion of oxygen through the SiO_2 scale. Slower oxidation kinetics at $1000°C$ prevented the rapid sealing of pores and cracks resulting in the greatest specific weight change. Measured specific weight change of SiC particulate – $Y_2Si_2O_7$ was an order of magnitude greater than that for CVD SiC at nearly all temperatures and times. In high-temperature high-velocity water vapor SiC particulate – $Y_2Si_2O_7$ specimens suffered from significant material loss due to the preferential oxidation/volatilization of SiC and erosion of $Y_2Si_2O_7$. Recession rates of SiC particulate – $Y_2Si_2O_7$ were greater than that for SiO_2 and SiC when exposed under similar conditions. The non-protective nature of the oxide scale and the poor thermochemical stability/erosion resistance in high-temperature water vapor demonstrates that a SiC particulate – $Y_2Si_2O_7$ matrix would significantly reduce the oxidation and water vapor resistance of a CMC.

6.6. Recommendations for Future Work

The maximum volume fraction of $Y_2Si_2O_7$ that could be incorporated into the matrix of a CMC by Rolls-Royce Corporation processing routes (2014) was investigated in this study thus it

is not recommended that other compositions of SiC particulate – $Y_2Si_2O_7$ that contain less $Y_2Si_2O_7$ be investigated since their oxidation behavior in air and thermochemical stability in water vapor will likely be worse than pure SiC.

A crack in the EBC should produce similar low velocity water vapor conditions to those seen in the region characterized near the bottom edge of the specimen where SiC oxidized to form SiO_2 (Figure 6.13 & Figure 6.14b). Additional additives to incorporate into SiC particulate – $Y_2Si_2O_7$ that will react with SiO_2 to form a more thermochemically stabile oxide than SiO_2 in water vapor can be explored. Formation of a new thermochemically stable oxide phase would limit further oxidation of the matrix and SiC fibers.

7. Thermochemical Stability of Yttrium Silicides

7.1. Objective

The objectives of this chapter are threefold. First, the oxidation behavior of yttrium silicides is characterized as a function of alloy composition, temperature and time. Second, the oxide morphology and kinetics are interpreted to identify the diffusion mechanism(s) that control oxide growth. Finally, the suitability of RE silicides for use as MI matrix materials in CMCs is evaluated.

7.2. Experimental

7.2.1. Thermodynamic Calculations

The oxide product formation from the Y_5Si_3, Y_5Si_4, YSi, Y_3Si_5 and YSi_2 phases was predicted by thermodynamic calculations using the equilibrium module in FactSage [108]. Inputs into the equilibrium module included 1 mole of the Y-Si phase of interest and 1 mole of O_2 at temperatures from 100 to 1500°C. Oxide product formation from the reaction of Y_2O_3 and SiO_2 was also predicted using inputs of 1 mole of Y_2O_3 and 1 or 2 moles of SiO_2 at temperatures from 100 to 1500°C. The SGPS database and custom databases for the $Y - Si$ and $Y_2O_3 - SiO_2$ systems were used for the thermodynamic calculations. Custom databases for the $Y - Si$ and $Y_2O_3 - SiO_2$ systems were constructed using thermodynamic data from Shukla et al. [91] and Fabrichnaya et al. [90] respectively.

7.2.2. Materials and Processing

Yttrium and silicon charges with the compositions of 41, 67 and 95 at% Si-Y were prepared for arc melting as described in Section 2.2.2. Alloyed yttrium silicide buttons were

sectioned into specimens for the oxidation experiments. The surface of each specimen was polished to a 1 µm finish with diamond.

7.2.3. Oxidation Experiments

Yttrium silicide specimens were oxidized in air for 0.5 – 24 hours at 1000°C and 1200°C using a box furnace. All specimens were placed on an Al_2O_3 boat and inserted and removed from the furnace at temperature. Following removal from the furnace the specimens were left in the Al_2O_3 boat to cool to room temperature in ambient conditions. Two to three repeats were completed at each exposure time and temperature.

7.2.4. Characterization

Weights of all specimens were measured before and after oxidation exposures to an accuracy of 0.05 mg. The surface area of each specimen was calculated using dimensions that were measured by a micrometer prior to oxidation. X-ray Diffraction (XRD) was performed on specimens before and after oxidation to determine the oxide phases formed and substrate phase changes that occurred during exposure. Specimen microstructures were characterized by Scanning Electron Microscopy (SEM) and Transmission Electron Microscopy (TEM). All SEM images were acquired using backscattered electrons and will be denoted as BSE/SEM images. Elemental analysis was performed using Energy Dispersive Spectroscopy (EDS), Electron Energy Loss Spectroscopy (EELS) and Energy Filtered Transmission Electron Microscopy (EFTEM). A Focused Ion Beam (FIB) was used to prepare specimens for TEM characterization.

7.3. Results

7.3.1. *Thermodynamic Calculations*

Thermodynamic calculations using FactSage [108] free energy minimization software predict that the Y_5Si_3 and Y_5Si_4 phases oxidize to form Y_2O_3 at all temperatures while the YSi, Y_3Si_5 and YSi_2 phases form Y_2O_3 at temperatures above 638°C. Below 638°C, the YSi, Y_3Si_5 and YSi_2 phases are predicted to form Y_2SiO_5 and $Y_2Si_2O_7$. In addition to forming an oxide the Y_5Si_3, Y_5Si_4, YSi and Y_3Si_5 phases were also predicted to form more Si-rich silicides on the phase diagram. The reaction of Y_2O_3 and SiO_2 was predicted to form $Y_2O_3 + Y_2SiO_5$ and $Y_2SiO_5 + Y_2Si_2O_7$ at all temperatures when 1 and 2 moles of SiO_2 were input into FactSage respectively.

7.3.2. *41 at% Si-Y Alloy*

The as-processed 41 at% Si-Y alloy contained the equilibrium $Y_5Si_3 + Y_5Si_4$ phases as well as minor amounts of a non-equilibrium Y_5Si_3 phase and surface cracks (Figure 7.1 & Figure 7.2). Phase composition identified by EDS analysis was consistent with XRD results. The 41 at% Si-Y alloy was oxidized in air for 3 hours at 1000°C and 1200°C. Macro images of specimens before and after oxidation show that the alloy has rapidly oxidized forming a cracked non-protective oxide scale (Figure 7.3). The specimen oxidized at 1000°C broke apart while the specimen oxidized at 1200°C remained intact. Cross-sections show that the entire base alloy was nearly consumed by the growing oxide scale at both temperatures (Figure 7.3e, f).
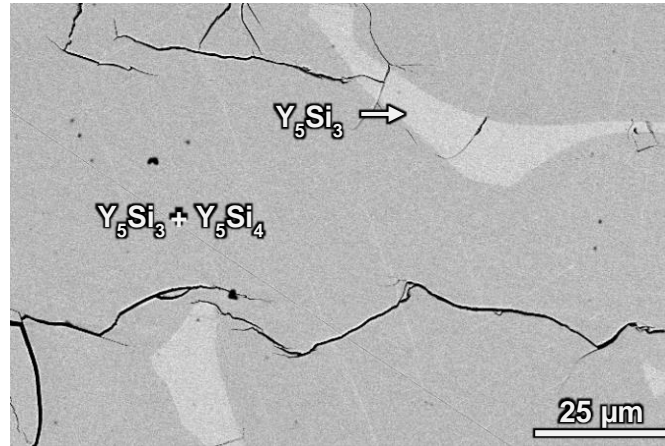
Figure 7.1. BSE/SEM image of as-processed 41 at% Si-Y alloy showing the presence of the equilibrium Y_5Si_3 + Y_5Si_4 phase field, minor amounts of a non-equilibrium Y_5Si_3 phase and surface cracks.
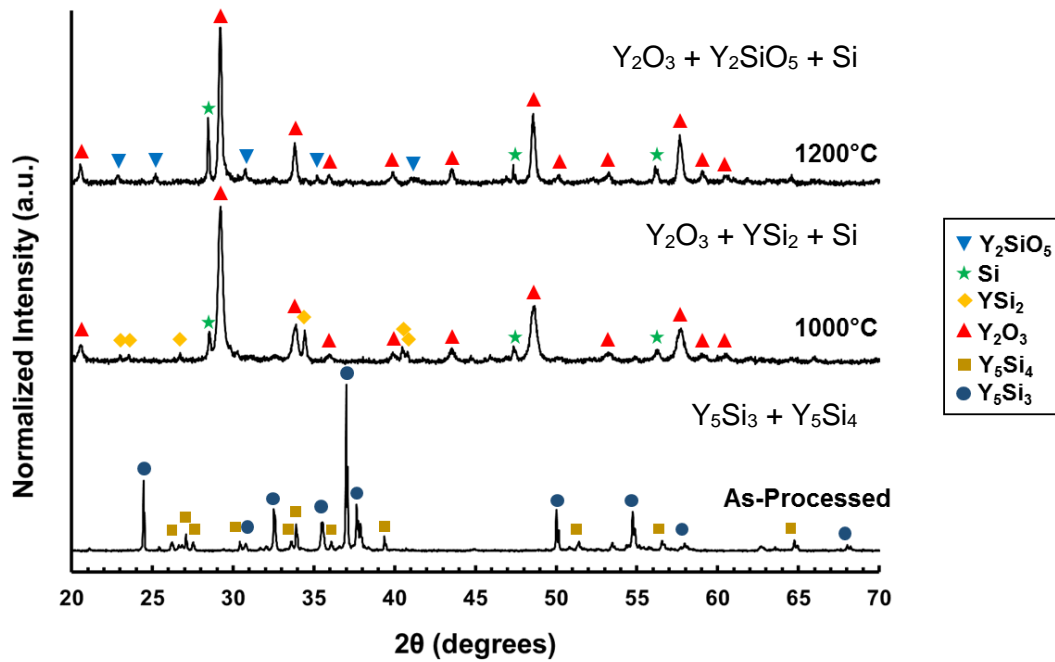
Figure 7.2. XRD of the as-processed 41 at% Si-Y alloy before and after oxidation in air for 3 hours at 1000°C and 1200°C.

176
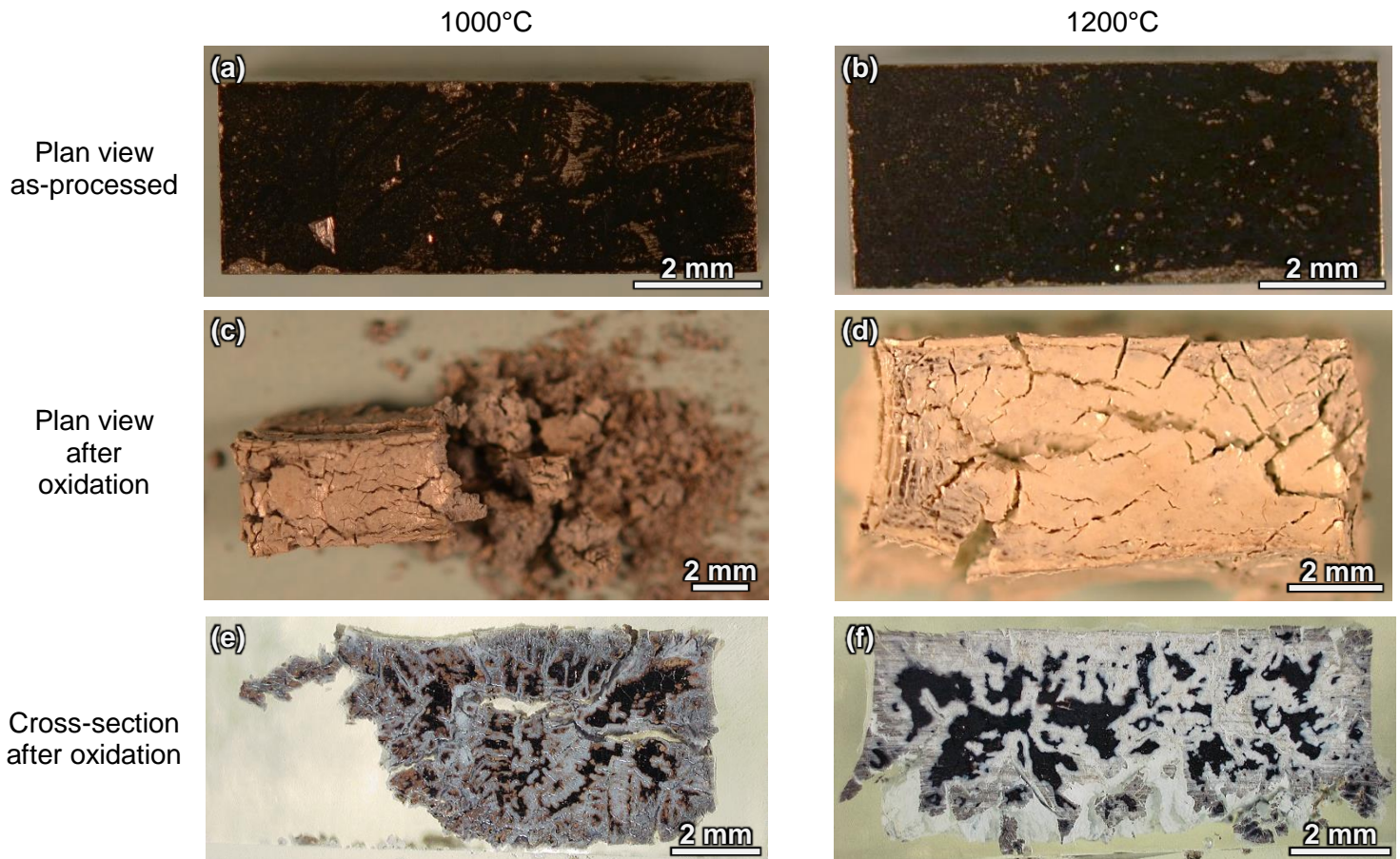
Figure 7.3. Macro images of the 41 at% Si-Y specimens before and after oxidation in air for 3 hours at 1000°C (a, c, e) and 1200°C (b, d, f). As-processed plan view (a,b), after oxidation plan view (c,d) and after oxidation cross-section (e,f).

Y_2O_3, YSi_2 and Si were identified by XRD analysis after oxidation at 1000°C for 3 hours (Figure 7.2). Major amounts of Y_2O_3 and minor amounts of Y_2SiO_5 and Si were identified after oxidation at 1200°C for 3 hours. The formation of YSi_2 and Si after oxidation can be attributed to the removal of yttrium from the base alloy to form Y_2O_3 and Y_2SiO_5, thereby enriching the underlying alloy in Si.

SEM and EDS characterization of cross-sectioned specimens after oxidation show the presence of a thick Y_2O_3 surface layer, subsurface regions of YSi_2, Si and Y_2SiO_5 and a significant amount of subsurface cracks (Figure 7.4 & Figure 7.5). Trace amounts of Si ($\sim1 - 5$ at%) in the Y_2O_3 surface scale were occasionally identified by EDS analysis. A secondary Y_2O_3 layer containing pockets of Si was observed below the thick Y_2O_3 surface layer on the specimen oxidized at 1000°C. The specimen oxidized at 1200°C contained fewer subsurface cracks and more regions of Si enrichment compared to the specimen oxidized at 1000°C. Specimens oxidized at 1200°C had a greater specific weight change than those oxidized at 1000°C (Figure 7.6). These specific weight changes are two orders of magnitude greater than those predicted from the results of Deal and Grove [107] for the oxidation of pure Si. Specific weight changes for all specimens can be found in Appendix O.
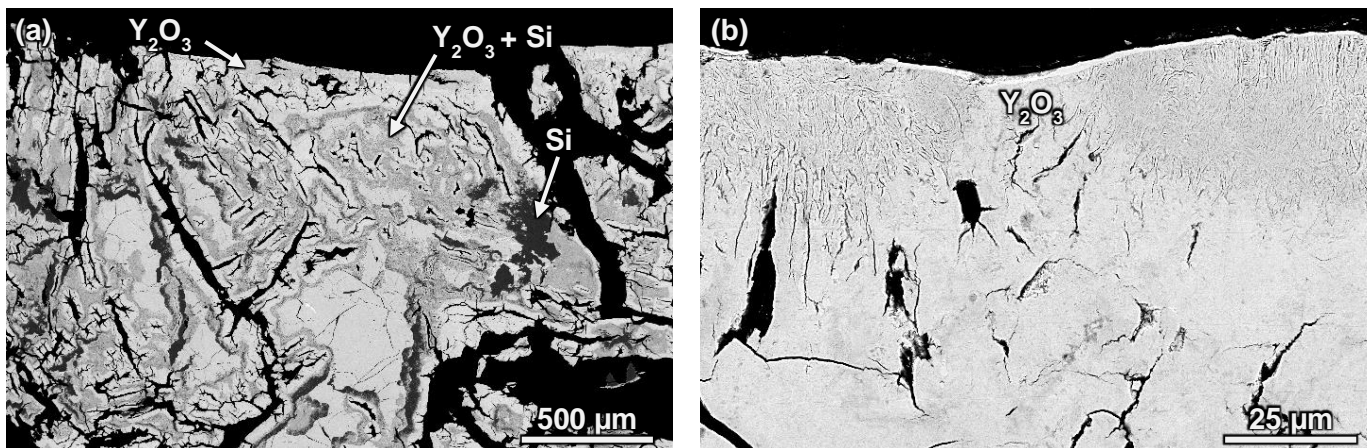
Figure 7.4. BSE/SEM cross-section images of a 41 at% Si-Y specimen after oxidation in air for 3 hours at 1000°C.
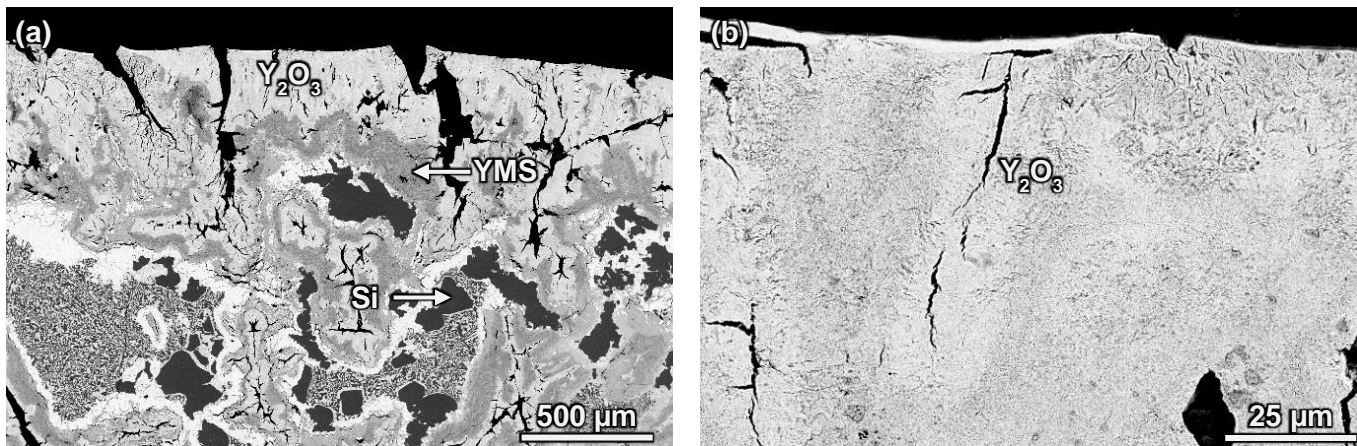
Figure 7.5. BSE/SEM cross-section images of a 41 at% Si-Y specimen after oxidation in air for 3 hours at 1200°C.
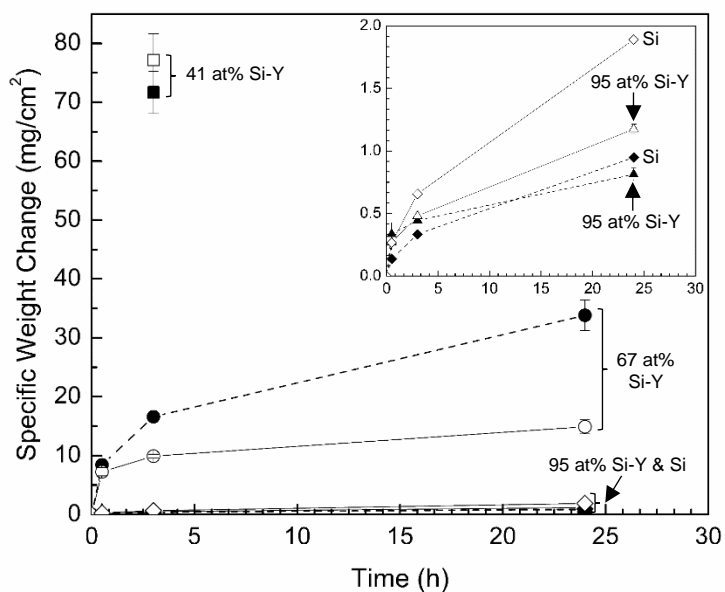
Figure 7.6. Specific weight change vs. time results for the 41, 67 and 95 at% Si-Y alloys and pure Si after oxidation in air at 1000°C (filled symbols) and 1200°C (empty symbols) for 0.5 – 24 hours. Results for Si are calculated for oxidation in air from rate constants provided by Deal and Grove [107].

7.3.3. 67 at% Si-Y Alloy

The as-processed 67 at% Si-Y alloy contained the equilibrium YSi_2 phase, minor amounts of a non-equilibrium Si phase and surface cracks (Figure 7.7 – Figure 7.9). Diffraction peaks at 2θ angles of $37.15°$ and $43.61°$ were not identified (Figure 7.8 & Figure 7.9). Excellent agreement was found between the phase composition identified by EDS and EELS analysis, both of which were consistent with XRD results. Despite the controversy in literature on the existence of the YSi_2 phase, the authors are confident the YSi_2 phase is present in the alloy based on the agreement between EDS, EELS and XRD results. The 67 at% Si-Y alloy was oxidized in air for 0.5, 3 and 24 hours at 1000°C and 1200°C. Macro images of specimens before and after oxidation in air for 3 hours at 1000°C and 1200°C are shown in Figure 7.10. The variety of colors in the oxide scale on each specimen indicates that a multi-phase oxide or an oxide with non-uniform surface coverage had formed (Figure 7.10c, d). Cross-sections of each specimen show that the oxide layer is thin and did not consume a significant amount of the bulk alloy (Figure 7.10e, f). A portion of the specimen oxidized at 1200°C broke off due to oxidation which occurred along a crack.
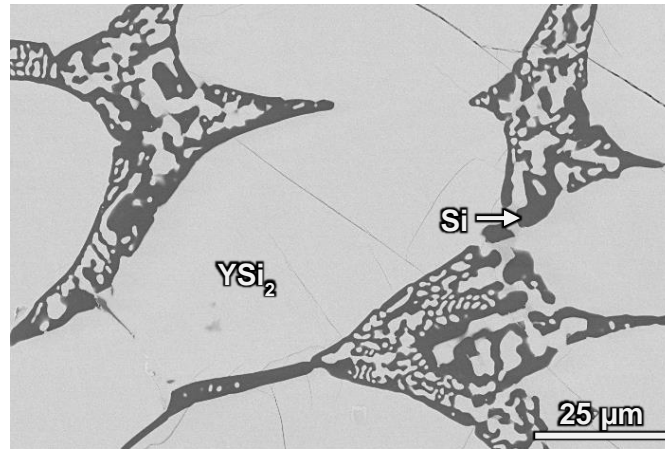
Figure 7.7. BSE/SEM image of as-processed 67 at% Si-Y alloy showing the presence of the equilibrium YSi_2 phase, minor amounts of a non-equilibrium Si phase and surface cracks.
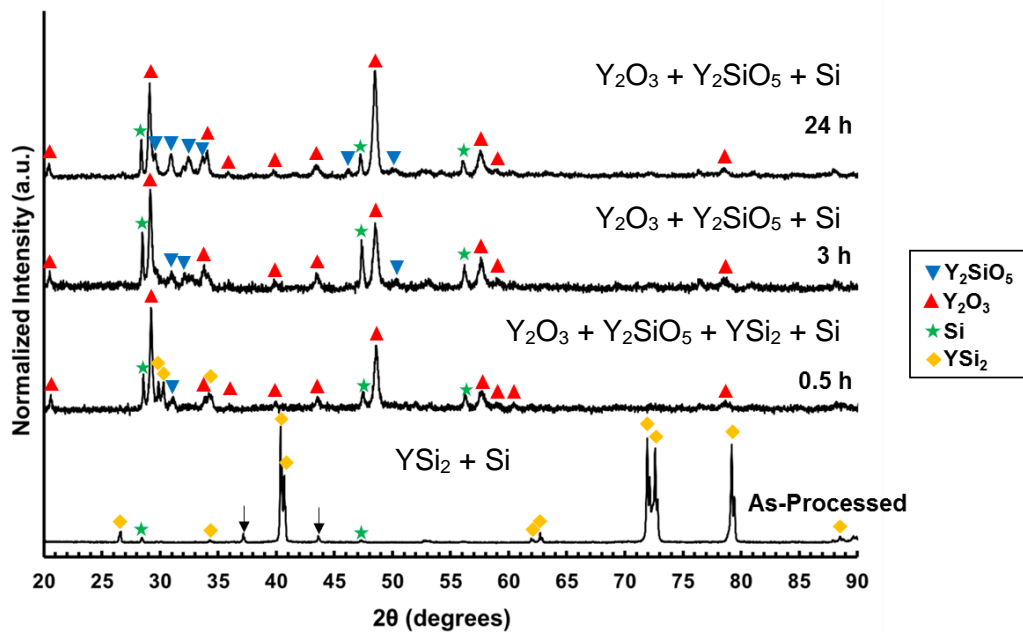
Figure 7.8. XRD of the 67 at% Si-Y alloy before and after oxidation in air for 0.5, 3 and 24 hours at 1000°C. Arrows indicate an unidentified phase.
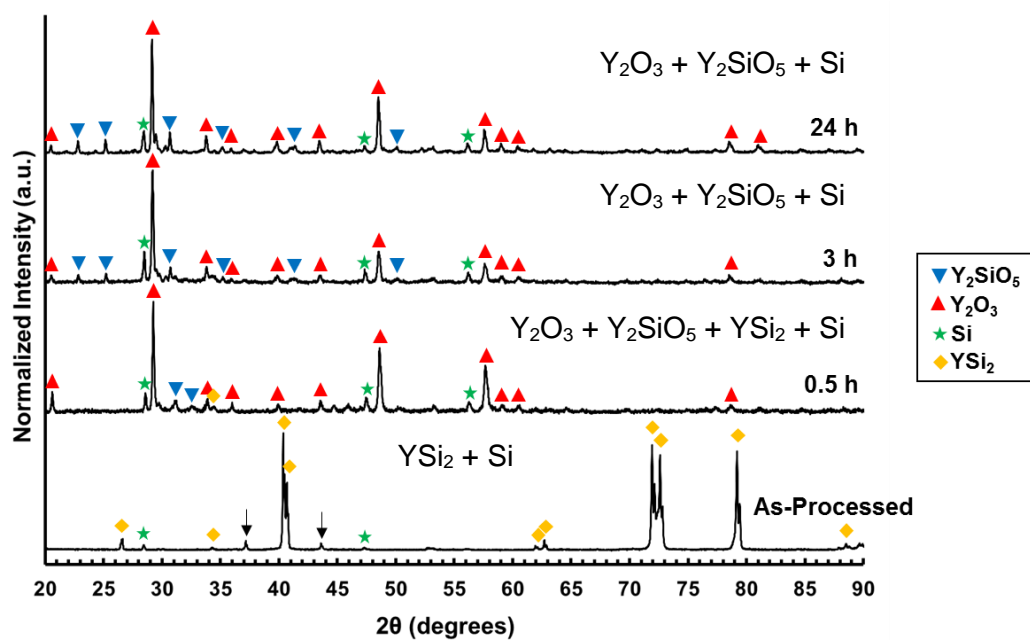
Figure 7.9. XRD of the 67 at% Si-Y alloy before and after oxidation in air for 0.5, 3 and 24 hours at 1200°C. Arrows indicate an unidentified phase.
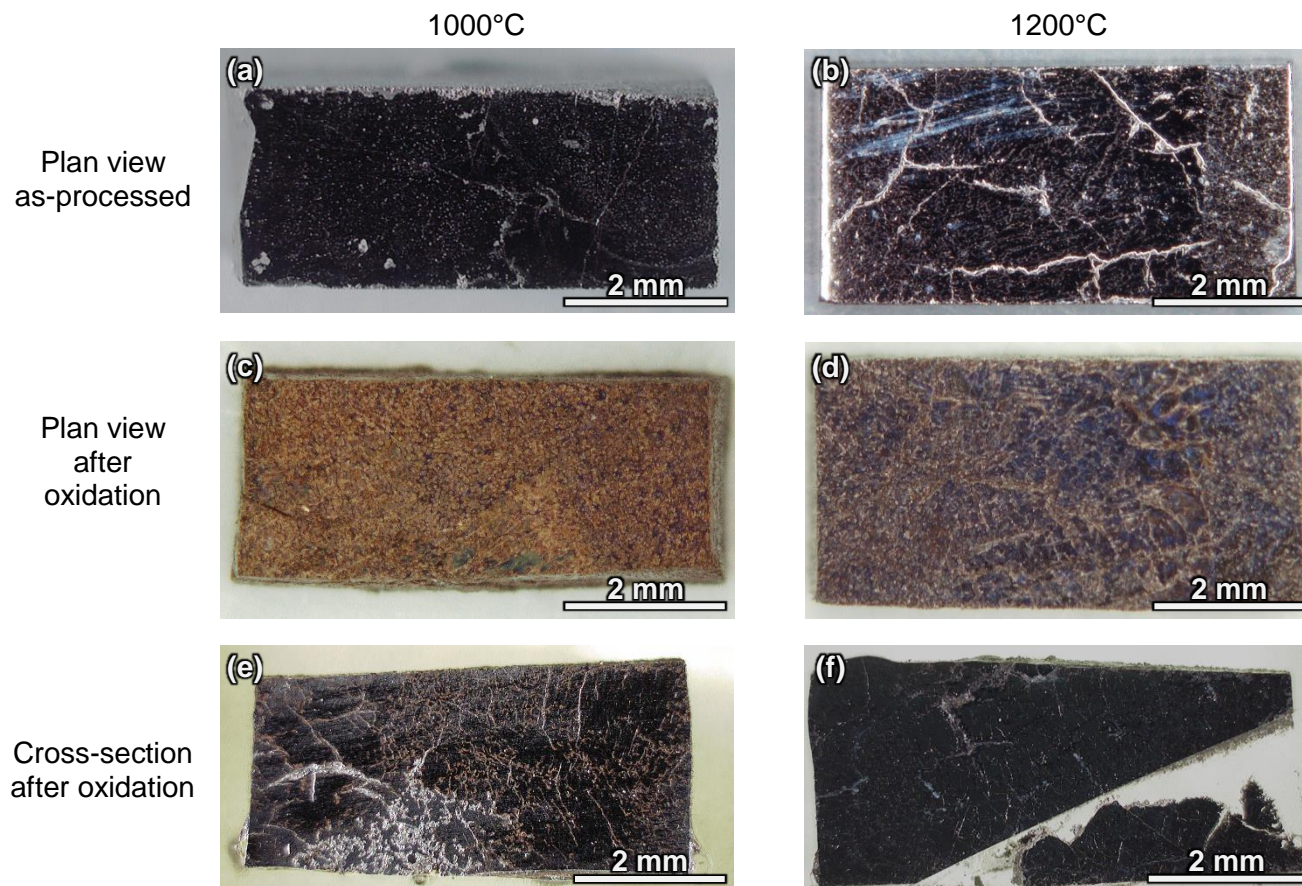
Figure 7.10. Macro images of the 67 at% Si-Y specimens before and after oxidation in air for 3 hours at 1000°C (a, c, e) and 1200°C (b, d, f). As-processed plan view (a,b), after oxidation plan view (c,d) and after oxidation cross-section (e,f).

Y_2O_3 and Y_2SiO_5 were identified by XRD analysis as the major and minor oxide phases respectively present after oxidation at 1000°C and 1200°C for all times (Figure 7.8 & Figure 7.9). The non-oxide phases of YSi_2 and Si were identified for specimens oxidized for 0.5 hours while only Si was identified for specimens oxidized for 3 and 24 hours.

SEM and EDS surface characterization of all specimens oxidized at 1000°C and 1200°C showed that the surface is comprised of large Y-Si-O regions which are surrounded by regions of SiO_2 (Figure 7.11a,d,g & Figure 7.12a,d,g). EDS analysis showed that the Y-Si-O regions have a Y:Si ratio of ~3 – 4: 1 indicating this is not an equilibrium phase from the $Y_2O_3 – SiO_2$ system (Figure 1.3). This result is confirmed by TEM analysis of cross-sections as described below. The Y-Si-O and SiO_2 have grown on top of the YSi_2 and Si regions respectively from the as-processed alloy. A significant amount of surface cracks formed in the Y-Si-O regions where some cracks spanned from the Y-Si-O regions into the surrounding SiO_2 regions. In addition, voids formed along the interface of the Y-Si-O regions and surrounding SiO_2.

SEM characterization of cross-sectioned specimens that were oxidized at 1000°C and 1200°C shows that a layered oxide has formed (Figure 7.11b,c,e,f,h,i & Figure 7.12b,c,e,f,h,i). Y_2O_3 was the major oxide phase present at all temperatures and times. The Y_2O_3 layer contained pockets of Si after oxidation at 1000°C whereas the specimens oxidized at 1200°C had a Si-free Y_2O_3 layer. The thickness of the Y_2O_3 layer increased with time from 0.5 to 3 hours while no apparent increase in thickness was observed from 3 to 24 hours. No quantitative measurements were made on the Y_2O_3 layer thickness due to its non-uniform nature. TEM characterization of a Si pocket in the Y_2O_3 layer on a specimen oxidized at 1000°C for 0.5 hours shows that a non-crystalline layer separates the Si pocket from the surrounding Y_2O_3 (Figure 7.13a,b). EFTEM elemental maps show that oxygen surrounds the pocket of Si indicating that the non-crystalline layer separating the Si pocket from the surrounding Y_2O_3 is amorphous SiO_2 (Figure 7.13c-f).
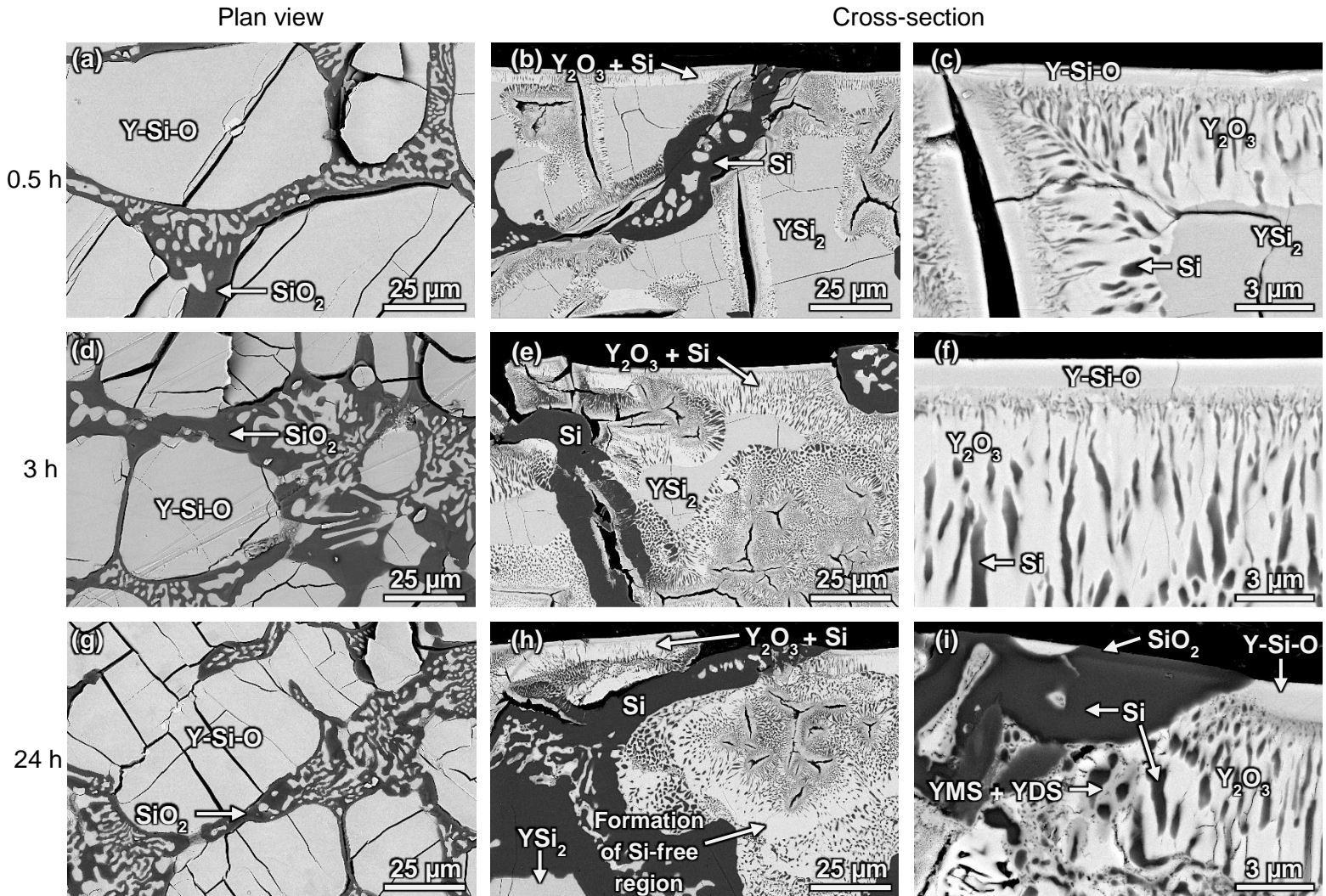
Figure 7.11. BSE/SEM surface (a, d, g) and cross-section (b, c, e, f, h, i) images of the 67 at% Si-Y specimens after oxidation in air for 0.5 (a, b, c), 3 (d, e, f) and 24 hours (g, h, i) at 1000°C.
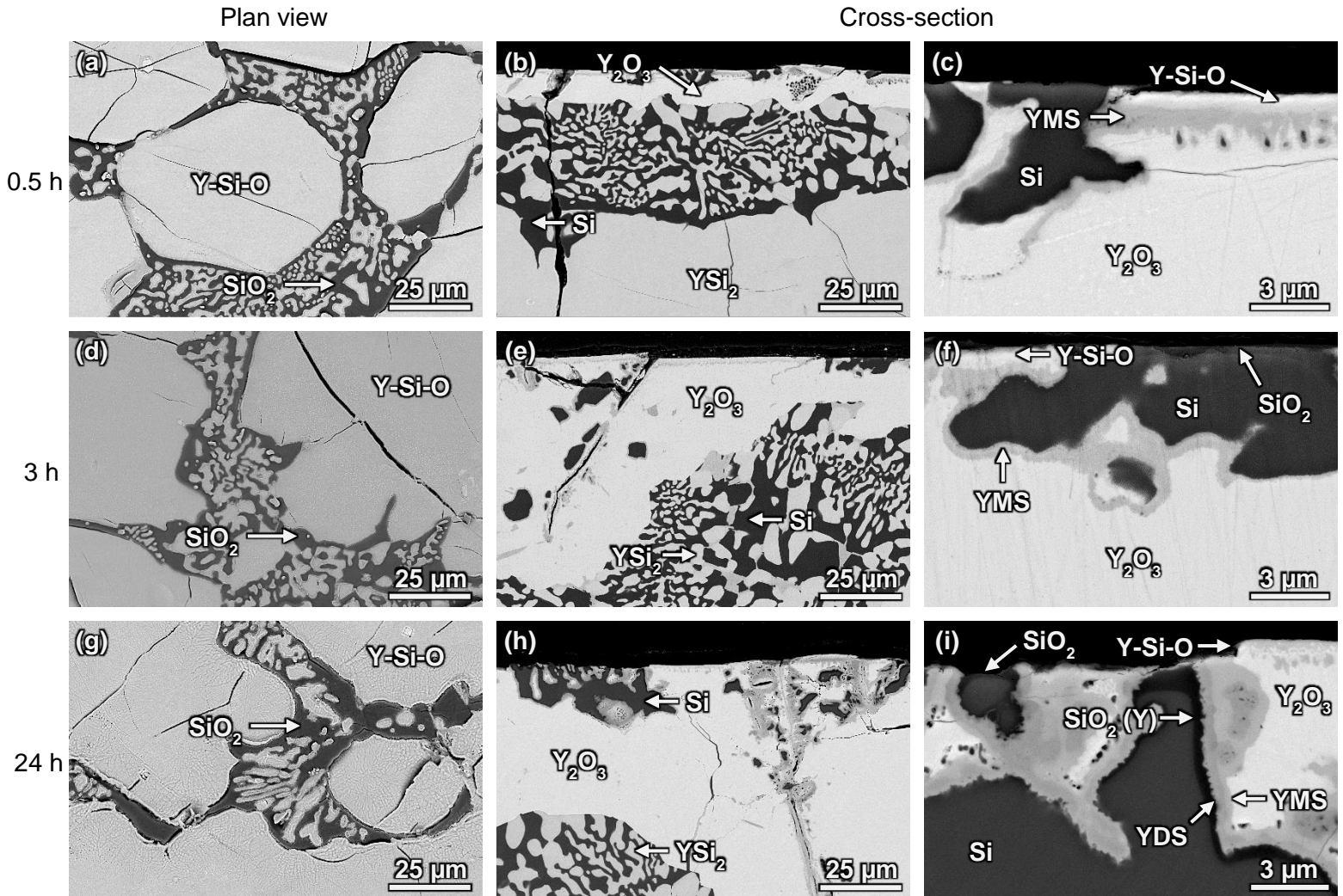
Figure 7.12. BSE/SEM surface (a, d, g) and cross-section (b, c, e, f, h, i) images of the 67 at% Si-Y specimens after oxidation in air for 0.5 (a, b, c), 3 (d, e, f) and 24 hours (g, h, i) at 1200°C.
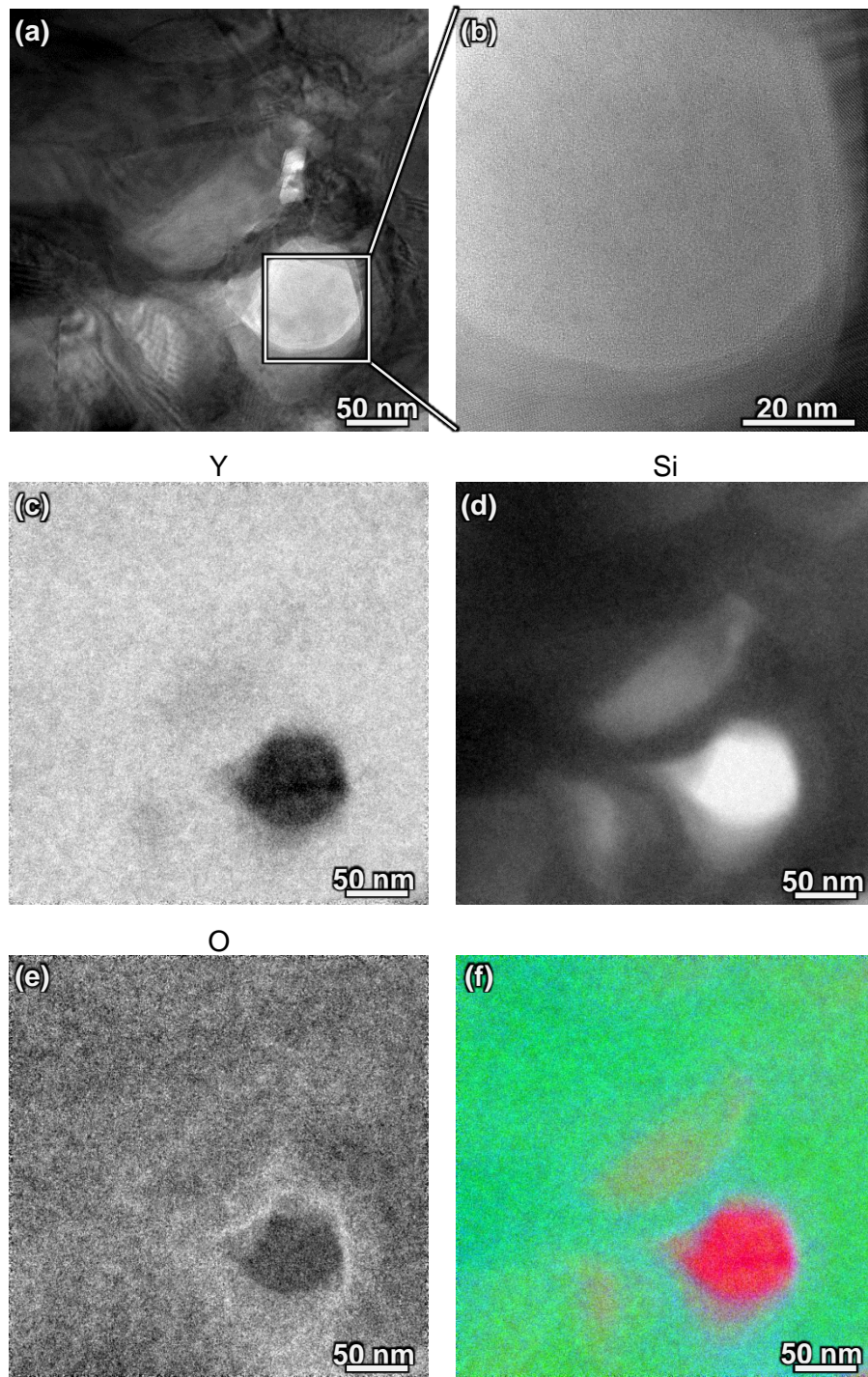
Figure 7.13. TEM images showing an amorphous ring around a pocket of Si in Y_2O_3 on a 67 at% Si-Y specimens after oxidation in air at 1000°C for 0.5 hours. (a, b). EFTEM elemental maps show Y (c), Si (d) and O (e) in the oxide layer. Greater intensity in the EFTEM elemental map indicates a higher concentration of the elemental species. The Y (green), Si (red) and O (blue) element maps have been combined in (f) to show the amorphous ring observed in (a,b) is SiO_2.

SEM and EDS characterization shows that a thin Y-Si-O surface layer (~0.25 – 2 µm) containing a Y:Si ratio of ~3 – 5: 1 formed at the surface above Y_2O_3 regions and along the borders of subsurface cracks after oxidation at 1000°C and above Y_2O_3 and Y_2SiO_5 regions at 1200°C (Figure 7.11c,f,i & Figure 7.12c,f,i). These Y:Si ratios are similar to those from the surface EDS analysis. Y-Si-O layers were thicker on specimens oxidized at 1000°C. The Y-Si-O layer thickness decreased with increasing time on specimens oxidized at 1200°C. TEM characterization shows the Y-Si-O layer is crystalline as it is comprised of grains with various orientations (Figure 7.14).
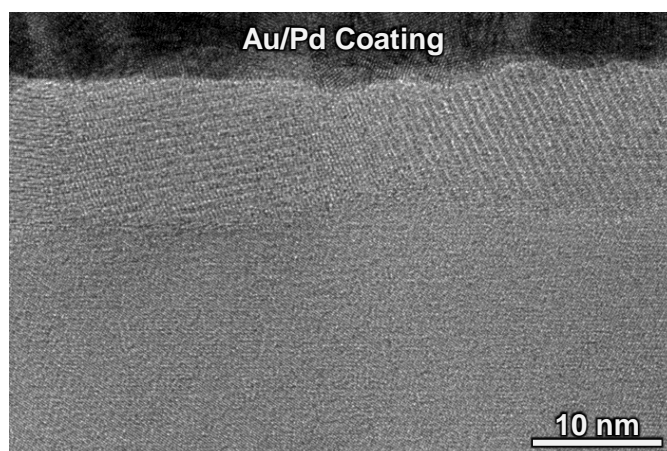
Figure 7.14. TEM image confirming the crystallinity of the Y-Si-O layer on a 67 at% Si-Y specimens after oxidation in air at 1000°C for 0.5 hours.

SEM characterization shows Y_2SiO_5 surrounded regions of pure Si at all temperatures and times. $Y_2Si_2O_7$ and a SiO_2 layer containing $\sim 2 – 8$ at% Y (SiO_2 (Y)) bordered regions of pure Si after oxidation for 24 hours (Figure 7.11i, Figure 7.12i, Figure 7.15). An EDS elemental concentration profile for Y, Si and O that was acquired along a phase boundary below the

specimen surface on a specimen oxidized for 24 hours at 1200°C shows that a layered oxide of SiO_2 (Y), $Y_2Si_2O_7$, Y_2SiO_5 and Y_2O_3 has formed (Figure 7.15). A SiO_2 scale grew on top of the pure Si regions that were present at the specimen surface for specimens oxidized at 1000°C for 24 hours and at 1200°C for 3 and 24 hours (Figure 7.11i & Figure 7.12f,i). Specimens oxidized at 1000°C contained a greater amount of subsurface cracks compared to specimens oxidized at 1200°C. YSi_2 and Si from the as-processed alloy were observed directly beneath the layered oxide scale (Figure 7.11b,e,h & Figure 7.12b,e,h).
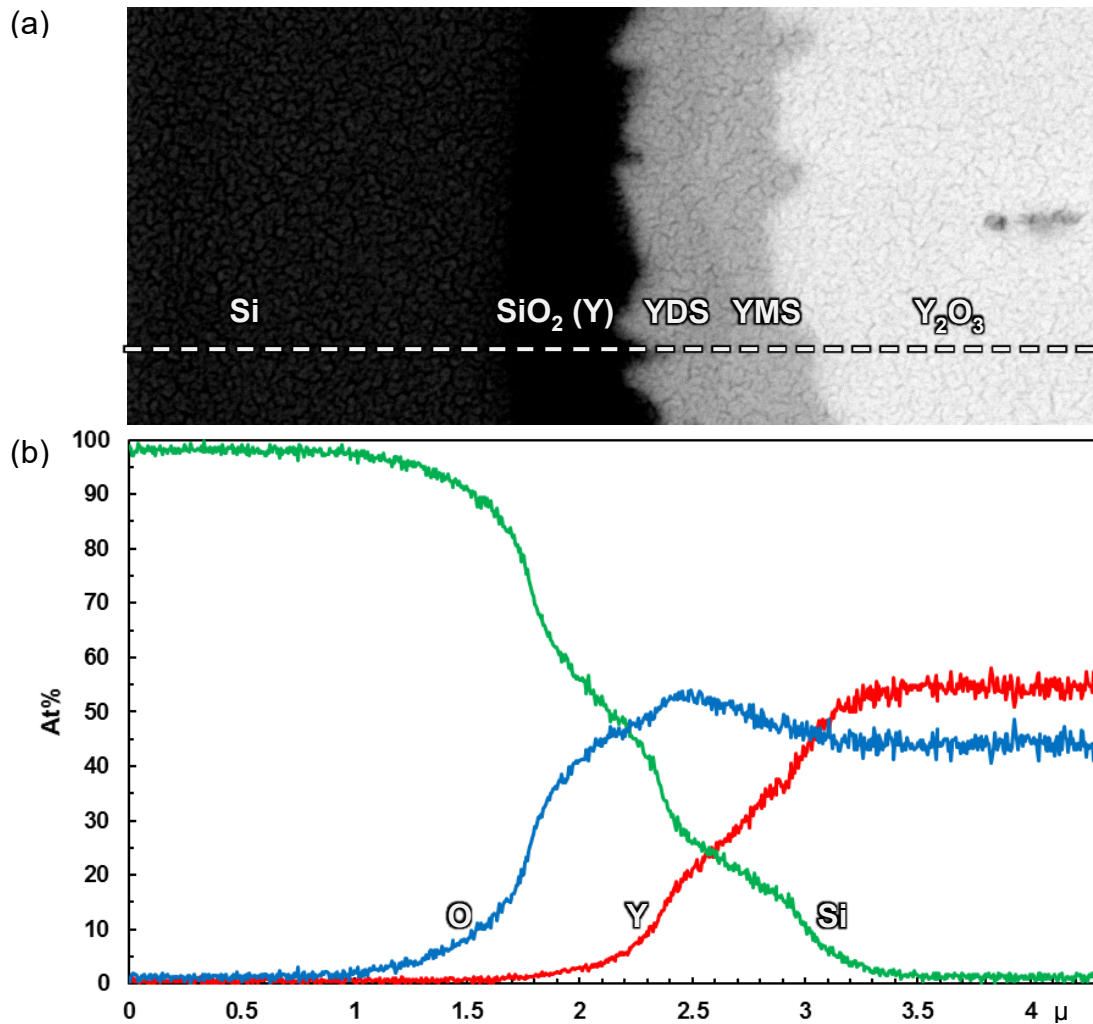
Figure 7.15. BSE/SEM cross-section image of the 67 at% Si-Y alloy specimen after oxidation in air for 24 hours at 1200°C (a) and the corresponding EDS elemental concentration profile for Y (red), Si (green) and O (blue) that was acquired along the dotted line (b).

Surprisingly, specimens oxidized at 1000°C had a greater specific weight change than those oxidized at 1200°C (Figure 7.6). The average specific weight change was found to slow with time for both oxidation temperatures. These specific weight changes are $1 - 2$ orders of magnitude greater than those predicted from the results of Deal and Grove [107] for the oxidation of pure Si. Specific weight changes for all specimens can be found in Appendix N.

7.3.4. 95 at% Si-Y Alloy

The as-processed 95 at% Si-Y alloy contained the equilibrium YSi_2 and Si phases (Figure 7.16 – Figure 7.18). Phase composition identified by EDS analysis was consistent with XRD results. The 95 at% Si-Y alloy was oxidized in air for 0.5, 3 and 24 hours at 1000°C and 1200°C. Macro images of specimens before and after oxidation in air for 3 hours at 1000°C and 1200°C are shown in Figure 7.19. The colored surface on each specimen after oxidation indicates that an oxide scale has grown (Figure 7.19c, d). The microstructure of the as-processed alloy can be seen where the dark regions on the specimen surface are the oxide that formed on YSi_2 while the colored regions are the oxide that formed on the Si. The oxide scale was not observable in the cross-section macro images (Figure 7.19e, f).
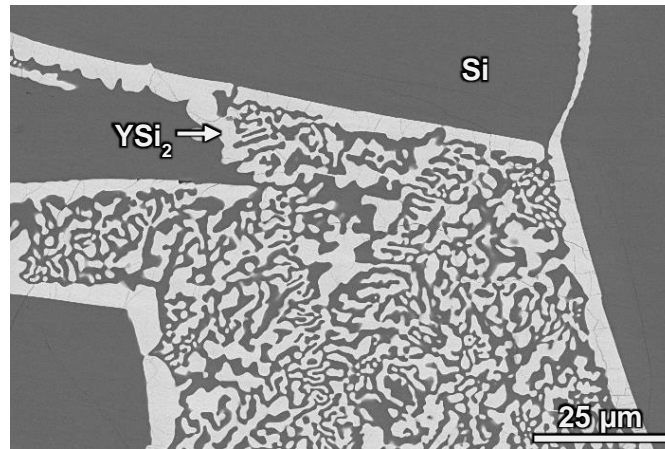
Figure 7.16. BSE/SEM image of as-processed 95 at% Si-Y alloy showing the presence of the equilibrium YSi_2 and Si phases.
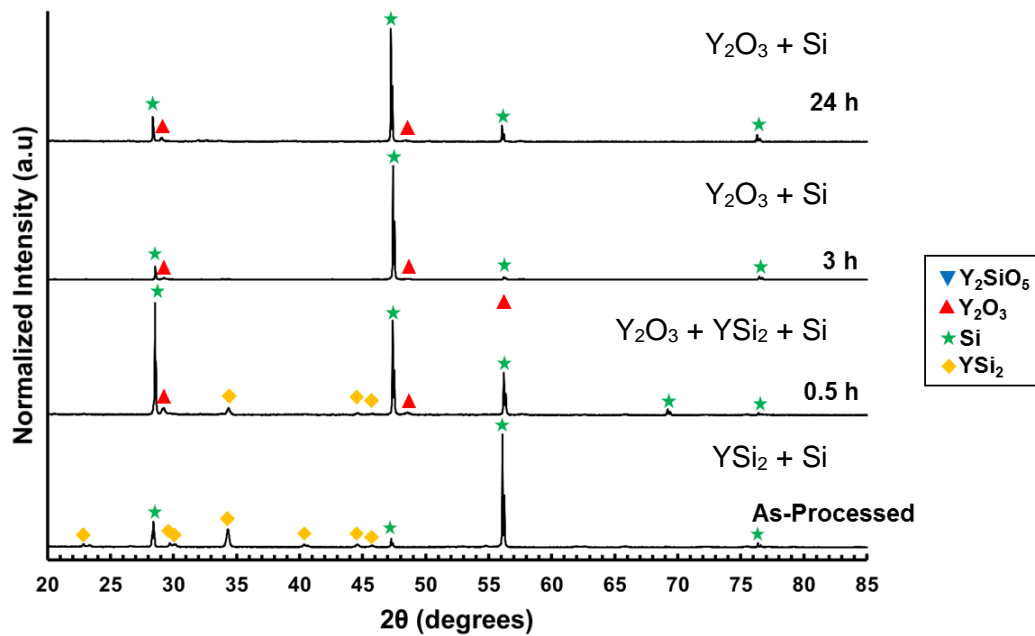
Figure 7.17. XRD of the 95 at% Si-Y alloy before and after oxidation in air for 0.5, 3 and 24 hours at 1000°C.

191
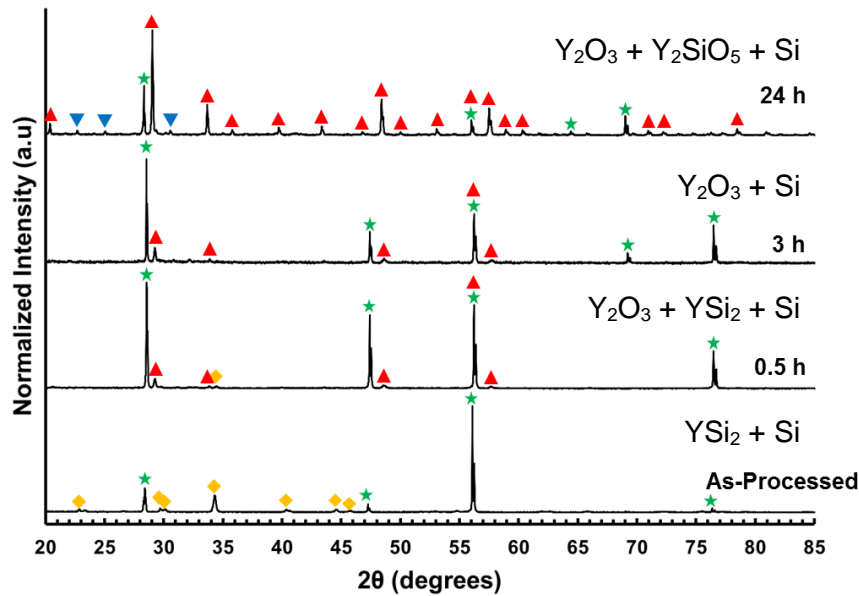
Figure 7.18. XRD of the 95 at% Si-Y alloy before and after oxidation in air for 0.5, 3 and 24 hours at 1200°C.
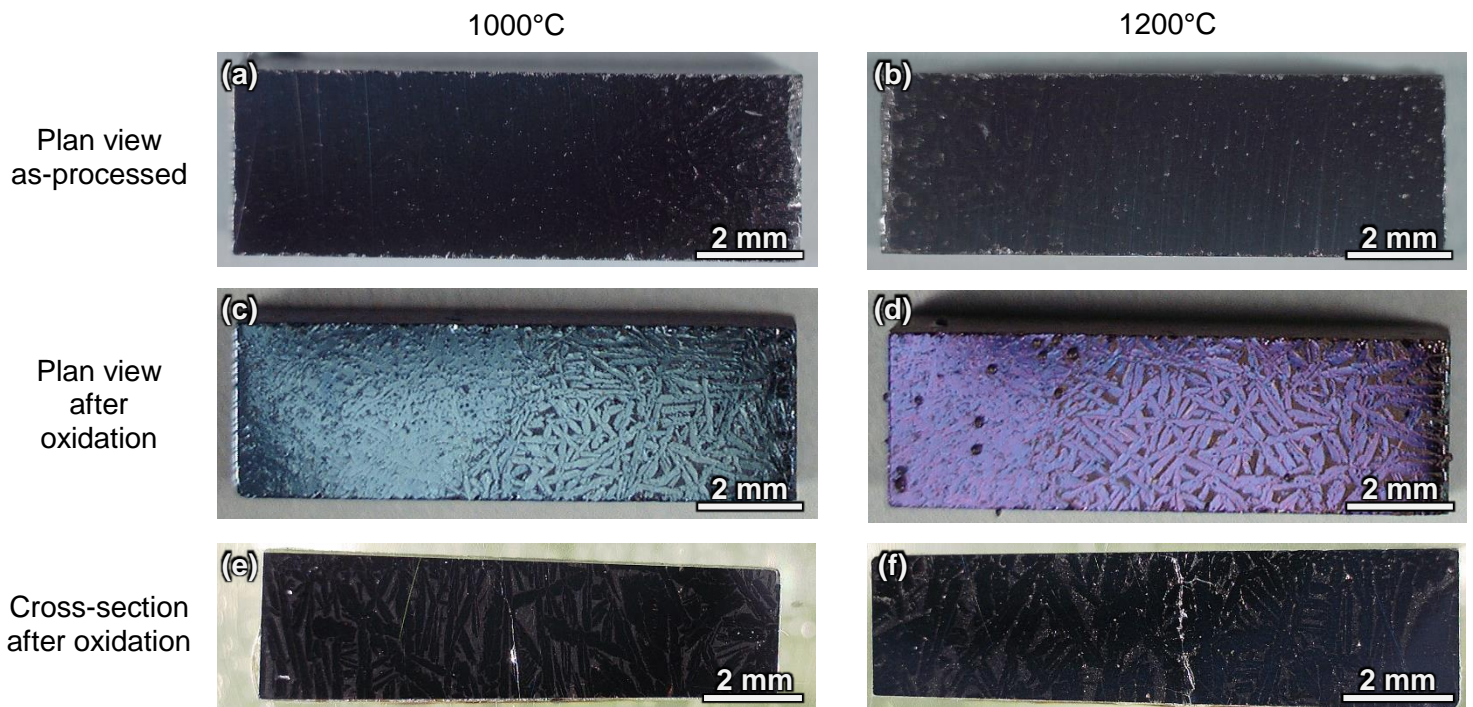
Figure 7.19. Macro images of the 95 at% Si-Y specimens before and after oxidation in air for 3 hours at 1000°C (a, c, e) and 1200°C (b, d, f). As-processed plan view (a,b), after oxidation plan view (c,d) and after oxidation cross-section (e,f).

Y_2O_3 was identified by XRD analysis as the major oxide phase present after oxidation at 1000°C and 1200°C for all times (Figure 7.17 & Figure 7.18). Y_2SiO_5 was identified as a minor oxide phase after oxidation at 1200°C for 24 hours. The non-oxide phases of YSi_2 and Si were identified for specimens oxidized for 0.5 hours while Si was identified for specimens oxidized for 3 and 24 hours.

SEM and EDS surface characterization of all specimens oxidized at 1000°C and 1200°C showed that a multi-phase oxide formed that consisted of Y-Si-O and SiO_2 (Figure 7.20 & Figure 7.21). EDS analysis showed that the Y-Si-O regions have Y:Si ratios that range from ~1 – 3: 1 indicating that some $Y_2Si_2O_7$ and Y_2SiO_5 may be present. The Y-Si-O and SiO_2 have grown on top of the YSi_2 and Si regions respectively from the as-processed alloy after oxidation at 1000°C for all times and at 1200°C for 0.5 hours (Figure 7.20 & Figure 7.21a, b). The growth of the Y-Si-O phase was observed to extend beyond the YSi_2 regions and into the surrounding SiO_2 after oxidation at 1200°C for 3 and 24 hours (Figure 7.21d – h). SiO_2 (Y) containing ~ 2 – 11 at% Y was observed to form along the Y-Si-O – SiO_2 interface at all temperatures and times. Minimal surface cracking was observed on all oxidized specimens.
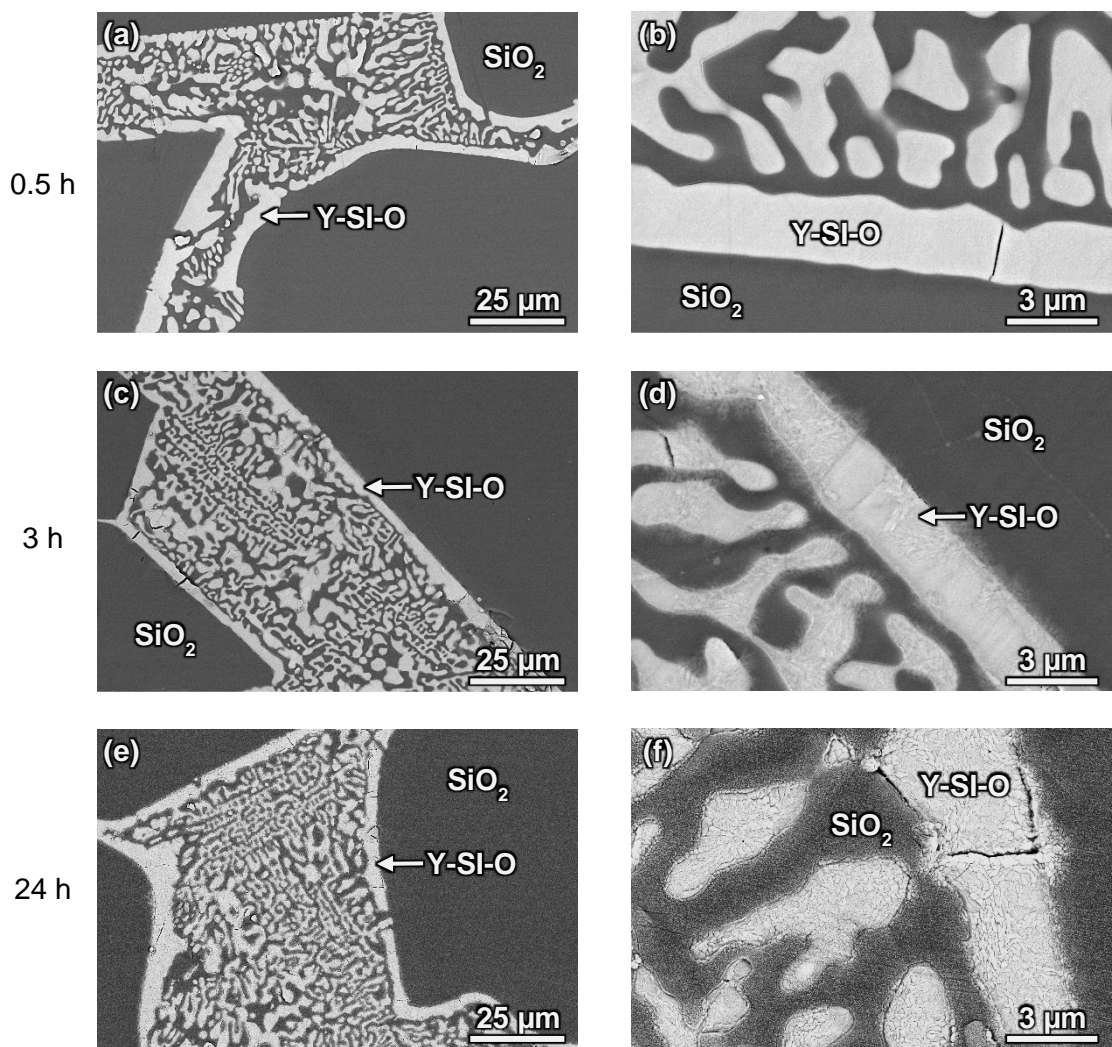
Figure 7.20. BSE/SEM surface images of the 95 at% Si-Y alloy specimens after oxidation in air for 0.5 (a, b), 3 (c, d) and 24 hours (e, f) at 1000°C.
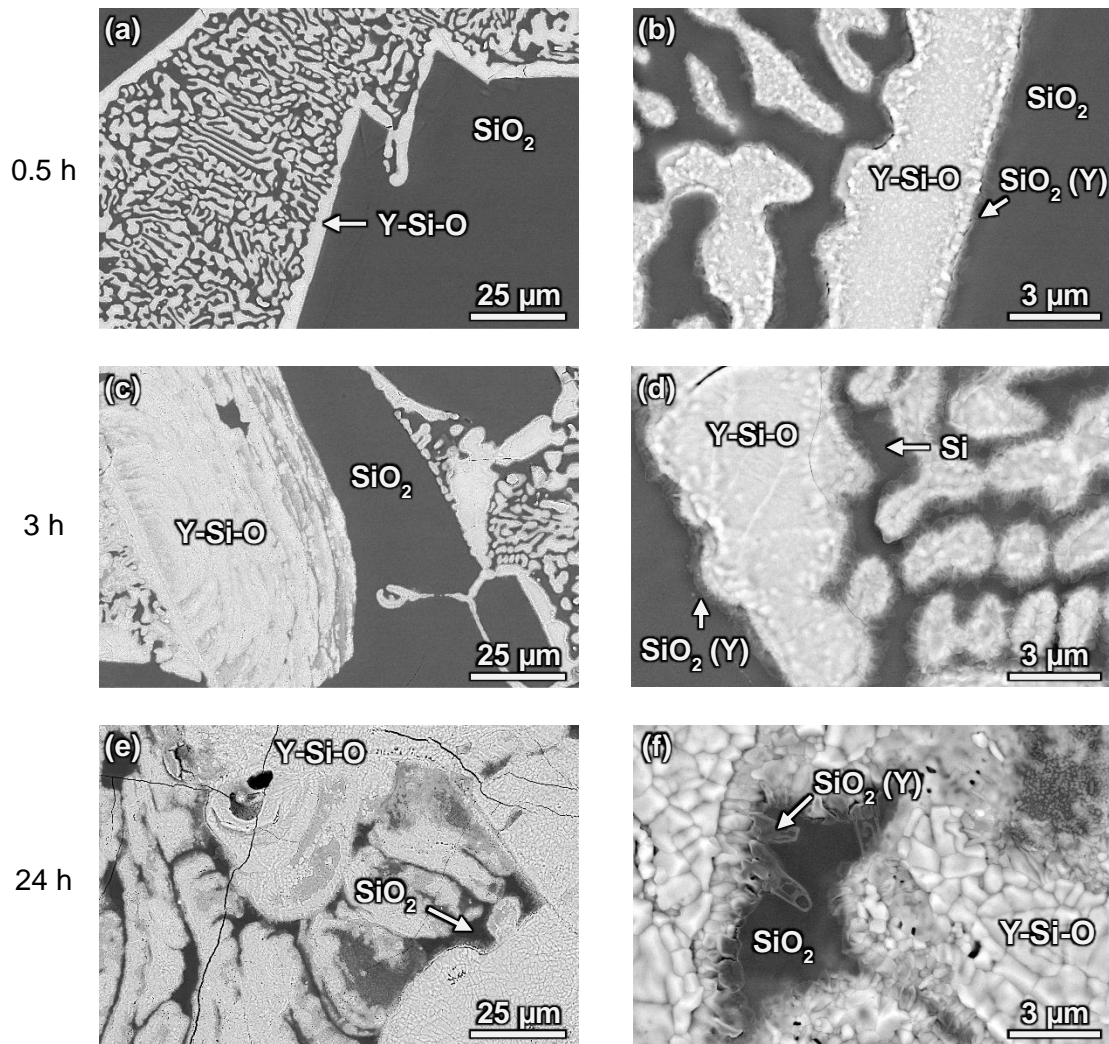
Figure 7.21. BSE/SEM surface images of the 95 at% Si-Y alloy specimens after oxidation in air for 0.5 (a, b), 3 (c, d) and 24 hours (e, f) at 1200°C.

SEM characterization of cross-sectioned specimens that were oxidized at 1000°C and 1200°C are shown in Figure 7.22 & Figure 7.23. Y_2O_3 was the major oxide phase present at all temperatures and times while minor amounts of Y_2SiO_5, $Y_2Si_2O_7$, Y-Si-O and SiO_2 (Y) were

also observed. The Y_2O_3 layer contained pockets of Si after oxidation at 1000°C whereas the specimens oxidized at 1200°C had a Si-free Y_2O_3 layer. These observations are similar to those made for the oxidized 67 at% Si-Y alloy. The microstructure of the as-processed alloy was still present after oxidation at 1000°C for all times (Figure 7.22). The yttrium- containing oxides that formed during oxidation were observed to grow from the YSi_2 regions while SiO_2 grew on the Si regions. The yttrium-containing oxides also grew from the YSi_2 regions at 1200°C however the microstructure of the as-processed alloy was observed to coarsen after 0.5 and 3 hours (Figure 7.23a, d). A large subsurface YSi_2 depletion zone and a thick Y_2O_3 scale at the surface were observed after 24 hours of oxidation (Figure 7.23g-i). These results indicate that the diffusion of yttrium in silicon is significantly greater at 1200°C than at 1000°C. The thickness of the Y_2O_3 layer increased with time for the specimens oxidized at 1200°C. Y_2SiO_5 formation was observed near the surface of the specimen and surrounding regions of pure Si at all temperatures and times. $Y_2Si_2O_7$ and a SiO_2 (Y) layer containing ~ 2 – 11 at% Y were found to border regions of pure Si after 24 hours of oxidation (Figure 7.22 & Figure 7.23i). A SiO_2 scale grew on top of the pure Si regions that were present at the specimen surface for specimens oxidized at 1200°C for 3 and 24 hours (Figure 7.23f,i). Subsurface cracks were observed in regions that formed yttrium containing oxides after oxidation at all temperatures and times. YSi_2 and Si from the as-processed alloy were also observed beneath the oxide scale after oxidation at all temperatures and times (Figure 7.22 & Figure 7.23).
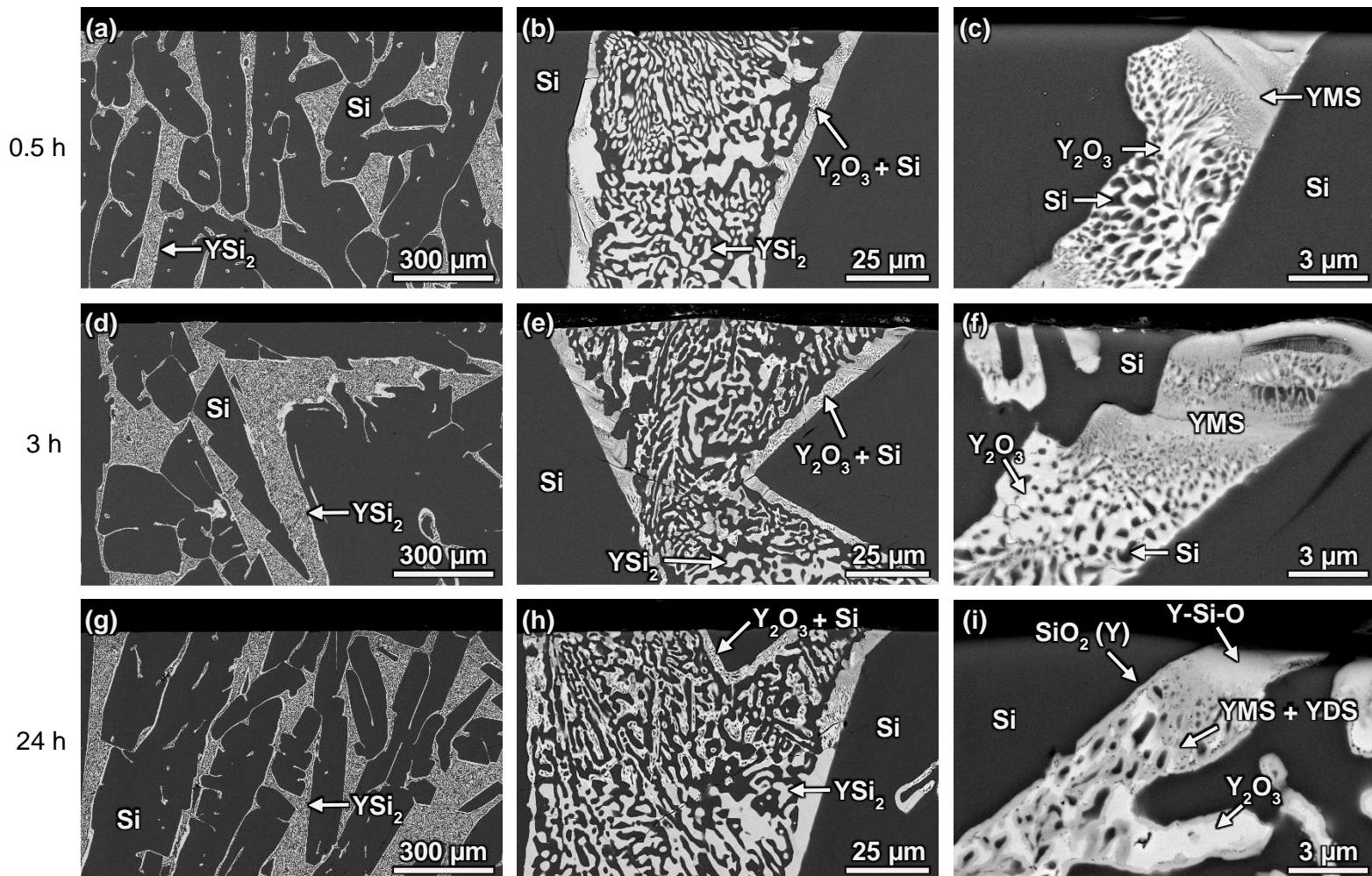
Figure 7.22. BSE/SEM cross-section images of the 95 at% Si-Y alloy specimens after oxidation in air for 0.5 (a-c), 3 (d-f) and 24 hours (g-i) at 1000°C.
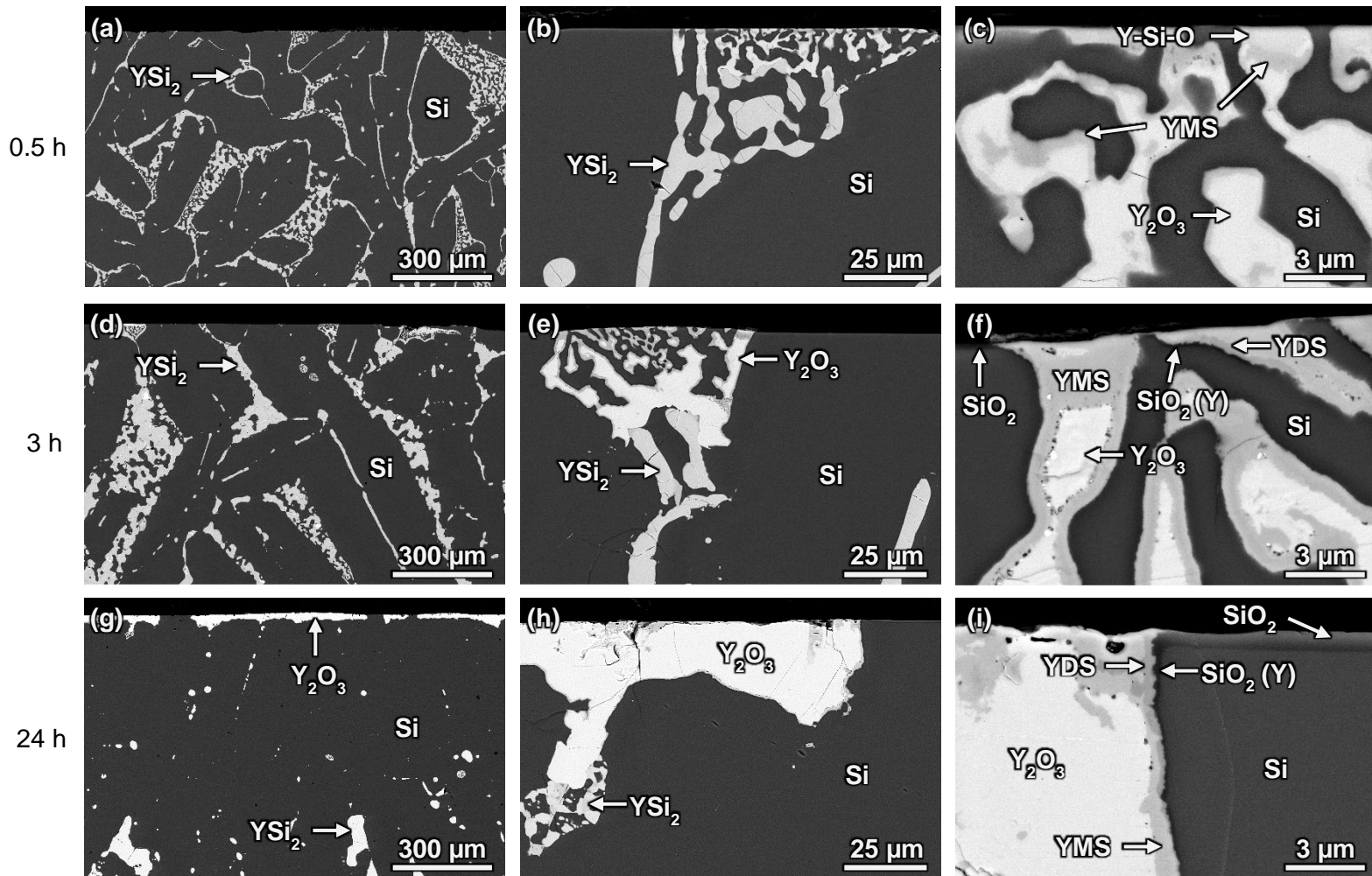
Figure 7.23. BSE/SEM cross-section images of the 95 at% Si-Y alloy specimens after oxidation in air for 0.5 (a-c), 3 (d-f) and 24 hours (g-i) at 1200°C.

Specimens oxidized at 1200°C were found to have a greater specific weight change than those oxidized at 1000°C with the exception of specimens oxidized for 0.5 hours (Figure 7.6). The average specific weight change was found to slow with time at both oxidation temperatures. These specific weight changes are slightly greater than that those predicted from the results of Deal and Grove [107] for the oxidation of pure Si at 1000°C and slightly less that of pure Si at

1200°C for nearly all oxidation times. Specific weight changes for all specimens can be found in Appendix N.

7.4. Discussion

7.4.1. Thermodynamic Calculations

Thermodynamic calculations using FactSage [108] did not predict all the oxide phases that were observed after oxidation at 1000°C and 1200°C. The formation of Y_2O_3 at both temperatures was accurately predicted however the presence of Y_2SiO_5 and $Y_2Si_2O_7$ was not.

The oxidation of a yttrium silicide results in the selective oxidation of yttrium to form Y_2O_3 and rejected silicon (Equation (7.1)).

$$a \cdot Y_2O_3 + \frac{3(a \cdot x)}{4} O_2(g) \rightarrow \frac{(a \cdot x)}{2} Y_2O_3 + (a \cdot y) \, Si \qquad (7.1)$$
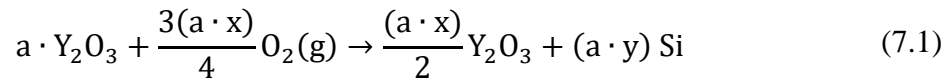
The presence of rejected silicon after the oxidation of a yttrium silicide was not predicted by FactSage. Instead, FactSage predicted that as each silicide oxidized to form Y_2O_3, more Si-rich silicides on the phase diagram would also form. This was only observed for the 41 at% Si-Y alloy after oxidation at 1000°C as determined by XRD analysis (Figure 7.2). We hypothesize that Y_2SiO_5 and $Y_2Si_2O_7$ are not formed from the oxidation of a yttrium silicide but rather from a reaction between the oxides of Y_2O_3 and SiO_2, consistent with the $Y_2O_3 - SiO_2$ phase diagram (Figure 1.3) and FactSage predictions. The Si on the $Y_2O_3 - Si$ phase boundary may oxidize due to oxygen diffusing through the Y_2O_3 scale or along the phase boundary itself. This results in the formation of a new phase boundary between Y_2O_3 and SiO_2 where the reactions to form Y_2SiO_5 and $Y_2Si_2O_7$ may take place. The diffusion mechanisms that control the formation of these oxides will be discussed in Section 7.4.3.

7.4.2. Specific Weight Change

7.4.2.1. Temperature Dependence

The specific weight change of the 41 at% Si-Y alloy increased with oxidation temperature. The large scatter in the specific weight change results is attributed to the extensive specimen cracking that occurred during oxidation. Specimens were observed to completely and partially break apart at both 1000°C and 1200°C. The specific weight change of the 95 at% Si-Y alloy increased with increasing oxidation temperature with the exception of the 0.5 hour exposure (Figure 7.6).

In contrast, faster oxidation rates were observed at lower oxidation temperatures under some conditions indicating that a fast oxidation path dominated at low temperatures. These fast paths include a greater number of phase boundaries or cracks. The decrease in specific weight change of the 67 at% Si-Y alloy with increasing oxidation temperature is attributed to the greater number of surface and subsurface cracks present at 1000°C compared to 1200°C. A greater specific weight change for the 95 at% Si-Y was observed after oxidation for 0.5 hours at 1000°C compared to 1200°C. This may also be attributed to the decrease in surface accessible volume of YSi_2 with time at 1200°C due to microstructural coarsening. In addition, slower SiO_2 growth at 1000°C prevents the rapid sealing of cracks which will result in higher overall specific weight changes. The diffusion mechanisms that effect the microstructure and oxidation behavior of yttrium silicides will be discussed in Section 7.4.3.

7.4.2.2. Time Dependence
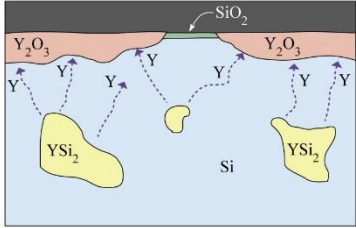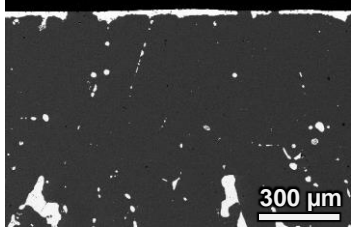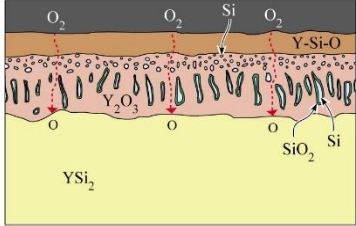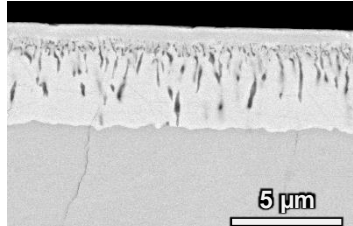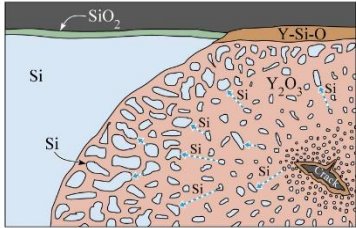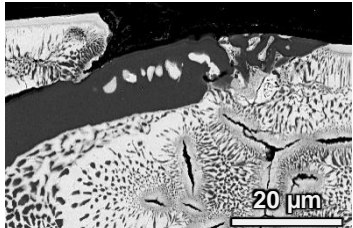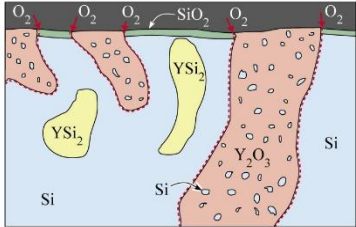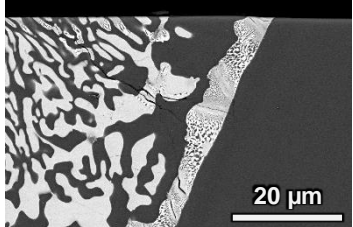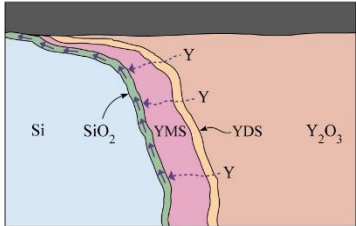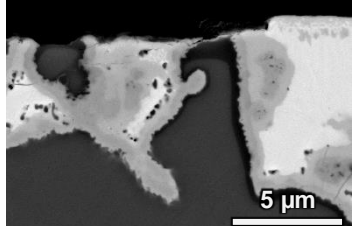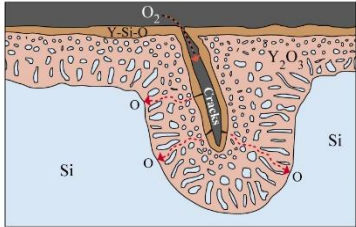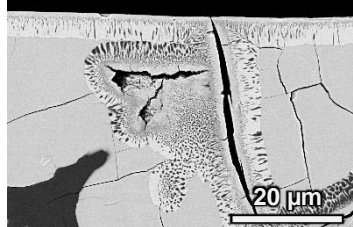
The specific weight change of the 67 and 95 at% Si-Y alloys increased with time at a decreasing rate after oxidation at both 1000°C and 1200°C. These results indicate that oxidation

is rate limited by a diffusion process in the oxide scale or in the alloy. The specific weight change of the 95 at% Si-Y alloy was slightly greater than that of pure Si at 1000°C and slightly less than that of pure Si at 1200°C for nearly all oxidation times. The authors currently do not have an explanation for this result.

7.4.3. *Diffusion Mechanisms that Control Oxide Microstructure and Growth*

The oxidation of yttrium silicides resulted in the diffusion of multiple species within oxides and the alloy. A summary of all the observed diffusing species is shown in Table 7.1. The diffusion mechanisms and their effect on the microstructure and oxidation rate of yttrium silicides will be discussed below.

Table 7.1. Summary of the observed diffusing species for each alloy at 1000°C and 1200°C.

Observed Diffusing Species X in phase Z (X_Z)	Alloy at 1000°C	Alloy at 1200°C	Illustration of Diffusion Mechanism	Example Micrograph
(a) Y_{Si}	n/a	**67**, **95**		
(b) O_{Y2O3}	**67**, **95**	n/a		
(c) Si_{Y2O3}	67, 95	n/a		
(d) $O_{phase\ boundaries}$	**95**	n/a		
(e) Y_{SiO2}	95	67, **95**		
(f) O_{cracks}	**41**, 67	**41**		

Compositions in bold indicate diffusing species may control oxide growth rate.
Example micrograph corresponds to the underlined composition.
Solid arrows serve as phase labels, dotted arrows indicate diffusing species.

202

7.4.3.1. *Formation and Growth of Y_2O_3*

All yttrium silicide specimens rapidly oxidized to form Y_2O_3 at 1000°C and 1200°C. The free energy of formation of Y_2O_3 (-1481 kJ/mol at 1200°C [160]) per mole of O_2 is greater than a factor of 2 more negative than that for SiO_2 (-649 kJ/mol at 1200°C). Additionally, the oxygen permeability in Y_2O_3 is ~2 orders of magnitude greater than that for SiO_2 (Figure 7.24) [161]. Therefore the formation of Y_2O_3 is both thermodynamically and kinetically more favorable than SiO_2 formation, consistent with the observations of this study.

It is important to note that the oxygen diffusivity in Y_2O_3 [105] is 7 – 8 orders of magnitude greater than SiO_2 (network exchange) [141] and similar to that for SiO_2 (permeation)[143] (Figure 5.23). The mechanism controlling the oxidation rate of Si at these temperatures is permeation of oxygen through SiO_2 [18, 107] which suggests the formation of Y_2O_3 is as kinetically favorable as SiO_2 formation. This is inconsistent with the observations of this study where Y_2O_3 forms significantly faster than SiO_2.

This inconsistency can be attributed to the fact that there is an oxygen chemical potential gradient present in the Y_2O_3 and SiO_2 scales as they form which acts as a driving force for oxygen to diffuse through the scale. The reported oxygen diffusion coefficients represent the self-diffusion of oxygen through the oxide scale without the presence of an oxygen chemical potential gradient. Therefore oxygen permeability in Y_2O_3 and SiO_2 is better suited to represent the oxygen transport kinetics during oxidation since permeability experiments are performed using an oxygen chemical potential gradient. Oxygen diffusion coefficients can still be used to assess the oxygen transport kinetics during oxidation since the oxygen permeability constant (P)

is equal to the product of the oxygen diffusion coefficient (D) and the solubility of oxygen in the oxide scale (S) (Equation (7.2)) [138].

$$P = DS \qquad\qquad (7.2)$$
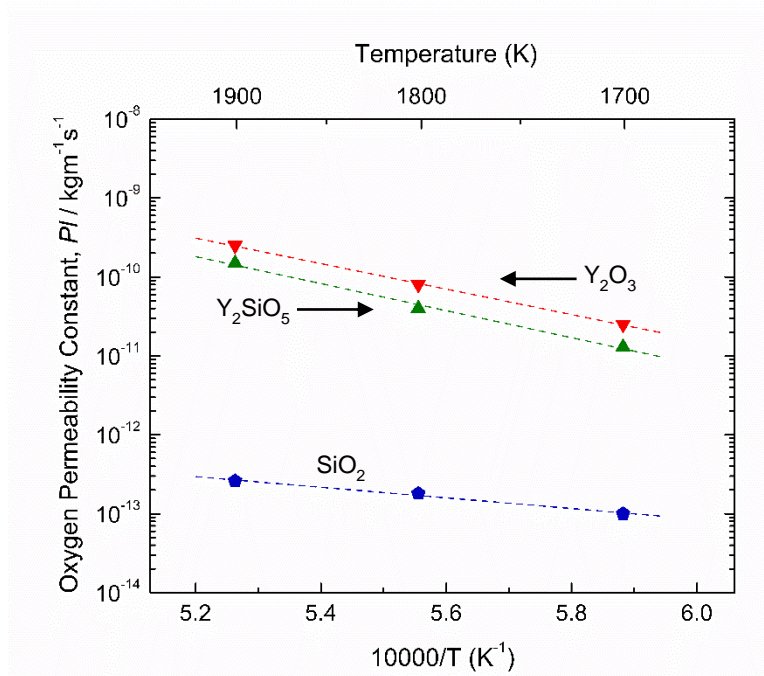
Figure 7.24. Oxygen permeability in Y_2O_3, Y_2SiO_5 and SiO_2 [161].

The formation of Y_2O_3 from yttrium silicides requires the selective oxidation of yttrium from the alloy and thus the growth rate of Y_2O_3 may be controlled by diffusion in the scale or in the alloy [162]. If the growth rate of Y_2O_3 were controlled by diffusion in the scale then Y_2O_3 would form at the same rate on yttrium silicides as it does on pure yttrium metal. Conversely, there would be significantly less Y_2O_3 formed on yttrium silicides than on pure yttrium metal if the growth rate were controlled by diffusion in the alloy. Oxidation studies of yttrium metal at $900 - 1400°C$ in air found that a fast growing Y_2O_3 scale formed that was rate limited by

diffusion of oxygen through the scale [88, 163]. The defect chemistry contributing to the transport of oxygen through Y_2O_3 is currently unknown.

In the current study, the increase in Y_2O_3 formation with increasing yttrium content in the alloy suggests that the growth rate of Y_2O_3 from yttrium silicides is controlled by yttrium diffusion in the alloy. However, the microstructural differences between the Y_2O_3 scale and the alloy beneath the Y_2O_3 scale after oxidation at 1000°C and 1200°C on the 67 and 95 at% Si-Y alloys indicate that there may be different rate limiting diffusion mechanisms that are controlling the growth of Y_2O_3. The regions of rejected Si and depleted YSi_2 directly beneath the dense Y_2O_3 scale on the 67 and 95 at% Si-Y alloys after oxidation at 1200°C (Figure 7.12 & Figure 7.23) indicate that the diffusion of yttrium to the metal/oxide interface is the rate limiting mechanism (Table 7.1a).

A different rate limiting mechanism may exist for the 67 and 95 at% Si-Y alloys at 1000°C since a dense region of YSi_2 is observed below the Y_2O_3 scale (Figure 7.11 & Figure 7.22) rather than regions of rejected Si and depleted YSi_2. The change in rate limiting mechanism may be attributed to the effects that the pockets of Si in the Y_2O_3 scale have on the diffusion of oxygen through Y_2O_3 at 1000°C. Oxygen diffusing through the Y_2O_3 scale oxidizes pockets of Si to form SiO_2 as shown in Figure 7.13. This results in a lower amount of oxygen that reaches the metal/oxide interface and thus a slower consumption of yttrium to form Y_2O_3. Therefore the diffusion of oxygen through the Y_2O_3 scale is the likely mechanism that is controlling the growth rate of Y_2O_3 at 1000°C for the 67 and 95 at% Si-Y alloys (Table 7.1b).

7.4.3.2.   Si Diffusion in Y_2O_3

All specimens oxidized at 1000°C formed a Y_2O_3 layer that contained a fine dispersion of pockets of rejected Si while specimens oxidized at 1200°C formed a Y_2O_3 layer that was

predominantly Si-free, however, some large isolated regions of Si were observed. The free Si in the Y_2O_3 layer is attributed to the Si that is rejected from yttrium silicides during oxidation to form Y_2O_3 (Equation (7.1)). Differences in the microstructure of Y_2O_3 at 1000°C and 1200°C must be attributed to the relative mobility of Si in Y_2O_3 at the respective temperatures under low $P(O_2)$ conditions. Ostwald ripening or "coarsening" of Si pockets with time resulted in the formation of Si-free regions of Y_2O_3 in specimens oxidized at 1000°C (Table 7.1c). The formation of Si-free regions in Y_2O_3 are best seen in the 67 at% Si-Y alloy after oxidation for 24 hours (Figure 7.11h). These results indicate that the reduction of interfacial free energy is the driving force for Si diffusion in Y_2O_3. The diffusion of Si in Y_2O_3 at 1200°C must be significantly greater than at 1000°C since very few Si pockets in the Y_2O_3 scale were observed at 1200°C. The transport mechanism for Si diffusion in Y_2O_3 is currently unknown. The diffusion of Si in Y_2O_3 does not appear to be a rate limiting mechanism for the growth of Y_2O_3.

7.4.3.3.   Oxide Formation along Phase Boundaries

The Si – YSi_2 phase boundaries of the as-processed alloy that were in contact with the specimen surface offered fast diffusion pathways for oxygen to penetrate to the interior Si and YSi_2 (Table 7.1d) resulting in the formation of subsurface SiO_2 and Y_2O_3. This diffusion mechanism appears to have significantly contributed to the rate at which the 95 at% Si-Y alloy oxidized at 1000°C, especially at short times (Figure 7.22). The creation of a SiO_2 – Y_2O_3 phase boundary establishes a diffusion couple between SiO_2 and Y_2O_3 leading to the formation of layered oxides: SiO_2 (Y), Y_2SiO_5 and $Y_2Si_2O_7$. The origin of yttrium in phase boundary SiO_2 can be attributed to Y that has diffused across the diffusion couple and dissolved in SiO_2 (Table 7.1e). The formation of the SiO_2 – Y_2O_3 diffusion couple is best seen in the 67 and 95 at% Si-Y alloys after oxidation for 24 hours at 1200°C (Figure 7.12i, Figure 7.15, Figure 7.23i). These

images show that the newly formed equilibrium phase boundaries between Y_2O_3, Y_2SiO_5, $Y_2Si_2O_7$ and SiO_2 appear in the same compositional sequence as the $Y_2O_3 - SiO_2$ phase diagram (Figure 1.3).

In many instances phase boundary SiO_2 (Y) and/or $Y_2Si_2O_7$ were not observed after oxidation while Y_2SiO_5 was observed for all compositions, temperatures and times. Based on predictions by FactSage the formation of Y_2SiO_5 cannot occur without the creation of a diffusion couple between SiO_2 and Y_2O_3, thus we hypothesize that phase boundary SiO_2 and $Y_2Si_2O_7$ must be very thin and could not be resolved by SEM.

7.4.3.4. *Yttrium Diffusion in Phase Boundary SiO₂*

The dissolved Y in phase boundary SiO_2 offers an additional method of supplying the surface with yttrium to form yttrium containing oxides (Table 7.1e). Similar observations have been made in oxidation studies of Si_3N_4 that contained Y_2O_3 sintering additives [154, 155]. The thermodynamic mechanism for cation diffusion through an amorphous intergranular phase in Si_3N_4 developed by Clarke [157] can be adapted for yttrium silicide oxidation and used to explain the transport of yttrium to the surface. An assumption has been made that the phase boundary SiO_2 is amorphous based on the result that shows the presence of an amorphous SiO_2 layer that surrounded a pocket of Si in the Y_2O_3 scale (Figure 7.13). The presence of dissolved Y creates a chemical potential gradient between the yttrium-rich amorphous SiO_2 phase boundary and the pure SiO_2 which forms on the surface during oxidation of the Si regions. The chemical potential gradient results in the diffusion of yttrium to the surface SiO_2 scale until the yttrium concentration is constant in both the phase boundary and at the surface. This situation cannot be achieved since SiO_2 is continually being formed at or below the surface. Finally, a crystalline yttrium containing oxide phase forms on the surface of the SiO_2 possibly due to the reduction in

free energy resulting from the formation of a more stable crystalline phase from an amorphous phase.

The supply of yttrium to the surface via phase boundary SiO_2 appears to significantly contribute to the growth of the Y-Si-O scale on the surface of the 95 at% Si-Y alloy after oxidation at 1200°C (Figure 7.21). The yttrium in the SiO_2 (Y) that borders regions of Y-Si-O oxidizes and reacts with SiO_2 to form more Y-Si-O which grows outward into the surrounding SiO_2. Cross-sections of the oxidized alloy show SiO_2 (Y) along phase boundaries that connect to the surface (Figure 7.23f,i). This SiO_2 (Y) was also observed in cross-sections of the 67 at% Si-Y alloy after oxidation at 1200°C (Figure 7.12i). The diffusion of yttrium to the surface via phase boundary SiO_2 does not appear to significantly contribute to the Y-Si-O oxide growth on the 67 at% Si-Y alloy since there are fewer regions of pure Si available to be oxidized at the surface. In addition, diffusion of phase boundary yttrium does not appear to contribute to the Y-Si-O growth on the 95 at% Si-Y alloy at the lower temperature, 1000°C, likely due to the slower dissolution rate of Y into SiO_2 and the slower oxidation rate of pure Si at the surface.

7.4.4. Crack Formation

The amount of cracks formed during oxidation increased with increasing yttrium content in the alloy and were predominantly observed in regions where Y_2O_3 had formed. These results indicate that growth stresses resulting from the rapid formation of internal Y_2O_3 were the primary cause of cracking and not the oxidation of surface Si. Volume differences between the oxide and the alloy (Table 1.2) and compositional changes in the alloy during oxidation (Equation (7.1)) are likely the predominant contributions to the growth stresses that lead to crack formation. Once a crack has formed, oxygen readily diffuses through it and oxidizes the alloy to form Y_2O_3 below the surface (Table 7.1f). Because the Y_2O_3 is confined, the volume increase associated with its

formation and growth imparts large stresses on the surrounding material which leads to further

crack formation and propagation. The extensive crack formation that occurred during oxidation

of the 41 at% Si-Y alloy at 1000°C and 1200°C indicates that the oxidation rate is dominated by

diffusion of oxygen through cracks. The cause of more extensive subsurface cracking at 1000°C

relative to 1200°C for all alloy compositions may be attributed to the slower oxidation kinetics

which prevent the rapid "sealing" of crack surfaces with a dense oxide layer.

7.4.5. *Implications for Yttrium Silicides and Other Rare-Earth Silicides as CMC Matrix Materials*

The fast growing Y_2O_3 scale formed on all yttrium silicide compositions poses significant

problems for use of yttrium silicides as matrix materials in CMCs. Firstly, CTE mismatch

stresses between SiC and Y_2O_3 would lead to cracking during thermal cycling events in a turbine

engine (Table 1.1). Additionally, CTE mismatch stresses may also develop between any of the

other subsurface oxides, alloys or metals. Secondly, the oxygen permeability in Y_2O_3 (Figure

7.24) is high, therefore, once formed it will continue to do so at a fast rate. The oxidation

resistance of the CMC would be reduced by replacing melt-infiltrated (MI) Si with a MI yttrium

silicide. Thirdly, the volume increase resulting from the rapid formation of Y_2O_3 from yttrium

silicides would impart large stresses on any surrounding material since the MI yttrium silicide

would be confined by the SiC matrix, SiC fibers, or a bond coat for the EBC. This would lead to

further crack formation which may compromise the CMC. Although the volume increase

resulting from the formation of SiO_2 from Si or SiC is larger than that for Y_2O_3 (Table 1.2), the

oxidation rate is significantly slower so less Si or SiC would be consumed compared to a yttrium

silicide. Fourthly, the formation of Y_2O_3 from yttrium silicides results in the continuous change

of the underlying alloy composition and microstructure. Rejected Si that results from the

oxidation of yttrium silicides (Equation (7.1)) limits the operating temperature of the CMC ($T_{m\,Si}$ =1414°C). Finally, cracks that result from CTE mismatch stresses and/or the volume increase from the rapid formation of interior Y_2O_3 provide fast diffusion pathways for oxygen and water vapor to oxidize and volatilize the SiC matrix and fibers.

The trends observed here for yttrium silicides are likely to be true for other rare-earth silicides. First, thermodynamic data for all other RE_2O_3 show that their free energies of formation (-1693 – -1946 kJ/mol) are very similar to Y_2O_3 (-1962 kJ/mol) [164]. These data indicate that it is thermodynamically favorable for all rare-earth silicides to oxidize and form RE_2O_3 rather than the desired rare-earth silicates ($Y_2Si_2O_7$ = -123 kJ/mol, Y_2SiO_5 = -104 kJ/mol) [90]. Second, rare-earth silicides are expected to have oxidation kinetics similar to yttrium silicides since the oxygen diffusivity in other RE_2O_3 (~3 x 10^{-10} – 2 x 10^{-8} cm^2/s) are similar to Y_2O_3 (~4 x 10^{-9} – 1 x 10^{-8} cm^2/s) at temperatures from 1000 – 1300°C [105]. Finally, the CTE of all other RE_2O_3 (~7 – 15 x 10^{-6} °C) are similar to Y_2O_3 (~8 - 10 x 10^{-6} °C) thus stresses due to CTE mismatch with SiC are expected during thermal cycling events in a turbine engine [103]. Given the similarity of the thermodynamic, kinetic and thermal expansion properties of all RE_2O_3 it can be concluded that the MI of any rare-earth silicide would be detrimental to the high temperature performance of a CMC.

7.5. Conclusions

The oxidation of the 41, 67 and 95 at% Si-Y alloys for 0.5 – 24 hours at 1000°C and 1200°C in air resulted in the rapid formation of Y_2O_3 and rejected Si. Additional minor oxide phases of Y-Si-O, SiO_2, Y_2SiO_5 and $Y_2Si_2O_7$ were observed to form on and beneath the specimen surface. Characterization of the microstructural evolution with time and temperature helped

elucidate the diffusion mechanisms that control oxide growth rates. The multiple diffusion processes include lattice diffusion of Y, Si and O in the alloy and oxide phases as well as fast paths for oxygen diffusion along cracks and phase boundaries. Diffusional processes associated with oxidation and microstructural coarsening led to rapid degradation of yttrium silicides. The formation of Y_2O_3 from the oxidation of yttrium silicides is both thermodynamically and kinetically favored relative to other oxide phases which poses significant problems for the use of yttrium silicides as matrix materials in CMCs. The high temperature performance of a CMC would be compromised due to Y_2O_3 CTE mismatch with SiC, high oxygen permeability and the large volume change associated with its rapid formation. In addition, the formation of Si rejected from the silicide during oxidation to form Y_2O_3 provides the same upper temperature limit as a melt-infiltrated Si matrix. The similar thermodynamic, kinetic and thermal expansion properties of other RE_2O_3 indicate that the melt-filtration of any rare-earth silicide would be detrimental to the high temperature performance of a CMC.

7.6. Recommendations for Future Work

The results of this study indicate that the oxidation behavior of all other rare-earth silicides will be similar to yttrium silicides. Therefore it is not recommended that other rare-earth silicide systems be investigated for use as a melt-infiltrated (MI) matrix for SiC-based CMCs. CMCs of the future that must operate at temperatures greater than 1414°C (melting temperature of Si) will require a MI material with a high melting temperature and good oxidation properties. Identification of other promising alloy systems that form thermochemically stable oxides in high-temperature water vapor can be performed using FactSage. The oxidation behavior of new candidate alloy systems can be assessed following the experimental procedure used in this study.

8. Summary and Conclusions

The objective of this research was to evaluate new matrix concepts for water vapor resistant SiC-based CMCs. A steam-jet furnace was optimized and validated as a method for testing candidate matrix materials in a high-temperature high-velocity water vapor environment representative of a gas turbine engine. Box furnaces and steam-jet furnace were used to assess the thermochemical stability of three matrix material concepts in high temperature oxidizing and water vapor environments. The three matrix material concepts include; (1) $Y_2Si_2O_7$, (2) SiC particulates – $Y_2Si_2O_7$ and (3) yttrium silicides.

The steam-jet furnace was validated through comparison of measured to calculated SiO_2 recession. Capabilities of the steam-jet furnace were demonstrated using binary metal oxides of SiO_2, TiO_2 and Y_2O_3. The results from this study demonstrated that the steam-jet furnace is an effective laboratory test that is capable of simulating a turbine engine environment and enables quantitative determination of material stability toward gaseous metal hydroxide formation in reasonable test times at a reasonable cost. The fused quartz capillary was found to limit the maximum test temperature for materials that readily form silicon containing oxides (e.g. Y_2O_3) or have low SiO_2 activities (e.g. Y_2SiO_5 + $Y_2Si_2O_7$), thereby identifying the need for a capillary made of a material that does not react with high temperature water vapor.

Exposure of $Y_2Si_2O_7$ to high-temperature high-velocity water vapor resulted in the selective volatilization of SiO_2 to form volatile $Si(OH)_4$ (g) and porous Y_2SiO_5. Characterization of the SiO_2 depleted microstructure as a function of time enabled identification of mechanisms such as i) $P(Si(OH)_4)$ formation reaction, ii) H_2O (g) and $Si(OH)_4$ (g) diffusion through pores by molecular and Knudsen diffusion, iii) Y_2SiO_5 coarsening and iv) development of tortuosity in the pore network can affect rates of SiO_2 depletion from $Y_2Si_2O_7$. Mechanisms (ii) through (iv) were

not previously considered prior to this study. This new information may be used to inform material and additive selection for the design of future matrices and EBCs for SiC-based CMCs. Formation of cracks in $Y_2Si_2O_7$ specimens after processing and steam-jet exposures can likely be attributed to the CTE mismatch between the β/γ and $\delta - Y_2Si_2O_7$ polymorphs. The low SiO_2 depletion at $1000 - 1200°C$ and the slowing SiO_2 volatilization kinetics with time at $1200°C$ demonstrate that $Y_2Si_2O_7$ possesses sufficient thermochemical stability to be a water vapor resistant matrix material for SiC-based CMCs.

The measured oxygen diffusivities in polycrystalline $Y_2Si_2O_7$ and Y_2SiO_5 at $1000 - 1300°C$ were not significantly different from one another and were all below the oxygen diffusivity benchmark of $1.1 \times 10^{-11} \, cm^2/s$. These results demonstrate that yttrium silicates are adequate oxygen barriers to protect SiC-based CMCs from oxidation. The oxygen diffusivity data measured in this study for polycrystalline $Y_2Si_2O_7$ and Y_2SiO_5 is the first of its kind which now enables the estimation of oxygen diffusion rates through yttrium silicate EBCs and ceramic composite matrices, critical for life prediction of engine components.

SiC particulate $- Y_2Si_2O_7$ was found to exhibit poor thermochemical stability in high-temperature oxidizing and water vapor environments. Oxidation in air resulted in the formation of a non-protective multiphase oxide scale consisting of SiO_2 and $Y_2Si_2O_7$ while exposure to high-temperature high-velocity water vapor resulted in significant material loss due to the preferential oxidation/volatilization of SiC and erosion of $Y_2Si_2O_7$. Oxidation and material recession rates of SiC particulate $- Y_2Si_2O_7$ were greater than that for SiC demonstrating that a SiC particulate $- Y_2Si_2O_7$ matrix would significantly reduce the oxidation and water vapor resistance of a CMC.

The oxidation of yttrium silicides at 1000 – 1200°C in air resulted in the rapid formation of Y_2O_3 and rejected Si. Characterization of the microstructural evolution with time and temperature identified that multiple diffusion processes, such as diffusion of Y, Si and O in the alloy and oxide phases and fast paths for oxygen diffusion along cracks and phase boundaries control oxide growth rates. The high temperature performance of a CMC would be compromised due to Y_2O_3 CTE mismatch with SiC, high oxygen permeability and the large volume change associated with its rapid formation. In addition, the formation of rejected Si during oxidation provides the same upper temperature limit as the melt-infiltrated (MI) Si matrix in current CMCs. The similar thermodynamic, kinetic and thermal expansion properties of other RE_2O_3 indicate that the MI of any rare-earth silicide would be detrimental to the high temperature performance of a CMC.

The findings in this dissertation demonstrate that the $Y_2Si_2O_7$ matrix is the most promising matrix concept as it possesses sufficient thermochemical stability in high-temperature water vapor and sufficiently low oxygen diffusivities. The multi-polymorph nature of $Y_2Si_2O_7$ does however introduce CTE mismatches between SiC, $\beta/\gamma - Y_2Si_2O_7$ and $\alpha/\delta - Y_2Si_2O_7$ that could lead to crack formation in the CMC during thermal cycling events in a gas turbine engine. Therefore other rare-earth disilicates that possesses similar thermochemical stability in high-temperature water vapor and oxygen diffusivities to $Y_2Si_2O_7$, have a good CTE match to SiC and do not have any polymorphs would be best suited as a water vapor resistant matrix material for SiC-based CMCs.

9. Appendix A. ANSYS Computation Fluid Dynamics (CFD) Model of the Steam-Jet Velocity

The CFD model was constructed using the Fluid Flow (CFX) analysis system in ANSYS (ANSYS CFX, ANSYS Inc., Canonsburg, PA). The model geometry can be seen in Figure A.1. The large outer cylinder represents the alumina tube while the smaller cylinder represents the fused quartz capillary. The diameter of the large cylinder is 34.29 mm, similar to the alumina furnace tube, while the length is 40 mm which is much shorter than the length of the alumina tube used in the steam-jet furnace (100 mm). Since the model is intended to simulate the water vapor velocity on and around the specimen the entire length of the alumina tube did not have to be included in the model geometry. The outer diameter of the smaller cylinder is 3 mm and the inner diameter is 1 mm, identical to the fused quartz capillary used in the steam-jet experiments. The length of the small cylinder was set to 15 mm since the liquid water is known to have vaporized at lengths greater than 15 mm from the capillary tip in steam-jet experiments. The 10 x 10 x 1 mm square positioned at a 45° angle relative to the small cylinder (capillary) represents the test specimen.
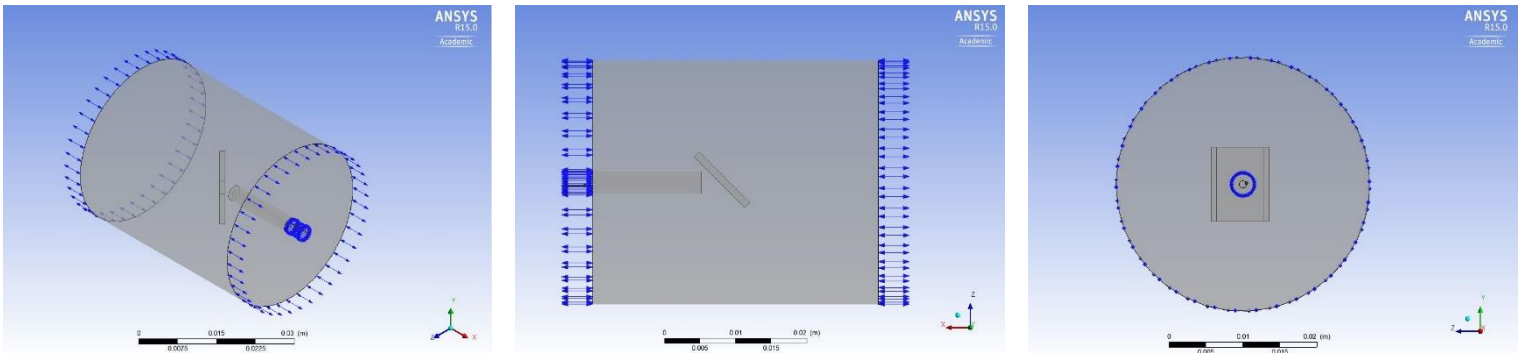
Figure A.1. ANSYS CFD model geometry.

The "domain", which encompasses all geometric components in the model space, was set as a fluid domain containing water ideal gas at a reference pressure of 1 atm. The fluid temperature was set to the experimental temperature of the steam-jet and the turbulence was set as None (Laminar). The inner diameter of the small cylinder (capillary) boundary type was set as an "inlet" where the flow regime was set to subsonic, the mass flow rate (g/s) was input as the mass flow rate of the liquid water measured during the experiment and the flow direction was set to normal to boundary condition. The two end faces of the large cylinder (alumina tube) were set as an "opening" (as shown by the double sided arrows in Figure A.1.) with a relative static pressure of 0 Pa, thus there is no change in pressure from the opening to the domain. The large cylinder outer wall has been set as a "wall" with no slip. The steam-jet velocity geometry and velocity profile output is shown in Figure A.2.
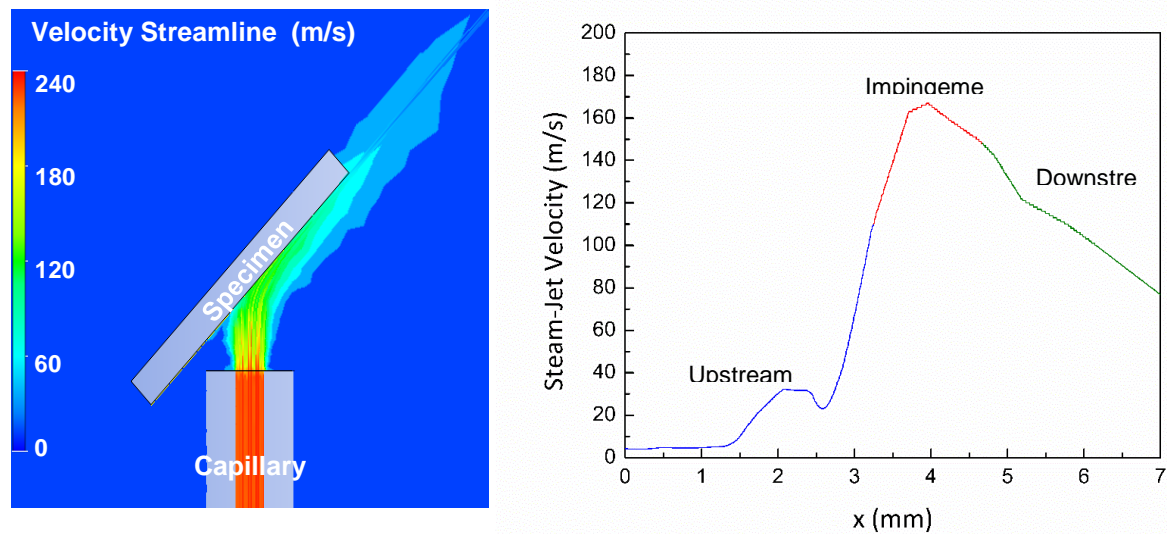
Figure A.2. ANSYS CFD model geometry (left) with corresponding steam-jet velocity profile (right). 0 mm in the steam-jet velocity profile (right) starts at the left edge of the specimen in the CFD model geometry (left). Simulation was for a temperature of 1300°C and a mass flow rate of 1.63 g/min.

10. Appendix B. Weight Change of Y_2O_3 Specimens After Steam-Jet Exposure at 1300°C for 100 Hours.

	Steam-jet velocity (m/s)	Change in weight (mg)
Specimen 1	173	0.57
Specimen 2	169	0.68

11. Appendix C. Summary of X-ray Diffraction Results for $Y_2Si_2O_7$ Before and After Steam-Jet Exposure

Specimen	Temperature (°C)	Time (h)	Major Polymorph/Phase	Minor Polymorph/Phase
YDS Powder (LOT 02-P6546SG)	n/a		β	γ, X2-YMS
#3 As-Processed	n/a		β	γ
#3-2	1300	125	γ	β
#4 As-Processed	n/a		δ	β
#4-1	1300	125	γ	β
#11 As-Processed	n/a		δ	
#11-1	1400	125	X	X
#11-3	1400	125	X	X
#11-4	1200	125	n/a	
#12 As-Processed	n/a		δ	β
#12-3	1200	125	β	δ, X2-YMS
#13 As-Processed	n/a		γ	δ
#13-4	1200	60	γ	β, X2-YMS, δ
#13-5	1200	250	γ	X2-YMS, β
#14 As-Processed	n/a		δ	β
#14-1	1200	250	β	X2-YMS, δ
#14-2	1200	250	β	X2-YMS, δ
#14-3	1200	12	δ	β
#14-4	1200	60	δ	β, X2-YMS
#15 As-Processed	n/a		γ	β
#15-1	1200	125	γ	X2-YMS, δ, β
#15-2	1200	250	γ	X2-YMS, β
#15-3	1200	60	γ	β, X2-YMS
#15-4	1200	125	γ	X2-YMS, β, δ
#15-5	1200	60	γ	δ, X2-YMS, β
#16 As-Processed	n/a		γ	δ

#16-1	1200	250	γ	X2-YMS
#16-2	1200	60	β	δ, γ
#16-3	1000	125	δ	β
#16-4	1200	125	γ	X2-YMS, β
#16-5	1100	125	γ	δ
#16-6	1100	125	γ	δ
#18 As-Processed	n/a		γ	δ
#18-1	1100	125	γ	δ, β, X2-YMS
#18-2	1000	125	δ	β, γ
#18-3	1000	125	δ	γ, β

YDS = $Y_2Si_2O_7$

YMS = Y_2SiO_5

The first digits in the specimen number identify which SPS processing batch the specimen came from and the second digit after the dash refers to the order in which the specimen was tested from that batch.

12. Appendix D. Measured Weight Change for $Y_2Si_2O_7$ Specimens After Steam-Jet Exposure

Temperature (°C)	Time (h)	Steam-Jet Velocity (m/s)	Specimen	Weight Change (mg)
1000	125	130	#16-3	-0.60
		130	#18-2	-0.68
		131	#18-3	-0.14
1100	125	153	#16-5	-0.26
		150	#16-6	-0.21
		149	#18-1	-0.66
1200	12	158	#14-3	-0.37
	60	171	#13-4	-0.25
		174	#14-4	-0.30
		170	#15-3	-0.38
		169	#15-5	-0.39
		161	#16-2	-0.78
	125	165	#11-4	-0.45
		164	#12-3	-0.61
		169	#15-1	-0.44
		170	#15-4	-1.53
		169	#16-4	-0.31
	250	169	#13-5	-1.64
		163	#14-1	-0.67
		171	#15-2	-0.86
		159	#16-1	-0.51
1300	125	174	#3-2	-0.08
		163	#4-1	-0.19
1400	125	184	#11-1	-0.12
		186	#11-3	specimen fractured

The first digits in the specimen number identify which SPS processing batch the specimen came from and the second digit after the dash refers to the order in which the specimen was tested from that batch.

13. Appendix E. Average SiO₂ Depletion Depth Measured in Cross-Section from Y₂Si₂O₇ Specimens After Steam-Jet Exposure for 60 – 250 Hours at 1000 – 1200°C.

Temperature (°C)	Time (h)	Steam-Jet Velocity (m/s)	Specimen	Average SiO$_2$ Depletion Depth (µm)
1000	125	130	#16-3	1.4 ± 0.7
		130	#18-2	0.8 ± 0.3
		131	#18-3	1.4 ± 0.5
1100	125	153	#16-5	1.3 ± 0.6
		150	#16-6	1.4 ± 0.6
		149	#18-1	1.6 ± 0.7
1200	60	171	#13-4	5.2 ± 1.9
		174	#14-4	7.1 ± 1.4
		170	#15-3	4.4 ± 0.8
		169	#15-5	2.2 ± 0.7
		161	#16-2	3.6 ± 1.0
	125	165	#11-4	10.6 ± 0.8
		164	#12-3	8.5 ± 1.3
		169	#15-1	5.5 ± 1.1
		170	#15-4	4.1 ± 0.9
		169	#16-4	4.8 ± 1.5
	250	169	#13-5	6.1 ± 1.2
		163	#14-1	17.5 ± 1.2
		171	#15-2	12.0 ± 1.3
		159	#16-1	8.2 ± 1.9

The first digits in the specimen number identify which SPS processing batch the specimen came from and the second digit after the dash refers to the order in which the specimen was tested from that batch.

14. Appendix F. Summary of X-ray Diffraction Results for a $Y_2Si_2O_7$ Specimen Before and After Intermittent Steam-Jet Exposure.

Exposure Time (h)	Major Polymorph/Phase	Minor Polymorph/Phase
As-Processed	δ	β
6	δ	β
9	δ	β
12	δ	β
15	δ	β
18	δ	β
24	δ	β
30	δ	β, X2-YMS
36	δ	β, X2-YMS
48	δ	β, X2-YMS
60	β	δ, X2-YMS
125	β	δ, X2-YMS
250	β	δ, X2-YMS

YMS = Y_2SiO_5

15. Appendix G. Plan view BSE/SEM Images Used for Image Analysis to Quantify Average Pore Size and Total Pore Area Fraction.
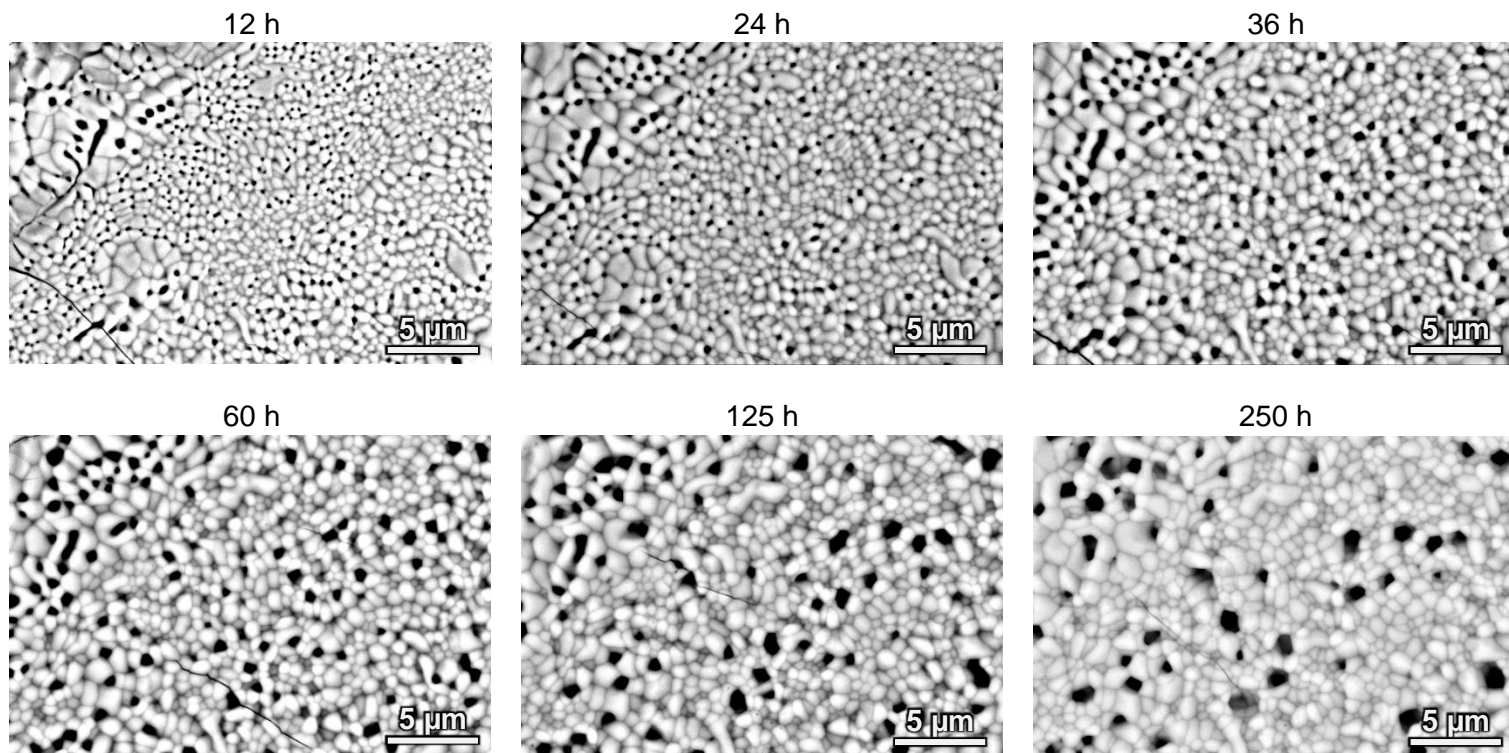
Images were acquired 3 mm downstream of the steam-jet impingement site on a $Y_2Si_2O_7$ (YDS) specimen after intermittent removal and exposure for 12 – 250 hours at 1200°C. $v_{(g)}$= 79 m/s, $P(H_2O)$= 1 atm.

Summary of average pore surface area and total pore area fraction measured at each exposure time.

Exposure Time (h)	Average Pore Surface Area (μm^2)	Total Pore Area Fraction
12	0.0122	0.0334
24	0.0199	0.0298
36	0.0433	0.0349
60	0.0609	0.0445
125	0.0994	0.0466
250	0.129	0.0383

16. Appendix H. Electron Backscatter Diffraction (EBSD) of $Y_2Si_2O_7$ Specimen Exposed in the Steam-Jet for 125 hours at 1300°C: Preliminary Results

Instrument Settings:
Accelerating Voltage: 25 kV
Spot Size: 5
Vacuum Pressure: 0.98 torr
Working Distance: 14.9 mm
Binning: 4 x 4
Gain: Low
Exposure Time: 73.17 ms
Frame Average: 2
Number of Frames: 64
Step Size: 0.93 µm
Signal: ~92%

The $Y_2Si_2O_7$ specimen was prepped for EBSD as described in Section 2.2.1. EBSD was performed ~2 – 3 mm downstream of the steam-jet impingement site. No correlation between faceting and $Y_2Si_2O_7$ polymorph was observed as both the β and δ polymorphs had grains that were unfaceted and facted (Figure H.1.). When only faceted δ – $Y_2Si_2O_7$ grains were selected their pole figures suggest that grains with <100> perpendicular to the specimen surface experience the greatest amount of faceting (Figure H.2.). When only unfaceted δ – $Y_2Si_2O_7$ grains were selected their pole figures suggest that grains with <010> perpendicular to the specimen surface experience the least amount of faceting (Figure H.3.)
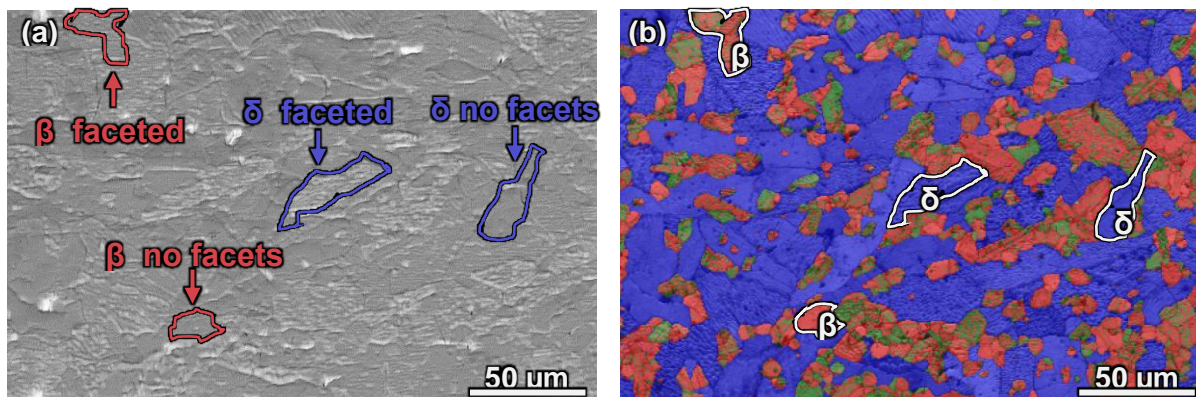
Figure H. 1. SE/SEM image of the area characterized by EBSD (a) and corresponding map showing β (red) and δ (blue) $Y_2Si_2O_7$ grains.
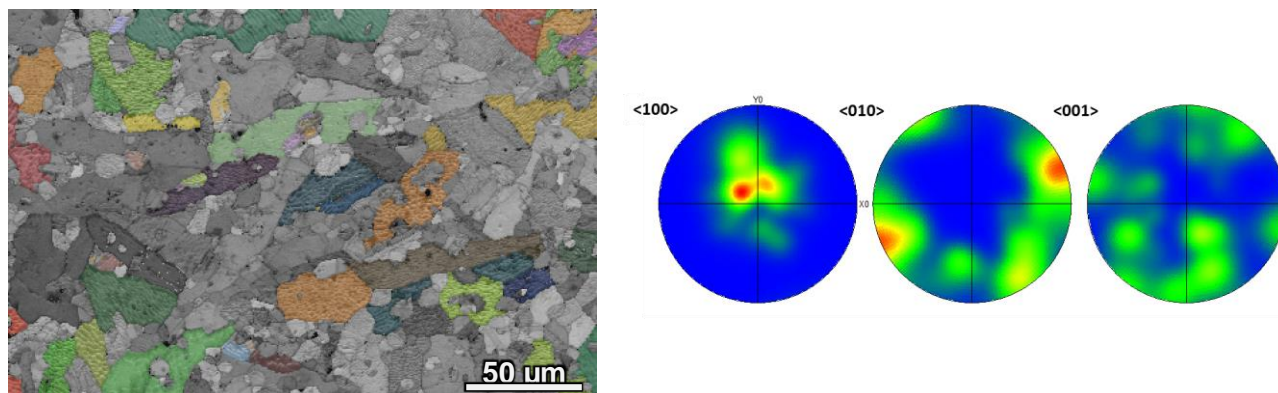
Figure H. 2. SE/SEM image of the area characterized by EBSD showing faceted δ grains in color (left) and corresponding pole figure (right).
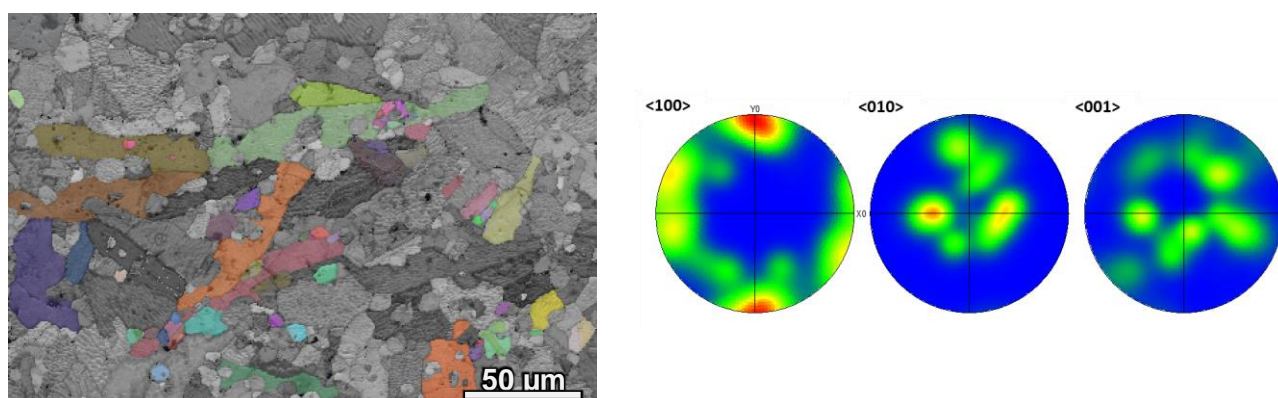
Figure H. 3. SE/SEM image of the area characterized by EBSD showing unfaceted δ grains in color (left) and corresponding pole figure (right).

17. Appendix I. Critical Pore Sizes for Knudsen Diffusion of H_2O (g) and $Si(OH)_4$ (g) Through Porous Y_2SiO_5.

When the pore diameter is smaller than the mean-free path of the diffusing gas molecules and the density of the gas is low, the gas molecules will collide with the pore walls more frequently than with each other. This process is known as Knudsen diffusion. The Knudsen number (K_n) is used as a measure of the relative importance of Knudsen diffusion and is given by [114],

$$K_n = \frac{\lambda}{d_{pore}}$$

where λ is the mean-free path length of the diffusing species and d_{pore} is the pore diameter. The mean-free path length is given by [114],

$$\lambda = \frac{k\,T}{\sqrt{2\pi}\,\sigma^2 P}$$

where k is Boltzmann's constant, T is temperature, σ is the Lennard-Jones molecular diameter (collision diameter) of the diffusing gas species ($\sigma(H_2O)$= 0.2641 nm, $\sigma(Si(OH)_4)$= 0.4880 nm) [115] and P is pressure. Since σ is not available for $Si(OH)_4$ (g) the value for SiF_4 was used as an approximation. Krikorian notes that hydroxides act as pseudo halides suggesting these approximations are reasonable [113].

The following criteria have been established for Knudsen diffusion [114].

$0.1 < K_n < 1$ Knudsen diffusion plays a measureable but moderate role in the overall diffusion process

$K_n > 1$ Knudsen diffusion becomes important

$K_n > 10$ Knudsen diffusion can dominate

Table showing the pore diameters resulting in values of K_n that satisfy the criteria above at 1000°C, 1100°C and 1200°C.

Vapor Species	Temperature (°C)	λ (µm)	d_{pore} (µm) for D_K Moderate	d_{pore} (µm) for D_K Important	d_{pore} (µm) for D_K Dominates
H_2O	1000	0.92	< 9.2	< 0.92	< 0.092
	1100	1.1	< 11	< 1.1	< 0.11
	1200	1.2	< 12	< 1.2	< 0.12
$Si(OH)_4$	1000	0.29	< 2.9	< 0.29	< 0.029
	1100	0.31	< 3.1	< 0.31	< 0.031
	1200	0.34	< 3.4	< 0.34	< 0.034

18. Appendix J. $^{16}O_2$ and $^{18}O_2$ Backfill Pressures at Each Diffusion Temperature.

Material	Diffusion Temperature (°C)	$^{16}O_2$ Backfill Pressure (atm)	$^{18}O_2$ Backfill Pressure (atm)
Y$_2$Si$_2$O$_7$	1100	0.26	0.29
	1200	0.24	0.27
	1300	0.23	0.25
Y$_2$SiO$_5$	1000	0.28	0.31
	1100	0.26	0.29
	1200	0.24	0.27

19. Appendix K. Summary of all Oxygen Tracer Diffusion Experiments

Material	Diffusion Temperature (°C)	^{18}O Diffusion Time (h)	D_b (cm²/s)	k_s (cm/s)	R^2	Comment
$Y_2Si_2O_7$	1100	20	n/a			Over exposed
		2.5	2.96 x 10⁻¹³	1.96 x 10⁻⁹	0.998	Best fit, C_{min}= 0.7%, x= 3.82 µm
		0.5	1.14 x 10⁻¹³	4.0 x 10⁻⁹	0.981	C_{min}= 0.8%, x= 1.80 µm
	1200	9	n/a			Over exposed
		1.25	8.85 x 10⁻¹³	2.1 x 10⁻⁹	0.995	Best fit, C_{min}= 2.8%, x= 3.16 µm
		0.33	3.37 x 10⁻¹³	2.97 x 10⁻⁹	0.960	Evidence of short circuit diffusion. C_{min}= 1.1%, x= 2.40 µm
	1300	2	n/a			^{18}O concentration profile observed, dominated by short circuit diffusion. Could not fit diffusion equation to data. C_{min}= 2%, x= 3.64 µm
		30	6.55 x 10⁻¹²	8.18 x 10⁻⁸	0.994	C_{min}= 3.5%, x= 4.31 µm
		10	1.22 x 10⁻¹²	1.96 x 10⁻⁸	0.994	Best fit, C_{min}= 0.5%, x= 3.29 µm
Y_2SiO_5	1000	15	n/a			Over exposed
		2	1.20 x 10⁻¹⁴	6.75 x 10⁻¹⁰	0.969	Best fit, evidence of short circuit diffusion. C_{min}= 0.3%, x= 4.11 µm
	1100	9	n/a			Over exposed
		3.5	n/a			^{18}O concentration profile observed, dominated by short circuit diffusion. Could not fit diffusion equation to data. C_{min}= 6.4%, x= 5.21 µm
		1.5	n/a			Forced fit, evidence of short circuit diffusion. C_{min}= 0.4%, x= 1.42 µm
	1200	3	n/a			^{18}O concentration profile observed, dominated by short circuit diffusion. Could not fit diffusion equation to data. C_{min}= 3.5%, x= 2.24 µm
		0.75	4.12 x 10⁻¹³	8.73 x 10⁻¹⁰	0.990	Best fit, C_{min}= 0.8%, x= 2.59 µm

C_{min} = minimum measured isotopic concentration when the ToF-SIMS analysis stopped. Note natural abundance of ^{18}O is 0.2%.

x= diffusion depth

Objective of ^{18}O exchanges was to capture the entire ^{18}O concentration profile (background 0.2% ^{18}O) within a sputter depth of 3.5 µm.

20. Appendix L. Measured Specific Weight Change for SiC Particulate – $Y_2Si_2O_7$ Specimens After Oxidation Exposures.

Temperature (°C)	Time (h)	Specimen	Specific Weight Change (mg)
1000	125	#17-2	1.31 (large crack in center of specimen)
		#17-8	0.3
		#18-9	0.746 (corner of specimen broke off)
1100	125	#17-9	0.267
		#18-10	0.246
		#18-11	0.22
1200	60	#17-4	0.245 [c]
		#18-2	0.28 [a]
		#18-8_2	0.37 [b]
	125	#17-3	0.397 [c]
		#18-5_1	0.46 [a]
		#18-5_2	0.55 [b]
	250	#17-6	0.45 [c]
		#18-6_1	0.73 [b]
		#18-8_1	0.57 [a]

The first digits in the specimen number identify which SPS processing batch the specimen came from and the second digit after the dash refers to what slice the specimen came from out of the as-processed puck. Specimens containing an "_" following the second digit after the dash indicate it is one of two specimens that came from the same slice.

Specimens oxidized at 1200°C in separate alumina boats during the same continuous run are denoted with the superscripts "a, b and c". Superscripts also indicate the order the experiments were performed.

21. Appendix M. Measured Specific Weight Change for CVD SiC Specimens After Oxidation Exposures.

Temperature (°C)	Time (h)	Specimen	Specific Weight Change (mg)
1000	125	#1	0.017
		#6	0.023
1100	125	#2	0.055
		#7	0.057
1200	60	#3	0.0549
		#8	0.0548
	125	#9	0.0801
		#10	0.0783
	250	#5	0.101
		#11	0.123

22. Appendix N. Measured Weight Loss for SiC Particulate – $Y_2Si_2O_7$ Specimens After Steam-Jet Exposures

Specimen	Weight Loss (mg)
#17-1	6.0
#18-7	5.29

The first digits in the specimen number identify which SPS processing batch the specimen came from and the second digit after the dash refers to what slice the specimen came from out of the as-processed puck.

23. Appendix O. Measured Specific Weight Change for Yttrium Silicides After Oxidation Exposures

Composition (at% Si – Y)	Temperature (°C)	Time (h)	Specimen	Average Specific Weight Change (mg/cm²)
41	1000	3	#5	75.2
			#7	68.1
	1200		#6	81.6
			#8	72.7
67	1000	0.5	#9	8.46
			#11	8.42
		3	#1	16.8
			#4	16.1
			#13	16.9
		24	#5	36.4
			#7	31.3
	1200	0.5	#10	6.74
			#12	6.75
			#15	8.25
		3	#2	10.3
			#3	9.51
			#14	9.97
		24	#6	15.3
			#8	13.2
			#16	16.0
95	1000	0.5	#14	0.215
			#16	0.375
			#18	0.417
		3	#1	0.433
			#6	0.427
			#10	0.475
		24	#5	0.889
			#8	0.768
			#12	0.782
	1200	0.5	#15	0.205
			#17	0.340
			#19	0.264
		3	#3	0.468
			#7	0.524
			#11	0.450
		24	#4	1.19
			#9	1.12
			#13	1.21
100 (Calculated from Deal and Grove [107] for air)	1000	0.5	n/a	0.137
		3		0.335
		24		0.948
	1200	0.5		0.268
		3		0.657
		24		1.89

24. References

1   M.P. Boyce, *Gas Turbine Engineering Handbook*, Fourth Edition. Butterworth-Heinemann, Oxford, 2012.

2   N.P. Padture, "Advanced structural ceramics in aerospace propulsion," *Nat Mater*, **15** [8] 804–809 (2016).

3   F.W. Zok, "Ceramic-matrix composites enable revolutionary gains in turbine engine efficiency," *Am. Ceram. Soc. Bull.*, **95** [5] 22–28 (2016).

4   D.R. Clarke, M. Oechsner, and N.P. Padture, "Thermal-barrier coatings for more efficient gas-turbine engines," *MRS Bull.*, **37** [10] 891–898 (2012).

5   J.H. Perepezko, "The Hotter the Engine, the Better," *Science*, **326** [5956] 1068–1069 (2009).

6   J.T. DeMasi-Marcin and D.K. Gupta, "Protective coatings in the gas turbine engine," *Surf. Coat. Technol.*, **68** 1–9 (1994).

7   J.C. Williams and E.A.S. Jr, "Progress in structural materials for aerospace systems1," *Acta Mater.*, **51** [19] 5775–5799 (2003).

8   N.R. Council, *Ceramic Fibers and Coatings: Advanced Materials for the Twenty-First Century*. The National Academies Press, Washington, DC, 1998.

9   I. Spitsberg and J. Steibel, "Thermal and Environmental Barrier Coatings for SiC/SiC CMCs in Aircraft Engine Applications*," *Int. J. Appl. Ceram. Technol.*, **1** [4] 291–301 (2004).

10   G. Gardiner, "Aeroengine Composites, Part 1: The CMC invasion," *Compos. World*, (2015).

11   R. Naslain and F. Christin, "SiC-Matrix Composite Materials for Advanced Jet Engines," *MRS Bull.*, **28** [9] 654–658 (2003).

12   J.A. DiCarlo and H.-M. Yun, "Non-oxide (Silicon Carbide) Fibers;" pp. 33–52 in *Handb. Ceram. Compos.* Edited by N.P. Bansal. Springer US, Boston, MA, 2005.

13   R. Naslain, "Design, preparation and properties of non-oxide CMCs for application in engines and nuclear reactors: an overview," *Compos. Sci. Technol.*, **64** [2] 155–170 (2004).

14   M. Rosso, "Ceramic and metal matrix composites: Routes and properties," *J. Mater. Process. Technol.*, **175** [1–3] 364–375 (2006).

15   A.G. Evans, F.W. Zok, and J. Davis, "The role of interfaces in fiber-reinforced brittle matrix composites," *Compos. Sci. Technol.*, **42** [1] 3–24 (1991).

16   J.J. Brennan, "Interfacial characterization of a slurry-cast melt-infiltrated SiC/SiC ceramic-matrix composite," *Acta Mater.*, **48** [18–19] 4619–4628 (2000).

[17] R.R. Naslain, "SiC-Matrix Composites: Nonbrittle Ceramics for Thermo-Structural Application," *Int. J. Appl. Ceram. Technol.*, **2** [2] 75–84 (2005).

[18] L.U. Ogbuji and E.J. Opila, "A Comparison of the Oxidation Kinetics of SiC and Si_3N_4," *J. Electrochem. Soc.*, **142** [3] 925–930 (1995).

[19] C.E. Ramberg, G. Cruciani, K.E. Spear, R.E. Tressler, and C.F. Ramberg, "Passive-Oxidation Kinetics of High-Purity Silicon Carbide from 800° to 1100°C," *J. Am. Ceram. Soc.*, **79** [11] 2897–2911 (1996).

[20] E.J. Opila, J.L. Smialek, R.C. Robinson, D.S. Fox, and N.S. Jacobson, "SiC Recession Caused by SiO_2 Scale Volatility under Combustion Conditions: II, Thermodynamics and Gaseous-Diffusion Model," *J. Am. Ceram. Soc.*, **82** [7] 1826–1834 (1999).

[21] E.J. Opila and R.E. Hann, "Paralinear Oxidation of CVD SiC in Water Vapor," *J. Am. Ceram. Soc.*, **80** [1] 197–205 (1997).

[22] E.J. Opila, "Oxidation Kinetics of Chemically Vapor-Deposited Silicon Carbide in Wet Oxygen," *J. Am. Ceram. Soc.*, **77** [3] 730–736 (1994).

[23] E.J. Opila, "Oxidation and Volatilization of Silica Formers in Water Vapor," *J. Am. Ceram. Soc.*, **86** [8] 1238–1248 (2003).

[24] N.S. Jacobson, "Corrosion of Silicon-Based Ceramics in Combustion Environments," *J. Am. Ceram. Soc.*, **76** [1] 3–28 (1993).

[25] E.J. Opila, D.S. Fox, and N.S. Jacobson, "Mass Spectrometric Identification of Si–O–H(g) Species from the Reaction of Silica with Water Vapor at Atmospheric Pressure," *J. Am. Ceram. Soc.*, **80** [4] 1009–1012 (1997).

[26] E.J. Opila, "Variation of the Oxidation Rate of Silicon Carbide with Water-Vapor Pressure," *J. Am. Ceram. Soc.*, **82** [3] 625–636 (1999).

[27] H. Klemm, "Silicon Nitride for High-Temperature Applications," *J. Am. Ceram. Soc.*, **93** [6] 1501–1522 (2010).

[28] I. Yuri, T. Hisamatsu, Y. Etori, and T. Yamamoto, "Degradation of Silicon Carbide in Combustion Gas Flow at High Temperature and High Speed," *JSME Int. J. Ser. Solid Mech. Mater. Eng.*, **44** [4] 520–527 (2001).

[29] R.C. Robinson and J.L. Smialek, "SiC Recession Caused by SiO_2 Scale Volatility under Combustion Conditions: I, Experimental Results and Empirical Model," *J. Am. Ceram. Soc.*, **82** [7] 1817–1825 (1999).

30   S.L. dos Santos e Lucato, O.H. Sudre, and D.B. Marshall, "A Method for Assessing Reactions of Water Vapor with Materials in High-Speed, High-Temperature Flow," *J. Am. Ceram. Soc.*, **94** s186–s195 (2011).

31   K.N. Lee, "Current status of environmental barrier coatings for Si-Based ceramics," *Surf. Coat. Technol.*, **133**–**134** [0] 1–7 (2000).

32   A.B. Gokhale and G.J. Abbaschian, "The Si−Y (Silicon-Yttrium) system," *Bull. Alloy Phase Diagr.*, **7** [5] 485–489 (1986).

33   K.M. Grant, S. Krämer, J.P.A. Löfvander, and C.G. Levi, "CMAS degradation of environmental barrier coatings," *Surf. Coat. Technol.*, **202** [4–7] 653–657 (2007).

34   N.L. Ahlborg and D. Zhu, "Calcium–magnesium aluminosilicate (CMAS) reactions and degradation mechanisms of advanced environmental barrier coatings," *Surf. Coat. Technol.*, **237** 79–87 (2013).

35   C.G. Levi, J.W. Hutchinson, M.-H. Vidal-Setif, and C.A. Johnson, "Environmental degradation of thermal-barrier coatings by molten deposits," *MRS Bull.*, **37** [10] 932–941 (2012).

36   H. Zhao, B.T. Richards, C.G. Levi, and H.N.G. Wadley, "Molten silicate reactions with plasma sprayed ytterbium silicate coatings," *Surf. Coat. Technol.*, **288** 151–162 (2016).

37   F. Stolzenburg, M.T. Johnson, K.N. Lee, N.S. Jacobson, and K.T. Faber, "The interaction of calcium–magnesium–aluminosilicate with ytterbium silicate environmental barrier materials," *Surf. Coat. Technol.*, **284** 44–50 (2015).

38   R.G. Wellman and J.R. Nicholls, "Erosion, corrosion and erosion–corrosion of EB PVD thermal barrier coatings," *Tribol. Int.*, **41** [7] 657–662 (2008).

39   D.S. Fox and J.L. Smialek, "Burner Rig Hot Corrosion of Silicon Carbide and Silicon Nitride," *J. Am. Ceram. Soc.*, **73** [2] 303–311 (1990).

40   N.S. Jacobson, "Kinetics and Mechanism of Corrosion of SiC by Molten Salts," *J. Am. Ceram. Soc.*, **69** [1] 74–82 (1986).

41   T.E. Strangman, "Thermal barrier coatings for turbine airfoils," *Thin Solid Films*, **127** [1] 93–106 (1985).

42   S.R. Choi, "Foreign Object Damage Phenomenon by Steel Ball Projectiles in a SiC/SiC Ceramic Matrix Composite at Ambient and Elevated Temperatures," *J. Am. Ceram. Soc.*, **91** [9] 2963–2968 (2008).

43 X. Chen, R. Wang, N. Yao, A.G. Evans, J.W. Hutchinson, and R.W. Bruce, "Foreign object damage in a thermal barrier system: mechanisms and simulations," *Mater. Sci. Eng. A*, **352** [1–2] 221–231 (2003).

44 K.N. Lee, D.S. Fox, J.I. Eldridge, D. Zhu, R.C. Robinson, N.P. Bansal, and R.A. Miller, "Upper Temperature Limit of Environmental Barrier Coatings Based on Mullite and BSAS," *J. Am. Ceram. Soc.*, **86** [8] 1299–1306 (2003).

45 K.N. Lee, D.S. Fox, and N.P. Bansal, "Rare earth silicate environmental barrier coatings for SiC/SiC composites and Si_3N_4 ceramics," *J. Eur. Ceram. Soc.*, **25** [10] 1705–1715 (2005).

46 M. Fritsch, H. Klemm, M. Herrmann, and B. Schenk, "Corrosion of selected ceramic materials in hot gas environment," *J. Eur. Ceram. Soc.*, **26** [16] 3557–3565 (2006).

47 P. Fielitz, G. Borchardt, M. Schmücker, H. Schneider, M. Wiedenbeck, D. Rhede, S. Weber, and S. Scherrer, "Secondary Ion Mass Spectroscopy Study of Oxygen^{-18} Tracer Diffusion in 2/1-Mullite Single Crystals," *J. Am. Ceram. Soc.*, **84** [12] 2845–2848 (2001).

48 Y. Ikuma, E. Shimada, S. Sakano, M. Oishi, M. Yokoyama, and Z. Nakagawa, "Oxygen Self-diffusion in Cylindrical Single-Crystal Mullite," *J. Electrochem. Soc.*, **146** [12] 4672–4675 (1999).

49 M. Fritsch, "Heiβgaskorrosion keramischer Werkstoffe in H_2O-Haltigen Rauchgasatmosphaٟren;" PhD dissertation, Fraunhofer-Institut fuٟr Keramische Technologien und Systeme IKTS, Dresden, Germany, 2007.

50 N. Maier, K.G. Nickel, and G. Rixecker, "High temperature water vapour corrosion of rare earth disilicates $(Y,Yb,Lu)_2Si_2O_7$ in the presence of $Al(OH)_3$ impurities," *J. Eur. Ceram. Soc.*, **27** [7] 2705–2713 (2007).

51 H.E. Eaton and G.D. Linsey, "Accelerated oxidation of SiC CMC's by water vapor and protection via environmental barrier coating approach," *J. Eur. Ceram. Soc.*, **22** [14–15] 2741–2747 (2002).

52 Y. Okada and Y. Tokumaru, "Precise determination of lattice parameter and thermal expansion coefficient of silicon between 300 and 1500 K," *J. Appl. Phys.*, **56** [2] 314–320 (1984).

53 M. Aparicio and A. Durán, "Yttrium Silicate Coatings for Oxidation Protection of Carbon–Silicon Carbide Composites," *J. Am. Ceram. Soc.*, **83** [6] 1351–1355 (2000).

54 M.D. Dolan, B. Harlan, J.S. White, M. Hall, S.T. Misture, S.C. Bancheri, and B. Bewlay, "Structures and anisotropic thermal expansion of the α, β, γ, and δ polymorphs of $Y_2Si_2O_7$," *Powder Diffr.*, **23** [01] 20–25 (2008).

55 K. Fukuda and H. Matsubara, "Thermal Expansion of δ-Yttrium Disilicate," *J. Am. Ceram. Soc.*, **87** [1] 89–92 (2004).

56 A.J. Fernández-Carrión, M. Allix, and A.I. Becerro, "Thermal Expansion of Rare-Earth Pyrosilicates," *J. Am. Ceram. Soc.*, **96** [7] 2298–2305 (2013).

57 J. Felsche, "Polymorphism and crystal data of the rare-earth disilicates of type $R.E._2Si_2O_7$," *J. Common Met.*, **21** [1] 1–14 (1970).

58 I.A. Bondar, "Rare-earth silicates," *Ceram. Int.*, **8** [3] 83–89 (1982).

59 D. Cupid and H. Seifert, "Thermodynamic Calculations and Phase Stabilities in the Y-Si-C-O System," *J. Phase Equilibria Diffus.*, **28** [1] 90–100 (2007).

60 J. Liu, L. Zhang, F. Hu, J. Yang, L. Cheng, and Y. Wang, "Polymer-derived yttrium silicate coatings on 2D C/SiC composites," *J. Eur. Ceram. Soc.*, **33** [2] 433–439 (2013).

61 D. Boyer and B. Derby, "Yttrium Silicate Powders Produced by the Sol–Gel Method, Structural and Thermal Characterization," *J. Am. Ceram. Soc.*, **86** [9] 1595–1597 (2003).

62 S. Ramasamy, S.N. Tewari, K.N. Lee, R.T. Bhatt, and D.S. Fox, "Slurry based multilayer environmental barrier coatings for silicon carbide and silicon nitride ceramics — I. Processing," *Surf. Coat. Technol.*, **205** [2] 258–265 (2010).

63 J. Liu, L. Zhang, J. Yang, L. Cheng, and Y. Wang, "Fabrication of $SiCN–Sc_2Si_2O_7$ coatings on C/SiC composites at low temperatures," *J. Eur. Ceram. Soc.*, **32** [3] 705–710 (2012).

64 M. Díaz, C. Pecharromán, F. del Monte, J. Sanz, J.E. Iglesias, J.S. Moya, C. Yamagata, and S. Mello-Castanho, "Synthesis, Thermal Evolution, and Luminescence Properties of Yttrium Disilicate Host Matrix," *Chem. Mater.*, **17** [7] 1774–1782 (2005).

65 S. Ueno, T. Ohji, and H.-T. Lin, "Recession behavior of $Yb_2Si_2O_7$ phase under high speed steam jet at high temperatures," *Corros. Sci.*, **50** [1] 178–182 (2008).

66 S. Ueno, D.D. Jayaseelan, T. Ohji, and H.-T. Lin, "Recession mechanism of $Lu_2Si_2O_7$ phase in high speed steam jet environment at high temperatures," *Ceram. Int.*, **32** [7] 775–778 (2006).

67 E. Courcot, F. Rebillat, and F. Teyssandier, "From the Volatility of Simple Oxides to that of Mixed Oxides: Thermodynamic and Experimental Approaches;" pp. 235–244 in *Des. Dev. Appl. Eng. Ceram. Compos.* John Wiley & Sons, Inc., 2010.

68 I. Yuri, T. Hisamatsu, S. Ueno, and T. Ohji, "Exposure Test Results of $Lu_2Si_2O_7$ In Combustion Gas Flow At High Temperature And High Speed," *Jpn. Soc. Mech. Eng.*, **44** [4] 520–527 (2001).

69 Z. Hong, L. Cheng, L. Zhang, and Y. Wang, "Water Vapor Corrosion Behavior of Scandium Silicates at 1400°C," *J. Am. Ceram. Soc.*, **92** [1] 193–196 (2009).

70 B.T. Richards, K.A. Young, F. de Francqueville, S. Sehr, M.R. Begley, and H.N.G. Wadley, "Response of ytterbium disilicate–silicon environmental barrier coatings to thermal cycling in water vapor," *Acta Mater.*, **106** 1–14 (2016).

71 S. Ueno, T. Ohji, and H.-T. Lin, "Recession behavior of Lu_2SiO_5 under a high speed steam jet at high temperatures," *Ceram. Int.*, **37** [4] 1185–1189 (2011).

72 N.S. Jacobson, "Silica Activity Measurements in the Y_2O_3–SiO_2 System and Applications to Modeling of Coating Volatility," *J. Am. Ceram. Soc.*, **97** [6] 1959–1965 (2014).

73 G.C.C. Costa and N.S. Jacobson, "Mass spectrometric measurements of the silica activity in the Yb_2O_3–SiO_2 system and implications to assess the degradation of silicate-based coatings in combustion environments," *J. Eur. Ceram. Soc.*, **35** [15] 4259–4267 (2015).

74 R.A. Golden and E.J. Opila, "A method for assessing the volatility of oxides in high-temperature high-velocity water vapor," *J. Eur. Ceram. Soc.*, **36** [5] 1135–1147 (2016).

75 A.B. Gokhale and G.J. Abbaschian, "The Sc−Si (Scandium-Silicon) system," *Bull. Alloy Phase Diagr.*, **7** [4] 333–336 (1986).

76 M.V. Bulanova, P.N. Zheltov, K.A. Meleshevich, P.A. Saltykov, G. Effenberg, and J.-C. Tedenac, "Lanthanum–silicon system," *J. Alloys Compd.*, **329** [1–2] 214–223 (2001).

77 M.V. Bulanova, P.N. Zheltov, K.A. Meleshevich, P.A. Saltykov, and G. Effenberg, "Cerium–silicon system," *J. Alloys Compd.*, **345** [1–2] 110–115 (2002).

78 A.B. Gokhale, A. Munitz, and G.J. Abbaschian, "The Nd-Si (Neodymium-Silicon) system," *Bull. Alloy Phase Diagr.*, **10** [3] 246–251 (1989).

79 A.B. Gokhale and G.J. Abbaschian, "The Si-Sm (Silicon-Samarium) system," *Bull. Alloy Phase Diagr.*, **9** [5] 582–585 (1988).

80 H. Okamoto, "Gd-Si (Gadolinium-Silicon)," *J. Phase Equilibria Diffus.*, **30** [2] 213–214 (2009).

81 M.V. Bulanova, J.C. Tedenac, H. Noël, K.A. Meleshevich, A. Haidoux, A.V. Samelyuk, and M.V. Pudovkina, "The Ti_5Si_3–Tb_5Si_3 section of the Ti–Tb–Si system," *J. Alloys Compd.*, **375** [1–2] 175–178 (2004).

82 V.N. Eremenko, V.E. Listovnichii, S.P. Luzan, Y.I. Buyanov, and P.S. Martsenyuk, "Phase diagram of the holmium-silicon binary system and physical properties of holmium silicides up to 1050 °C," *J. Alloys Compd.*, **219** [1–2] 181–184 (1995).

83 S.P. Luzan, V.E. Listovnichii, Y.I. Buyanov, and P.S. Martsenyuk, "Phase diagram of the binary erbium-silicon system and physical properties of erbium silicides up to 1050°C," *J. Alloys Compd.*, **239** [1] 77–82 (1996).

84 A. Palenzona, P. Manfrinetti, S. Brutti, and G. Balducci, "The phase diagram of the Yb–Si system," *J. Alloys Compd.*, **348** [1–2] 100–104 (2003).

85 S. Brutti, G. Balducci, A. Ciccioli, and G. Gigli, "Thermodynamic assessment of the Yb–Si system," *Calphad*, **29** [3] 254–261 (2005).

86 T.S. Verkhoglyadove and L.A. Dvorina, *High-Temperature Oxidation of Silicides of Some Rare-Earth Metals*, (1967).

87 S.Y. Chiam, W.K. Chim, A.C.H. Huan, J. Zhang, and J.S. Pan, "Coverage dependent reaction of yttrium on silicon and the oxidation of yttrium silicide investigated by x-ray photoelectron spectroscopy," *J. Vac. Sci. Technol. A*, **25** [3] 500–507 (2007).

88 J.A. Haefling, F.A. Schmidt, and O.N. Carlson, "Air oxidation of yttrium and some yttrium-base alloys," *J. Common Met.*, **7** [6] 433–440 (1964).

89 D.L. Poerschke and C.G. Levi, "Yttrium Bearing Silicon Carbide Matrices for Robust Ceramic Composites," *J. Am. Ceram. Soc.*, **96** [4] 1300–1308 (2013).

90 O. Fabrichnaya, H.J. Seifert, R. Weiland, T. Ludwig, F. Aldinger, and A. Navrotsky, "Phase Equilibria and Thermodynamics in the Y_2O_3-Al_2O_3-SiO_2 System," *Z. Für Met.*, **92** [9] 1083–1097 (2001).

91 A. Shukla, Y.-B. Kang, and A.D. Pelton, "Thermodynamic assessment of the Ce–Si, Y–Si, Mg–Ce–Si and Mg–Y–Si systems," *Int. J. Mater. Res.*, **100** [2] 208–217 (2009).

92 J. Ito and H. Johnson, "Synthesis and Study of Yttrialite," *Am. Mineral.*, **53** 1940–1952 (1968).

93 S. Kumar and C.H. Drummond, "Crystallization of various compositions in the Y_2O_3–SiO_2 system," *J. Mater. Res.*, **7** [04] 997–1003 (1992).

94 K. Fukuda and H. Matsubara, "Anisotropic thermal expansion in yttrium silicate," *J. Mater. Res.*, **18** [07] 1715–1722 (2003).

95 J. Parmentier, P.R. Bodart, L. Audoin, G. Massouras, D.P. Thompson, R.K. Harris, P. Goursat, and J.-L. Besson, "Phase Transformations in Gel-Derived and Mixed-Powder-Derived Yttrium Disilicate, $Y_2Si_2O_7$, by X-Ray Diffraction and ^{29}Si MAS NMR," *J. Solid State Chem.*, **149** [1] 16–20 (2000).

96 J. Felsche, "The crystal chemistry of the rare-earth silicates," *Struct. Bond.*, **13** 99–199 (1973).

97 A.I. Becerro, M. Naranjo, M.D. Alba, and J.M. Trillo, "Structure-directing effect of phyllosilicates on the synthesis of y-$Y_2Si_2O_7$. Phase transitions in $Y_2Si_2O_7$," *J Mater Chem*, **13** [7] 1835–1842 (2003).

98 N. Maier, G. Rixecker, and K.G. Nickel, "Formation and stability of Gd, Y, Yb and Lu disilicates and their solid solutions," *J. Solid State Chem.*, **179** [6] 1630–1635 (2006).

99 J.W. Nowok, J.P. Kay, and R.J. Kulas, "Thermal expansion and high-temperature phase transformation of the yttrium silicate Y_2SiO_5," *J. Mater. Res.*, **16** [08] 2251–2255 (2001).

100 N.A. Toropov and I.A. Bondar, "Silicates of the rare earth elements," *Bull. Acad. Sci. USSR Div. Chem. Sci.*, **10** [4] 502–508 (1961).

101 C. Argirusis, G. Antonaropoulos, G. Sourkouni, and F. Jomard, "Oxygen tracer diffusion in single crystalline yttrium silicate," *Solid State Ion.*, **262** 548–550 (2014).

102 C. Argirusis, T. Damjanović, and G. Borchardt, "Yttrium silicate coating system for oxidation protection of C/C–Si–SiC composites: Electrophoretic deposition and oxygen self-diffusion measurements," *J. Eur. Ceram. Soc.*, **27** [2–3] 1303–1306 (2007).

103 S. Stecura and W.J. Campbell, *Thermal expansion and phase inversion of rare-earth oxides*. U.S. Dept. of the Interior, Bureau of Mines, 1961.

104 P. Zhang, A. Navrotsky, B. Guo, I. Kennedy, A.N. Clark, C. Lesher, and Q. Liu, "Energetics of Cubic and Monoclinic Yttrium Oxide Polymorphs: Phase Transitions, Surface Enthalpies, and Stability at the Nanoscale," *J. Phys. Chem. C*, **112** [4] 932–938 (2008).

105 M.F. Berard, C.D. Wirkus, and D.R. Wilder, "Diffusion of Oxygen in Selected Monocrystalline Rare Earth Oxides," *J. Am. Ceram. Soc.*, **51** [11] 643–647 (1968).

[106] I. Mayer and I. Felner, "High-temperature X-ray study of rare-earth silicides," *J. Common Met.*, **29** [1] 25–31 (1972).

[107] B.E. Deal and A.S. Grove, "General Relationship for the Thermal Oxidation of Silicon," *J. Appl. Phys.*, **36** [12] 3770–3778 (1965).

[108] C.W. Bale, E. Bélisle, P. Chartrand, S.A. Decterov, G. Eriksson, A.E. Gheribi, K. Hack, I.-H. Jung, *et al.*, "FactSage thermochemical software and databases, 2010–2016," *Calphad*, **54** 35–53 (2016).

[109] A.V. Plyasunov, "Thermodynamic properties of H_4SiO_4 in the ideal gas state as evaluated from experimental data," *Geochim. Cosmochim. Acta*, **75** [13] 3853–3865 (2011).

[110] Q.N. Nguyen, D.L. Myers, N.S. Jacobson, and E.J. Opila, "Experimental and Theoretical Study of Thermodynamics of the Reaction of Titania and Water at High Temperatures," *NASA Tech. Memo.-2014-218372*, (2014).

[111] S. Ueno, D.D. Jayaseelan, N. Kondo, T. Ohji, and S. Kanzaki, "Anisotropic Behavior of Water Vapor Corrosion of Rutile TiO_2 at High Temperature," *Mater. Trans. JIM*, **45** [2] 281–283 (2004).

[112] E. Courcot, F. Rebillat, F. Teyssandier, and C. Louchet-Pouillerie, "Stability of rare earth oxides in a moist environment at high temperatures—Experimental and thermodynamic studies. Part I: The way to assess thermodynamic parameters from volatilisation rates," *J. Eur. Ceram. Soc.*, **30** [9] 1903–1909 (2010).

[113] O.H. Krikorian, "Predictive calculations of volatilities of metals and oxides in steam-containing environments," *High-Temp. High-Press.*, **14** 387–397 (1982).

[114] J. Welty, *Fundamentals of Momentum, Heat, and Mass Transfer*. Wiley, 2001.

[115] R.A. Svehla, *Estimated Viscosities and Thermal Conductivities of Gases at High Temperatures*, (1962).

[116] G.H. Geiger and D.R. Poirier, *Transport phenomena in metallurgy*. Addison-Wesley Pub. Co., MA, 1973.

[117] T.K. Sherwood, R.L. Pigford, and C.R. Wilke, *Mass Transfer*. McGraw-Hill, 1975.

[118] F.M. White, *Fluid Mechanics*. McGraw Hill, 2011.

[119] E.J. Opila and N.S. Jacobson, "Stability of Materials in High Temperature Water Vapor: SOFC Applications;" in *Proc. 34th Int. Conf. Adv. Ceram. Compos.* Daytone Beach, FL, 2010.

[120] N. Birks, G.H. Meier, and F.S. Pettit, *Introduction to the High Temperature Oxidation of Metals*. Cambridge University Press, 2009.

[121] P.J. Heaney, C.T. Prewitt, and G.V. Gibbs, *Silica: Physical Behavior, Geochemistry & Materials Applications*. Mineralogical Society of America, 1994.

[122] M.D. Beals and S. Zerfoss, "Volume Change Attending Low-To-High Inversion Of Cristobalite," *J. Am. Ceram. Soc.*, **27** [10] 285–292 (1944).

[123] D.R. Peacor, "High-temperature single-crystal study of the cristobalite inversion," *Z. Für Krist.-Cryst. Mater.*, **138** [JG] 274–298 (1973).

[124] E. Courcot, F. Rebillat, F. Teyssandier, and C. Louchet-Pouillerie, "Thermochemical stability of the Y_2O_3–SiO_2 system," *J. Eur. Ceram. Soc.*, **30** [4] 905–910 (2010).

[125] K.N. Lee and R.A. Miller, "Development and environmental durability of mullite and mullite/YSZ dual layer coatings for SiC and Si_3N_4 ceramics," *Surf. Coat. Technol.*, **86**–**87**, **Part 1** [0] 142–148 (1996).

[126] K.N. Lee, "Key Durability Issues With Mullite-Based Environmental Barrier Coatings for Si-Based Ceramics," *J. Eng. Gas Tubines Power*, **122** [4] 632–636 (2000).

[127] R.N. Patil and E.C. Subbarao, "Axial thermal expansion of ZrO_2 and HfO_2 in the range room temperature to 1400C," *J. Appl. Crystallogr.*, **2** [6] 281–288 (1969).

[128] E.J. Opila, N.S. Jacobson, D.L. Myers, and E.H. Copland, "Predicting oxide stability in high-temperature water vapor," *JOM*, **58** [1] 22–28 (2006).

[129] P.J. Meschter, E.J. Opila, and N.S. Jacobson, "Water vapor–mediated volatilization of high-temperature materials," *Annu. Rev. Mater. Res.*, **43** 559–588 (2013).

[130] S. Ueno, T. Ohji, and H.T. Lin, "Corrosion and recession behavior of zircon in water vapor environment at high temperature," *Corros. Sci.*, **49** [3] 1162–1171 (2007).

[131] Z. Sun, M. Li, and Y. Zhou, "Recent progress on synthesis, multi-scale structure, and properties of Y–Si–O oxides," *Int. Mater. Rev.*, **59** [7] 357–383 (2014).

[132] I. MacLaren, R. Schierholz, P.A. Trusty, and C.B. Ponton, "Silica Glass Segregation in 3 wt% LiF-Doped Hot-Pressed $Y_2Si_2O_7$," *J. Am. Ceram. Soc.*, **90** [10] 3307–3310 (2007).

[133] A.W. Searcy, D.V. Ragone, U. Colombo, and F. Donegani, *Chemical and mechanical behavior of inorganic materials*. Wiley-Interscience, 1970.

[134] N. Epstein, "On tortuosity and the tortuosity factor in flow and diffusion through porous media," *Chem. Eng. Sci.*, **44** [3] 777–779 (1989).

135 C.E. Curtis, L.M. Doney, and J.R. Johnson, "Some Properties of Hafnium Oxide, Hafnium Silicate, Calcium Hafnate, and Hafnium Carbide," *J. Am. Ceram. Soc.*, **37** [10] 458–465 (1954).

136 J.A. Kilner, B.C.H. Steele, and L. Ilkov, "Oxygen self-diffusion studies using negative-ion secondary ion mass spectrometry (SIMS)," *Solid State Ion.*, **12** 89–97 (1984).

137 R.A.D. Souza, J.A. Kilner, and J.F. Walker, "A SIMS study of oxygen tracer diffusion and surface exchange in $La_{0.8}Sr_{0.2}MnO_{3+\delta}$," *Mater. Lett.*, **43** [1–2] 43–52 (2000).

138 J. Crank, *The mathematics of diffusion*. Clarendon Press, 1975.

139 D. Reed and B.J. Wuensch, "Ion-Probe Measurement of Oxygen Self-Diffusion in Single-Crystal Al_2O_3," *J. Am. Ceram. Soc.*, **63** [1–2] 88–92 (1980).

140 S. Cooper, "Quantifying the Transport Properties of Solid Oxide Fuel Cell Electrodes;" PhD Dissertation, Imperial College, London, United Kingdom, 2016.

141 J.D. Cawley and R.S. Boyce, "A solution of the diffusion equation for double oxidation in dry oxygen including lazy exchange between network and interstitial oxygen," *Philos. Mag. A*, **58** [4] 589–601 (1988).

142 J.D. Kalen, R.S. Boyce, and J.D. Cawley, "Oxygen Tracer Diffusion in Vitreous Silica," *J. Am. Ceram. Soc.*, **74** [1] 203–209 (1991).

143 F.J. Norton, "Permeation of Gaseous Oxygen through Vitreous Silica," *Nature*, **191** [4789] 701 (1961).

144 A. Atkinson, F.C.W. Pummery, and C. Monty, "Diffusion of ^{18}O Tracer in NiO Grain Boundaries;" pp. 359–370 in *Transp. Nonstoichiom. Compd.* Edited by G. Simkovich and V.S. Stubican. Springer US, Boston, MA, 1985.

145 Y. Oishi and W.D. Kingery, "Self-Diffusion of Oxygen in Single Crystal and Polycrystalline Aluminum Oxide," *J. Chem. Phys.*, **33** [2] 480–486 (1960).

146 R.T.P. Whipple, "CXXXVIII. Concentration contours in grain boundary diffusion," *Lond. Edinb. Dublin Philos. Mag. J. Sci.*, **45** [371] 1225–1236 (1954).

147 A.D.L. Claire, "The analysis of grain boundary diffusion measurements," *Br. J. Appl. Phys.*, **14** [6] 351 (1963).

148 Y. Chung and B.J. Wuensch, "An improved method, based on Whipple's exact solution, for obtaining accurate grain-boundary diffusion coefficients from shallow solute concentration gradients," *J. Appl. Phys.*, **79** [11] 8323–8329 (1996).

149 B. Liu, J. Wang, F. Li, J. Wang, and Y. Zhou, "Mechanisms of Mono-Vacancy and Oxygen Permeability in Y_2SiO_5 Orthosilicate Studied by First-Principles Calculations," *J. Am. Ceram. Soc.*, **95** [3] 1093–1099 (2012).

150 B. Good, "Kinetic Monte Carlo Silumation of Oxygen Diffusion in Ytterbium Disilicate;" in 2015.

151 B. Good, "Kinetic Monte Carlo Simulation of Oxygen Diffusion in Ytterbium Disilicate," *MRS Adv. Mech. Behav. Fail. Mater.*, **1** [17] 1203–1208 (2016).

152 D.S. Fox, E.J. Opila, and R.E. Hann, "Paralinear Oxidation of CVD SiC in Simulated Fuel-Rich Combustion," *J. Am. Ceram. Soc.*, **83** [7] 1761–1767 (2000).

153 J.A. Costello and R.E. Tressler, "Oxidation Kinetics of Hot-Pressed and Sintered α-SiC," *J. Am. Ceram. Soc.*, **64** [6] 327–331 (1981).

154 D. Cubicciotti and K.H. Lau, "Kinetics of Oxidation of Yttria Hot-Pressed Silicon Nitride," *J. Electrochem. Soc.*, **126** [10] 1723–1728 (1979).

155 D.M. Mieskowski and W.A. Sanders, "Oxidation of Silicon Nitride Sintered with Rare-Earth Oxide Additions," *J. Am. Ceram. Soc.*, **68** [7] C-160–C-163 (1985).

156 F.F. Lange, B.I. Davis, and H.C. Graham, "Compressive Creep and Oxidation Resistance of an Si3N4 Material Fabricated in the System Si_3N_4-Si_2N_2O-$Y_2Si_2O_7$," *J. Am. Ceram. Soc.*, **66** [6] C-98–C-99 (1983).

157 D.R. Clarke, "Thermodynamic Mechanism for Cation Diffusion Through an Intergranular Phase: Application to Environmental Reactions with Nitrogen Ceramics;" pp. 421–426 in *Prog. Nitrogen Ceram.* Edited by F.L. Riley. Springer Netherlands, 1983.

158 E. Opila, "Influence of Alumina Reaction Tube Impurities on the Oxidation of Chemically-Vapor-Deposited Silicon Carbide," *J. Am. Ceram. Soc.*, **78** [4] 1107–1110 (1995).

159 Z. Zheng, R.E. Tressler, and K.E. Spear, "The effect of sodium contamination on the oxidation of single crystal silicon carbide," *Corros. Sci.*, **33** [4] 545–556 (1992).

160 I. Barin, O. Knacke, and O. Kubaschewski, *Thermochemical properties of inorganic substances*. Springer Berlin Heidelberg, Berlin, 1977.

161 Y. Ogura, M. Kondo, T. Morimoto, A. Notomi, and T. Sekigawa, "Oxygen Permeability of Y2SiO5," *Mater. Trans.*, **42** [6] 1124–1130 (2001).

162 J. Young, "Chapter 5 Oxidation of Alloys I: Single Phase Scales;" pp. 185–246 in *High Temp. Oxid. Corros. Met.* Edited by D.J. Young. Elsevier Science, 2008.

[163] H.J. Borchardt, "On the oxidation of yttrium," *J. Inorg. Nucl. Chem.*, **26** [5] 711–719 (1964).

[164] M. Zinkevich, "Thermodynamics of rare earth sesquioxides," *Prog. Mater. Sci.*, **52** [4] 597–647 (2007).